Computational Nanoscience and Molecular Modelling of shock wave interactions with biological membranes

Damiani Sourmaidou

Submitted for the Degree of Ph.D.

Department of Fluid Mechanics and Computational Sciences
Cranfield University
Cranfield, UK

2011

Cranfield University

School of Engineering

PhD

Damiani Sourmaidou

Computational Nanoscience and Molecular Modelling of shock wave interactions with biological membranes

Supervisors: Dr. Nikolaos Asproulis
Prof. Dimitris Drikakis

2011

Abstract

Lateral diffusion of membrane components (lipids and proteins) is an important membrane property to measure since the essential process of absorption of anti-cancer and other drugs -some of which are not soluble in lipids and therefore would not be able to penetrate the cell membrane through passive diffusion- lies on it. In particular, the procedure of diffusion into the cell cytoplasm is reliant on free volumes in the membrane (passive diffusion) as well as carrier proteins (facilitated diffusion). By enhancing the mobility of lipids and/or proteins, the possibility of the carrier protein to "encapsulate" pharmacological components maximizes, as a "scanning" of the proteins gets performed due to the fluid phase of a biological membrane. At the same time, the increased mobility of the lipids facilitates the passage of lipid-soluble molecules into the cell. Thus, given that the success of anticancer treatments heavily depends on their absorption by the cell, a significant enhancement of the cell membrane permeability (permeabilisation) is rendered vital to the applicability of the technique. For this reason, there is augmented interest in combined methods such as Nanotechnology based drug delivery that is focused on the development of optimally designed therapeutic agents along with the application of shock waves to enhance the membrane permeability to the agents. This study examines the impact of shock waves on a numerical model of a biological membrane. This biological membrane is a 1-palmitoyl-2-oleoyl-sn-glycero-3-phosphocholine (POPC) lipid bilayer model consisted of 52 lipids on the upper layer and 52 lipids on the lower one, while 15134 water molecules and 59338 atoms are employed for the modeling of the complete system. Simulations were carried out using Cranfield University's HP computer "Astral" to monitor a number of properties related to the membrane such as membrane thickness, area per lipid, and lateral diffusion. The method that was employed is Molecular Dynamics, a principal computational tool in the theoretical study of biological systems. Two sets of shock wave configurations were tested: normal and oblique shock waves. Each of these sets was further examined under two sets of conditions: i) conserved number of moles (N), pressure (P), and temperature (T)- NPT ensemble, and ii) fixed number of moles (N), volume (V), and energy (E)- NVE ensemble. Regarding the perpendicular to the membrane shock wave configuration, the shock impulse applied varied between $0.33 mPa \cdot s$ and $10 mPa \cdot s$, while the thicknesses of the shock waves were 5Å, 7Å, 10Å, and 12Å. In the case of oblique shock waves, shock impulses varied from $0.33 mPa \cdot s$ to $2 mPa \cdot s$ and the incidence angles applied varied between 10° and 80°. The results of this study show that for the normal shock configuration there is significant dependance between the thickness of the shock and the diffusion coefficient, which increases as the thickness of the shock increases until a maximum value is obtained and then follows a small decay. It has been further shown that in overall diffusion coefficients that resulted from simulations run with NVE ensemble were higher than those obtained under the NPT ensemble. As the incidence angle is introduced an initial increase of lateral diffusion is observed due to

the increase of the parallel to the wall shock velocity components. Concluding, additional studies have to be performed aiming to study the response of more complicated membrane models where proteins are also considered. Defining the self diffusion coefficients of the surface proteins will have a great contribution towards a better understanding of the mechanisms for optimising the drug delivery and drug adsorption. Finally, longer simulation time would perhaps enhance the understanding of the biological response presented in the current study.

Keywords:

Molecular Dynamics, biological membrane, cancer treatment, incident angle, lateral diffusion, drug delivery, NAMD

Acknowledgements

I would like to express my sincere gratitude to my supervisors, Dr. Nikolaos Asproulis and Prof. Dimitris Drikakis, for the invaluable guidance during the course of this PhD.

At the same time, I am deeply thankful to my parents for providing for the financial needs of this PhD, as well as for the moral support. This work is dedicated to them.

"I am indebted to my parents for living, but to my teacher for living well."

Alexander The Great

Contents

List of Figures

List of Tables

Latin Symbols

m_a	mass of atom a (in atomic mass units)
$\vec{r_a}$	position of atom a
d	particle displacement (in Å)
up	shock-induced speed of particle
K	partition coefficient
D	diffusion coefficient (in cm^2/s or $\mu m^2/s$ or nm^2/ms)
D_{lat}	lateral diffusion coefficient (in cm^2/s)
Dx	thickness cell membrane
P_c	permeability coefficient (in cm/sec)
P_{aq}	permeability coefficient of unstirred water layer
f_{HA}	fraction of unionised species
$U(total)$	total potential energy
r_{ij}	distance between pair of covalently bonded atoms
k	spring constant
k_θ	angle constant
$k_{\mathrm{ub}}(r_{ik} - r_{\mathrm{ub}})^2$	Urey-Bradley term
r_{ik}	distance between (i,k)-pair of atoms
r_{ub}	equilibrium distance
n	constant of periodicity
q_i	atomic charge
C	Coulomb constant
V	system volume
W	piston mass
$\vec{R_i}$	noise on atoms
R_e	noise on piston
P	pressure (in atm or bar or MPa)
T_{I_p}	duration of impulse application
A	area
m	mass of water molecule
N_w	number of water molecules in water slab
T_{sw}	shock wave thickness
N_L	number of lipids
$r_i(t)$	position of lipid i at time t
$\langle\rangle$	average of time steps and/or particles
N	number of atoms in the system
m_i	mass of atom i
t	time point

Greek Symbols

ϵ_0	dielectric constant

ϵ_{14}	scaling factor equal to 1
θ	incident angle
θ_0	equilibrium angle
ψ	angle formed by the (i, j, k)-plane and the (j, k, l)-plane
ϕ	phase shift angle
τ	oscillation period
υ_i	velocity of atom i
η	viscosity

List of Abbreviations

MD	molecular dynamics
MSD	mean square displacement
EMD	equilibrium molecular dynamics
NEMD	non-equilibrium molecular dynamics
NVE	micro-canonical ensemble
NPT	isothermal isobaric ensemble
NAMD	nano-molecular dynamics
VMD	visual molecuar dynamics
DPPC	1,2-Dipalmitoyl-sn-glycero-3-phosphocholine
DMPC	1,2-Dimyristoyl-sn-glycero-3-phosphocholine
POPC	1-Palmitoyl-2-oleoyl-sn-glycero-3-phosphocholine
POPE	1-Palmitoyl-2-oleoyl-sn-glycero-3-phosphoethanolamine
PLPC	palmitoyl-linoleoyl-phosphatidylcholine
DPPS	dipalmitoylphosphatidylserine
DOPC	dioleoyl-phosphatidylcholine
$mPa \cdot s$	millipascal-second
PA	phosphatic acid
PG	phosphatidylglycerol
PE	phosphatidylethanolamine
PC	phosphatidylcholine
PS	phosphatidylserine
PI	phosphatidylinositol
COM	centre of mass
PDT	photodynamic therapy
ECT	Enhanced local chemotherapy of solid cancer Tumours
ArF	argon fluoride laser
LSW	laser-induced stress waves
ESW	extracorporeal shock waves
NMR	Nuclear magnetic resonance
FPR	Fluorescence photobleaching and recovery
NMF	N-methylformamide
GUV	giant unilamellar vesicle
PEG	Polyethylene glycol
CG	coarse-grain
FITC-D	fluorescein isothiocyanate dextran
HL60	Human promyelocytic leukemia cells

CHAPTER 1

Introduction

Every year more than 8 million people die due to cancer, making it a leading cause of death in the Western World [15, 16]. Thus, efforts to establish new methods that improve drug delivery and efficiency have been increased. Cancer treatment research involves various methods, from the development of vaccines to the use of advanced surgical procedures. The effectiveness of the treatment lies on the suitability of the pharmacological compound and its delivery to the desired pathological area [15]. Therefore, scientists have been researching techniques to increase drug absorption into the cell cytoplasm, via generating transient permeabilisation of the cell membrane [13, 15]. This transient permeabilisation can be induced using two different methods [15]. The first one is altering the composition of lipids in the lipid bilayer with the introduction of detergents [17], bacterial toxins [18], or virus mediated fusogenic lyposomes [19]. A second method is applying electric fields [20], ultrasounds [10, 21], or shock and stress waves [22–25].

Experimental procedures when applied to micro and nano scales are usually associated with financial burden and technical difficulties in obtaining accurate measurements. Therefore, the scientific community has embraced computational tool as a viable approach for performing complementary studies on biological systems aiming at establishing ways to enhance drug diffusion through the cell membrane [15].

The significance of computer models is that they allow for the implementation of conditions that may currently be hard to reproduce in vitro or have not yet been studied experimentally. In that sense, through computational studies it is feasible to assess diffusion amongst other mechanisms as well as test a new theory or hypothesis or even make a prediction about a biological response [26]. At the same time, computer models can be employed to rule out certain mechanisms from a list of potential explanations for a biological phenomenon observed in vivo.

The current chapter serves as a background on the topic of biological membranes and their main structure and functions, provides an overview of approaches towards enhancing drug delivery especially in the area of cancer therapy, and discusses the limitations related

with each strategy. Finally the main aims and objectives of the current study are being introduced.

1.1 Biological Membranes and Cancer Treatment

1.1.1 Biological Membranes

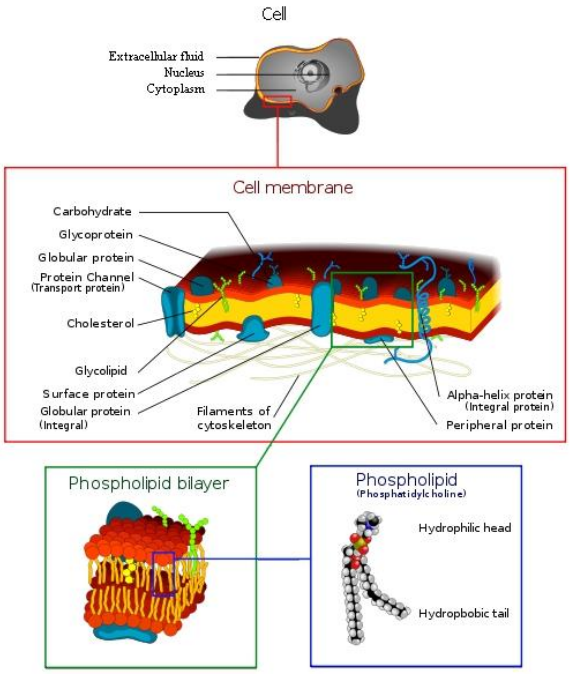

Figure 1.1: Illustration of a Eukaryotic cell membrane [1]

Biological membranes (bio-membranes) are also known as cell membranes and consist of lipids and proteins. In their simplest form, which is the lipid bilayer, they consist of two layers of lipid molecules (lipid monolayers). The lipid composition of a membrane is mainly phospholipids that appear to have hydrophobic (non-polar) ends or tails and hydrophilic (polar) ends or heads [27] (see figure 1.2).

Common polar head groups of lipids of an amphipathic membrane are alcohols such as ethanolamine, choline, serine, glycerol and inositol (see figure 1.3). The polar groups are attached to fatty acids such as oleic acid to form the membrane lipids [28]. In particular in the absence of a head group, the relevant phospholipid is the phosphatic acid (PA), while glycerol, ethanolamine, choline, serine and inositol give phosphatidylglycerol (PG), phosphatidylethanolamine (PE), phosphatidylcholine (PC), phosphatidylserine (PS), and phosphatidylinositol (PI), respectively [29]. At the same time, sphingolipids form

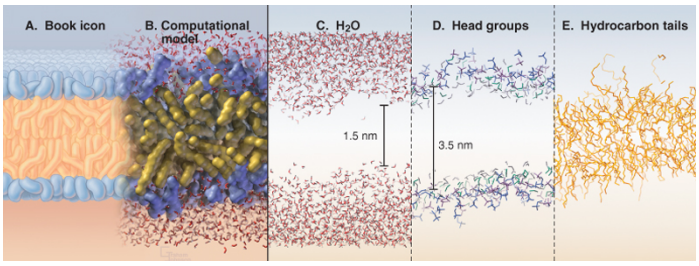

Figure 1.2: Lipids and their hydrophilic and hydrophobic parts [2].

from sphingosine and sphingomyelin is the derivative of a phosphocholine or phosphoethanolamine head group [28, 29]. Finally, cholesterol (see figure 1.4) is an important lipid component of cell membranes with a hydroxyl as its polar group [28, 29].

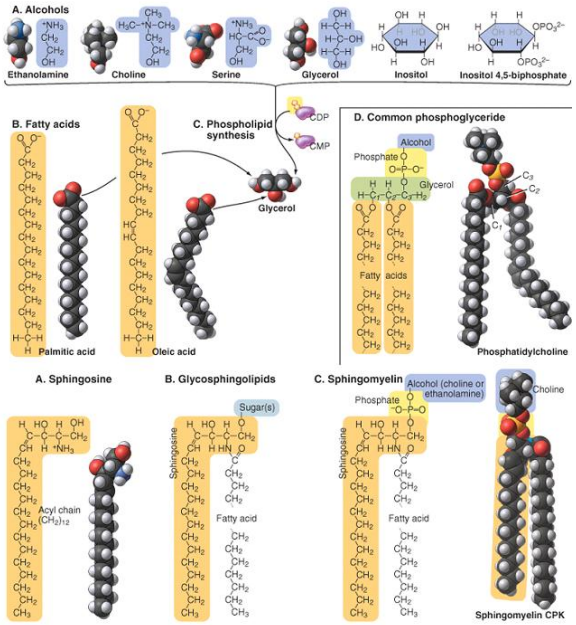

Figure 1.3: Lipid composition [2].

Bio-membranes are approximately 7nm wide and surround the cells, define the cells' physical boundaries and disable certain substances from entering the cell. The study of the (ultra)structure of biomembranes has led to the development of theories that attempted to describe it and have evolved since the early 1920s [2].

In 1926 Gorder and Grendel suggested a model of a simple lipid bilayer [2]. During the following decade scientists realised that this model could not explain the mechanical properties of the membrane and in 1943 Davson and Danielli suggested a membrane model according to which a surface coating of proteins was added to the initial model of the lipid bilayer [2]. In 1972 the concepts about membrane structure further developed to the

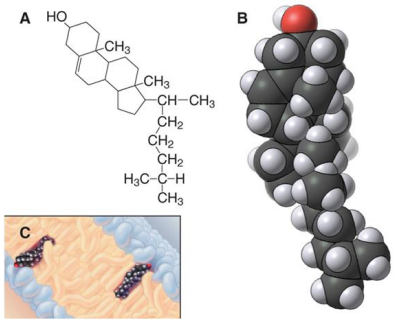

Figure 1.4: Atomic representation of lipids (cholesterol) in a lipid bilayer [2].

"fluid mosaic model" [30] by Singer and Nicholson, which introduced a transmembrane floating of proteins in a fluid-like lipid bilayer [30]. Finally, in 2001 the atomic level version of the "fluid mosaic model" was created, by involving high resolution peripheral and integral protein structures [2] (see figure 1.5). This last lipid bilayer model is the one that is currently accepted and is characterised as semi-permeable.

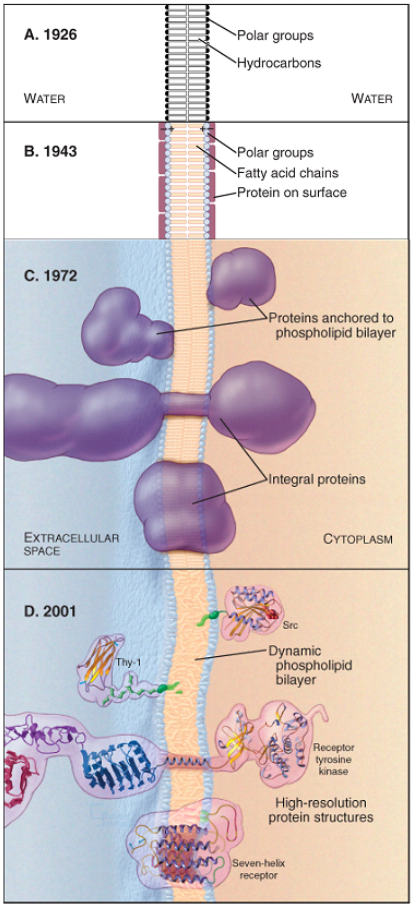

Figure 1.5: The development of concepts about the bio-membrane structure [2]

Lipid bilayers are thought to be partially permeable [31], since they allow the penetration of specific molecules into the cell or out of it - depending on whether they are essential for the life of the cell or need to be disposed by the cell, respectively. In particular, small molecules, hydrophobic molecules, pass across the membrane easily, whereas large molecules, such as amino acids and sugars cannot.

Other characteristics that may exist in the biomembrane are the heterogeneity of the lipids, as well as the asymmetrical positioning of the lipids between its upper and lower monolayer (asymmetric membrane), as shown in figure 1.6 [2]. An asymmetric lipid bilayer can appear to have a different composition or ratio of constituents - such as amphipathic lipid-based molecules and proteins- on one leaflet than on the other. Both the aforementioned cell membrane characteristics are responsible for the net negative charge of the cytoplasmic surface (the inner membrane monolayer), and the existence of rafts formed by cholesterol and sphingolipids [2].

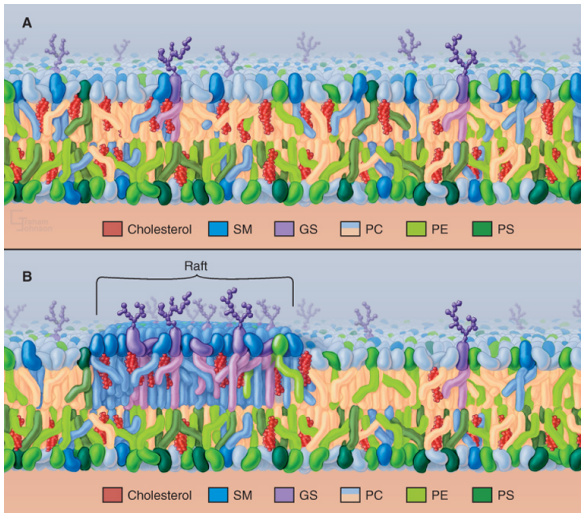

Figure 1.6: The heterogeneity and asymmetrical lipid distribution between the two leaflets (monolayers) of a biological membrane. SM: Sphingomyelin GS: Glycosphingolipid PC: Phosphatidylcholine PE: Phosphatidylethanolamine PS: Phosphatidylserine [2]

Porasso and Cascales created an asymmentric membrane in an effort to have a model that resembles a eukaryotic cell membrane. This model has dipalmitoylphosphatidylcholine (DPPC) on one leaflet while the other one consists of both dipalmitoylphosphatidylcholine and dipalmitoylphosphatidylserine (DPPS)[3] (see figure 1.7). It must be noted, however, that the biological membrane as described above is related to healthy cells. In the case of a cancer disease being suffered by the cell, the cell membrane may be dramatically affected.

It is a shared view that cancer is either caused by an inherited cancer susceptibility gene or is an acquired molecular genetic disease, characterised by genetic instability, altered cellular behaviour, and altered cell extracellular matrix interactions [16]. Reported differences in the appearance and therefore functionality of the membrane include change in the type and concentration of lipids, proteins, enzymes, receptors and antigens [32]. Studies on

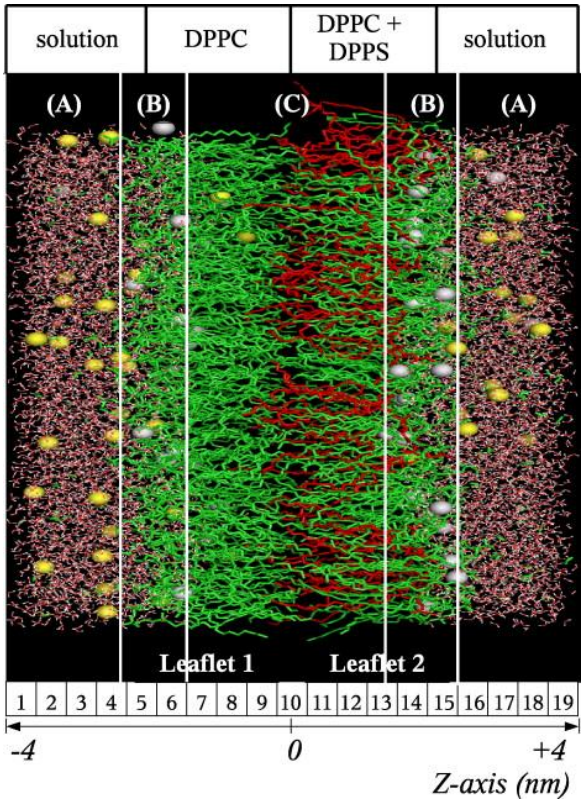

Figure 1.7: The lipid bilayer with calcium ions in white, chloride ions in yellow and water molecules as red and white sticks. DPPS is in red and DPPC has green wireframes. [3]

cancer cells have shown a decrease in the concentration of some lipids and an increase of others, while proteins of high molecular weight have been reported to decrease or disappear in transformed cells [33]. Furthermore, it has been noticed that in most membranes certain receptors had increased in number, although the total number of cell receptors may have remained the same [34] and there was a qualitative or quantitative difference in some antigens of malignant cells [33]. Finally, in some cases, formations of cytoplasm protrusions known as "microvilli" [32, 35] occurred (see figure 1.8) and gave the cell surface a sparking appearance [4]. Under the application of shock waves, microvilli disappear from the cell surface [36] and numerous dimples(diameters distributed from 0.05 to 0.5 microns) form, enabling reagents such as propidium iodide or 5(6)-carboxyfluorescein to enter the cell [37], as observed with scanning and transmission electron microscopes. It is to be underlined that it has been evident that even when there are no apparent differences in the membrane, its ultrastructure could have altered [34].

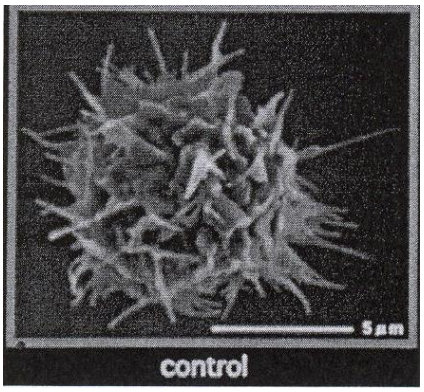

Figure 1.8: Microvilli on cancer cells. [4]

1.1.2 Drug Delivery and Cancer treatment

Cancer drug delivery within the recent years has been trying to bring different technologies together with the purpose of building a robust strategy that could treat cancer. Nanotechnology, advanced polymer chemistry, and electronic engineering, amongst others, are combined with chemotherapy and radiotherapy in order to provide a new approach to cure the disease while preventing destruction of healthy tissues as well as resistance to the drug.

In particular, the relevant strategies employed involve the direct introduction of anti-cancer drugs into the neoplasm, choosing particular pathways for the drug delivery, the systemic delivery targeted to the tumor, the tumor blood vessel targeted drug delivery, special carriers and formulations of anti-cancer drugs, transmembrane delivery to intracellular targets, and biological therapies [38].

The direct introduction of anti-cancer drugs can be achieved through the use of techniques such as electrochemotherapy, which is a drug delivery enhanced by electroporation. A route-related drug delivery strategy is the transdermal one [38]. The systemic delivery includes techniques like heat activated targeted drug delivery and filtration of the anti-cancer drug across the vessels to the cancerous tumor by the application of pressure [38]. A targeted to cancer blood vessels strategy is the angiolytic therapy [38]. The strategy about the use of special carriers and formulations can imply chemotherapy enhanced by carbohydrates [38]. One way of achieving transmembrane delivery is through the use of vitamins loaded with anti-cancer agents, and lastly gene therapy is a typical biological therapy [38].

Notable examples of recent combined methods to cure cancer consist of UV light-induced drug penetration into the tumor, different approaches involving carbon materials for malignant cells, and cancer drug delivery with polymer nanoparticles. In the first case, scientists have applied light illumination to promote the permeation of the polymer-cell-penetrating peptide conjugates into the cancer cells in vivo [39]. This combined technique resembles the photodynamic therapy (PDT), which applies light with the sole purpose of

A. Cellular and tumor integrity
   1. Inherent nature of cell
      a) Growth rate or doubling time
      b) Membrane fluidity
      c) Ability to repair damage
      d) Genetic and molecular status
   2. Stage of cellular growth
   3. Nutritional status of cell
   4. Cell concentration or cell density
   5. Vascularization and oxygen tension within the tumors
   6. Immunological response

B. Stress induced by ultrasound
   1. Ultrasound intensity
   2. Sound frequency
   3. Wave form
   4. Duration of exposure
   5. Cavitational potential
      a) Gas saturation and the type of gas
      b) Use of microbubbles

C. Other physical factors
   1. Temperature
   2. Osmotic pressure
   3. Viscosity of the medium
   4. Ambient pressure

D. Chemical factors
   1. Presence of substance active against the tumor
   2. Presence of potentially radical-producing substances
   3. Increased uptake of harmful substances
   4. Increased concentration or accumulation of substances within the exposed site
   5. Other factors such as acidity of the substance
   6. Other possible reactions for the potentiation of the substance by ultrasound

Figure 1.9: Possible determinants of the applicability of ultrasound therapy with anticancer agents [5].

killing cancerous cells as well as tumor components, and considerably assists the traditional polymer-cell-penetrating peptide method which is highly efficient in vitro but totally fails to achieve cell-specific delivery in vivo. Regarding the case about the carbon materials, scientists have managed to increase the drug intake by the cancer cells in vivo and in vitro by applying nano-graphene and carbon nanotubes, that are both carbon nano-materials, along with photothermal (by employing continuous near infrared laser), photoacoustic (by using pulsed near infrared laser), and radiofrequency ablation therapy (by creating a radiofrequency field) [40]. Lastly, researchers have been investigating the combined effects of initially applying radio waves via a thermal source, such as a radio frequency generator, on a tumor site and then injecting into the blood a drug enclosed in a bio-compatible material, such as curcumin-loaded (thermoresponsive) polymeric nanoparticles [41], as well as ultrasounds and anticancer agents. However, the suitability of the combined methods lies on many parameters (see figure 1.9).

It is evident that a crucial part of drug delivery is the efficiency of absorption of the drug from the cancer cell. The absorption of the anti-cancer as well as any pharmacological compound further lies in the permeability of the cell membrane as well as the selective penetration of the active pharmacological components into the diseased cells. Nanomedicine has been developing new methods for the selective absorption of the anti-cancer agents from the cancer cells, as well as designing new carrier systems to decrease biodegradation of the anti-cancer substance, such as iron oxide nanoparticles [42]. At the same time, scientists have been testing and developing techniques that could enhance the permeability of the cell membrane to drugs. This transient permeability can be achieved with the application of electric fields [20], ultrasounds [10] [21], or stress waves [22] [23] [24] [25].

Electroporation

Electroporation is a method used to increase the permeability of a biomembrane to hydrophilic pharmacological compounds by inducing an electric field [43, 44]. The method can be used for drug as well as gene delivery in the cell cytoplasm [45].

Electropulsation In the case of electropulsation, the application of an electric pulse initially increases the potential difference between the membrane monolayers, creating local defects, when a critical strength value (approximately 200 mV) [43, 46, 47] is reached (induction step). For as long as the field is maintaned and characterised by a threshold intensity value that is larger than the critical one, these defects become bigger (expansion step). The stabilisation step takes place when the applied strength value is reduced, which stops the expansion of the pores and finally increases the permeability of the membrane. Should there be a significant delay between two successive applied electric pulses (when the duty cycle, which is the ratio of the time duration of the application of the pulse to the time duration until the next pulse, is less than one), the pores will slowly reseal [43, 48–50].

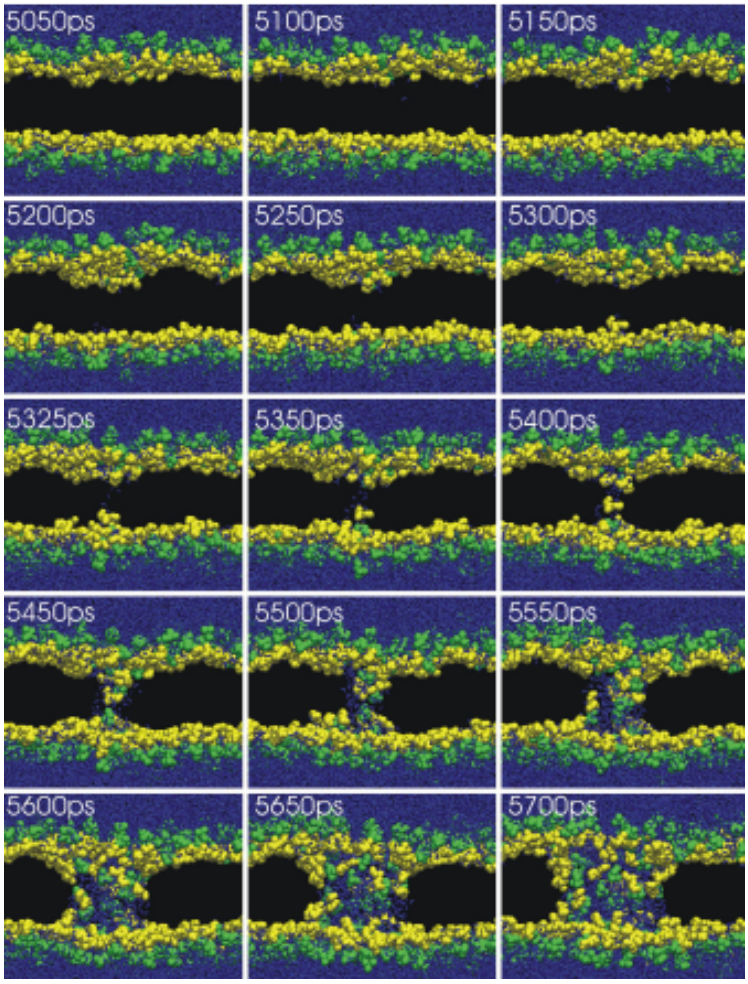

Figure 1.10: Snapshots of pore formation after the application of an electic field of 0.5 V/nm to a DOPC (dioleoyl-phosphatidylcholine) bilayer. The lipid headgroups appear divided in their choline part (green) and the phosphate/glycerol part (yellow). The top monolayer is positively charged with reference to the bottom one [6]

It has been experimentally proven that the biological response (no permeabilization, permeabilization, or rupture of the cell membrane) to the application of electropulsation on the membrane depends on parameters such as the electric field strength, the pulse duration, and the number of pulses, as well as the nature of the lipids [43, 51–54].

According to Weaver [44] there is an effective drug used in clinical trials for solid cancer tumors, which poorly crosses the membrane. The author comments that if bleomycin or any other approved drug was loaded onto highly charged molecules in an effort to enhance the penetration, the drug would become unapproved. A second thought seems to be the adherence of the drug to charged groups introduced via electroporation that could be captured by the intracellular enzymes. However, finding the appropriate structural derivative of the parent compound would be very expensive.

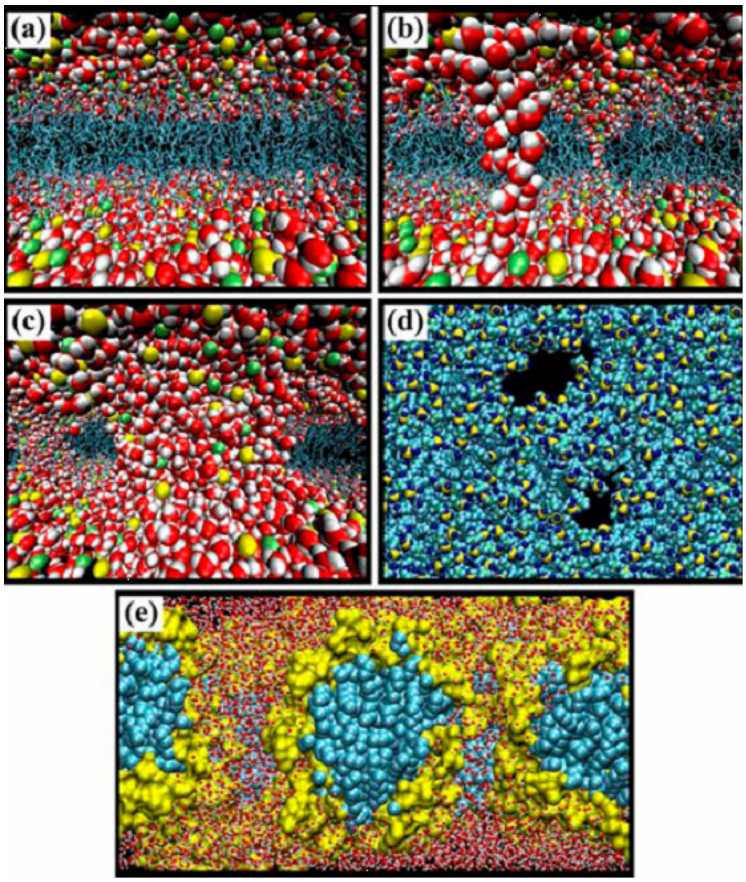

Figure 1.11: Electroporation and formation of water wires under the application of a transverse electric field. In the first three panels oxygen atoms are red, hydrogen atoms are white, lipid phosphate is yellow and nitrogens are green. In the last snapshot the hydrophilic lipid headgroups are yellow and the hydrophobic acyl chains are cyan [7]

Tielemman [6] investigated the phenomenon via molecular dynamics simulations [55–60]. It is interesting that in some cases water molecules can be found within the hydrophobic area of the membrane. The author concludes that pore formation is enhanced in the lipid membrane after the application of an electric field (see figure 1.10). In the case of a membrane with increased levels of cholesterol, or other hydrophobic polymers, the pore formation is debilitated [61–63]. The electric charge of the lipid headgroups and the ionic concentration in the surrounding solution does not affect significantly the pore formation [61–63].

Other Molecular Dynamics simulations for biological membranes show formation of water wires in the beginning of the electroporation under the application of a transverse electric field (see figure 1.11). At a later stage the lipid headgroups stabilise the large water pores [7].

Tielman's simulations show that right after the formation of defects, the lipid bilayer

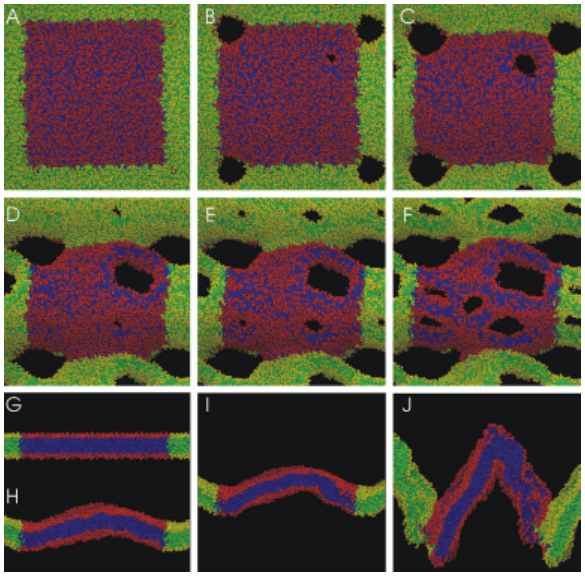

Figure 1.12: Pore formation over time of a lipid bilayer and its final curvature after the application of an electric field [6]

appears curved (see figure 1.12). According to his experiments [6], the critical voltage required to create pores is between 0.25V and 0.50V, whereas his simulations suggest higher voltages.

Finally, simulations as well as experimental data suggest that lipid bilayers do not become significantly thinner under the application of potential difference (figure 1.13).

Transmembrane Ionic Charge Imbalance Gurtovenko and Vattulainen [8] introduce another way in which electroporation can enhance the permeability of the membrane to selected drugs, which is by inducing transmembrane ionic charge imbalance. This method is based on the concept that membranes have ions on their monolayers that are in electrostatic equilibrium which cannot cause transfer of molecules through the hydrophobic region.

The imbalance can be created by adding ions to the outer monolayer and that will lead to excess of ions compared to their concentration in the inner monolayer. The subsequent electrostatic field will apply a force to the ions and the ones that are in excess will start crossing through the membrane hydrophobic region until the equilibrium is reinstated.

According to the authors, the pore that occurs is due to the chain of water molecules that suddenly penetrates the membrane, attracting the hydrophilic headgroups around it. The Na+ ions start to permeate the membrane through this channel until the point when the ionic imbalance no longer permits it.

Complimentary, Weaver [44] reports that Enhanced local chemotherapy of solid cancer

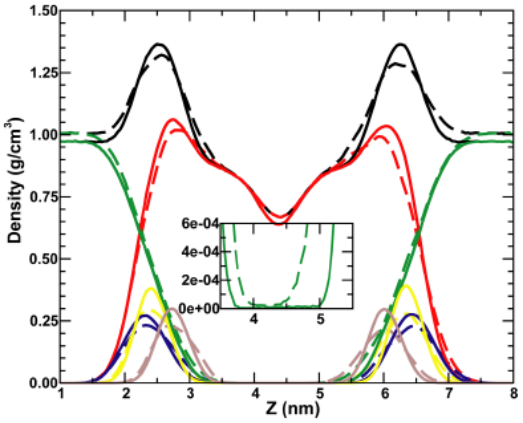

Figure 1.13: Density profile of the membrane under the application of a field of 0.33 V/nm. We can compare the distribution of water (green), lipids (red), phosphate (yellow), choline (blue), glycerol (brown) and all substances (black) when under the external field (dashed lines) to the one without field [6].

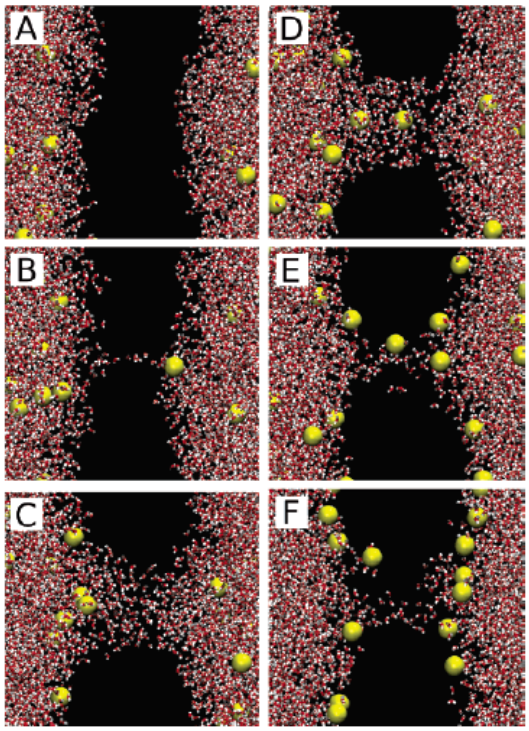

Figure 1.14: Pore formation and ion penetration caused by ion imbalance between the two monolayers of a lipid bilayer. Water appears in red white and Na+ ions in yellow. The direction of the penetration is from the left monolayer with excess Na+ to the right one [8].

Tumours (ECT) is researched in clinical trials using highly charged drug molecules. It could be assumed that the charge of the molecules could be the reason for the creation of the imbalance between the two monolayers that Gurtovenko and Vattulainen [8] describe. The moment an ion crosses through the bilayer, a pore forms that can allow other extracellular solute molecules to penetrate through the hydrophobic region (see figure 1.14).

At the same time, Molecular Dynamics simulations [8] that were performed on protein free membranes involved the creation of a field of 0.41V/nm strength and a transmembrane voltage potential of approximately $2.85 \pm 0.49V$, which supports the literature [6, 8, 64, 65]. Furthermore, an electric field of approximately 0.29 V/nm was proven to able to induce pore formation, although the lowest reported values are of the order of 0.4V/nm.

Stress waves

In the present study the terminology shock wave is extensively employed, however this primarily corresponds to an acoustic wave behaviour and actual shock waves can be generated only under nanobubbles collapsing such as cavitation.

The general term stress wave is used to describe "a compressive wave with a fast rise time which is not necessarily a shock wave in the strict sense" [66], as they are also (mostly) compressive waves, broadband and unipolar. Stress waves form in deformable solid bodies when part of their surfaces becomes subjected to an external load. Initially, the surface particles of the affected area move away from their equilibrium positions, causing a deformation. This deformation is due to the relative motion between surface particles and their neighbouring ones, giving rise to internal stresses as each of these groups of particles apply acting and reacting forces to one another [67]. Subsequently, the neighbouring particles also start to move away from their equilibrium positions, but their motion starts later than the surface particles due to the inertia of particles. Thus, the disturbances caused by an external load on the surface gradually propagate to the rest of the solid body, and stress waves are formed. Some examples of stress waves and their effects can be seen in sound (acoustic) waves, shock waves, and the oscillating motion of the earth caused by earthquakes [67].

When applying stress waves to biological cells and tissues a number of different mechanisms take place (heat, cavitation, plasma and free radicals) resulting in complex biological effects [66]. Hence, it is difficult in some cases to avoid the cell damage since there are too many factors that need to be considered before applying a stress wave (temperature rise issue, cavitation and its concomitants, mechanical stresses and other physical factors) [66].

It seems that the level of the biological response of the cell is defined by the stress gradients and especially the rise time. In particular cell damage depends on stress rate of change more than on peak stress. Although the exact biological effects of the application of stress waves on cells are not known, Doukas et al. [66] conclude that the differences

that appear between the experimental data reports and the literature regarding the number of pulses that are able to lead to such cell phenomena are possibly due to the rise time as well as other characteristics of stress waves (stress duration, decay).

Acoustic (sound) waves Acoustic waves, or sound waves, are mechanical waves which transfer energy from one place to another in the form of pressure variations. Sound waves travel in two distinct forms, which are dependent on the medium it travels through, and the direction of vibration. A wave in which its vibration is perpendicular (transverse) to the direction of motion is known as a transverse wave [67]. Conversely, a wave whose vibration is along the same direction of travel is known as a longitudinal wave. In addition, when a sound wave travels through a fluid, it will travel as a longitudinal wave, and when it travels through a solid it will travel as a transverse wave.

Sonoporation According to Bao et al. [68], sonoporation is "the ultrasonic induction of membrane permeabilisation and resealing". This method involves the creation of oscillating cavitation bubbles (see figure 1.18) that are formed by both the application of ultrasounds onto already existing gases inside the liquid (dissolved gases) and the simultaneous rise in the temperature of the liquid (gases as vaporised liquid) [10].

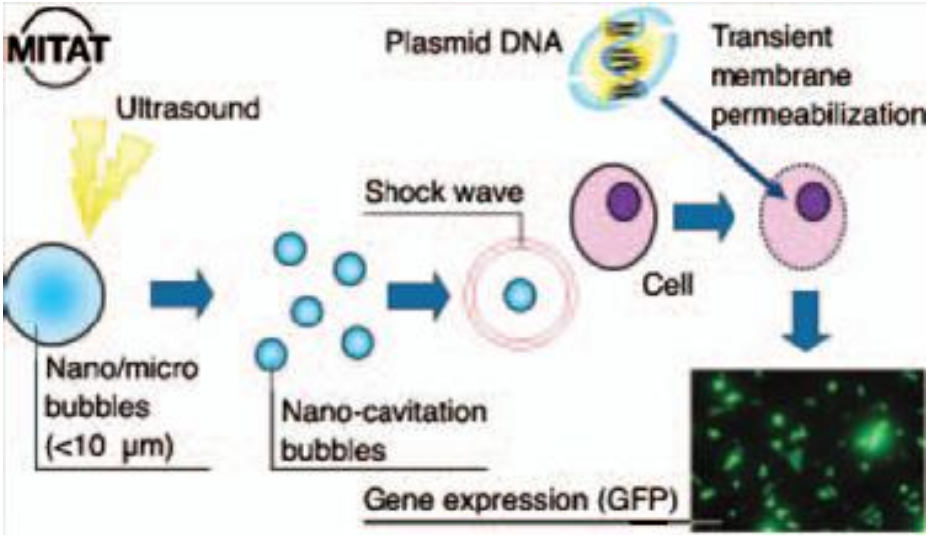

Figure 1.15: Molecular delivery into cells using ultrasounds and nano/microbubbles [9]

A stable cavitation occurs when the pressure from the ultrasound wave on the surface of the bubble alternates from a high peak to a low peak, making the bubble oscillate (i.e. shrink and grow in size) [10]. After a few cycles of greater ultrasound pressures, a violent implosion of the bubbles occurs, subsequently inducing a high velocity liquid microjet. This transient cavitation can have additional side effects, such as the transient significant rise in the local temperature and pressure, the sonoluminesence (emission of light), and the creation of temporary free radicals [10].

Liu [10] suggests that an interesting phenomenon occurs when the apparatus employed resonates. The apparatus in this study is an ultrasound exposure chamber that consists of a cylindrical piezoelectric transducer (lead zirconate titanate, 5 cm OD, 4.5 cm ID, 2.5 cm length) in between two 10 cm lengths of 1.5 inch Schedule 40 PVC pipe, while the bottom of the chamber is sealed on a clear polycarbonate base. The resonation happens when the transducer's amplitude of vibrations reaches a critical value for the specific system (apparatus). Consequently, the pressure that corresponds to the fundamental ultrasonic frequency will increase, as well as the ones that correspond to its harmonics. At the same time, there will be additional pressure as a result of the oscillation of the bubbles. This is important because there seems to be a variety of pressures and frequencies throughout the phenomena (see figure 1.19).

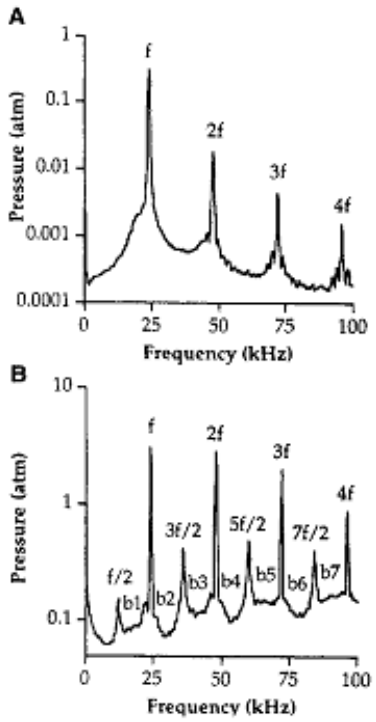

Figure 1.16: (A) The acoustic spectra when there is no cavitation (low pressure ultrasound exposures) and (B) when extensive cavitation occurs (at high pressure ultrasounds). The ultrasound applied is f = 24kHz. In the second picture the harmonics are higher and cavitation generates additional signals (the subharmonic f/2 and its ultraharmonics, and a high broadband "noise" level) [10].

Miller and Dou [69] have studied the application of ultrasounds of a specific frequency range to cells that had contrast agent gas bodies added onto their surface. These contrast agent gas bodies are bubbles used in vitro to increase the total number of bubbles in the system. The experiments determined the pressure amplitude at each frequency above which membrane damage will occur.

Finally, Liu et al. [10] state that the permeabilisation of the membrane depends on a

strong incident pressure (the pressure that actually reaches the cell surface) as well as on the total exposure time. This implies that certain combinations of pressure and duration can be selected to determine the biological response of the membrane.

Shock waves A shock wave is a type of stress wave defined as a discontinuity in stress (pressure), density, particle velocity and internal energy [70], and biological effects [71]. It travels at or higher than the speed of sound and is also a nonlinear and finite amplitude wave that induces critical characteristics to the fluid at which it travel through [13]. The displacement, d, of the affected particle is given by the equation $d = (up) \times (dt)$, where up stands for is the induced speed of the particle which is inversely proportional to its density, and dt is the duration of the motion of the particle, which is equal to the pulse duration [13].

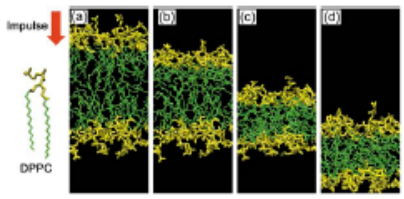

Figure 1.17: The collapse and rebound of a DPPC (dipalmitoylphosphatidylcholine) lipid bilayer under the application of a shock wave of impulse $50\mu Pa/sec$. The headgroups are in yellow and the acid chains in green. Water molecules are not displayed for clarity [11].

Kodama et al. [13] have applied shock waves from three different sources onto biological cells and studied the subsequent cytoplasmic molecular delivery. The authors state that the shock waves caused shape changes to the cells, expressed as cellular displacement.

Furthermore, it has been shown [13, 72] that shock waves can deliver large molecules into the cells avoiding cytotoxicity. Kodama et al. [13] conclude that this might have happened because of an induced change in the permeability of the membrane, the most important factor of which should have been the shock wave impulse (i.e. the pressure integrated over time) rather than the peak pressure.

Koshiyama et al. [11] performed MD simulations to study the structural changes on lipid bilayers and the water penetration induced by shock waves. The authors emphasise that this method is "definitely suitable for applications in gene therapy and anticancer drug delivery since shock waves can be focused into specific target sites of patients' bodies noninvasively" [11]. They explain that MD simulations is the way to obtain information about the molecular transport through a biological membrane.

They define the shock wave as a "high pressure wave with a steep wave front that propagates at a supersonic speed, and it passes the cell membrane within a very short time of the order of picoseconds" [11]. The simulation showed that there are two stages in the process. During the first stage the bilayer's thickness reduces (see figures 1.15, 1.16) and at

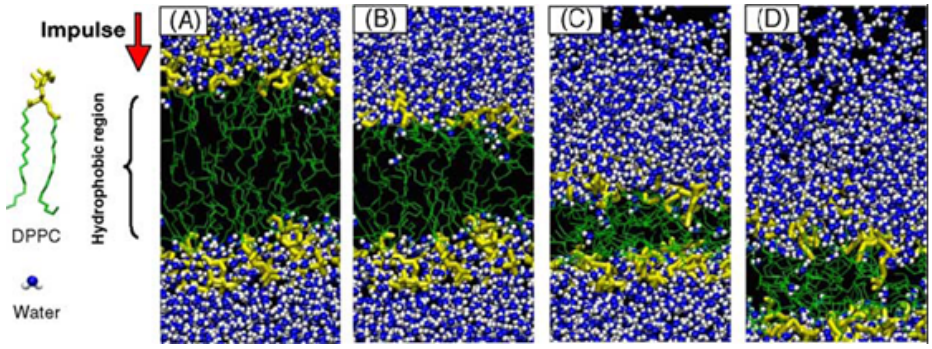

Figure 1.18: The water penetration under the action of shock impulse to the bilayer. Water molecules are in blue and lipid tails are in green. [12] It is interesting that even at the rebound stage water molecules continue penetrating the hydrophobic barrier [11].

the second stage the bilayer recovers relatively slowly. The collapse and rebound of a lipid bilayer relates to the excess momentum. As shown in figure 1.16, the excess momentum of a shock impulse that is propagated downwards, initially pushes down the upper bilayer only, while the lower layer remains intact, until the point when the excess momentum gets transferred to the lower bilayer and has the same effect on it, too. At this point, the excess momentum has already passed the upper bilayer and the force pushing it down is now weak. As a result, the membrane rebounds.

It is at the latter stage that the water molecules overcome the hydrophobic barrier. The higher the applied impulse value the higher the number of water molecules that penetrated the bilayer, which agrees with similar experimental studies [13]. In addition, they indicate that the larger the molecules, the larger the impulse required to overcome the hydrophobic barrier. Finally the orientation of lipids changes under the application of shocks (see figure 1.17).

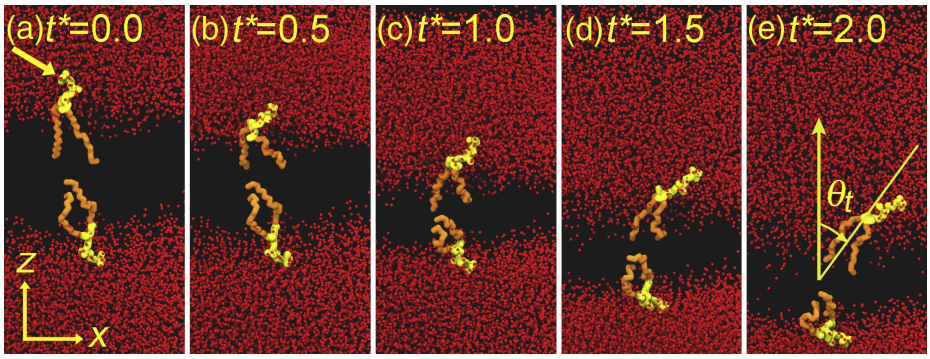

Figure 1.19: Lipid molecules in both layers change positions under the effect of a shock wave ($\theta = 60°$). Headgroups appear in yellow, tails in orange, and waters in red. [11]

1.1.3 Limitations of the methods

There are limitations related with both the experimental as well as the computational methods used in order to construct a robust strategy that would help cure cancer.

Computational techniques demand long simulations to be run for every solute used in order to get well converged data [73]. At the same time, the computational membrane models to be used should be small; thus simulations that involve the insertion of large solutes in a model lipid membrane are bound to cause artifacts. [74]

On the other hand, experimental procedures when applied to micro and nano scales are usually associated with financial burden and technical difficulties in obtaining accurate measurements. For instance, in experiments aiming at active targeting, which involves active ligands that lead the pharmacological substances to antigens or receptors on the target cells, there are limitations associated with low heterogeneity of receptors of different cancer cells, as well as differences in ligand-receptor affinity and internalisation rates mediated by the receptor. [39]. Furthermore, liposomal drug carrier therapies in vivo have been characterized by poor encapsulation, fast clearance from the circulation of the body, non-specific intake by the targeted cells, low degree of control over the pharmacological compound after its release from the liposome [75, 76]. The main limitation regarding photo-therapies is related to the cells ability to absorb the light and scatter it afterwards [40]. At the same time, a great concern about methods studied that involve graphitic nanomaterials is the possible toxicity they may cause [40]. Traditional techniques that make use of anticancer drugs suffer from limitations related to poor solubility of its substances in water, short circulation duration in the body, incorrect biodistribution, and possible side-effects [77]. All aforementioned limitations compromise the accuracy and efficiency of the therapeutic methods followed.

1.2 Aim and Objectives

The aim of this research project is to study the biological response of the application of shock waves on biological membranes and relate the findings to cancer therapy. The main objectives are:

- To build an understanding about how different membrane properties change under the effect of a shock.
- To study a set of shock waves with varying parameters, and draw conclusions regarding the viability and biological response of the membrane (i.e. membrane permeabilization or rupture) due to these shocks.

- To determine the optimum setup for enhancement of diffusion coefficients of the membrane lipids.
- To examine the shock thickness as well as the angle of attack effect on lateral diffusion of lipids.

1.3 Thesis Overview

Chapter 2

The second chapter of this report reviews the experimental studies that have been undertaken by scientists in the field of cancer therapy and/or cell biology. Initially, findings regarding the permeability of biological membranes in vivo and in vitro are being introduced with the purpose of summarising the different experimental techniques that can lead to membrane permeabilisation as well as the optimum setups employed. Furthermore, the main works on calculating the lateral diffusion of membrane lipids or proteins is being presented which allows for an examination of the strategies employed by researchers in order to experimentally (mainly) assess diffusion and other membrane properties. Finally, a summary of in vivo and in vitro applications of shock waves of cancerous tumors and their results is being presented.

Chapter 3

Chapter 3 summarises the basic theory used in the computations via Molecular dynamics (MD), which was employed to calculate all acting forces on the atoms of the molecular system and thus compute the motion of the molecules in the system. At the same time, the main computational membrane models are introduced. Finally, the shock wave implication in the system and its computational model is explained.

Chapter 4

In chapter 4, attention has been drawn to the effects of perpendicular to the a 1-palmitoyl-2-oleoyl-sn-glycero-3-phosphocholine (POPC) membrane shock waves. The biological response of the membrane to a variety of shocks of different impulse and thickness is being presented. The findings of the simulations suggest dramatic changes in the kinetic energy of the system under examination, the thickness of the lipid bilayer, the centre of mass of the lipids, their mean square displacement and their lateral diffusion. The computations have been carried out under two different sets of conditions characterising the system regarding constant pressure-temperature and constant volume-energy. Shock impulses varied from $0.33 mPa \cdot s$ to 10mPa s and shock thicknesses from 5Å to 12Å.

Chapter 5

The main focus of chapter 5 is to elaborate on the effects of oblique shock waves on a 1-palmitoyl-2-oleoyl-sn-glycero-3-phosphocholine (POPC) membrane. The study is about the biological response of the membrane to a combination of shocks of different impulse, thickness and angle of attack. The findings of the simulations are presented with respect to the altered properties of the system: the kinetic energy of the system, the thickness of the lipid bilayer, the centre of mass of the lipids, the mean square displacement of lipids and their lateral diffusion. The computations have been carried out under two different sets of conditions for constant pressure and temperature and for constant volume and energy. Shock impulses varied from $0.33 mPa \cdot s$ to 10mPa s, shock thicknesses from 5Å to 12Å, and angles of attack from 10° to 80°.

Chapter 6

Chapter 6 summarises the conclusions drawn from the analysis of the results as they were previously discussed in chapters 4 and 5, as well as presents a proposal for future work that could be done to enhance the study and promote continuation of the work that has been undertaken in the present report.

CHAPTER 2

Biological Membrane and Shock Waves

2.1 Introduction

It has been discovered that substances that dissolve in lipids pass more easily into the cell than those that dissolve in water which provided scientists with a proof biological cells were surrounded by a lipid membrane. The lipid membrane regulates the permeation of molecules into a cell and acts as a boundary to passive diffusion of water-soluble molecules. On the contrary, substances that dissolve in lipids pass more easily through the membrane to the intracellular area. The correlation between permeability and solubility is described in Overton's Rule [78]. The rate of diffusion of a substance through the membrane and into a cell is related to the substance's concentration and other parameters. The permeability of molecules across a membrane is given by $P_c = KD/Dx$ [78, 79], where P_c is the permeability coefficient for a particular substance in cm/sec [78], K is the partition coefficient, D is the diffusion coefficient, and Dx is the thickness or width of the cell membrane. The diffusion coefficient (D) is a measure of the rate of penetration into the intracellular area and depends on the molecular weight or size of the molecule. The partition coefficient is a measure of the solubility of the substance in lipids. Small values of K indicate a nearly not soluble molecule in lipid (water). Therefore, the permeability of molecules through a cell membrane can be explained by a linear function of the partition coefficient with slope dependent on the molecule size.

There are substances, such as water, ions, and molecules that are important for cellular processes and thus can enter and leave the cells by a passive process (diffusion). Diffusion involves a net direction toward regions of lower concentration in order to establish an equilibrium. Passive diffusion occurs when small molecules pass through the lipid bilayer with ease. Active (facilitated) diffusion depends on carrier proteins that are found imbedded inside the membrane in order to allow specific substances to pass through them by creating a channel. The rate of diffusion is affected by properties of the cell, the diffusing molecule, and the solution [80]. The rate of simple diffusion can be expressed by a modification of Fick's Law for small, non polar molecules [80]. The rate of diffusion, is the change in the

number of diffusing molecules inside the cell over time [80]. Since the net movement of diffusing molecules depends on the concentration gradient, the rate of diffusion is directly proportional to the concentration gradient across the membrane [80]. The concentration gradient, dC/dx, is the difference in molecule concentration inside and outside of the cell across a cell membrane of thickness dx. When the extracellular concentration is larger than the intracellular, the concentration gradient is positive, and the net movement will be into the cell [80]. The rate of diffusion increases as the concentration gradient increases [80]. If the concentration of molecules in the extracellular area is very high compared to the intracellular concentration, the rate of diffusion will be high. When both concentrations in the intracellular and extracellular area are similar, which further implies low concentration gradient, the rate of diffusion is low [80].

Unlike passive diffusion, facilitated diffusion involves a limited number of carrier proteins. At low concentrations, molecules pass through the carrier proteins in a way similar to that of passive diffusion through the membrane. At high solute concentrations, however, all the proteins are occupied with the diffusing molecules [80]. The rate of diffusion increases with increasing solute concentration until it approaches the saturation rate Vmax [80]. At this point, the carrier proteins become saturated and increasing the solute concentration further will not change the rate of diffusion. In contrast, passive diffusion of solute into a cell will always linearly increase with increasing concentration, and theoretically will have no limit.

2.2 Permeability of biological membranes

The permeability of a membrane is the indicator of the easiness with which molecules move across it (permeants) and is a characteristic of the cell membrane which grants it vital to the maintenance of intracellular and extracellular difference in ionic composition, as well as the internal fluid pressure, and thus the cell's shape [81]. This is dependent on the electric charge of the molecules and its molar mass. The hydrophobic nature of the cell membrane makes it more permeable to molecules as they decrease in size and/or charge or polarity [81]. Cell membrane permeability is therefore essential for the life and function of the cell as it enables amino acids, fatty acids, sugars, vitamins and hormones to infiltrate [81]. At the same time, after the production of proteins, hormones, neurotransmitters, and other substances important to the living organism as well as cellular waste, the membrane, due to its permeability, facilitates their passing through it to the extracellular area [81]. Finally, the cell membrane's permeability is selective, since it allows certain essential substances to enter the cell while it prevents other harmful ones from reaching the intracellular area [81].

However, in the case of drug and gene delivery for therapy, it is essential that scientists overcome this barrier of selective permeability and that they manage to permeabilise the membrane to the selected pharmacological compound, which is believed to be difficult due to the existence of microtubules occupying 40-50% of the cytosolic volume [82], as

well as other organelles [83]. In order to achieve transient permeabilisation of the membrane to various molecular components, researchers have carried out numerous experimental studies and their findings are presented here. They performed in vitro as well as in vivo experimental studies making use of ultrasounds, stress waves, shock waves, and various molecular substances in order to measure permeability (or permeabilisation) with reference to parameters such as osmotic water movement, pH, permeant size, temperature, number of shocks, and ultrasound pressure, exposure time, pulse length, duty cycle, have been discussed.

In order to find the correlation between permeant size and permeability as well as pH and permeability, scientists measured the permeability coefficients and bulk hydrocarbon/-solvent partition coefficients of 24 solutes across planar lipid bilayers of egg lecithin/decane [84] by using statistical mechanical theory [85]. It was found through experiments that the apparent permeability coefficients (P_{app}) were not dependent on pH when the pH concentration was low. Permeability coefficients were obtained for the spectrum of pH values where where apparent permeability coefficients decreased while the pH values increased. The acids used in the experiment were α- and β-naphthoic acid. The (P_{app}) was derived from the equation $\frac{1}{P_{app}} = \frac{1}{P_m \times f_{HA}} + \frac{1}{P_{aq}}$, where P_{aq} is the permeability coefficient of the unstirred water layer and f_{HA} is the fraction of unionised species.

In the same set of experiments researchers tried to correlate the permeability of the membrane to solutes with their molecular volume. The molecular volume of the 24 solutes varied from 20.6Å^3 to 452Å^3, which was estimated by using the atomic increment method [86], and the permeability coefficients from $(9.4 \pm 0.7) \times 10^{-7}$ cm/sec to $(1.7 \pm 0.2) \times 10^{1}$ cm/sec [83]. These measurements took place at temperature 25°C and according to the authors demonstrated size-dependent permeability [83].

Lee et al. [87] experimentally studied the kinetics of stress wave-induced permeabilization of cell membranes. These stress waves were created by ablation of polyimide film with an ArF excimer laser [87]. Lee et al. employed time-resolved fluorescence imaging techniques and used calcein, a fluorescent probe to study the kinetics of the transient membrane permeability. The use of time-resolved fluorescence imaging provided the collection of images of calcein molecules as they travelled through the cell membrane. It was found that laser-induced stress waves produced a transient increase in cell membrane permeability. The increase in membrane permeability allowed an influx and efflux of calcein molecules through the cell membrane. Lee et al. argue that the reason behind this molecular movement is due to the tendency of intracellular and extracellular concentration balancing.

Laser-induced stress waves are also commonly used in the field of biological membrane research. These laser induced stress waves are generated by tightly focusing an infrared pulse laser into a cell culture medium using a microscope objective lens. The very high transient light energy levels from the laser create a stress wave which propagates from the laser focal point through shockwave and cavitation bubble generation.

Researchers have studied the membrane response to stress waves, while looking for

the optimum setup for maximum permeabilisation of the membrane to thymidine (a radiolabeled compound) molecules [83]. It has been concluded [83] that maximum intracellular concentration of thymidine into cells (2×5^{10} molecules, which corresponds to 10% of the concentration in the extracellular area) can be reached with 2 or 3 stress waves. It has also been shown that the biological response to stress waves relies on peak stress, number of pulses, and rise time [66, 83, 88]. For the aforementioned experiment, the laser source was an ArF (argon fluoride laser) -193nm, 200mJ- the peak stress was 380 ± 40 bar, and the rise time of the stress wave and its duration were approximately 10ns and 80nsec, respectively. The membrane permeabilises in less than 60ms and recovers in 10-80sec, suggesting the existence of two different mechanisms for each phenomenon [83]. Other studies showed that after the application of stress waves, red blood cells released hemoglobin [83, 88, 89] and dye penetrated the membrane [83, 90, 91]. At the same time, in vitro studies support the strategy of applying stress waves along with drugs such as cisplatin [92–94], doxorubicin [95], and adriamycin [96] for cell therapy. It was observed [83] that the transient permeability that laser-induced stress waves (LSW) create has also been achieved by extracorporeal shock waves (ESW) [22, 97–99] and electroporation [100].

It has also been reported that studies in vitro and in vivo have shown transient permeabilisation of the membrane under the effect of high intensity acoustic waves: shocks and ultrasounds [13, 101–106]. Scientists believe that this phenomenon occurs due to non-thermal cavitation-related effects, such as microjets and shock-wave-induced cavitation bubbles [107]. Studies suggest that shock waves and ultrasounds can be an effective strategy for drug and gene therapy [5, 22, 45, 98, 108] (see figure 2.1), while it was noted that both waves are sound waves and therefore very similar, especially in the case of low frequency and considerably high intensity ultrasounds that fall into the very definition of a shock wave [5].

Permeability studies in vitro showed some connection between cell viability and membrane permeability and the number of lithotripter shock waves of 20KV intensity and one shock per second frequency [97]. A number of shocks varying from 60 to 300 were applied to human neutrophils and scientists observed cellular perturbations. An exposure to more than 140 shocks lead to thinning of the cell, while 60 to 300 shocks were able to cause significant cytotoxicity of the cells. When the cells were loaded with adriamycin or fluorescein and then exposed to shocks an influx of extracellular fluid and efflux of intracellular took place, suggesting permeabilisation of the membrane, although some shocks were bound to result in membrane rupture. Sixty shocks appeared to have reduced cytotoxic effects for the cell while cellular changes were still evident.

Studies making use of ultrasounds and red blood cells [10] demonstrated that transient membrane permeabilisation is enhanced with pressure, total time of exposure to the ultrasound (above 100ms), while there seems to be little relevance with pulse length (maximum was reached at 3ms), and no relevance with duty cycle. Finally, in the case of ultrasound applied in vitro, it was observed that acoustic signals also correlated to the permeabilisation of the membrane of the cells. To further elaborate, according to the same researchers, bovine red blood cells were submitted to ultrasounds of as low frequency as 24kHz and the

indicator of permeabilisation of the membrane of the cells was the efflux of hemoglobin. The authors observed that the permeabilisation of the membrane is a function of incident pressure, since it increases almost linearly with incidence pressure for values greater than almost 0.5atm. Also, they found that the correlation between permeabilisation and the pressure at half the driving frequency (12kHz) and its ultraharmonics, while the driving frequency and its harmonics the smallest correlation. At the same time, cell damage was observed for pressure at driving frequency equal with pressure at 12kHz [10, 109] and $20\times$ 12kHz [10, 110].

In terms of the dependance between erythrocyte cell membrane permeabilisation and exposure time to the ultrasound, researchers [10] observed that an ultrasound at 24kHz and incident pressures of 0.89 atm, 2.7 atm, and 8.9 atm can promote transient membrane permeabilisation which increases in all three cases with exposure time above approximately 100msec, thus above a certain threshold [10, 111, 112]. This threshold (minimum ultrasound exposure time needed for an increase of the permeabilisation to occur) of 100msec may be explained as being the time needed for bubble to grow (and even collapse, possibly) after many cycles [10]. The effect of pulse length was considered while applying pulses of various lengths that had total application or "on" time equal to 10 sec for the same three incident pressures. The authors concluded that there was almost no correlation between permeabilisation of the membrane and pulse length, although at 3 msec there was a maximum in membrane permeability in both cases of pressure 2.7atm and 8.9atm. Lastly, no dependence on duty cycle appeared exist, either, for incidence pressure 2.7atm and pulse lengths 0.1sec and 1sec.

It is well understood that water transport through the cell membranes is vital for the cell function[113, 114]. It is important to underline the existence of different "permeabilities" as well as ways of measuring them. The osmotic permeability is measured with reference to the cell size change as a result of an alteration in extracellular liquid (chemical potential of water) [115, 116]. In the case of diffusional permeability, the molecules are labeled and usually the extracellular area gets loaded with a "paramagnetic relaxation agent" (NMR -Nuclear magnetic resonance- method) [117]. Alternatively, apparently diffusion coefficients are measured avoiding the introduction of an substances [117–120]. According to some researchers [121, 122] membrane permeability to water correlates with the cell volume, while others believe that the direction of the osmotic water towards the intracellular (influx) or extracellular (efflux) area induces altered permeability [123]. To further examine the matter scientists performed experiments on a fibroplast cell that show hydraulic conductivity that correlates more with the volume of the cell than the osmotic pressure gradient [123]. Finally, transport across the membrane was measured experimentally by using NMR techniques, which, according to the results, increased cell permeability with increasing temperature [117].

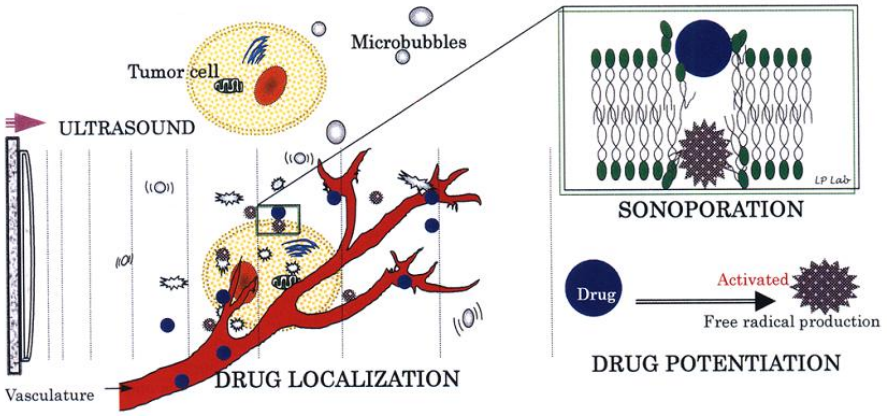

Figure 2.1: Combined anticancer agent and ultrasound treatment [5].

2.3 Diffusion in biological membranes

Lateral diffusion is the translation in the plane of the membrane. It is a characteristic of both lipids and proteins of the cell membrane. Frye and Eddin (1970) created one of the first graphic representations to describe lateral diffusion which involved cells from a mouse line and a human line [124]. The cells were bound to fluorescent antibodies to antigens found in cell surface [124]. The spectra that appeared in the fluorescent microscope reflecting the fluorescent antibodies of the human cells had different colors to the one coming from the mouse [124]. Each cell type was fused by Sendai virus in order to form a new (hybrid) cell and initially the fluorescent antibodies remained in the hemisphere corresponding to the cell type of origin [124]. With time, the colors of the spectra appeared to mix, which indicated that the labelled proteins had diffused over the hybrid cells surface [124]. Hence, regarding these labelled components it was decided that the cell surface allowed for lateral diffusion to take place [124].

Although it is not always shown, both lipids and proteins are capable of diffusing laterally within cell membranes. In order to measure the lateral diffusion of a lipid, there are mainly techniques that involve fluorescence of probe molecules in the membrane or antibodies bound to membrane components and are generally associated with the bleaching of certain chromosomes of the membrane that are traced at a defined timed on a particular spot on the membrane surface. The diffusion coefficient is then obtained from the rate that a random pattern gets formed by the fluorescent probes in the surface.

The diffusion coefficients of different membrane components seem to follow a certain pattern [124]. It was evident that for instance all the lipids that formed cell membranes or model membranes were associated with similar values of diffusion coefficient [124]. A main perturbant on the lateral diffusion is the liquid-crystalline-to-gel phase transition [124]. Gel phase is the one that dramatically decreases the diffusion coefficient, the rate of lateral diffusion [124].

Fluorescence photobleaching and recovery (FPR) is a technique which is used to measure translational diffusion D_{lat} in membranes [125]. This technique consists of bleaching a spot on a uniformly fluorescent surface using a blue or green light from a continuous laser output [125]. Subsequently, "the initial fluorescence in the spot and the recovery after bleaching are monitored with the laser light attenuated 1000-10,000 times" [125]. Some of the fluorescent labels used with the FPR method include: lipophilic dyes, covalently bound haptens, antibody fragments, antibodies, and lectins [125]. D_{lat} measurements of $5 \times 10^{-9} cm^2/sec$ for rhodopsin fluorescent-labels have been made using FPR [125].

In the work carried out by Fan and Fan [126] a simple, analytical model was used to study the impact of protein size and membrane fluid velocity on the lateral diffusion of membrane proteins. The model used in this study is based on the fluid mosaic model by Singer and Nicolson, but simplified by using a linear diffusion equation and ignoring the complex relationship between diffusion coefficient D_{lat} and chemical potential. Fan and Fan assume that the protein membrane is spherical in shape with infinite viscosity, and is smaller in size compared to the thickness of the cell membrane. Three main findings result from this study. Firstly, the D_{lat} is a dominant factor of the protein motion. Fan and Fan attribute this to the fact that D_{lat} is the deflection of the physical property of the membrane-protein systems, which describes the nature of the interaction between the protein molecules and membrane molecules. Viscosity η of the cell membrane has been reflected indirectly through the quantity "D_{lat}". Secondly, lateral diffusion decreases with increasing velocity of the membrane flow [126]. Thirdly, protein size has an effect on diffusion, with small particles fusing more strongly than the larger particles [126].

In addition to the findings of cell permeability, Lee et al. [87] investigated the diffusion process of cell molecules after a laser-induced shock wave was applied. The results of the experimental studies were compared to those of a mathematical model based on diffusion principles. This model used first-order approximations and three different diffusion constants. Two of these constants were used to represent the different diffusion rates, inside and outside the cell, and a third time-dependent constant to compensate for the transient membrane permeability. The numerical results demonstrated a high-level of correlation with experimental data; therefore, concluding that the calcein molecular movement could be described as a diffusion process. The numerical averaged diffusion constant was $2.2 \pm 1.3 \times 10^{-7} cm^2/s$.

In the study by Dibner et al. [127] the effects of polar organic solvents on membrane viscosity in human colon cancer cells were investigated. The polar organic solvents used included N-methylformamide (NMF), N,N-dimethylformamide, and dimethyl sulfoxide. Membrane viscosity was assessed by calculating the lipid lateral diffusion using photobleaching techniques of a fluorescent lipid probe. The results from this study demonstrate that cells exposed to any of the three polar organic solvents increase membrane viscosity, and therefore, decrease membrane lipid lateral diffusion. In addition, these changes are accompanied by a variation in growth rate and cell morphology.

Wang et al. [128] created a model membrane system composed of a ruptured giant

unilamellar vesicle (GUV) at the upper layer, a PEG (Polyethylene glycol) polymer in the mid-layer, and a lipid bilayer base supported on glass. The ruptured GUV forms into single, planar lipid bilayer circular patches, referred to as "GUV pancakes" [128], whose diameters vary from 20 to $50\mu m$. This type of membrane model proves to be superior to other models because of the use of the PEG polymer mid-layer, which increases the space between the GUV pancakes and the supporting solid surface. This space is important in model membrane systems because it increases the lateral mobility of lipids and membrane proteins. In this study, single-particle tracking experiments were carried out in order to measure lateral mobility of AF633-Syx (AlexaFluor 633) or DiD labels. DiD and AlexaFluor 633 labels were used to characterize the movement of lipids and integral membrane proteins, respectively. A 633 nm laser (HeNe, Coherent) was used to excite either label. The laser intensity was $0.04kW/cm^2$ to locate and characterize the GUVs and $0.32kW/cm^2$ for single-particle tracking. The single-particle tracking experiment results demonstrate that at least 80% of DiD lipid probes and at least 80% of integral membrane protein AF633-Syx in the GUV pancakes ruptured on the passivating layer, display free, homogeneous diffusion. In both cases, the diffusion coefficient, $D0 \approx 5\mu m^2 \times s^{-1}$, is more than 10 times faster than that observed in GUV pancakes ruptured directly on glass.

In the work of Orsi and Essex [129], a novel dual-resolution molecular dynamic computational model is constructed and used to simulate passive permeation of β-blocker drugs and steroid drugs through a lipid bilayer. This model combines the accuracy of atomic-level (AL) force fields with the efficiency of coarse-grain (CG) models. Permeant molecules are represented with standard AL models, while lipid and water molecules are described by CG models. In this study both normal and lateral diffusion coefficients were calculated. The results from these calculations show that normal diffusion coefficients remain relatively constant throughout the bilayer, with values in the range of $50100nm^2/ms$. Lateral diffusion coefficients are generally lower than normal diffusion coefficients. This is attributed to the fact that lipid molecules are on average oriented and stretched along the normal axis; therefore, voids through which permeants diffuse are then also likely to be elongated and orientated in the normal direction, hence the higher diffusion rates in the normal direction. However, Orsi and Essex do mention that the lower lateral diffusion coefficients maybe larger than what was calculated in their study. This is because the lateral diffusion coefficients do not correspond to "free" [129] diffusing particles, but rather to molecules which are constrained in a particular plane. All numerical results correlate well with previous published studies. In terms of computational speed, the dual-resolution molecular dynamic model is approximately twice as fast when compared to standard atomic-level counterparts.

2.4 Shock waves for cancer treatment

Polar molecule absorption occurs naturally in cells by either the use of transmembrane carriers (e.g. proteins) or the process of endocytosis. Enhancing polar molecule absorption by increasing cell permeability would mean further facilitating the penetration of therapeutic

Year	Drugs	Shock Wave	Biological Model	Endpoint
2000	Bleomycin	SW 480 with pressure peak 40 MPa (2000 shots)	Human colon cancer line Nude mice	Apoptosis, cell proliferation
1997	Bleomycin Cisplatin; 5-Fluorouracil	SW 480	Various human cancer cells Gastric cell line (GCIY) Nude mice	Cell survival
1996	Bleomycin Cisplatin 5-Fluorouracil		GCIY cells from human gastric cancer, LS 174 T and SW 480 cells derived from human colon cancers Nude mice	Tumor growth
1995	Cisplatin THP-Adriamycin Methotrexate Carboplatin	HESW (10,000 to 20,000 shots)	57-y.o. with poorly differentiated adenocarcinoma of the prostate	Tumor size
1995	Cisplatin	2000 HESW	MH 134 hepatoma in a mouse	Tumor growth
1994	Mitomycin C Cisplatin Methotrexate; Adriamycin	19 kV (500-2500 shock waves) [EDAP lithotriptor LT 01]	Human bladder cancer cell line (KK-47)	Cell survival Traces of cell membrane damage indicator: GOT, ALP, CPK, and LDH
1994	Cisplatin Mitomycin C Actinomycin D	0.33 or 0.6 mJ/mm², (200-300 pulses) [Siemens lithotripter]	Bladder cancer cell lines (RT 4, J 82, MGH-U 1)	Cellular integrity Cell proliferation
1994	5-Fluorouracil	60 MPa, 1 Hz (0-500 shots), [Sonolith 3000]	HT-29 cells	Clonogenic survival Cell proliferation
1994	Cisplatin	62 MPa, 20 V, 80 nF, (500 shots at 100 shots/min) 1 MPa peak pressure	Amelanotic melanomas (A-Mel 3) Cisplatin-resistant fibrosarcoma (SSK 2/O, SSK 2/R 2) Syrian golden hamsters	Tumor growth
1993	THP-Adriamycin	HESW (underwater), (6,000-10,000 shots)	Rabbit bladder VX 2 cancer Normal bladder tissue	THP-ADM concentration
1992	THP-Adriamycin	Focused HESW (6,000-10,000 at 5 shots/s),	Rabbit urinary bladder cancer (VX 2); rabbits	Tumor size
1991	TNF-alpha; IFN-alpha	HESW 800 SW, 18.4 kV, 37.5 MPa, (Siemens Lithostar)	Five human kidney cancer xenografts in mice (NU-1, NU-3, NC-65, NU 10, NU 12)	Tumor growth
1990	Adriamycin and other cytotoxic drugs	HESW (100 shots/min)	Urological tumors (R 3327, PAT-2 prostate CA, NC-65, NU-1) Lewis rats	Doubling time Tumor volume
1989	Adriamycin Cisplatin	500 SW at 25 kV	L 1210 mouse leukemia cells	Cell growth
1989	Vinblastin	HESW (1,000-3,000 shots at 80 shots/min), 19 kV	Dunning R-3327 Pat-2 rat prostate cancer subline	Cell growth
1988	Cisplatin Adriamycin	1400 SW (800-2,000 shots at 100 shots/min), ESW, 18 kV	Renal cell carcinoma (RCC) Human embryonic kidney (NHEK) C3H/He mice	Cell viability Cell growth Cell attachment Tumor growth

Figure 2.2: Combined anticancer agent and shock wave treatment [5].

pharmacological compounds to the cell, such as cisplatin and bleomycin, in the case of cancer therapy.

A method which increases cell permeability is the application of shock waves. The first attempts of using shock waves on cancerous cells were used for the intake of propodium iode and fluorescein isothiocyanate dextran (FITC-D) [13]. Subsequent studies [13, 23, 83, 87, 130, 131] followed which furthered the understanding of cancerous cell permeability with the application of shock waves. In these studies, two types of shock wave generators were used. One method used laser technology and the other shock tubes. Figure 2.3 presents a schematic diagram of a standard experimental set-up used in these studies.

In studies using laser-induced stress waves, Figure 2.3A, cells were placed in polystyrene test tubes sealed at one end with a polystyrene plate. Pressure measurements were made by a hydrophone positioned inside the test tube downstream of the cells. Experiments using test tubes, Figure 2.3B, consisted of a high-pressure chamber, a low-pressure channel, and a reduction nozzle. In these experiments pressure measurements were also made by a hydrophone positioned downstream of the centrifuge tube.

One of the laser generators is the ArF excimer laser. It must be noted that there have been studies [13, 83] showing that ArF excimer lasers can generate a single shock that was enough to permeabilise the membrane of the erythrocytes. According to Kodama et al. 2000 [13], HL60 (Human promyelocytic leukemia) cell membrane, on the contrary, fails to be permeabilised when the configuration of the experiment is the same because erythrocytes' degree of fluidity is high which makes them more likely to get pore formation in their membranes when osmotic lysis takes place, and thus under the application of the shock to form water-channels in their permeabilised membranes [83].

Furthermore, researchers attempted to find a relation between the number of the shocks that are applied on the membrane and the absorption of thymidine molecules by the cell [13]. They observed that the degree of thymidine uptake was twice as high when two single pulses were applied than when there was only one single shock wave [13]. At the same time, they noticed that no major differences appeared amongst the cases of 2, 3, and 5 shock waves when the laser pulse was 1Hz [13].

In studies where extracorporeal lithotripters were used, scientists reported that shock pressures within the range of 24MPa and 50MPa damage the tissues [13]. In particular, it was shown that hemorrhage is bound to occur in murine kidney when the pressure of the shock wave (5-200shots) is 3-10MPa, in murine intestine when the shock wave (100-200 shots) pressure is 1-4MPa, and in murine skin when the induced pressure by a shock of 100 shots is 0.6-1.6MPa [13]. However, in rabbit liver, tissue and structural damage occurred with the application of only one shot of pressure that was smaller than 25MPa, as it was induced by detonating an explosive micropellet [131]. Also, in the case of rat liver submitted to a single shock wave from a shock tube, both hemorrhage and structural damage were reported [13].

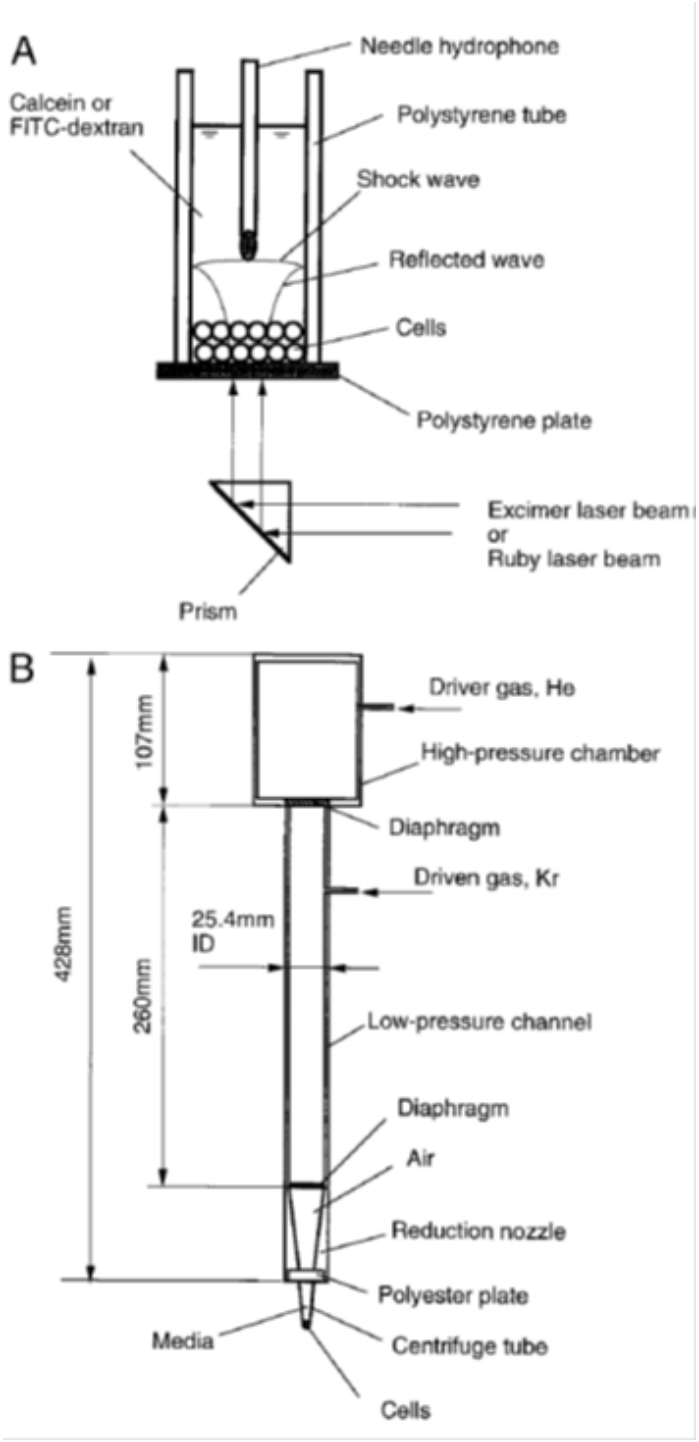

Figure 2.3: Shock wave generators: Laser technology (A) and shock tubes (B) [13].

On the other hand, scientists [13] believe that tissue damage can happen in vivo even when the pressure applied is lower and the shots are fewer than what has been discussed regarding damaging cells in vitro. According to Kodama et al. 2000 [13], this can be explained by the fact that in vitro experiments, cells, as well as the surrounding liquid, all move towards the direction of the shock, since both the cell and the liquid have almost the same density. In vivo, however, cells are fixed to basement membranes, neighbouring cells, and extracellular matrix; therefore, they promote anisotropic and nonlinear or inhomogeneous behaviour in the macroscopic world.

In humans, it has been recorded that different tissues have different tensile strength. It can be 3.4MPa in cases of human cornea, 0.057MPa for renal parenthyma, and as for aorta between 1.1 and 1.6MPa [13]. In general, tissue damage may be a result of progressively decreasing tensile strength of the tissue due to the shock application [13]. Finally, shock waves may also be applied deep inside the body of the patient should a reflector or acoustic lens be employed.

CHAPTER 3

Modeling Biological Membranes

3.1 Molecular Dynamics

3.1.1 Introduction

Molecular dynamics (MD) is an effective computational tool employed in structure studies of solids, liquids and gases as well as to analyse the atomistic mechanisms governed by the bulk properties of the material. The bulk properties are the structure, such as crystal structure, predicted x-ray, and neutron diffraction patterns, the thermodynamic properties, such as enthalpy, temperature, and pressure, and the transport properties, like thermal conductivity, viscosity, and diffusion. Molecular dynamics calculates all acting forces on the atoms of the molecular system and computes the motion of the molecules with the use of the appropriate numerical integrator.

A numerical integrator solves Newton's equations of motion for all atoms of the system. Initially the positions of the atoms are known as well as their velocities. The initial positions, velocities and forces, in accordance with Newton's laws, enable the further calculation of the positions and velocities of the atoms after a time interval called time step. A time step is usually of the order of 1 femtosecond (fs). The re-appointment of positions and velocities happens for thousands of time steps in the course of a full simulation.

During the calculation of the atomic forces in a molecular dynamics simulation it is usually assumed that the forces between the atoms of the system are pair forces that act solely between pairs of atoms. However, should there be complex molecular structures involving higher order forces of three or four body forces then these forces may be considered as well. If the constituent atoms in the system are N, there will be maximum $N(N-1)/2$ unique atom pairs and thus related forces to compute. In order to enable computing the forces more efficiently, a cut-off radius can get introduced at a certain interatomic separation over which the acting force is assumed to be zero. The calculation of the forces is almost always

based on an empirical potential such as the Lennard-Jones potential.

A key notion of molecular dynamics is the concept of periodic boundary conditions which allows for a system of few hundred atoms to be computed as though it was part of an infinite system, achieving, thus, results characteristic of the bulk material. A construct related to the periodic boundary conditions is the "minimum image" which restricts an atom to interact with only one of the equivalent images of any other atom of the system.

An important step right after the initialisation of the system is the equilibration period that may last for a few thousand time steps. The aim of the equilibration period is to bring the system to the desired thermodynamic condition. Lastly, a molecular dynamics simulation needs to run for thousands of time steps in order to accurately describe the phenomenon under examination. During this step, the trajectories of the molecules get saved for further analysis.

The molecular dynamics method, is a great computational technique in that it offers information about time dependent phenomena by representing the molecular system as a function of time. In this study the molecular dynamics software used is NAMD - Molecular Dynamics simulator [132, 133] and its visualisation tool VMD - Molecular Graphics viewer [134, 135], both developed by University of Illinois in Urbana-Champaign in United States.

3.1.2 Equation of motion

The application of Isaac Newton's equations of motion to molecular systems is the basis of molecular dynamics. The laws are the following:

1. A body keeps its state of rest or of uniform motion in a straight line, unless a force acts upon it.
2. The applied on the body force is equal to the rate of momentum change of the body.
3. Two isolated bodies act upon each other with equal and opposite forces.

Molecular dynamics solves the Newtonian equation of motion for each atom of the system [15, 132]. The total force F exerting on an atom is the sum of all forces from the atoms in the system acting upon it, by adopting an empirical interatomic potential function, such as the Lennard-Jones potential [15, 132].

$$F = m_a \ddot{\vec{r_a}} = \frac{\vartheta}{\vartheta \vec{r_a}} U_{total}(\vec{r_1}, \vec{r_2}, ..., \vec{r_N}), a = 1, 2, ..., N \tag{3.1.1}$$

where m_a is the mass of an atom a, $\vec{r_a}$ denotes its position, and $U(total)$ is the total potential energy based on the positions of the atoms. In other words, the force is the negative gradient of a scalar potential energy function [136]

$$\vec{F}(\vec{r}) = -\nabla U(\vec{r}) \tag{3.1.2}$$

which for biomolecular systems involve the bonded and non-bonded interactions [136]

$$U(\vec{r}) = \sum U_{\text{bonded}}(\vec{r}) + \sum U_{\text{nonbonded}}(\vec{r}) \tag{3.1.3}$$

Bonded potential energy/interactions

The bonded potential energy involves two-body, three-body, and four-body interactions of covalently bonded atoms.

The two-body potential describes the stretching interaction between an (i, j)-pair of covalently bonded atoms and its harmonic vibrational motion [136].

$$U_{\text{bond}} = k(r_{ij} - r_0)^2 \tag{3.1.4}$$

where, $r_{ij} = \|\vec{r}_j - \vec{r}_i\|$ denotes the distance between the atoms and thus the bond stretching, r_0 symbolises the equilibrium distance, and k is the spring constant [136].

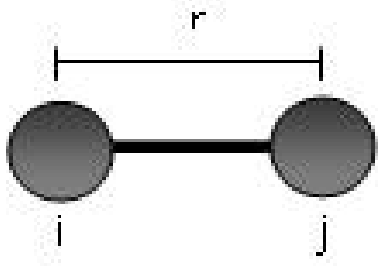

Figure 3.1: Bond stretching

The three-body angular bond potential describes bending interaction of an (i, j, k)-triple of covalently bonded atoms and its angular vibrational motion [136].

$$U_{\text{angle}} = k_\theta(\theta - \theta_0)^2 + k_{\text{ub}}(r_{ik} - r_{\text{ub}})^2 \tag{3.1.5}$$

where, θ is the angle (in radians) formed by vectors $\vec{r}_{ij} = \vec{r}_j - \vec{r}_i$ and $\vec{r}_{kj} = \vec{r}_j - \vec{r}_k$, θ_0 is the equilibrium angle, k_θ is the angle constant,$k_{\text{ub}}(r_{ik} - r_{\text{ub}})^2$ is the Urey-Bradley term that describes a noncovalent spring between the outer atoms i and k, with the condition that $k_{\text{ub}} \neq 0$, $r_{ik} = \|\vec{r}_k - \vec{r}_i\|$ is the distance between an (i,k)-pair of atoms, and r_{ub} is the equilibrium distance [136].

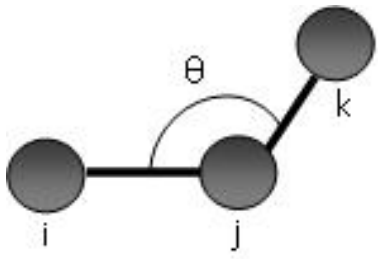

Figure 3.2: Bond bending

The four-body torsion or dihedral angle potential describes the angular spring between the (i, j, k)-plane and the (j, k, l)-plane of a consecutively bonded (i, j, k, l)-quadruple of atoms [136],

$$U_{\text{tors}} = \begin{cases} k(1 + \cos(n\psi + \phi)) & \text{if } n > 0, \\ k(\psi - \phi)^2 & \text{if } n = 0, \end{cases} \tag{3.1.6}$$

where, ψ is the angle (in radians) formed by the (i, j, k)-plane and the (j, k, l)-plane, n is nonnegative integer constant demonstrating periodicity. If $n > 0$, ϕ is the phase shift angle and k is the multiplicative constant. If $n = 0$, ϕ is an equilibrium angle and the units of k then become potential/rad^2 [136].

Non-bonded potential energy/interactions

The non-bonded interactions involve all (i, j)-pairs of atoms, usually eliminating pairs of atoms related with bonded interactions.

The Lennard-Jones potential is responsible for the weak dipole attraction between distant atoms and the strong repulsion of atoms approaching each other [136]

$$U_{\text{LJ}} = (-E_{\text{min}})[(\frac{R_{min}}{r_{ij}})^{12} - 2(\frac{R_{min}}{r_{ij}})^6] \tag{3.1.7}$$

where, $r_{ij} = \|\vec{r}_j - \vec{r}_i\|$ is the distance between the (i, j)-pairs of atoms. The Lennard-Jones potential becomes almost 0 as r_{ij} increases and thus is usually truncated to 0 over a cutoff radius [136].

The electrostatic potential or Coulomb interaction is caused by the attraction and repulsion between atomic charges with the same sign and with opposite signs respectively [136]

$$U_{\text{elec}} = \epsilon_{14} \frac{C q_i q_j}{\epsilon_0 r_{ij}} \tag{3.1.8}$$

where, $r_{ij} = \|\vec{r}_j - \vec{r}_i\|$ is the distance between the (i, j)-pairs of atoms, q_i and q_j are the atomic charges, C is Coulomb's constant, ϵ_0 is the dielectric constant, ϵ_{14} is a (unitless) scaling factor with value equal to 1, except for a modified 1-4 interaction, where the pair of atoms is separated by a sequence of three covalent bonds (so that the atoms might also be involved in a torsion angle interaction), in which case $\epsilon_{14} = \varepsilon$, for a fixed constant $0 \leq \varepsilon \leq 1$ [136].

3.1.3 Periodic boundary conditions

A periodic boundary is an important molecular dynamics technique. It makes a simulation that constitutes of only a few hundred atoms behave as if it was infinite. The aim is to eliminate the surface effects that a finite sample of matter has, so that the internal structure of the sample is not dominated by surface forces but by bulk forces. Figure 3.3 depicts the notion of periodic boundary conditions. The highlighted box acts as the molecular dynamics system of the simulation and all other boxes are its copies in a way that every particle of the simulation cell has a duplicate in every cell, the velocities of the duplicate particles are the same as the ones the particles in the simulation box have, and finally it is supposed to be the case infinitely. In this way, if the motion of an atom leads it to leave the simulation box, it gets replaced by another atom, its duplicate, that has the same velocity, and enters from the opposite cell face. Ultimately, the periodic boundaries allow for the number of atoms in the box to be conserved.

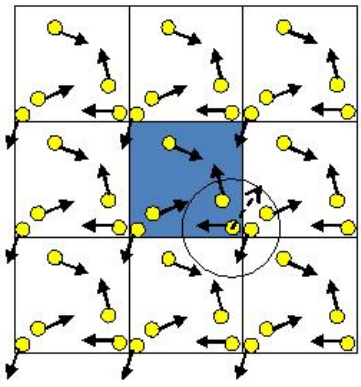

Figure 3.3: Periodic Boundary Conditions

The cutoff radius that appears as a dashed line in Figure 3.3 is usually applied when

calculating the force between two particles. It is shown in the figure that a particle may interact with other particles of the surrounding cells for as long as they are within the cutoff radius and ignore equivalent particles within the simulation cell if they happen to be further away [132]. The interaction to be calculated is always the one with the closest image, known as the minimum image convection [137], and the cutoff radius can be equal to or smaller than half the width of the cell. The main idea behind the minimum image and the periodic boundary conditions is that the size of the box along with the cut-off distance should be such that it will not allow the force from a particle and its mirrored one to simultaneously contribute to the force acting in other particles within the system.

The use of periodic boundary conditions in the present case should be performed very carefully because it is associated with a high risk that the shock wave will travel through the computational domain several times. In order to avoid this problem the simulation time has been cautiously selected and is in the same order of magnitude with computational studies published in the literature like Koshiyama et al. 2006 [11].

3.1.4 Equilibrium and non-equilibrium molecular dynamics

Molecular dynamics are categorised into equilibrium molecular dynamics simulations (EMD) and non-equilibrium molecular dynamics simulations (NEMD). EMD refers to a system in thermodynamic equilibrium, which presupposes thermal, mechanical, radiative, and chemical equilibrium. A system is at equilibrium if it is:

- isolated, which implies constant number of atoms, volume, and energy, while its entropy is invariable, or
- at fixed temperature and constant volume, while Helmholtz free energy is maintained, or
- at constant temperature and pressure, while Gibbs free energy is fixed.

NEMD simulations can be induced with the introduction of surface/boundary effects to the system where particles interact with external momentum, or by adding a perturbation in the equations of motion of the particles. The system responds proportionally to the time-integrated correlation functions when a constant perturbation is imposed. A pulse perturbation makes the system react proportionally to the correlation functions. Sinusoidal oscillating perturbation leads the system to correspond proportionally to the real and imaginary parts of the Fourier-Laplace transformed correlation functions.

3.1.5 The Isobaric-Isothermal and the Microcanonical ensembles

An ensemble is a collection of all systems with different microscopic states but identical macroscopic or thermodynamic state. There exist different ensembles with different characteristics. In the current study the ensembles that have been used are an isothermal and an adiabatic ensemble [133]:

- the Isobaric-Isothermal Ensemble (NPT), which is represented by a fixed number of atoms, N, a fixed pressure, P, and a fixed temperature, T, and
- the Microcanonical ensemble (NVE), whose thermodynamic state is described by a fixed number of atoms, N, a fixed volume, V, and a fixed energy, E and is indicative of an isolated system

There are methods, using statistical ensembles, to control the temperature and the pressure of the system when this is required to study a molecular system. The statistical ensemble to be chosen depends on the state variables to be kept constant. The NPT ensemble is particularly important when running an equilibration simulation, and whenever the aim of the simulation is to acquire more realistic results. This is achieved by maintaining the correct values of pressure and temperature. Also, it is used before running a simulation that utilises the NVE ensemble. This is the ensemble of choice when the correct pressure, volume, and densities are important in the simulation. Moreover, when applying an NPT ensemble, the unit cell vectors are allowed to change and the pressure is adjusted by adjusting the volume.

In simulations, the "instantaneous (kinetic) temperature" is usually computed from the system's total kinetic energy (equipartition theorem). By employing a thermostat, the correct average temperature of a system is ensured, rather than the fixing of the total kinetic energy through constant temperature, since, for instance, the latter would not meet the targets of an NPT ensemble. If the kinetic energies of few molecules of a fluid system were measured in a small area of the container that restricts the fluid in it, it would be shown that it does not remain exactly constant but the small number of particles results in fluctuations in the kinetic energy. By averaging over larger numbers of molecules, the fluctuations in the average would get smaller and thus by averaging over the whole fluid system it would appear that the temperature is constant. Molecular dynamics simulations that involve small water-membrane systems are associated with bigger fluctuations and a thermostat is employed to ensure the correct average temperature of the system and fluctuations of the correct magnitude [138].

In the case of the NPT ensemble, a temperature bath takes place to keep the thermodynamic temperature fixed [133]. In the case of employing Langevin dynamics, temperature is controlled by balancing friction with random noise in order to lead each atom of the system towards the target temperature. At the same time, pressure is controlled through

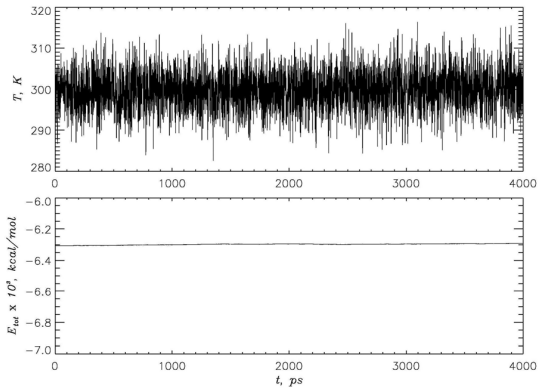

Figure 3.4: The upper panel shows fluctuations in the instantaneous temperature and the lower an approximately constant total energy for NVE simulations of polyvaline [14].

modifications in the volume of the simulation cell [133]. The actual parameters of the Nose-Hoover Langevin piston method control the target pressure and the dynamical properties of the barostat. A "piston" with a longer period (i.e., larger mass) will better damp out fluctuations in the instantaneous pressure. Langevin dynamics is applied to the piston itself coupling it to a heat bath with a damping constant of 1 over the oscillation decay time. Oscillation decay time is set smaller than the oscillation period to ensure that harmonic oscillations in the periodic cell are overdamped.

Through the use of the NAMD software [133], constant-pressure simulations are facilitated by a modified Nose-Hoover method where pressure fluctuations are controlled with the application of Langevin dynamics (a temperature control method) Nose-Hoover-Langevin (NHL) thermostat [139].

The Langevin piston Nose-Hoover method used by NAMD [133] is a merger of the Nose-Hoover constant pressure method [133, 140] and the piston fluctuation control of Langevin dynamics [133, 141].

Through the use of an algorithm embedded in NAMD software [133], used for molecular dynamics simulations, values such as pressure, oscillation and temperature of the piston, and atom temperature can be specified (Langevin dynamics) [133]. The equations of motion therefore become [133, 140]:

$$\frac{d\vec{r_1}}{dt} = \frac{\vec{p_i}}{m_i} + \frac{d_e}{dt}\vec{r_i} \tag{3.1.9}$$

$$\frac{\vec{p_i}}{m_i} = \vec{F_i} - \frac{d_e}{dt}\vec{p_i} - g\vec{p_i} + \vec{R_i} \tag{3.1.10}$$

$$\frac{d_e}{dt} = \frac{1}{3V}\frac{d_V}{dt} \tag{3.1.11}$$

$$\frac{d^2e}{dt^2} = \frac{3V}{W}(P - P_0) - g_e\frac{d_e}{dt} + \frac{R_e}{W} \tag{3.1.12}$$

$$W = 3N\tau^2kT \tag{3.1.13}$$

$$< \vec{R_i}^2 >= \frac{2mgkT}{h} \tag{3.1.14}$$

$$< R_e^2 >= \frac{2Wg_ekT}{h} \tag{3.1.15}$$

Where, V is the volume of the system, τ is the oscillation period, W is the piston mass and $\vec{R_i}$ and R_e the noise on the atoms and the piston, respectively [133, 140].

In the case of an NVE ensemble, energy is conserved and no heat exchange takes place since there is not a need for temperature and pressure to be controlled (adiabatic ensemble). However, it is to be noted that there tends to be fluctuations in the energy profiles acquired with the implementation of this ensemble, due to rounding and truncation errors during the integration process. The NVE ensemble is obtained by solving Newton's equation without any temperature and pressure control, while energy gets conserved. Constant-energy simulations are not recommended for equilibration because without the energy flow facilitated by the temperature control methods, the desired temperature cannot be achieved while the energy flow is vital for the specification of the temperature. On the contrary NPT is more suitable for equilibrating density and can relieve artefacts that may occur if the system has not been optimally packed. During equilibration, NPT is usually employed to maintain a constant density and allow the simulation box to reduce to the "proper" size for the number of solvent molecules of a water-membrane system. However, NPT is computationally more expensive than NVE because the pressure scaling is not free. NVE ensemble is useful during the data collection phase, as it facilitates exploring the constant-energy surface of the conformational space, as well as can be generated to avoid the perturbation introduced by temperature- and pressure-bath coupling.

3.2 Membrane models in MD

Molecular dynamics simulations are employed to construct lipid bilayers of different composition. In general, a lipid bilayer forms spontaneously when phospholipids are placed in water, and amphipathic lipids (lipids with polar and non-polar regions) orient their hydrophilic ends towards the outside and inside of the cell, while the hydrophobic tails get in between the polar heads of the lipid molecules. However, it has been found both experimentally [142] and numerically [143] that very few water molecules exist beyond the carbonyl group in the sn-1 chain in equilibrium states. Thus, molecular models of lipid bilayers always appear to have (thick) layers of water molecules on top of each leaflet.

The following five computational models correspond to lipids bilayers consisting of

5 different types of lipids (DPPC, DMPC, POPC, POPE and PLPC). The structure files for the visualisation of the membranes were downloaded from online links [144, 145] and uploaded to VMD software [134]. Simulations were run under different configurations for these 5 computational models to be finally created.

The computational model of a 1,2-Dipalmitoyl-sn-glycero-3-phosphocholine (DPPC) below consists of 128 lipids and 2460 water molecules in total for 1600 ps simulation time.

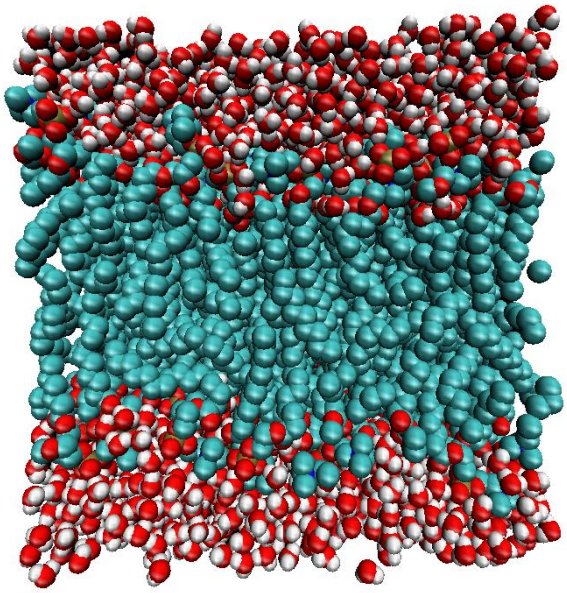

Figure 3.5: DPPC bilayer with 128 lipids

Below (figure 3.6) is shown a computational model of a 1,2-Dimyristoyl-sn-glycero-3-phosphocholine (DMPC) of 72 lipids for NPT simulation of 40ns. In figure 3.7 a 1-Palmitoyl-2-oleoyl-sn-glycero-3-phosphocholine (POPC) of 72 lipids is demonstrated. The simulation time was 1ns and anisotropic pressure coupling had been applied. Figure 3.8 shows a 1-Palmitoyl-2-oleoyl-sn-glycero-3-phosphoethanolamine (POPE) with 340 lipids after 10ns simulation time. Lastly a palmitoyl-linoleoyl-phosphatidylcholine (PLPC) lipid bilayer is shown and consists of 128 lipids.

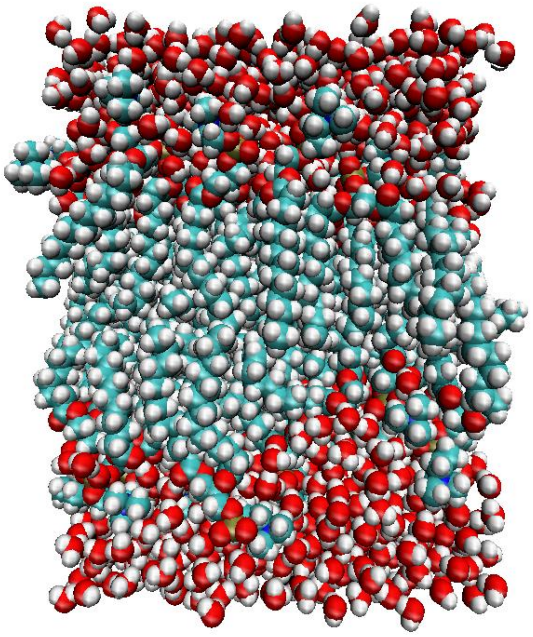

Figure 3.6: DMPC bilayer with 72 lipids

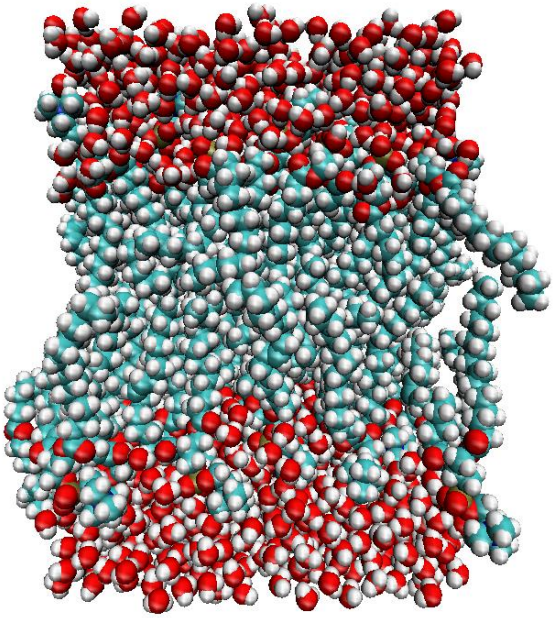

Figure 3.7: POPC bilayer with 72 lipids

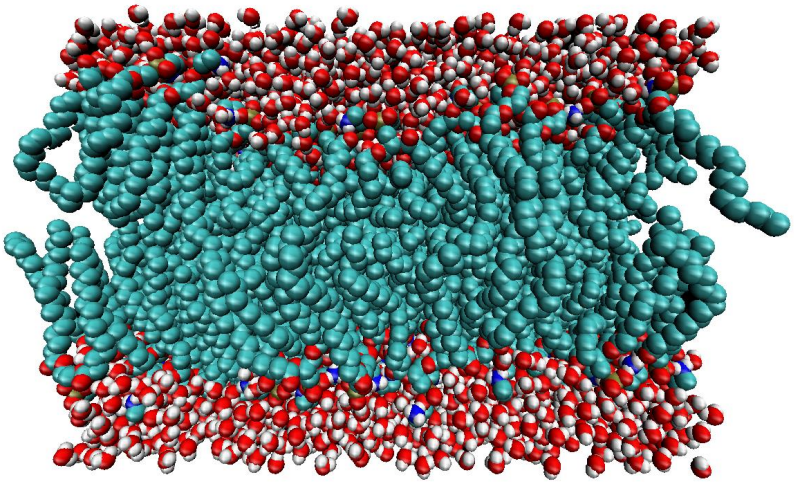

Figure 3.8: POPE bilayer with 340 lipids

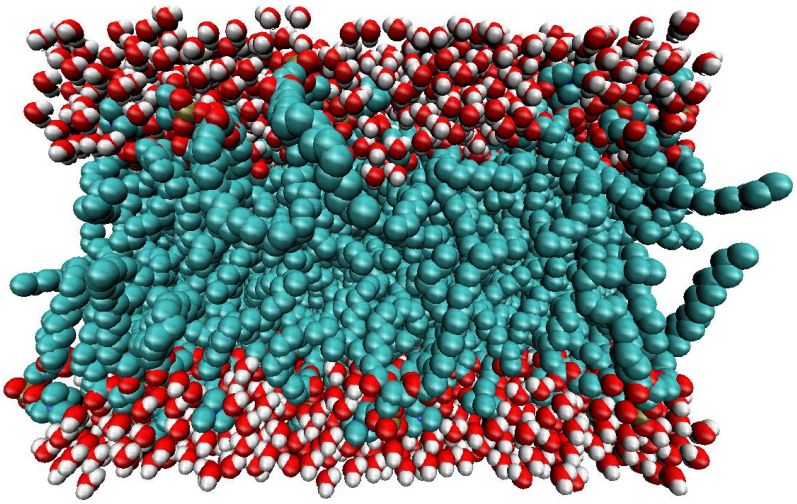

Figure 3.9: PLPC bilayer with 128 lipids

3.3 Shock wave modeling

The present method is in reality a momentum pulse; however, in the literature it is also called as shock. Furthermore, a shock wave can be generated only through cavitation effects where the nanobubbles collapse as low and high momentum impulses travel through them. In this study [15] the shock wave strength is provided through the shock impulse which is defined as the time integral of pressure over the shock-pulse duration [13]:

$$I = \int_0^{T_{I_p}} Pdt \tag{3.3.1}$$

where P is the instant pressure while the impulse is being applied and T_{I_p} is the duration. A shock wave is a high pressure wave with a steep wave front that propagates at supersonic speed and passes the cell membrane within a very short time in the order of picoseconds. This is a high-speed phenomenon due to the short distance that the shock travels. Membrane thicknesses are in the order of nanometers, and thus, the study of the interaction of a shock with a membrane through molecular dynamics is limited towards simulating the effects of the application of a shock impulse on a membrane. Researchers [13, 66] have experimentally demonstrated that the permeability of cell membrane can be enhanced by the increase of the shock wave impulse, irrespective of the peak pressure of the shock wave.

The shock waves applied on the membrane have been modeled as a rise in the momentum of the upper water layer that was under the effect of the shocks. It is assumed that the shock hits directly the upper water layer of the membrane as a pulse and there is no rarefaction; hence it is modeled as a momentum increase and transfer. The new velocities that the water molecules of the upper layer will have, are determined by the incident angle θ, the impulse, and the thickness of the shock. The average velocity of the water molecules that is added to the thermal velocity in the water slab is calculated as [107]:

$$\upsilon = \frac{I_p * A}{m * N_w} \tag{3.3.2}$$

Accordingly, the volume of the water slab will be [15, 107]:

$$V_{waterslab} = T_{sw} * A \tag{3.3.3}$$

where A is the area in the XY plane of the membrane, $m = 2.99146 \times 10^{-26}$ kg is the mass of a water molecule, and N_w is the number of water molecules in the water slab dictated by the thickness of the shock wave impact, T_{sw}. The incident angle θ is determining the impulse value which decomposes into perpendicular components as shown below [15,

107]:

$$I_p = \left\{ \begin{array}{c} I_{p,y} = I_p * sin\theta \\ I_{p,x} = I_p * cos\theta \end{array} \right\}$$

In the current study the incident angle was implemented in the z and y axis. Nevertheless, the impulse could have been analysed on the z and x direction, instead.

Once the velocity impulse is introduced into the system the total energy of the system drastically changes, and whichever ensemble is employed in the simulation (microcanonical NVE or isothermal-isobaric NPT), the kinetic energy of the system behaves differently. Therefore, it is important to monitor these value and understand if the simulation proceeds towards the correct direction. For example, for NPT ensemble, the additional energy that is introduced into the system is dissipated through the Nose-Hoover thermostat, leading to lower values of kinetic energy. The motion of the COM is important for visualising and providing indications regarding the relative movements of the lipids. Although periodic boundary conditions are employed, the lipid coordinates are un-wrapped, meaning that every time that a molecule pass through the boundary is stored in the memory and this value is taken into account in the final computation. Especially, in the case with the incidence angles the COM reveals important information regarding the relative movement of the membrane's lipids.

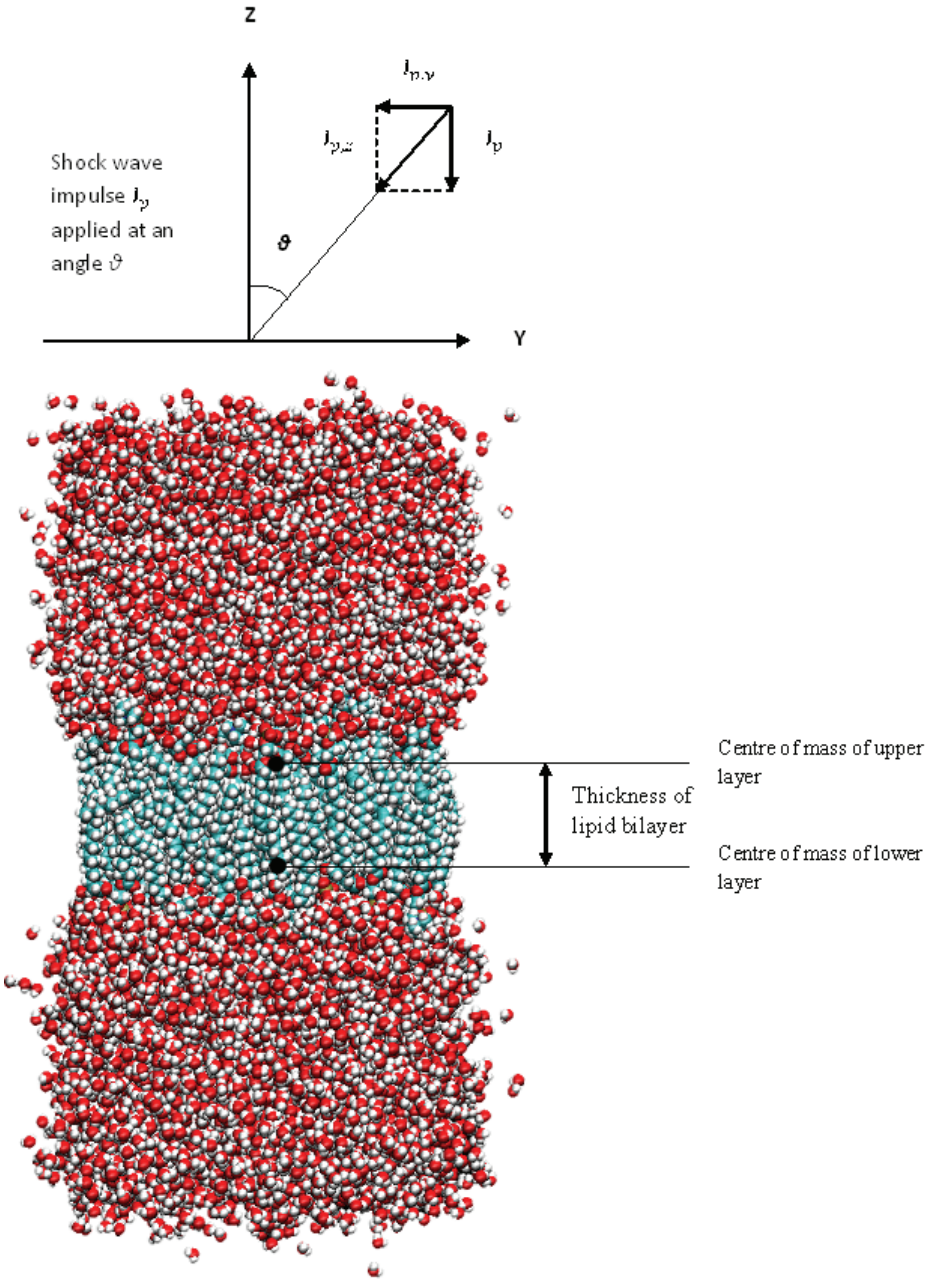

Figure 3.10: Schematic of a biological membrane and oblique shock wave implementation [15].

3.4 Lateral diffusion and other system properties

Lipid bilayers in their fluid phase behave as a two dimensional (2D) fluid and the lateral (self) diffusion coefficient of lipids within a membrane monolayer has been determined both experimentally by the use of different methods [146–152] and via computer simulations [153–158]. Diffusion rates of lipids can be calculated using Albert Einstein's equation, which demonstrates the relationship between mean square displacement (MSD) and diffusion coefficient of particles moving at random [159], as a function of observation time. This relationship is shown below:

$$D = \frac{1}{6}[\lim_{x\to\infty}(\frac{d}{dt}(MSD))] \tag{3.4.1}$$

For this study, equation 3.4.1 has been modified to fulfill the case of two dimensions (see equation 3.4.2), since it was used to measure the lateral diffusion of the lipids in the XY plane [15, 159].

$$D = \frac{1}{4}[\lim_{x\to\infty}(\frac{d}{dt}(MSD))] \tag{3.4.2}$$

The MSD is a measurable quantity which directly relates to the underlying motion and the diffusion of particles. It is the average displacement squared of a given particle moving at random within a fluid and is defined by equation 3.4.3.

$$MSD = \langle\frac{1}{N_L}[\sum_{i=1}^{N_L}[r_i(t) - r_i(0)]^2]\rangle \tag{3.4.3}$$

where N_L is the number of lipids, $r_i(t)$ the position of lipid i (denoting the center of mass of a lipid molecule in the 2D membrane plane) at time t, and the symbol $\langle\rangle$ denotes an average of time steps and/or particles, performed over all lipid molecules and initial time origins. The averaging of the time steps in this fashion allows for any time step to be considered the time zero in the equation, because the equation is only looking at observation times (relative times or elapsed times) rather than some absolute time.

During simulations, centre of mass velocities of the water-membrane system are removed. However, there may still be some motion of the bilayer as a whole with respect to the centre of mass of the water-membrane system or some motion of the two leaflets with respect to each other. This kind of motions should be negligible for large systems [157], but for small ones, like the ones in the current study, the mean motion of the layer as a whole must be subtracted from the calculations.

It can be observed from equation 3.4.1 and equation 3.4.2 that the MSD is proportional to the diffusion coefficient. In fact, typical MSD measurements plotted as a function of time will follow a linear trend, and if the slope of this plot is taken, the diffusion coefficient can readily be obtained. Previous studies [160–164] have experimentally demonstrated that the use of the above equations correlate to a level of accuracy within repeatability; therefore, the author of the present study will use these equations to calculate all diffusion coefficients within this document.

Experiments suggest that there are at least two relevant length/time scales associated with the lateral diffusion of lipids in a lipid bilayer [165]. Experimental studies designed to examine motion on picosecond time scales measure a diffusion coefficient that can be one to two orders of magnitude larger than the diffusion coefficient measured in experiments that probe motion on nanosecond time scales. It has been found that the time evolution of the mean square displacement of lipid molecules demonstrates three separate dynamical regions: (i) ballistic, for simulation time up to 10fs, (ii) sub-diffusive, for simulation time between 10ps and 10ns, and (iii) Fickian diffusion, for over 30ns of simulation time. The lateral diffusion coefficient calculation in the present study falls into the sub-diffusive category.

At the same time, the lack of the knowledge regarding the mechanism of the increase in permeability, still prevents the development of applications that involve shockwave-membrane interactions. The molecular transport across the membrane can be obtained by molecular dynamics (MD) simulations, where the dynamical process of structural changes in lipid bilayers can be clarified. Thus, in order to understand the biological response of a membrane to the application of a shock it is essential that changes in parameters such as the kinetic energy of the system, the thickness of the membrane, the centre of mass (COM), the MSD, and the diffusion coefficients are monitored throughout the simulations (see Appendix A).

The kinetic energy of a system is calculated by making use of the following formula:

$$E_k(t) = \sum_{i=1}^{N} [\frac{1}{2} m_i v_i^2(t)] \tag{3.4.4}$$

where N is the number of atoms in the system, m_i the mass of an atom i, and υ_i, its velocity at a time point t. When a shock is applied, momentum gets transferred to the molecules in the upper water layer of the water-membrane system, thus, the velocities in the upper water layer change. The significance of the velocities change lies in the strength of the shock and the thickness of the membrane under study. Every molecule in the water-membrane system that gets affected by the shock will result in acquiring an increase in velocity that is proportional to the intensity of the impulse as well as new kinetic energy, as explained in the previous section (Section 3.3). Moreover, the kinetic energy of a water-membrane system can be conserved by regulating the temperature of the system, and thus

manipulating the velocities of each atom in the simulation via the use of a thermostat as described in Section 3.1.5.

The COM of the lipid bilayer has been determined by initially calculating the COM of the upper and lower lipid bilayer separately (also see schematic in figure 3.10). The COM of each layer has been measured by finding the COM of each lipid in x and y direction, based on the trajectories of each lipid. The thickness of the lipid bilayer is representing the distance between the COM of each monolayer (see figure 3.10).

CHAPTER 4

Shock thickness effects

4.1 Membrane domain selection

In general, biological membranes are complex structures consisting of phospholipids, proteins, and carbohydrates and the computational and mathematical tools that describe them keep getting revised and updated, as discussed in Chapter 1. The fluid mosaic model has been developed to define asymmetric models with lipid rafts. However, the fundamental and common feature of all biological membranes is the lipid bilayer. Although the fluid mosaic model is a simplification of the real membrane, it is extensively applied in computational modeling over the past decades [166–168]. In numerical terms, the representation challenges are primarily associated with the force fields employed. In the present study the well-established AMBER is employed for the modeling of a POPC membrane. The AMBER force field takes into account the bonds, the angles, the torsions and the van der Waals interactions and is the most widely used force field for modeling biomolecules.

In the current study simulations were run for three POPC lipid bilayers consisting of 33, 52, and 80 lipids on each monolayer. The volumes of the three bilayers were 56Å $\times$ 55Å $\times$ 54Å, 66.2Å $\times$ 65.0Å $\times$ 54Å, and 79.7Å $\times$ 80.2Å $\times$ 54Å, respectively. All lipid bilayers had a thickness of 54Å in accordance with experimental studies [166–168] and were fully hydrated (the thickness of the water molecules on each monolayer was 51Å). The three water-lipid systems were initially minimized and equilibrated for a total time equal to 50ps. In the first 1ps the systems were minimised, followed by 1ps where the temperature increased from 0K to 230K. Subsequently, for 3ps the pressure of the systems increased from 734bar to 1779bar, and finally in the remaining 45ps the systems were being equilibrated. After equilibration, the three systems were computationally submitted to a set of normal shock waves of thickness 5, 7, 10, and 12Å, and impulse that varied between $0.33 mPa \cdot s$ and $10 mPa \cdot s$. All simulations were run under the NPT ensemble as it is described in the following section. The two largest lipid bilayers produced results concerning the final positions and velocities of every atom in the systems after 150ps of simulation time, as well as presented membrane rupture due to excessively high velocity

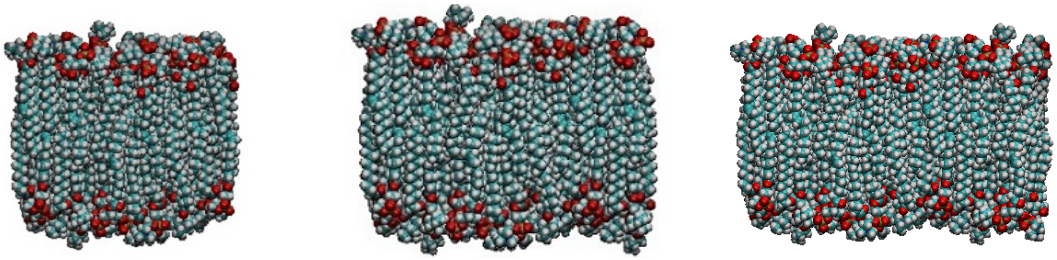

(a) POPC membrane of 66 lipids (b) POPC membrane of 104 lipids (c) POPC membrane of 160 lipids

Figure 4.1: POPC membrane models before minimisation. The water molecules are not displayed for clarity.

of atoms under the same conditions of combined shock thicknesses and impulses. However, the smallest membrane system of only 66 lipids was corrupted during the simulations for smaller values of shock thickness and impulse. Table 4.1 demonstrates which simulations delivered results and when the membrane was ruptured. It was therefore concluded that the water-membrane model that adequately captures the membrane behaviour with the minimum of computational cost is the POPC bilayer with a total of 104 lipids.

Combined shock wave effects:Successful simulation(ran),membrane rupture(failed)				
t_{shock} (Å)	i ($mPa \cdot s$)	POPC(66lipids)	POPC(104lipids)	POPC(160lipids)
5	0.33	ran	ran	ran
	0.66	ran	ran	ran
	0.99	ran	ran	ran
	2	failed	ran	ran
	3	failed	ran	ran
	4	failed	ran	ran
	5	failed	failed	failed
	6	failed	failed	failed
	7	failed	failed	failed
	8	failed	failed	failed
	9	failed	failed	failed
	10	failed	failed	failed
7	0.33	ran	ran	ran
	0.66	ran	ran	ran
	0.99	ran	ran	ran
	2	failed	ran	ran
	3	failed	ran	ran
	4	failed	ran	ran
	5	failed	ran	ran
	6	failed	failed	failed
	7	failed	failed	failed
	8	failed	failed	failed
	9	failed	failed	failed
	10	failed	failed	failed
10	0.33	ran	ran	ran
	0.66	ran	ran	ran
	0.99	ran	ran	ran
	2	ran	ran	ran
	3	failed	ran	ran
	4	failed	ran	ran
	5	failed	ran	ran
	6	failed	ran	ran
	7	failed	ran	ran
	8	failed	failed	failed
	9	failed	failed	failed
	10	failed	failed	failed
12	0.33	ran	ran	ran
	0.66	ran	ran	ran
	0.99	ran	ran	ran
	2	ran	ran	ran
	3	ran	ran	ran
	4	failed	ran	ran
	5	failed	ran	ran
	6	failed	ran	ran
	7	failed	ran	ran
	8	failed	ran	ran
	9	failed	ran	ran
	10	failed	ran	ran

Table 4.1: Simulations of three water-membrane models

4.2 Simulation Description

The physical interaction between a shock wave and a cell membrane is complex, often involving various mechanisms such as radiation, heat, cavitation, and plasma [66]. Moreover, the time scales in which these mechanisms occur can range from nano- to pico-seconds. The experimental studies carried out to investigate such interactions are done in a well controlled environment such that the observed phenomena are solely due to shock waves [130] while minimising various side effects which can lead to cytotoxicity. For example, in order to reduce cavitation and radiation effects, cell membranes are generally placed in a liquid medium and shielded by protective films (e.g. polyimide or polystyrene) as they are subjected to single or numerous shock waves of various strengths and duration. The sources for these shock waves are typically high-energy lasers [23, 83, 87, 130, 131] or shock tubes [13]. In the case of laser induced shock waves (LSW), shock waves are generated by ablation of the polystyrene (or polyimide) film, and focused at a desired locus by an acoustic lens. For shock tube induced shock waves, shock waves are generated by the explosion of a diaphragm separating two different gas chambers, a high-pressure and low-pressure chamber. A schematic of an experimental arrangement for both laser- and shock tube-induced shock waves has already been presented in Figure 2.3.

For LSW experiments, cell membranes are typically placed immediately adjacent to the polymide film; thus, as the shock wave is induced by this film it immediately impacts the cells. Reflected waves have been observed, but the intensity of these cells is negligible in comparison to the primary shock wave [13]. The intensity of shock waves is generally measured as a pressure of the surrounding medium. This is practically done by a needle hydrophone which is positioned downstream of the cells as previously shown in Figure 2.3. Figure 4.2 shows a typical pressure distribution with respect to time for both LSW, plot (a) and (b), and shock tube-induced shock waves, plot (c). As the LSW is applied to the cells, there is a sudden rise in pressure followed by a smaller, second pressure peak. The second pressure rise is the result of the reflected waves discussed above, and can be observed that their intensity is significantly lower in comparison to the first pressure rise. The pulse duration of the shock wave generated by the shock tube, plot (c), was longer than those of pulses of the excimer and ruby lasers [13].

Figure 4.2 is indicative of the short time scales and the rapid changes in dynamics involved in the shock wave and cell membrane interactions. A typical shock wave velocity has been calculated to be $2366ms^{-1}$ [13].

In the present study, molecular dynamic simulations were carried out to investigate the effects of perpendicular LSW on the lateral diffusion of a biological membrane. Experiments [13] regarding shock wave applications on a membrane involved shock wave pulses whose duration was at least 180ns, which corresponds to the pulse width of $\sim 270\mu m$ in water. The period of time required for the wave to travel through the computational box is in the order of picoseconds. Thus, it is impossible or prohibitively expensive to reproduce such shock waves in the simulation box with the application of periodic boundary

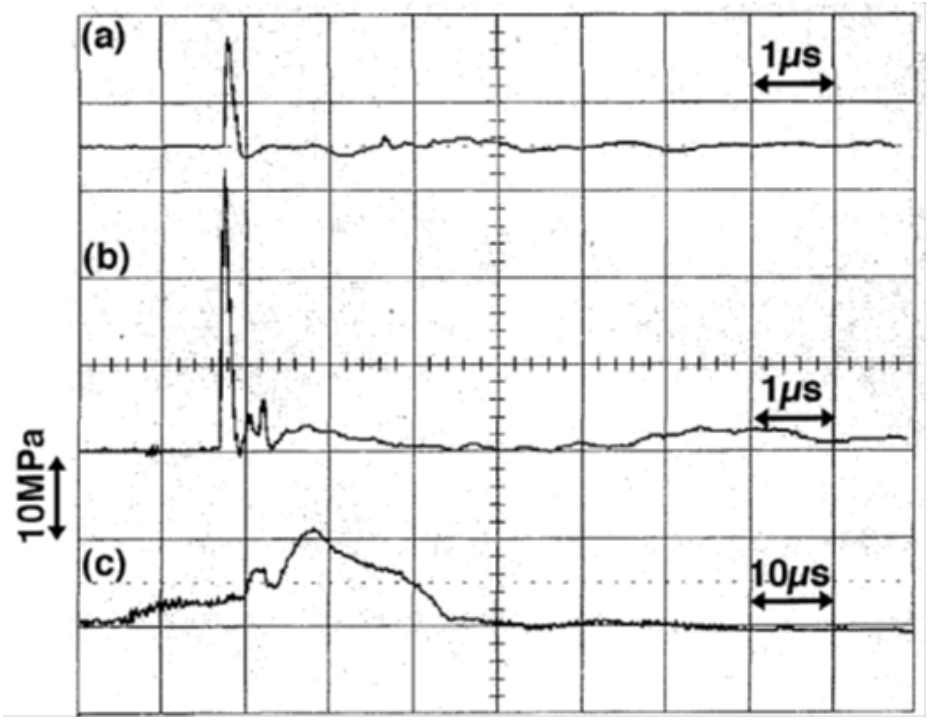

Figure 4.2: Pressure wave profiles for an excimer laser (a), a ruby laser (b), and a shock tube (c) [13].

conditions.

In the literature there are two main approaches for modeling a shockwave in MD simulation. In the first approach the entire computational domain is assigned a specific velocity (piston velocity) which impacts towards a reflective wall, therefore generating a shockwave which passes through the box. This approach of implementing a shockwave has been proved to be effective for gas flow cases; however, if complicated structured bonds are present this technique is susceptible to breakage of the bonds and consequently destroying the biological structures. Therefore, aiming to minimize the side effects from the shockwave implementation the approached proposed in Koshiyama et al. 2006 [11] is employed where the velocity component of the water molecules within a small bin near the upper boundary is increased to pre-defined piston velocity (velocity impulse). This velocity impulse acts as piston generating a shock wave through the computational domain. It has to be noted though, that throughout the document we follow the notation and terminology used in Koshiyama et al. 2006 [11], particularly when the term shockwave is used we do not refer to the speed of sound through the water molecules but to the speed of momentum transfer from the upper water molecules to the end of the simulation box.

In the present study the effects of perpendicular shock waves on the lateral diffusion of a biological membrane through molecular dynamics simulations are investigated. The biological membrane employed consists of 104 1-palmitoyl-2-oleoyl-sn-glycero-3-

phosphocholine (POPC) phospholipids with 52 lipids on the upper layer and 52 lipids on the lower one. Computational experiments have been carried out by utilising the NPT and the NVE ensemble (see chapter 5) with shock impulses varying from $0.33mPa \cdot s$ to $10mPa \cdot s$.

The impulse used in the simulations is small compared to experiments [13] where it is typically $100Pa \cdot s$, although the average velocity in the simulations is large. For impulse values close to $100Pa \cdot s$, the required average velocity becomes larger than the speed of sound in water, which is in agreement with another numerical study [11]. However, the average velocity represents the increase of momentum of water molecules due to the application of a shock wave and therefore, does not corresponds to the speed of sound in liquid water nor to the propagation speed of the shock wave (also see section 3.3 and 3.4). By modeling the shock waves as a velocity impulse (also see section 3.3 and 3.4) it is made feasible to qualitatively compare the numerical results of this work with previous experimental ones.

Furthermore, Kodama et al. [13] experimentally observed that the density change of the cell membrane and the surrounding fluid reduced less than 1% for a shockwave travelling above Mach 1 and for a laser fluence of $40.3Jcm^{-2}$. Therefore, similarly to Kodama et al., in this paper the cell membrane has been treated as an incompressible fluid.

The POPC membrane under study is in the *cis* unsaturated form (i.e. hydrogen atoms are on the same side of the double bond) and has been hydrated with water molecules on top of the hydrophilic heads of both monolayers. This results in a total number of 15134 water molecules and 59338 atoms being employed for the modeling of the complete system. The computational box spans 66.2Å, 65.0Å, and 155.9Å in the x, y and z respectively, with periodic boundary conditions applied in each direction.

The pressure and temperature remain constant throughout the simulation and equal to 1atm and 310K. The time-step used is 1fs, non-bonded interactions have been calculated every 2fs and full electrostatics every 4fs. The total simulation time is 200ps.

The shock impulse applied varied between $0.33mPa \cdot s$ and $10mPa \cdot s$, while the thicknesses of the impulses were 5Å, 7Å, 10Å, and 12Å. These thicknesses represent the thickness of the shock layer that gets applied to the water slab, where the momentum transfer initially takes places (also see section 3.3 and 3.4 for a more analytical description). Shock thicknesses actually refer to the length of the upper water layer which an impulse is applied to. It should be noted that throughout this report we will be referring to the thickness of this area of the water layer as shock thickness. The simulations have been performed through the NPT and NVE ensemble in order to examine the different response of the membrane to the different ensembles.

The water-membrane system is initially minimized and equilibrated for a total time equal to 50ps. During the first 1ps the minimization process takes place followed by 1ps where temperature increase from 0K to 230K. During the next 3ps, pressure increases from

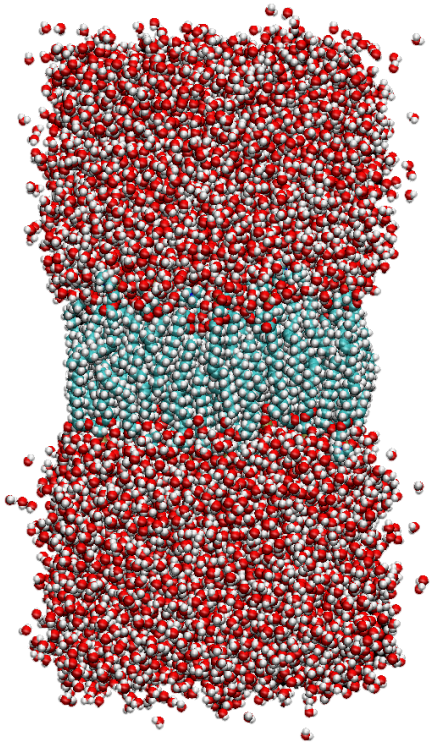

Figure 4.3: Snapshot of POPC bilayer after minimization and equilibration. Water molecules appear in red and white and lipids in blue and white.

734bar to 1779bar and then the simulation runs for 45ps until the system is finally equilibrated. Figure 4.3 shows a snapshot of the entire system after minimization and equilibration. The obtained equilibrated water-bilayer system was utilized for the preparation of the initial configuration for the shock wave simulations, with the addition of momentum (equal to the respective impulse value times the cross-sectional area of the simulation box) to the water molecules in the volume, defined by the respective shock thickness each time, as analytically explained in section 3.3.

Simulations were performed through the NPT and NVE ensemble in order to examine the different response of the membrane to the different ensembles. Owing to the periodic boundary conditions, the simulations were terminated at the time when the effect of the shock impulse reached the boundary at the opposite side of the simulation box in the z direction. The time of the simulation was monitored carefully and each simulation was terminated just before the acoustic wave approached the lower boundary. The same approach for estimating the total simulation time was also followed in Koshiyama et al. 2006 [11] and Koshiyama et al. 2008 [107].

4.3 Results and Discussion

4.3.1 Effects on Kinetic Energy - NPT ensemble

The initial aim of this study is to investigate the effect of shock wave thickness. To this end, a number of simulations involving various shock thicknesses and impulses are examined and presented here. More specifically, shock wave thicknesses used vary from 5Å to 12 Å. Figure 4.4 shows the time variation of the system's kinetic energy for various values of shock thickness and impulse. A common element observed is a rapid increase in the kinetic energy at the time that the shock is introduced to the system (t=25ps). As the simulation evolves, the kinetic energy for all values of shock thickness decreases and relaxes almost at the same mean value for the various thicknesses. This is expected since the ensemble used is the NPT along with the implementation of Nose-Hoover-Langevin dynamics (see section 3.1.5. for detailed explanation).

The rapid increase of the system's energy, as implied in figure 4.4, was expected since through the application of the shock wave essentially additional momentum and consequently kinetic energy is introduced to the system. As the shock thickness increases a small decrease in the maximum kinetic energy can be identified. The thickness of the shock does not alter the total momentum transferred to the system, which is determined by the impulse, but it mainly affects the velocity distribution across the water molecules. To further elaborate, larger thickness implies that the shock will be applied to a larger number of water molecules increasing therefore the total mass. As a consequence, a reduced velocity is applied (see equation 3.3.2).

It is thus apparent that higher impulses result in higher initial kinetic energies that eventually end up relaxing around almost the same mean value throughout the course of the simulation. The significance of the shock impulse has been emphasised by the results from the work of Liu et al. [10] and Kodama et al. [13], who further experimentally demonstrated the enhancement of permeability with an increase in shock impulse, irrespective of the peak pressure of the shock wave. In particular, it was shown [13] that the transport of fluorophores across the membranes of leukemia cells is governed by the shock impulse rather than the maximum pressure. The penetration of water molecules in the hydrophobic region of the bilayer was also proven to be enhanced by the shock wave impulse [11]. Furthermore, the modeling of shock waves by the impulse makes the qualitative comparison possible between the numerical results in this work and previous ones [11, 13, 107, 169].

When the applied impulse is $5mPa \cdot s$ and the shock wave thickness 5Å, the velocities of the water molecules rise significantly to the point that the simulation becomes unstable. The same happens as the impulse gets stronger -$6mPa \cdot s$ and $7mPa \cdot s$- for shock waves thickness of 5Å and 7Å. This can be understood by the fact that, as explained above, small shock thicknesses result in higher kinetic energies.

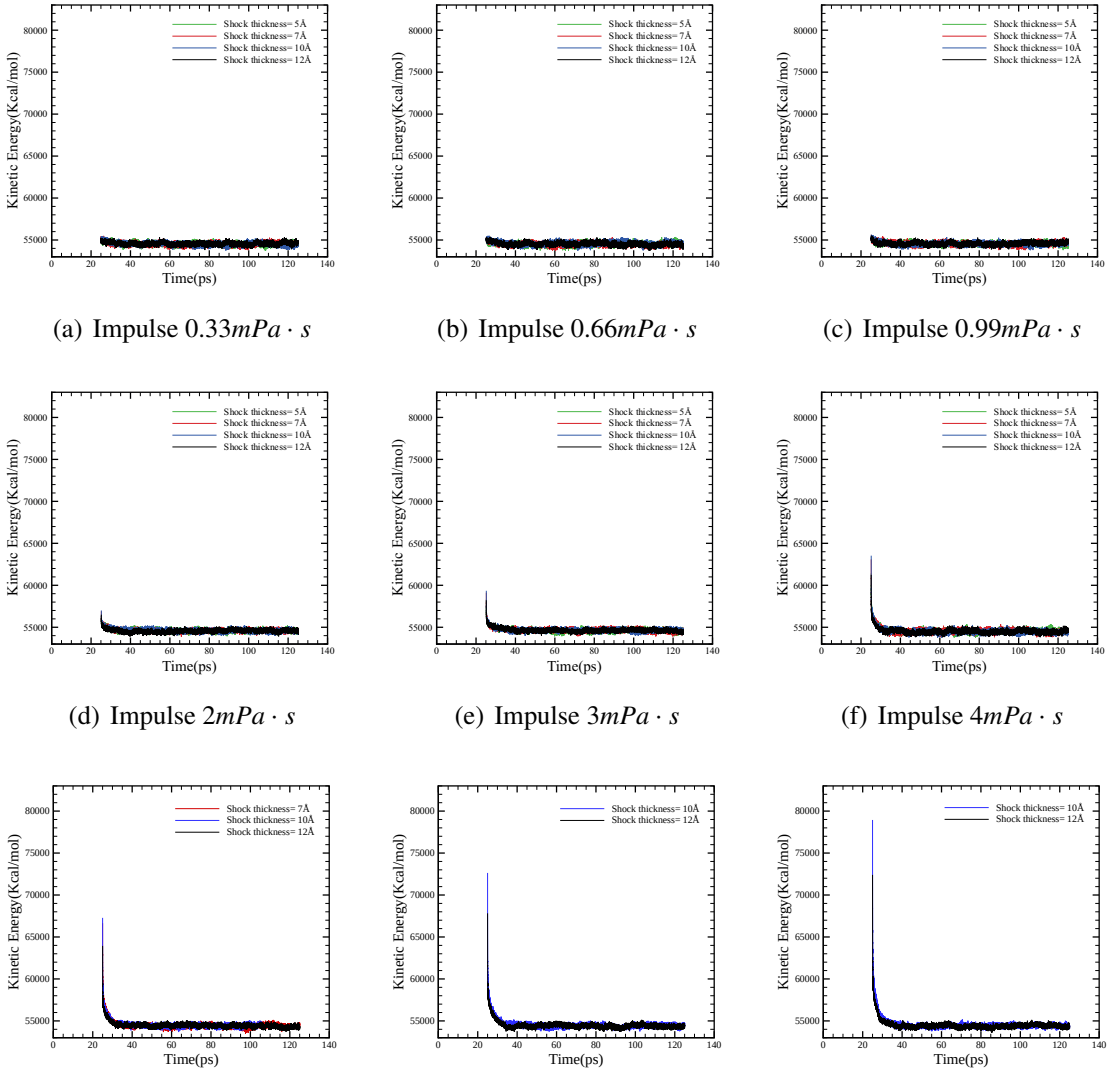

(a) Impulse $0.33mPa \cdot s$ (b) Impulse $0.66mPa \cdot s$ (c) Impulse $0.99mPa \cdot s$

(d) Impulse $2mPa \cdot s$ (e) Impulse $3mPa \cdot s$ (f) Impulse $4mPa \cdot s$

(g) Impulse $5mPa \cdot s$ (h) Impulse $6mPa \cdot s$ (i) Impulse $7mPa \cdot s$

Figure 4.4: Shock wave effects on Kinetic Energy at various shock wave thicknesses

Finally, for impulse higher that $7mPa \cdot s$ the kinetic energy of the water molecules is too high to maintain the membrane for shock thicknesses of 5Å, 7Å and 10Å. Only a shock with 12Å thickness can increase the kinetic energy of the membrane without damaging it for shock impulses up to $10mPa \cdot s$.

4.3.2 Effects on Membrane Thickness - NPT ensemble

The following figure (figure 4.5) presents the time variation of membrane thickness for different impulses and values of shock thickness. At the beginning of the simulation after minimization and equilibration the thickness of the membrane is the same for the examined cases and a common trend is noticed with the membrane thickness to decrease until a local equilibrium is reached. Although, small differences between the different shocks exist, it can be observed that towards the end of the simulation the minimum membrane thickness is obtained for shock thickness equal to 12Å when the impulse is $0.33mPa \cdot s$.

As the impulse increases, from $0.33mPa \cdot s$ to become $0.66mPa \cdot s$, it appears to be more efficient in reducing the membrane thickness when the shock is of 12Å, which underlines the significance of impulse in reducing the membrane thickness. For the case for $0.99mPa \cdot s$ it is observed that a shock thickness 5Å is able to result in the maximum reduction of the membrane thickness. The same happens for impulse 2mPa s and $3mPa \cdot s$. This is mainly linked to the efficiency of the momentum transfer across the water membrane interface. Smaller values of shock's thickness imply that the mechanism involving momentum exchange is based on larger water velocities and small application time whereas larger values of shock thickness mean that a shock with smaller velocity will hit the membrane for a longer period of time.

It is also shown that a shock of 5Å results in a momentum transfer able to give the water molecules very high kinetic energy that causes the simulation to be unstable. The same happens for impulses $6mPa \cdot s$ and $7mPa \cdot s$ and for shock thickness 5Å and 7Å, which is why in plots 4.5(g), 4.5(h) and 4.5(i) the kinetic energy over time is not presented for all the shock thicknesses.

4.3.3 Effects on membrane centre of mass (COM) - NPT ensemble

In Figure 4.6 the corresponding movement of membrane center of mass for impulses from $0.33mPa \cdot s$ to $7mPa \cdot s$ and for shock thickness 5Å-12Å. The centre of mass is moving due to the momentum increase of the lipids followed by the application of the momentum impulse. Although periodic boundary conditions are used, the particle coordinates are "unwrapped", therefore showing the net motion of the particles. As expected, for smaller values of thickness the COM remains closer to its original position whereas for higher values a larger disparity it noticed. Smaller thickness implies smaller application time for

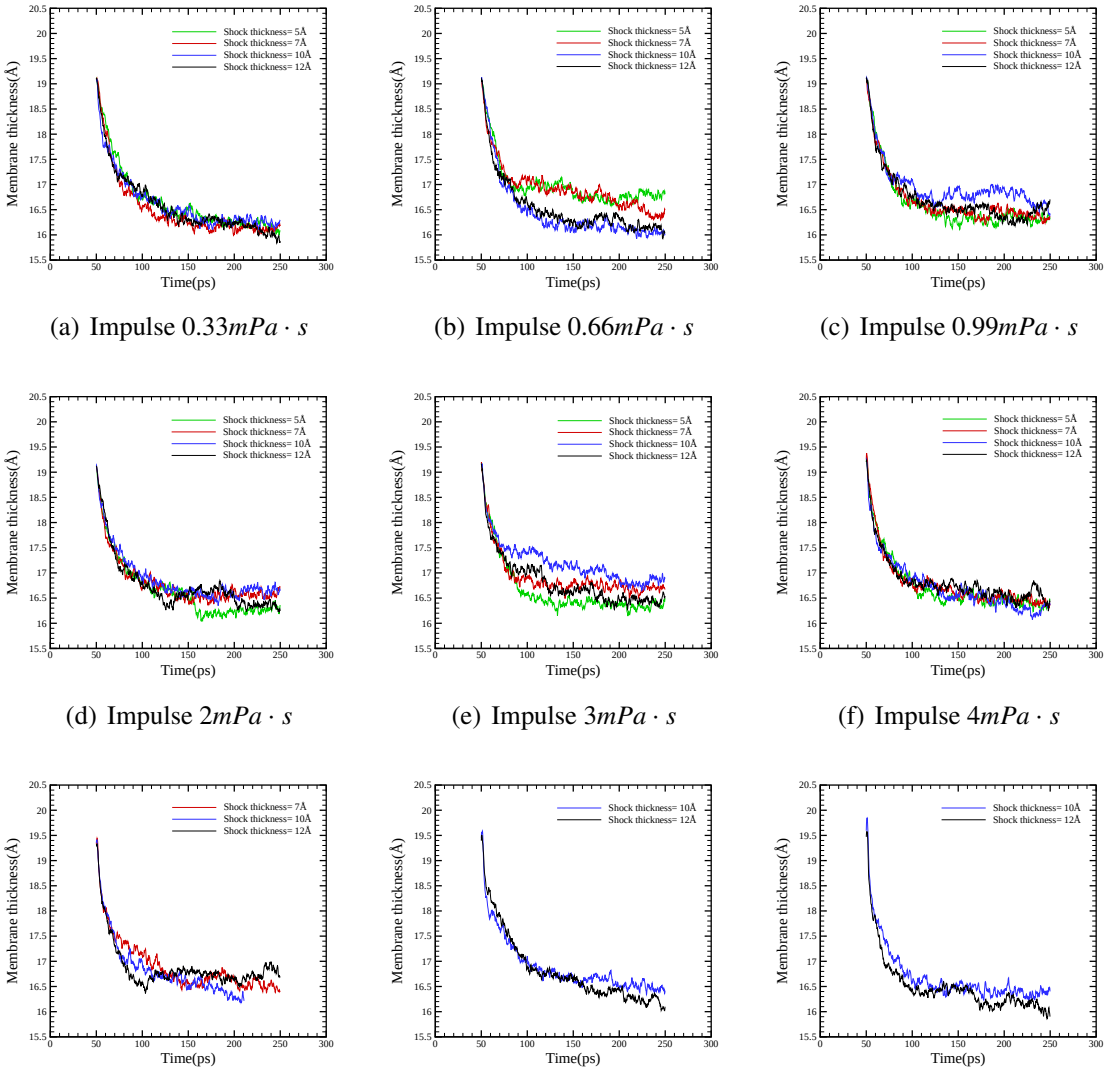

(a) Impulse $0.33mPa \cdot s$ (b) Impulse $0.66mPa \cdot s$ (c) Impulse $0.99mPa \cdot s$

(d) Impulse $2mPa \cdot s$ (e) Impulse $3mPa \cdot s$ (f) Impulse $4mPa \cdot s$

(g) Impulse $5mPa \cdot s$ (h) Impulse $6mPa \cdot s$ (i) Impulse $7mPa \cdot s$

Figure 4.5: Shock wave effects on Membrane Thickness at various shock wave thicknesses

the shock and therefore the COM remains in the vicinity of its original place. This is particularly noticeable when the impulse is $0.33mPa \cdot s$, $0.99mPa \cdot s$, $4mPa \cdot s$, since a shock of 5Å appears to allow the membrane COM to stay closer to its original place more than any other shock thickness.

4.3.4 Mean square displacement (MSD) and Lateral Diffusion - NPT ensemble

Figure 4.7 shows the mean square displacement of the membrane as a function of time for different shock thicknesses. The slope of the MSD is linked with the diffusion coefficient of the lipids and larger slopes imply higher lipid mobility within the membrane. Initially, there is motion due to interface energy and momentum transfer and this motion is then translated to lateral diffusion. The MSD slopes and therefore the lipid diffusivity are dependent on the efficiency of the momentum transferred from the water molecules to the upper layer of the membrane. More efficient momentum transfer implies higher slopes and consequently larger diffusion coefficients.

As figure 4.7 demonstrates, the highest slope is being noticed for shock thickness 7Å and Impulse $3mPa \cdot s$, while the smallest slope corresponds to shock thickness 10Å and Impulse $2mPa \cdot s$. In fact, from impulse $0.33mPa \cdot s$ to $4mPa \cdot s$ all 4 different cases for shock thickness are included in the plots and it is therefore advisable to make comparisons and draw conclusions within this area of results. In principal, the best combination of shock thickness and impulse capable of delivering the greatest value of MSD should be such that a relatively small shock thickness of a relatively strong shock is applied to the membrane. This is due to the fact that small shock thicknesses involve fewer water molecules and therefore grants them with higher velocities. At the same time, the higher the impulse the higher its effect on the membrane, so the momentum transfer is maximum. This also explains why as the impulse gets progressively higher the smaller shock thicknesses cause rupture of the membrane, as this is demonstrated in figure 4.7 for stronger shocks (from $5mPa \cdot s$ to $7mPa \cdot s$).

It is of great importance to understand the mechanisms behind lateral diffusion as a membrane property. To this end the estimation of the MSD as well as lateral diffusion has taken place for both the whole lipid bilayer but also each of the monolayers separately. The results are presented below, in figures 4.5, 4.8 and 4.9. It is apparent that both the upper and the lower layer of the membrane follow similar trends with the ones for the whole membrane. In particular, the maximum slope is again recognised when the shock thickness is 10Å and the impulse is $2mPa \cdot s$. Indicatively, it can be noted that for an impulse as strong as $2mPa \cdot s$ the maximum slope is noticed when the thickness of the shock is the smallest, 5Å. This is the case for the the upper layer as well as the whole membrane and the lower layer. At the same time, when the impulse is $3mPa \cdot s$, the highest shock thickness, 12Å, is the one that corresponds, as expected, to the minimum slope, for the reasons discussed in the previous sections of this chapter.

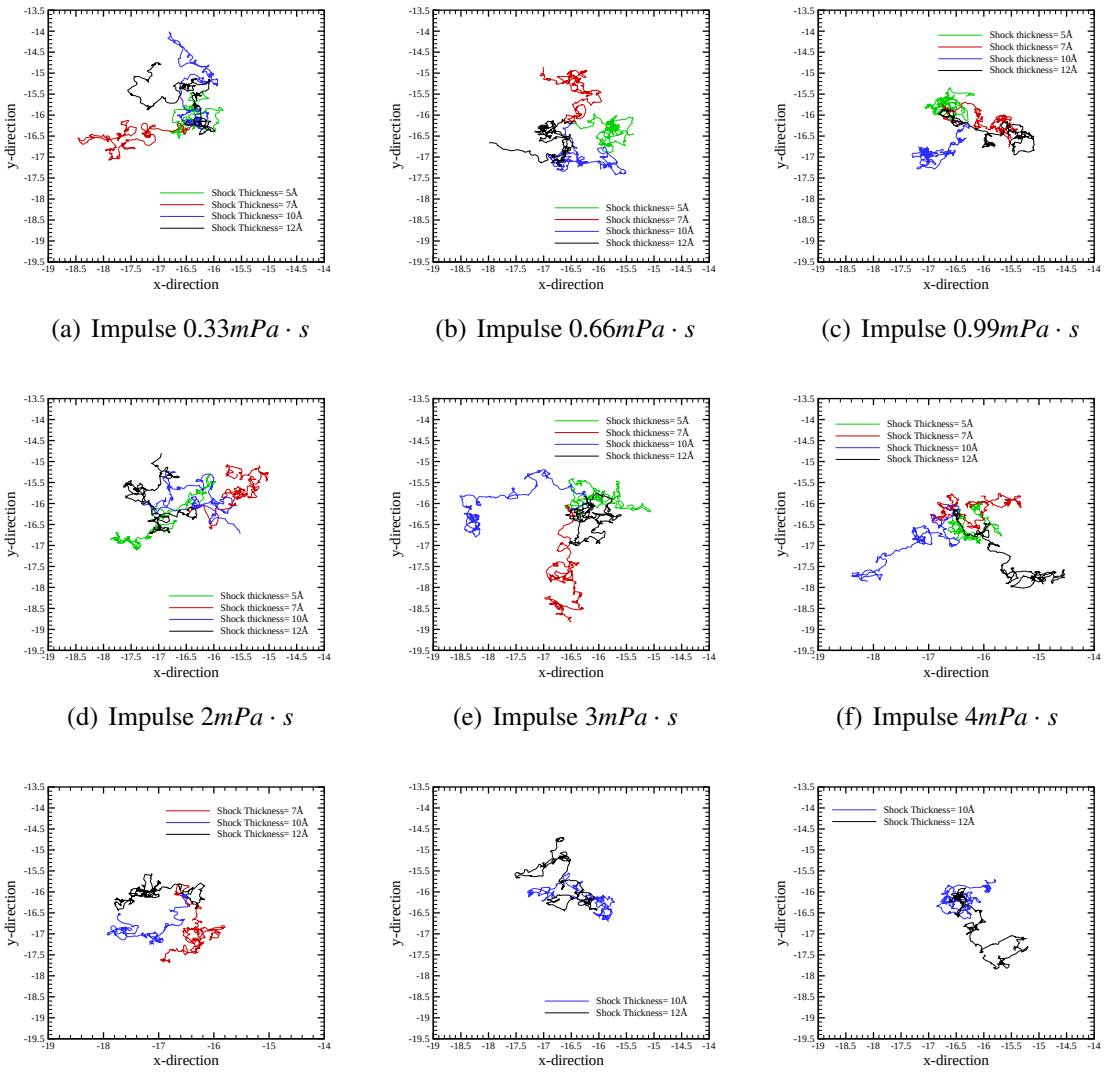

(a) Impulse $0.33mPa \cdot s$ (b) Impulse $0.66mPa \cdot s$ (c) Impulse $0.99mPa \cdot s$

(d) Impulse $2mPa \cdot s$ (e) Impulse $3mPa \cdot s$ (f) Impulse $4mPa \cdot s$

(g) Impulse $5mPa \cdot s$ (h) Impulse $6mPa \cdot s$ (i) Impulse $7mPa \cdot s$

Figure 4.6: Shock wave effects on the COM of the lipids of the membrane at various shock wave thicknesses

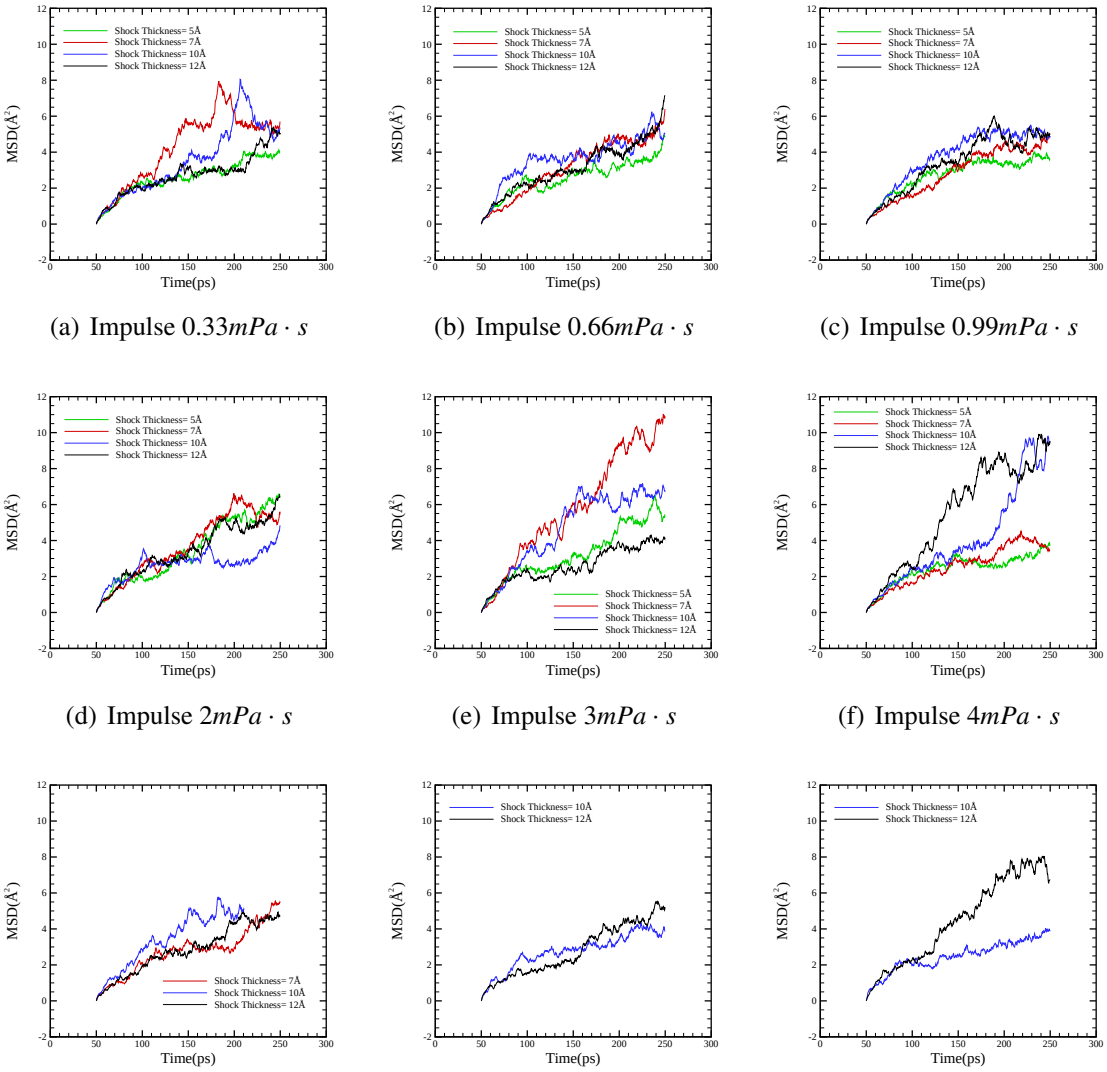

(a) Impulse $0.33mPa \cdot s$ (b) Impulse $0.66mPa \cdot s$ (c) Impulse $0.99mPa \cdot s$

(d) Impulse $2mPa \cdot s$ (e) Impulse $3mPa \cdot s$ (f) Impulse $4mPa \cdot s$

(g) Impulse $5mPa \cdot s$ (h) Impulse $6mPa \cdot s$ (i) Impulse $7mPa \cdot s$

Figure 4.7: Shock wave effects on the MSD of the membrane at various shock wave thicknesses

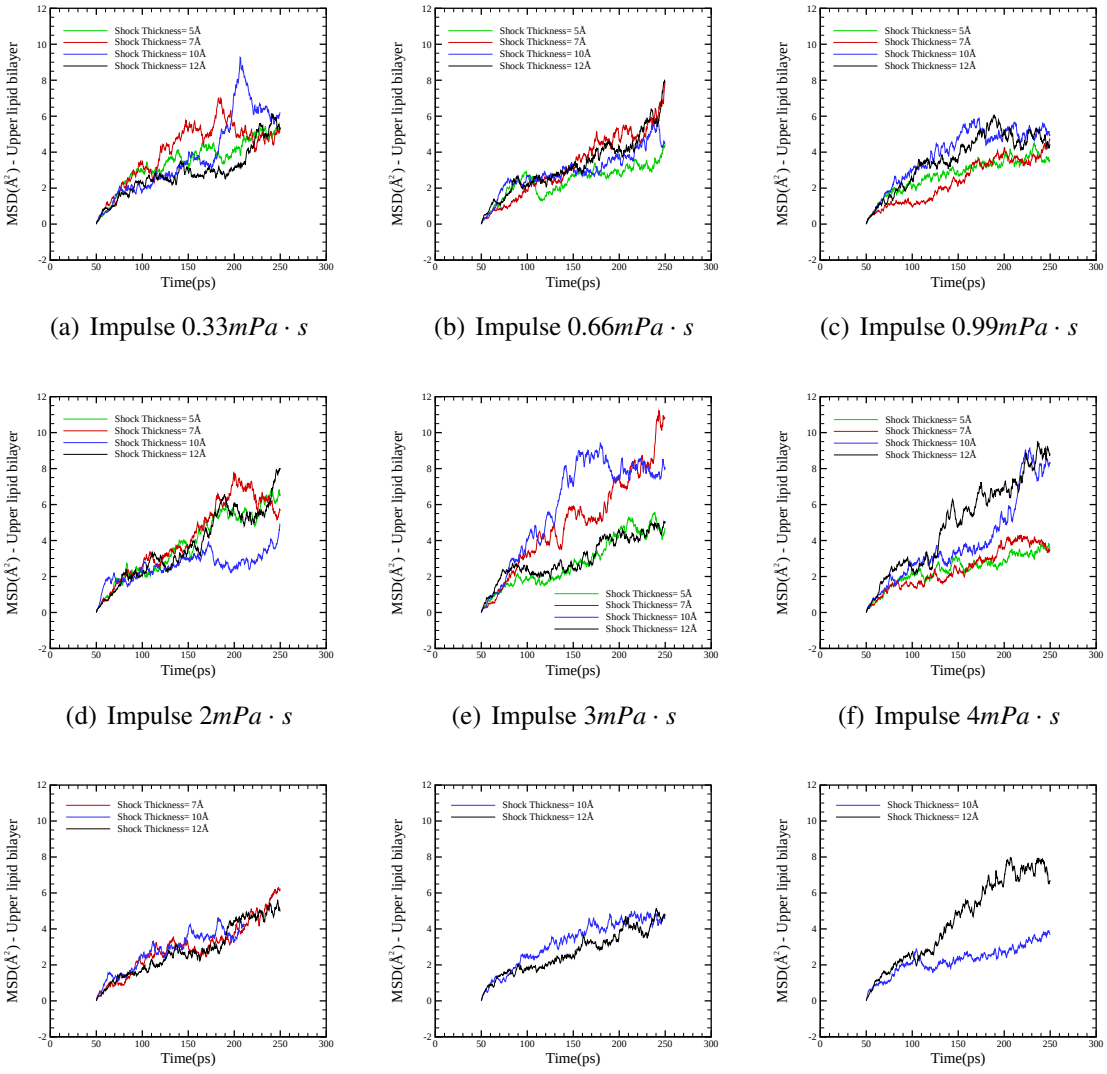

(a) Impulse $0.33mPa \cdot s$ (b) Impulse $0.66mPa \cdot s$ (c) Impulse $0.99mPa \cdot s$

(d) Impulse $2mPa \cdot s$ (e) Impulse $3mPa \cdot s$ (f) Impulse $4mPa \cdot s$

(g) Impulse $5mPa \cdot s$ (h) Impulse $6mPa \cdot s$ (i) Impulse $7mPa \cdot s$

Figure 4.8: Shock wave effects on the MSD of the upper bilayer at various shock wave thicknesses

While observing the results for the lower and upper layer and comparing them with the ones for the whole membrane, a number of conclusions can be further drawn. It is worth pointing out certain tendencies as they appear in the graphs. When the impulse is $0.66 mPa \cdot s$ and the shock 10Å, which suggests a relatively and weak shock of great thickness, the velocities of the water molecules in the upper layer are small and therefore the momentum transfer is not efficient. Thus, the diffusion coefficient of the upper layer, as it appears in the following figures, is relatively small and smaller that the slope that corresponds to the lower layer. It is also observed that when the impulse is $3 mPa \cdot s$ and the shock 5Å or 7Å, then the MSD of the whole membrane is relatively high and as a strong shock although of small thickness, is involved, the velocities of the water molecules will be high enough so the slope of the MSD in the upper layer for both shock thicknesses appears relatively steep. The momentum transfer is so efficient that the diffusion coefficient, or slope of the MSD of the lower layer is similar to the one of the upper membrane as well. However, when the momentum is not effectively transferred, due to small water velocities, related to shocks of relatively large thickness, then the MSD slope of the lower layer is less steep that the one for the upper layer, which is the case when the impulse is $3 mPa \cdot s$ and the thickness of the shock 12Å. The same phenomenon can be noticed for the same impulse and again a relatively long shock, 10Å.

A safe indicator of lipid mobility is the diffusion coefficients as estimated and presented in the MSD plots. The results of diffusion coefficient as a function of impulse for various shock wave thicknesses are presented in Figure 4.8. The results show that for the whole lipid bilayer, plot (*a*), the diffusion coefficient varies between a minimum of $0.07 \cdot 10^{-7} \cdot cm^2 \cdot s^{-1}$ and a maximum of $0.05 \cdot 10^{-7} \cdot cm^2 \cdot s^{-1}$. In case of the upper and lower lipid bilayer, plot (b) and (c), the minimum and maximum diffusion coefficients are $0.01 \cdot 10^{-7} \cdot cm^2 \cdot s^{-1}$ and $0.045 \cdot 10^{-7} \cdot cm^2 \cdot s^{-1}$, and $0.01 \cdot 10^{-7} \cdot cm^2 \cdot s^{-1}$ and $0.06 \cdot 10^{-7} \cdot cm^2 \cdot s^{-1}$, respectively.

Figure 4.11 summarises the diffusion coefficient values for the whole membrane, the upper layer, and the lower layer as function of shock thickness for different impulse values. It can be seen that for all different values of impulse, that correspond to different values of momentum, the lateral diffusion coefficient initially increases as the shock thickness is increased until a maximum is achieved. The maximum corresponds to the optimum scenario for the momentum to be transported in the membrane. Following the maximum and as the shock thickness continuous to increase the efficiency of momentum transfer drops and the values of the diffusion coefficient drop accordingly. It is being noticed that if the impulse is $2 mPa \cdot s$ for a set shock thickness 5Å, then in all three cases -whole membrane, upper layer, lower layer- the diffusion coefficient is maximum ($0.0325 * 10^{-7} cm^2 s^{-1}$, $0.03 * 10^{-7} cm^2 s^{-1}$, $0.0293 * 10^{-7} cm^2 s^{-1}$, respectively), which underlines the importance of impulse.

In principle, an ensemble average can be employed, however the calculation of the mean square displacement (MSD) refer to instantaneous displacements, and therefore ensemble averages are not primarily employed in the literature for such computations. The fluctuations noticed in these graphs are of the typical order of magnitude of any MSD calculation [168, 170].

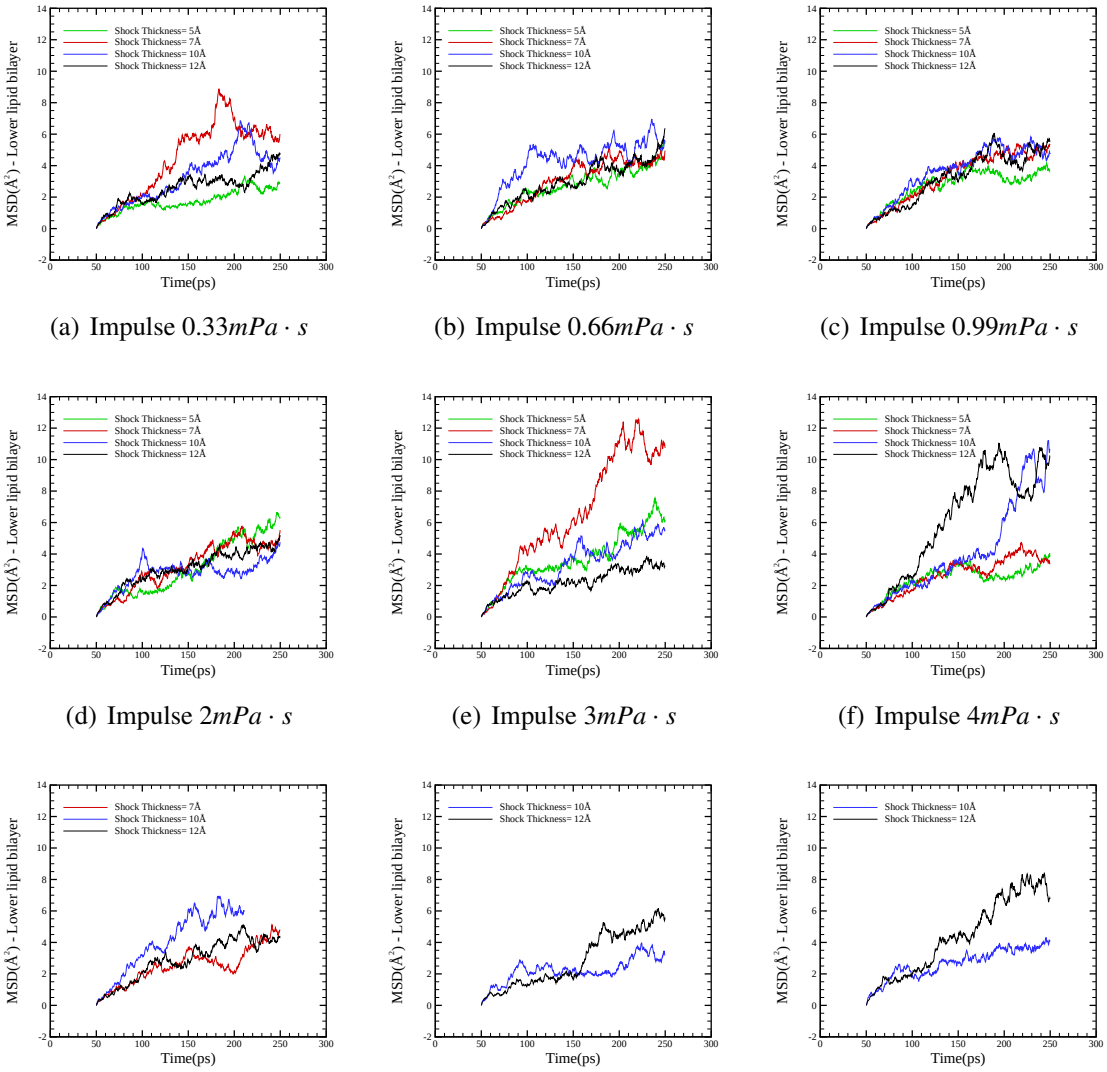

(a) Impulse $0.33 mPa \cdot s$ (b) Impulse $0.66 mPa \cdot s$ (c) Impulse $0.99 mPa \cdot s$

(d) Impulse $2 mPa \cdot s$ (e) Impulse $3 mPa \cdot s$ (f) Impulse $4 mPa \cdot s$

(g) Impulse $5 mPa \cdot s$ (h) Impulse $6 mPa \cdot s$ (i) Impulse $7 mPa \cdot s$

Figure 4.9: Shock wave effects on the MSD of the lower bilayer at various shock wave thicknesses

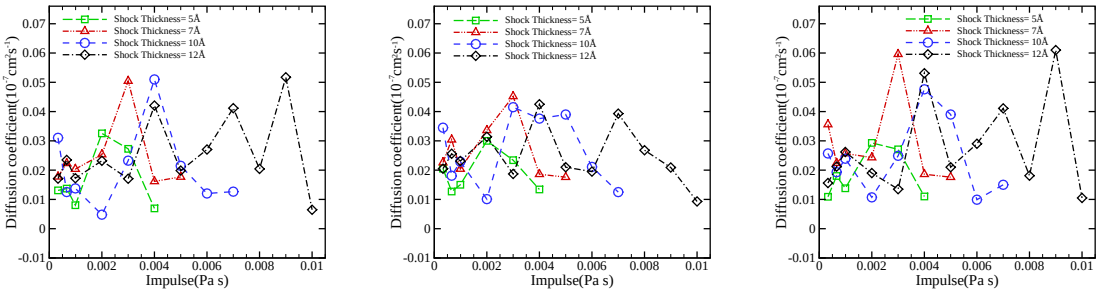

(a) Whole lipid bilayer (b) Upper lipid bilayer (c) Lower lipid bilayer

Figure 4.10: Diffusion coefficient as function of impulse at various shock wave thicknesses

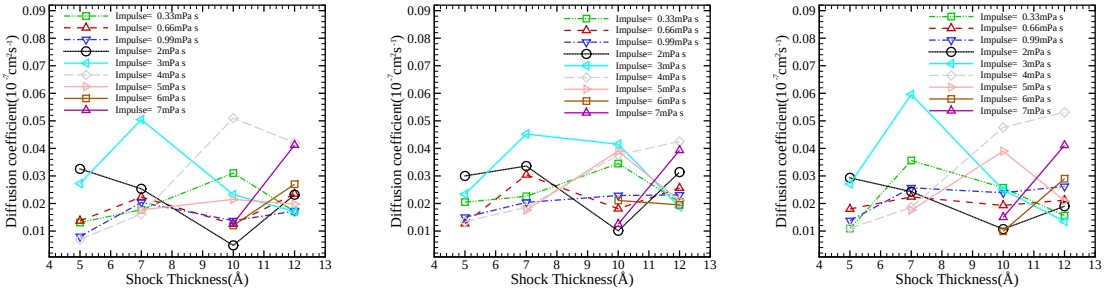

(a) Whole lipid bilayer (b) Upper lipid bilayer (c) Lower lipid bilayer

Figure 4.11: Diffusion coefficient as function of shock wave thickness at various impulses

4.3.5 Effects on Kinetic Energy - NVE ensemble

Again simulations involving various shock thicknesses and impulses initially for the 0° incident angle are examined. Shock wave thicknesses involved in the study vary from 5Å to 12Å. The ensemble used is the NVE ensemble, since it aims at extracting dynamical data as well as structural. Figure 4.12 shows the time variation of the system's kinetic energy for various values of shock thickness and impulse.

It is observed that as the impulse of the shock gets stronger, especially in the area between $3mPa \cdot s$ and $6mPa \cdot s$, the highest kinetic energy profile is achieved when the shock thickness is 10Å. This suggests that the water molecules of the system oscillate significantly more under a thickness of 10Å than 5Å, 7Å, or 12Å. It is also to be noted that for high shock impulses ($5mPa \cdot s$ and $6mPa \cdot s$) and shock thickness 5Å, 7Å, the simulation becomes unstable due to excess in kinetic energy of the molecules of the system. Thus, in plots (g) and (h) the kinetic energy profiles for shock thickness 5Å and 7Å do not appear.

4.3.6 Effects on Membrane Thickness - NVE ensemble

The following figure presents the time variation of membrane thickness for different impulses and values of shock thickness. At the beginning of the simulation after minimization and equilibration the thickness of the membrane is the same for the examined cases and a common trend is noticed with the membrane thickness to decrease.

As observed in the following membrane thickness plots for impulses from $0.33mPa \cdot s$ to $6mPa \cdot s$, the membrane appears to rebound really quick when the shock is weak and as it increases the thinning of the membrane continues for a longer period of simulation time. It is important that the simulations run for longer so that it can be observed if the thinning and rebounding of the membrane continues, which is expected due to the nature of the ensemble, and also to specify the frequency of the phenomenon. However, as it seems in figure 4.13, the "recovery" of the membrane does not occur at the same time in all cases.

4.3.7 Effects on membrane's centre of mass (COM) - NVE ensemble

The following figure 4.14 shows the corresponding movement of membrane COM, which is with respect to time in x and y direction, for impulses spanning from $0.33mPa \cdot s$ to $6mPa \cdot s$ and for shock thickness from 5Å to 12Å. In order to provide an interpretation of the results it is important to relate them to the previous plot 4.13 describing membrane thickness with time.

It is observed that when the impulse is $0.33mPa \cdot s$ and the thickness of the shock

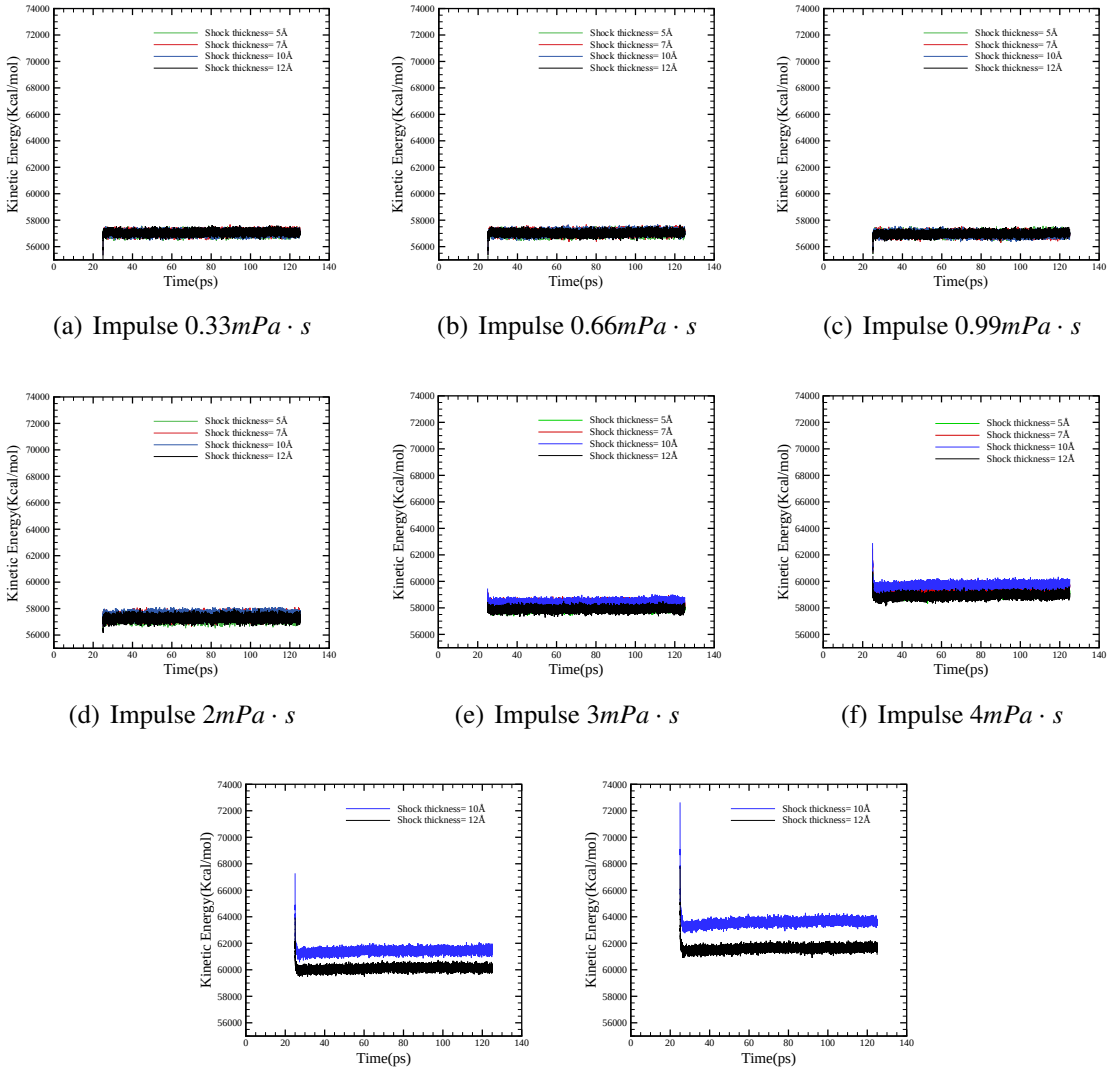

(a) Impulse $0.33mPa \cdot s$ (b) Impulse $0.66mPa \cdot s$ (c) Impulse $0.99mPa \cdot s$

(d) Impulse $2mPa \cdot s$ (e) Impulse $3mPa \cdot s$ (f) Impulse $4mPa \cdot s$

(g) Impulse $5mPa \cdot s$ (h) Impulse $6mPa \cdot s$

Figure 4.12: Shock wave effects on Kinetic Energy at various shock wave thicknesses

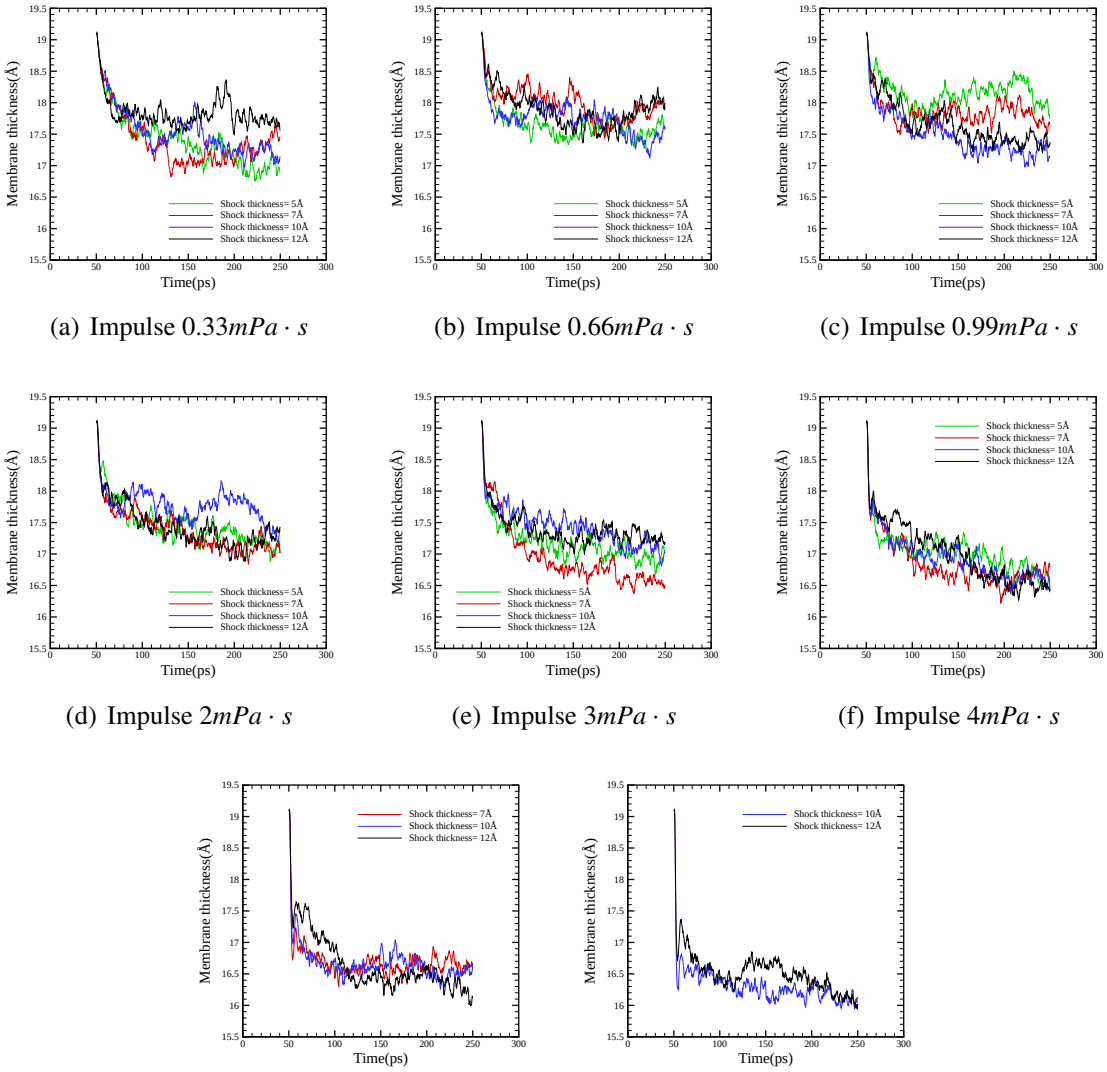

(a) Impulse $0.33mPa \cdot s$ (b) Impulse $0.66mPa \cdot s$ (c) Impulse $0.99mPa \cdot s$

(d) Impulse $2mPa \cdot s$ (e) Impulse $3mPa \cdot s$ (f) Impulse $4mPa \cdot s$

(g) Impulse $5mPa \cdot s$ (h) Impulse $6mPa \cdot s$

Figure 4.13: Shock wave effects on Membrane Thickness at various shock wave thicknesses

7Å, the centre of mass of the lipid bilayer tends to initially move away from its original vicinity with time towards the positive y direction, then it moves backwards until close to the end of the simulation it moves away again towards the positive x direction. This can be explained by taking into account the thinning of the membrane with time for the very same case. Indeed, the membrane initially gets thinner with time under the application of the shock, which implies decreasing in the z direction. Given that the ensemble for the current simulations is the NVE, the volume must be kept fixed and therefore the simulation box has to expand in directions x and y to meet this requirement. For this reason, the COM moves away from the original position. However, when the membrane reaches the point when it starts to rebound, and therefore to increase slightly in size in the z direction, then for the same reason explained the simulation box contracts in the x-y plane. Thus, the COM appears to be moving closer to the initial position.

When the thickness is 5Å and the impulse $0.66 mPa \cdot s$, a shock wave of small shock thickness hits the upper layer of the membrane and results in a significant thinning of the membrane with time, since as explained in the previous sections of this chapter, this shock thickness configuration involves a small total mass of molecules in the water slab. However, greater thinning of the membrane results in greater expansion in x-y, which is apparent in figure 4.14.

Figure 4.14 also presents the COM of the membrane when the impulse is $2 mPa \cdot s$ and the shock thickness is 5Å and 7Å. It is noticed that unlike the cases of shock thickness 10Å and 12Å, when the shock is small the COM appears to significantly move away from its initial place. This is due to the fact that after the application of the shock of impulse $2 mPa \cdot s$ and thickness 5Å or 7Å the membrane gets thinner very fast and keeps reducing in size in the z direction, as figure 4.11 suggests.

4.3.8 Mean square displacement (MSD) and Lateral Diffusion - NVE ensemble

In this section there is a discussion regarding the mean square displacement of the membrane lipids and how we can derive the lateral diffusion values from that. Figure 4.15 presents the mean square displacement of the membrane as a function of time for different shock thicknesses. Similarly to the results gathered when the ensemble was the NPT one, larger slopes imply higher lipid mobility within the membrane. The MSD slopes and therefore the lipid's diffusivity are dependent to the efficiency of the momentum transfer from the water molecules to the upper layer of the membrane. More efficient momentum transfer implies higher slopes and consequently larger diffusion coefficients.

The MSD plots below (figure 4.15) are particularly interesting as they not only show a tendency of the (mean square) displacement of the lipids of the membrane, but they also allow for a more pedantic examination of the MSD in particular points of simulation time that appear to have a significantly high value of MSD.

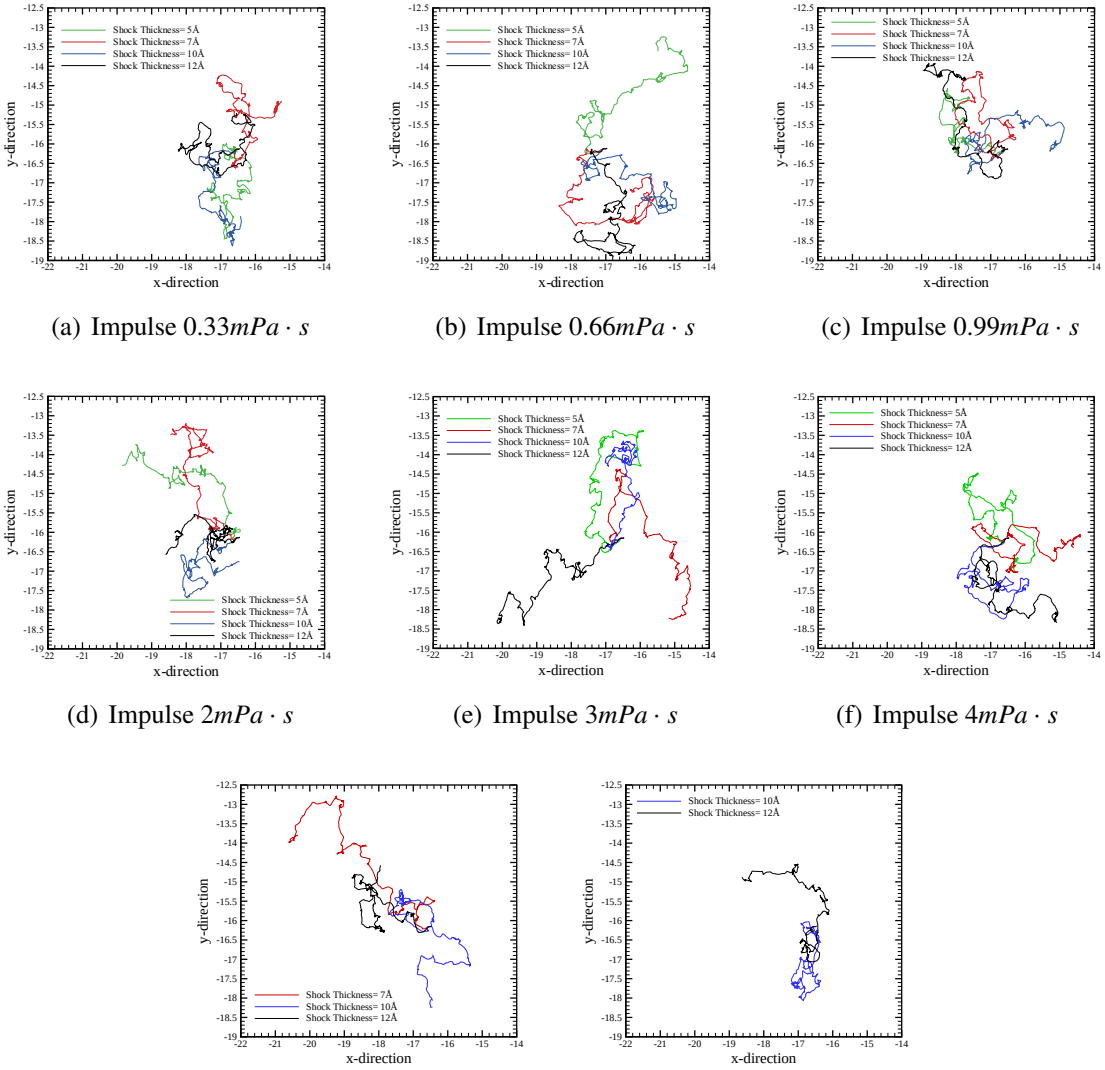

(a) Impulse $0.33mPa \cdot s$ (b) Impulse $0.66mPa \cdot s$ (c) Impulse $0.99mPa \cdot s$

(d) Impulse $2mPa \cdot s$ (e) Impulse $3mPa \cdot s$ (f) Impulse $4mPa \cdot s$

(g) Impulse $5mPa \cdot s$ (h) Impulse $6mPa \cdot s$

Figure 4.14: Shock wave effects on the COM of the membrane at various shock wave thicknesses

It has been underlined earlier, in chapters 1 and 2, that it is of crucial importance for cancer drug delivery to provide the infected with cancer area with the anticancer agent when the membrane is transiently permeabilised. To this end, it is vital that areas where the MSD value (in the plots presented in this section) is identified to be increasing dramatically, are further studied.

The current study examines diffusion coefficient values directly from the MSD values gathered in the course of the simulation. However, it is important that these findings get enriched with more specific results related to areas where the current MSD plots demonstrate significant increase.

The differences that appear within the same plots regarding the particular point in time when each MSD graph of different thickness and same impulse reaches a maximum value is in consistency with the plots demonstrating the COM of the lipids changing with time.

In figure 4.15, it is apparent that when the impulse is $0.33 mPa \cdot s$ and the shock thickness 5Å, the MSD increases with time until it reaches a maximum value and then reduces again. This can be explained by referring to the corresponding graph of the COM with time. As the graph suggests (figure 4.14), the COM for this set of impulse and shock thickness covers a wide area around its original vicinity until it starts moving towards the initial point. Besides, the MSD represents a surface.

Similarly, in the same plot, when the thickness is 7Å, the same trend is followed as the surface gets covered while the COM is moving away from the initial point, as the COM plot suggests, reaches the most distant point and then starts to move towards the initial point again, although it ends up moving away from it and towards the positive x direction. The same happens when the impulse is $5 mPa \cdot s$ and the thickness 7Å. This is followed in the MSD plots referring to the upper and lower bilayer lipids, too.

However, a safe indicator of lipid mobility is the diffusion coefficients as estimated from the related MSD plots. The following figure 4.18 summarises the diffusion coefficient values for the whole membrane, the upper layer, and the lower layer as function of shock thickness for different impulse values.

It is observed that when the impulse increases the diffusion coefficients increase, too. However, this trend is followed up to a point and then follows a decay. The plot also shows what the greatest impulse to be applied for a given shock thickness should be in order for cytotoxicity to be avoided, since not all pairs of shock thickness and impulse are presented in the plots (also, see Appendix B).

The results of diffusion coefficient as a function of shock wave thickness for various impulses are presented in Figure 4.19. The results show a similar trend for all three cases: the whole lipid bilayer, and both the upper and lower lipid bilayer. In plot (a) of Figure 4.19, it can be observed that the diffusion coefficient varies between a minimum of $0.02 \cdot 10^{-7} cm^2 s^{-1}$ and a maximum of $0.16 \cdot 10^{-7} cm^2 s^{-1}$. In case of the upper and lower lipid bilayer, plot (b)

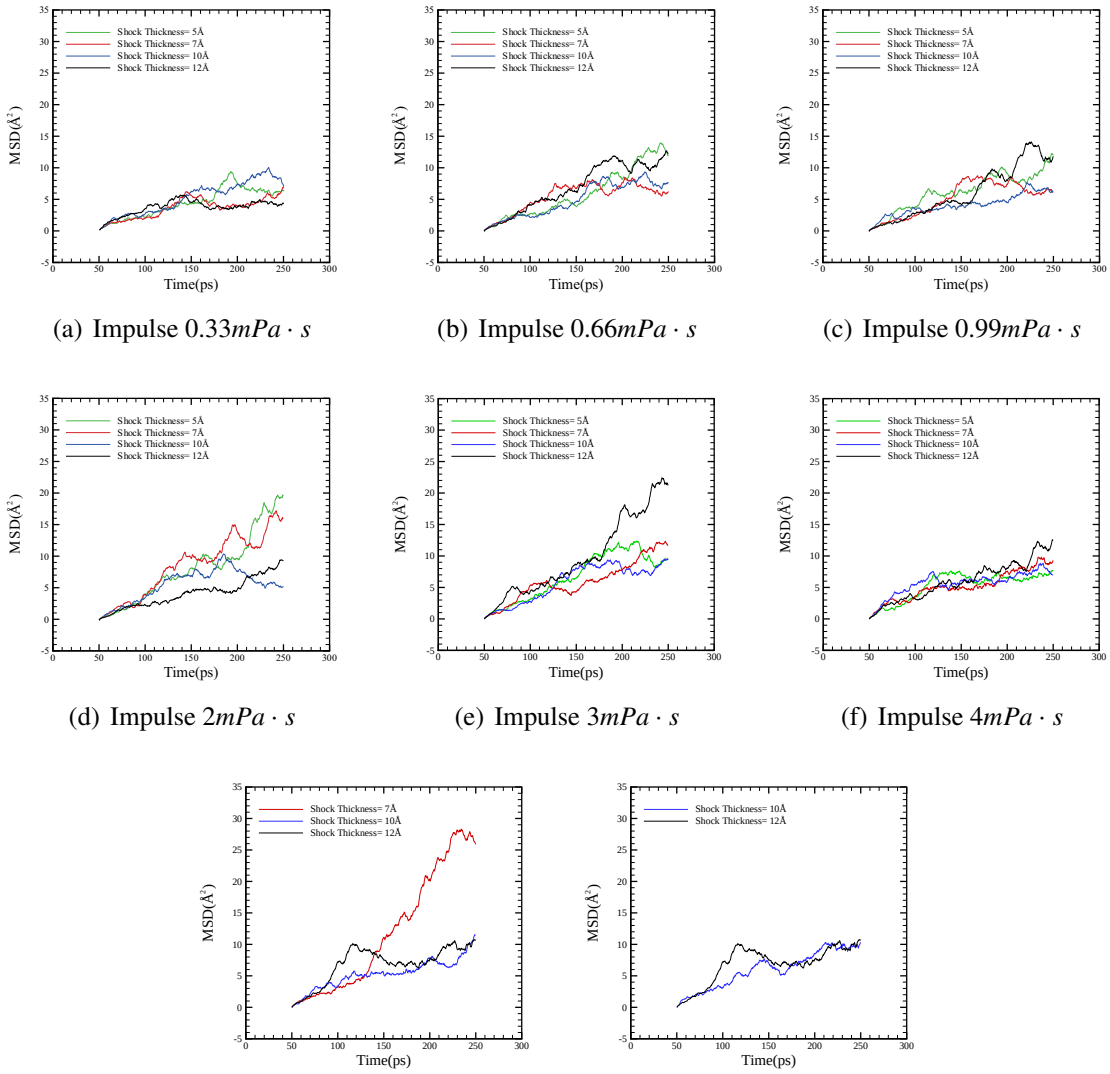

(a) Impulse $0.33mPa \cdot s$ (b) Impulse $0.66mPa \cdot s$ (c) Impulse $0.99mPa \cdot s$

(d) Impulse $2mPa \cdot s$ (e) Impulse $3mPa \cdot s$ (f) Impulse $4mPa \cdot s$

(g) Impulse $5mPa \cdot s$ (h) Impulse $6mPa \cdot s$

Figure 4.15: Shock wave effects on the MSD of the membrane at various shock wave thicknesses

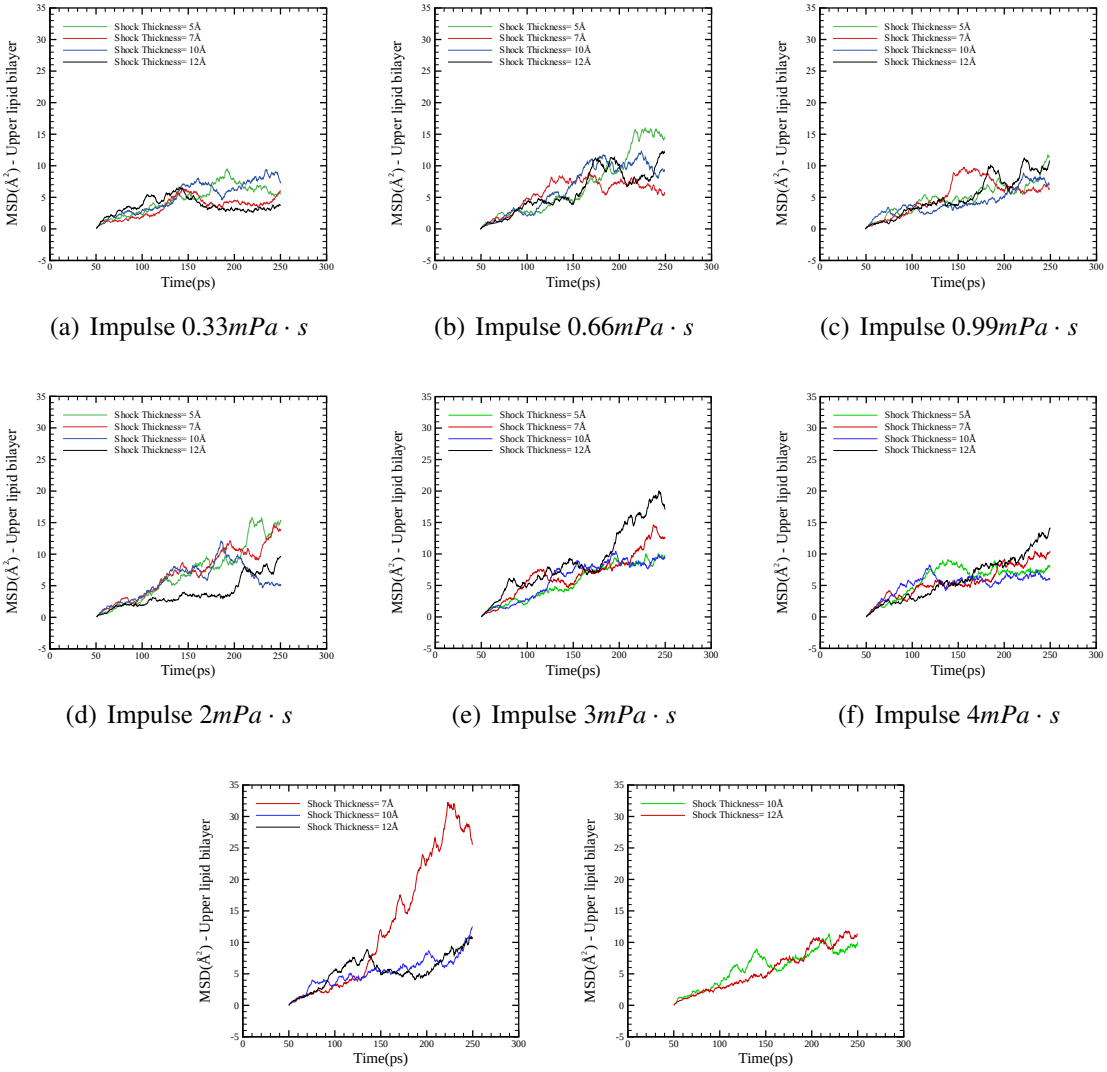

(a) Impulse $0.33mPa \cdot s$ (b) Impulse $0.66mPa \cdot s$ (c) Impulse $0.99mPa \cdot s$

(d) Impulse $2mPa \cdot s$ (e) Impulse $3mPa \cdot s$ (f) Impulse $4mPa \cdot s$

(g) Impulse $5mPa \cdot s$ (h) Impulse $6mPa \cdot s$

Figure 4.16: Shock wave effects on the MSD of the upper bilayer at various shock wave thicknesses

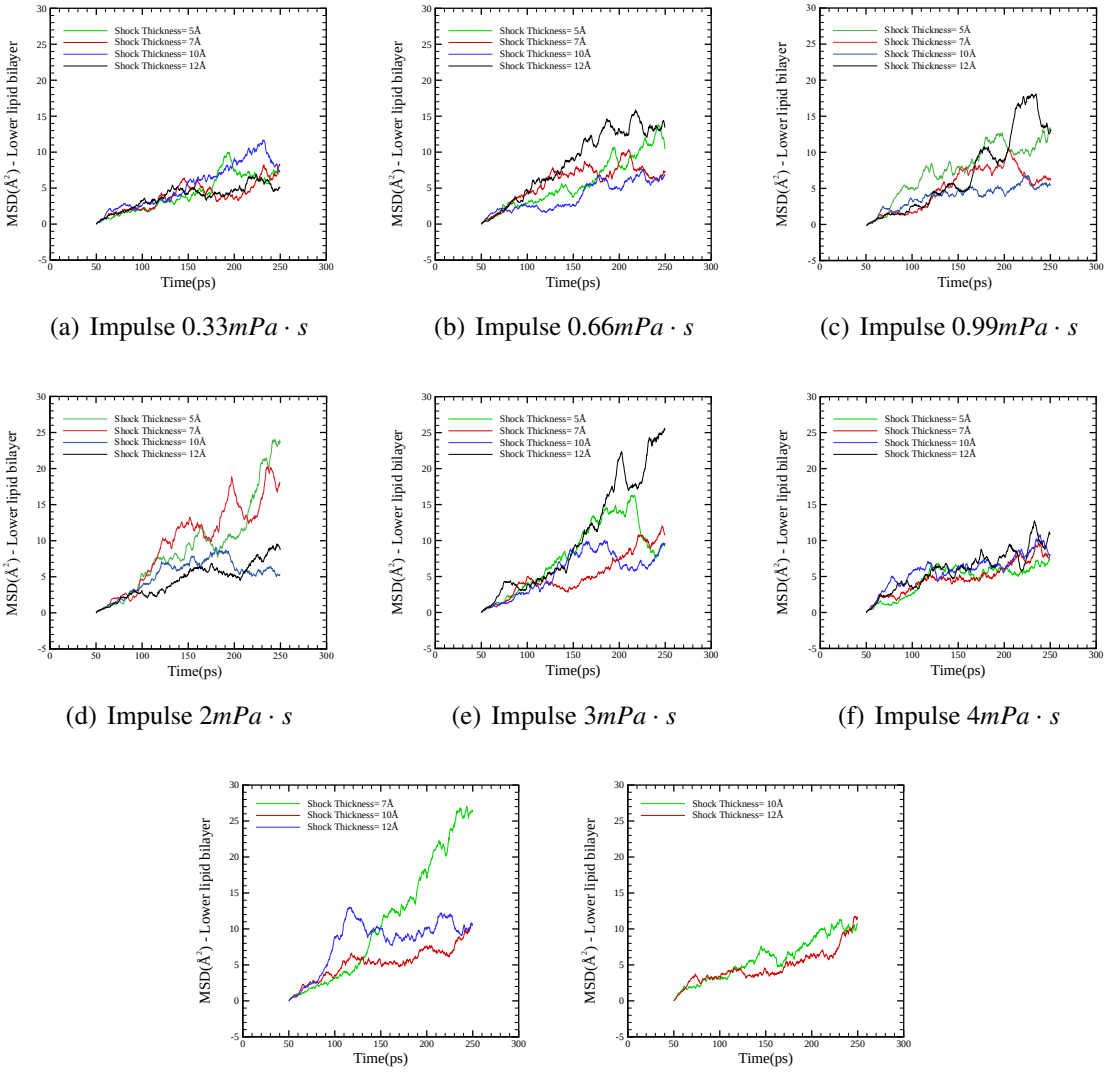

(a) Impulse $0.33 mPa \cdot s$ (b) Impulse $0.66 mPa \cdot s$ (c) Impulse $0.99 mPa \cdot s$

(d) Impulse $2 mPa \cdot s$ (e) Impulse $3 mPa \cdot s$ (f) Impulse $4 mPa \cdot s$

(g) Impulse $5 mPa \cdot s$ (h) Impulse $6 mPa \cdot s$

Figure 4.17: Shock wave effects on the MSD of the lower bilayer at various shock wave thicknesses

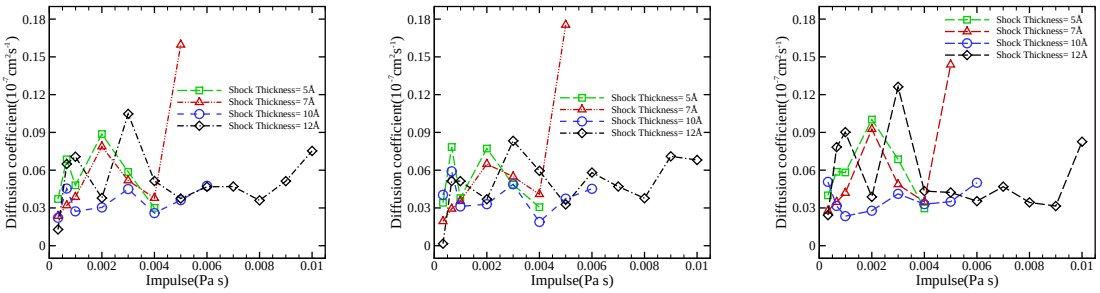

(a) Whole lipid bilayer (b) Upper lipid bilayer (c) Lower lipid bilayer

Figure 4.18: Diffusion coefficient as function of impulse at various shock wave thicknesses

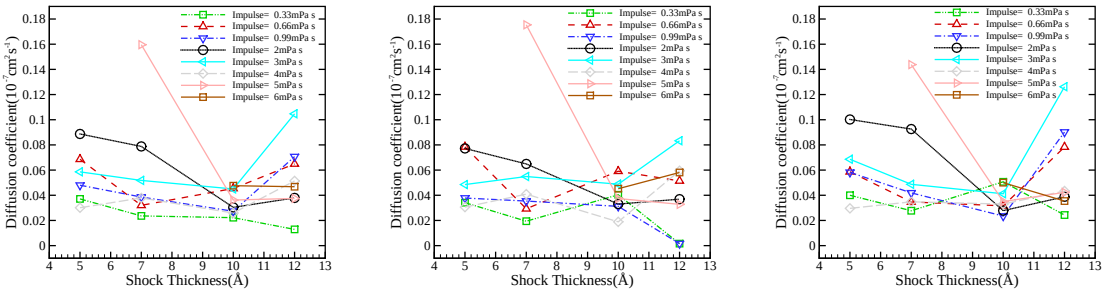

(a) Whole lipid bilayer (b) Upper lipid bilayer (c) Lower lipid bilayer

Figure 4.19: Diffusion coefficient as function of shock wave thickness at various impulses

and (c), the minimum and maximum diffusion coefficients are $0.0129 \cdot 10^{-7} cm^2 s^{-1}$ and $0.1754 \cdot 10^{-7} cm^2 s^{-1}$, and $0.0235 \cdot 10^{-7} cm^2 s^{-1}$ and $0.1438 \cdot 10^{-7} cm^2 s^{-1}$, respectively.

4.4 Conclusions

In the present study attention has been drawn to the effects of shock waves on the lateral diffusion coefficient of a POPC membrane. A characteristic of the shock wave that affects the amount of momentum propagated from the water molecules to the membrane is the shock thickness. As the thickness of the shock becomes larger the diffusion coefficient initially increases until a maximum value is obtained followed by a small decay.

The simulations ran for a great range of impulses and shock thicknesses in accordance with the NPT and the NVE ensemble separately. Lateral fluidity was measured through the use of diffusion coefficients as opposed to accumulated lateral displacement that was studied by other authors [11]. It has been shown that in overall diffusion coefficients that

resulted from simulations run with NVE were greater in value that those obtained under the NPT ensemble.

NPT and NVE produce different results because we conserve different physical properties. In the NVE ensemble we keep constant the number of atoms, the volume and the total energy, and we also allow the system to evolve in time. The main rationale behind the use of this ensemble is that we want to conserve the energy of the system and visualise the effect of the shock for a system which is isolated from its environment. Such an approach is extensively employed for the study of shock waves through polycrystalline materials and this is the approach used by Lechuga et al. [168]. However, if we focus on biological systems such as membranes, the system is not isolated from its environment and temperature along with pressure are variables that do not present large variation. As a result, we also performed simulations with the NPT ensemble aiming to compare the results and conclude which is more appropriate for our case.

The observations made in the present study have an entirely different focus compared to Koshiyama et al. [11]. In the aforementioned study the authors analyse just the response of the membrane for very specific conditions. In contrast, in the present study we performed simulations for a very wide range of parameters and we looked at the conditions that optimise the momentum transfer across the shock wave and the membrane and those that can also maximise the drug adsorption through the cell.

It has been concluded that for both sets of simulations following the two ensembles it appears that the maximum values for diffusion coefficient are given when the thickness of the shock is 7Å. This conclusion is of great importance since it is not an ensemble-dependent result. Furthermore, it underlines the importance of a shallow shock rather than a deep one which can be explained by considering the momentum transfer to fewer water molecules in the upper lipid bilayer (water slab).

The lateral diffusion values reported in the present thesis differ up to 5% from previous computational studies reported in the literature [168, 170] and up to 30% compare to experimental values [11]. Taking into account the simplification used regarding the membrane representation and the relative small figures of lateral diffusion coefficient ($\sim 10^{-7} cm^2 s^{-1}$) a relative error of 30% is within the acceptable limits.

Furthermore, the importance of impulse has been demonstrated which also agrees with the findings of earlier studies [13, 169]. Finally, the values of diffusion coefficients gathered are in the order of $10^{-7} cm^2 s^{-1}$, which is in agreement with previous experimental and computational studies [169, 171, 172].

CHAPTER 5

Oblique shock wave effects

5.1 Simulation Description

Additional computations have been carried out to study the effects of the incidence angle of the shock to the 1-palmitoyl-2-oleoyl-sn-glycero-3-phosphocholine (POPC) membrane system. Again, each shock is applied in the water slab as explained in chapters 3 and 4. Pressure and temperature remain constant through the simulation and equal to 1atm and 310K, respectively. The time-step used is 1fs, non-bonded interactions have been calculated every 2fs and full electrostatics every 4fs. The total simulation time is 200ps. Computational experiments have been carried out by utilising the NPT ensemble and the NVE ensemble with shock impulses varying from $0.33 mPa \cdot s$ to $2 mPa \cdot s$. The incidence angles applied vary between 10° and 80°, corresponding to the almost vertical and almost tangential case respectively.

The application of the oblique shock wave introduces perpendicular and parallel to the membrane surface momentum components of impulse. The perpendicular component reduces in absolute terms, leading to small diffusion coefficients, in principal [168], while it is anticipated that the parallel component of impulse will contribute to increased lipid lateral mobility and thus, enhanced lipid lateral diffusion. It is also shown that membrane thickness gets thinner under the application of a shock and the area per lipid is reduced.

5.2 Results and Discussion

5.2.1 Effects on Kinetic Energy - NPT ensemble

The following figure shows the kinetic energy of the water-membrane system as function of time for different incidence angles and thickness when the impulse is $0.33 mPa \cdot s$. The

kinetic energy is monitored in order to show the energy transfer from potential energy to kinetic and the dissipation of kinetic energy to heat.

Similarly to the kinetic energies discussed in chapter 4, the kinetic energy gets suddenly increased the moment the shock is introduced and as the simulation evolves any excessive heat generated by the additional kinetic energy that occurs gets dissipated through the applied Langevin dynamics. The variations in the angle of attack of the shock affect the distribution of energy along the perpendicular and longitudinal direction. As a consequence, smaller values of the incidence angle result in larger perpendicular to the membrane surface velocity components. Due to the presence of periodic boundary conditions additional time is required for the energy to be dissipated resulting to slightly larger oscillations, around the mean kinetic energy, for the smaller angles (see figures 5.1-5.4).

The variations of incidence angle do not alter the total kinetic energy introduced to the water-membrane system. However, it is shown that greater values of impulse for a given shock thickness and angle of attack lead to greater values of kinetic energy for the system. This can be explained by considering the relation between the kinetic energy of a system and the impulse applied on it, $E_k = \frac{I^2}{2m}$.

In figure 5.3 the profiles of kinetic energy over time for various shock thicknesses while the impulse is $0.99 mPa \cdot s$ are presented. The angle of attack varies between 10° and 60°, since greater values of attack result in excessive kinetic energy transferred to the parallel to the membrane surface component of the velocities of the atoms of the upper layer of the membrane. At the same time when the angle of attack is 50° and 60°, the simulation becomes unstable for shock thickness 5Å due to excessive initial rise in the kinetic energy of some atoms of the upper membrane.

Finally it is observed that in all cases of impulse varying between $0.33 mPa \cdot s$ and $2 mPa \cdot s$, the initial rise in the kinetic energy gets higher as the angle of attack increases. This can be understood by taking into account that the tangential to the membrane surface impulse component increases as the angle of attack increases and therefore contributes to higher parallel to the membrane surface velocities.

In figure 5.4 the kinetic energy of only 3 shock wave thicknesses and 2 angles of attack is presented, since the simulation becomes unstable for the rest of the cases, because the kinetic energy of the atoms becomes too high. As already explained in chapter 4, smaller shock thicknesses may lead to higher momentum for a given impulse.

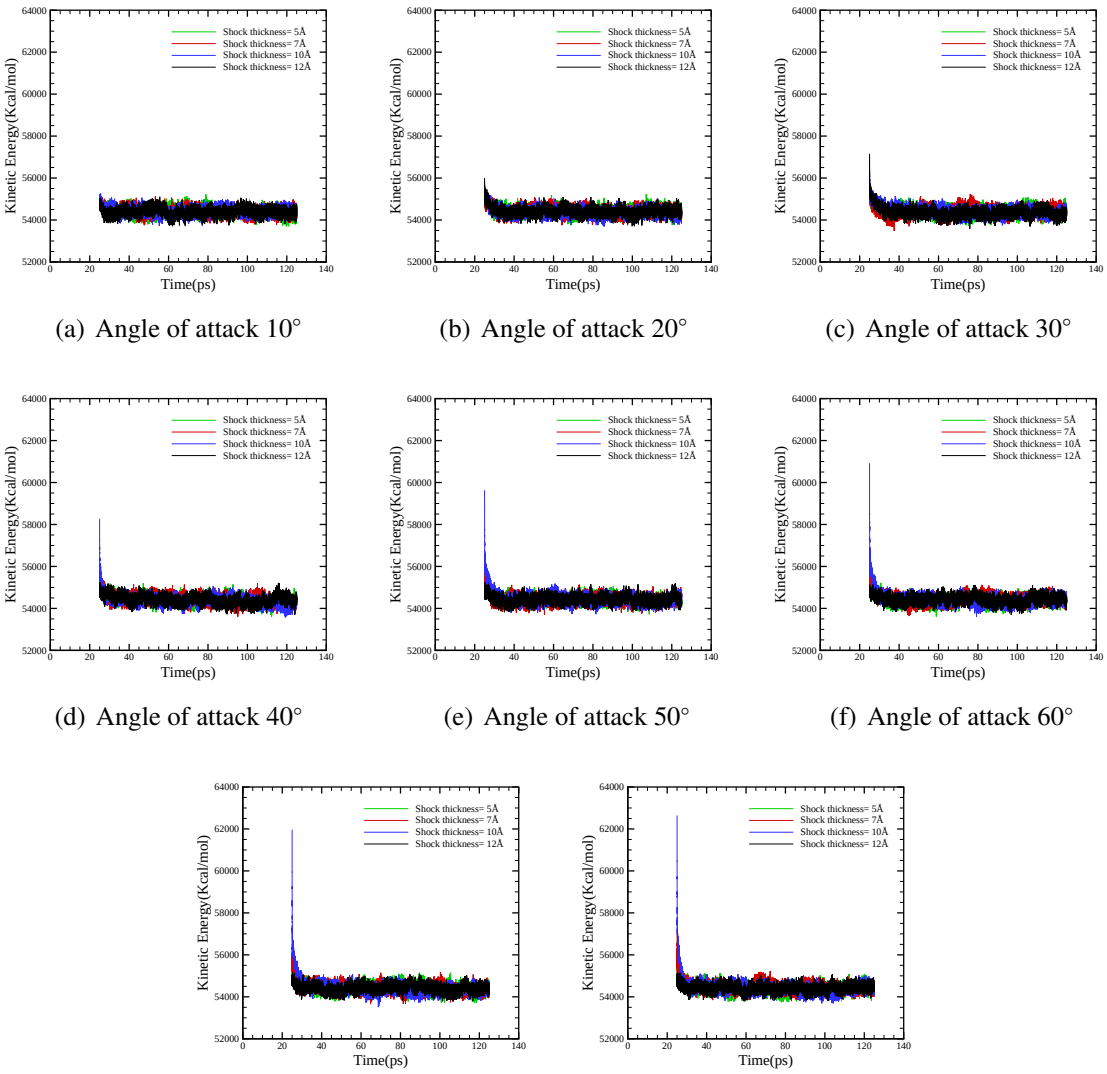

(a) Angle of attack 10° (b) Angle of attack 20° (c) Angle of attack 30°

(d) Angle of attack 40° (e) Angle of attack 50° (f) Angle of attack 60°

(g) Angle of attack 70° (h) Angle of attack 80°

Figure 5.1: Shock wave effects on Kinetic Energy at various shock wave thicknesses and angles of attack when the impulse is $0.33 mPa \cdot s$

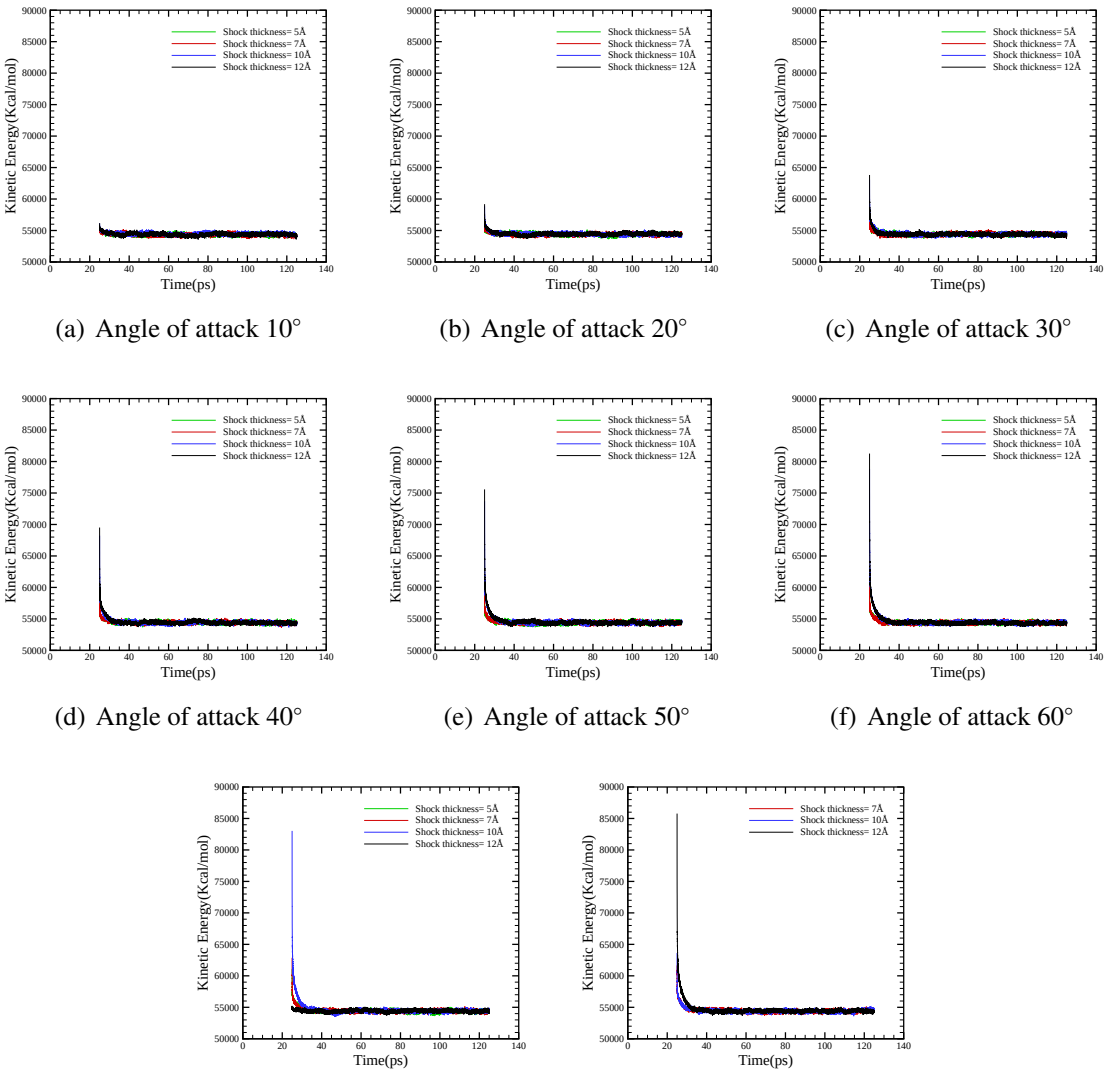

(a) Angle of attack 10° (b) Angle of attack 20° (c) Angle of attack 30°

(d) Angle of attack 40° (e) Angle of attack 50° (f) Angle of attack 60°

(g) Angle of attack 70° (h) Angle of attack 80°

Figure 5.2: Shock wave effects on Kinetic Energy at various shock wave thicknesses and angles of attack when the impulse is $0.66 mPa \cdot s$

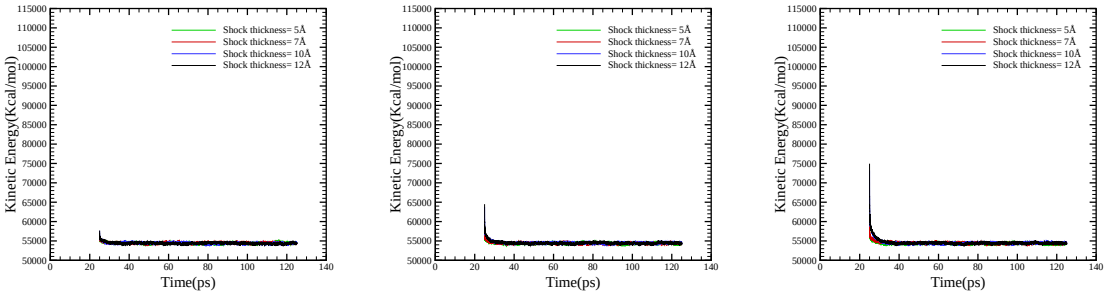

(a) Angle of attack 10° (b) Angle of attack 20° (c) Angle of attack 30°

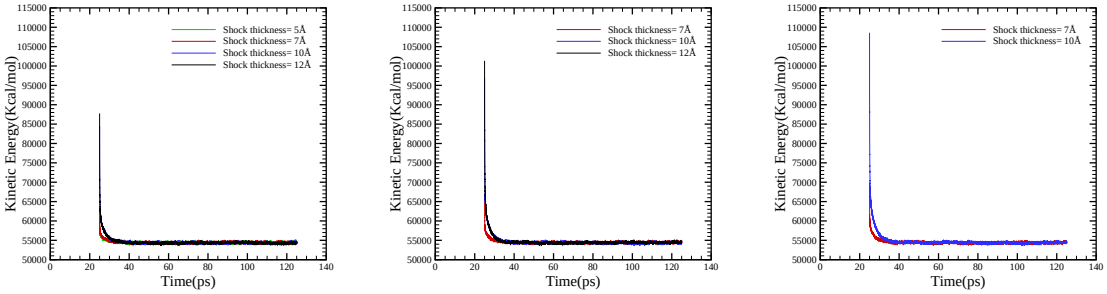

(d) Angle of attack 40° (e) Angle of attack 50° (f) Angle of attack 60°

Figure 5.3: Shock wave effects on Kinetic Energy at various shock wave thicknesses and angles of attack when the impulse is $0.99mPa \cdot s$

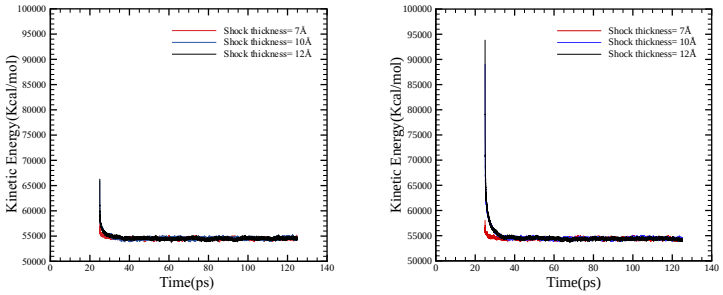

(a) Angle of attack 10° (b) Angle of attack 20°

Figure 5.4: Shock wave effects on Kinetic Energy at various shock wave thicknesses and angles of attack when the impulse is $2mPa \cdot s$

5.2.2 Effects on Membrane Thickness - NPT ensemble

Figures 5.5-5.7 show the membrane thickness as a function of time for impulses varying from $0.33mPa \cdot s$ to $0.66mPa \cdot s$ (for more results, impulses from $0.99mPa \cdot s$ to $2mPa \cdot s$,

see Appendix C) at various shock thicknesses and incidence angles. The same behaviour of membrane thickness is noticed under all incidence angles applied, with the membrane to shrink after the application of the oblique shock, with a reduced rate until it relaxes at a local equilibrium state.

Figure 5.5 shows the membrane thickness as function of time for all incidence angles at different shock thicknesses each time, when the impulse is $0.33 mPa \cdot s$. The trend for the various angles is similar with minor differences being noticed in the initial decrease rate of the membrane thickness. It is observed that towards the end of the simulation the membrane gets thinner particularly when the shock gets applied with an angle 30° for 12Å of shock thickness, 40° for 5Å of shock thickness, and 50° if the shock thickness is 7Å or 10Å. This can be mainly explained by acknowledging that when the thickness is small, the velocity components are high, due to the small mass to which the momentum gets transferred; therefore, even a relatively large angle of attack may lead to a great reduction membrane thickness. In the case of applying a large shock thickness, a significant reduction in membrane thickness can be achieved by increasing the mobility in the perpendicular velocity component to the membrane surface, which can happen with a smaller comparably angle of attack.

Figures that correspond to greater values of impulse ($0.99 mPa \cdot s$ and $2 mPa \cdot s$), as they appear in Appendix C, present the same tendency explained above. However, it is implied that in some cases the simulation has to be run for a longer period of time so that the trend followed can be better understood. At the same time, longer simulation time could result in allowing the membrane to rebound, which appears to be the case when the angle of attack is 20° for shock thickness 7Å and impulse $0.33 mPas$.

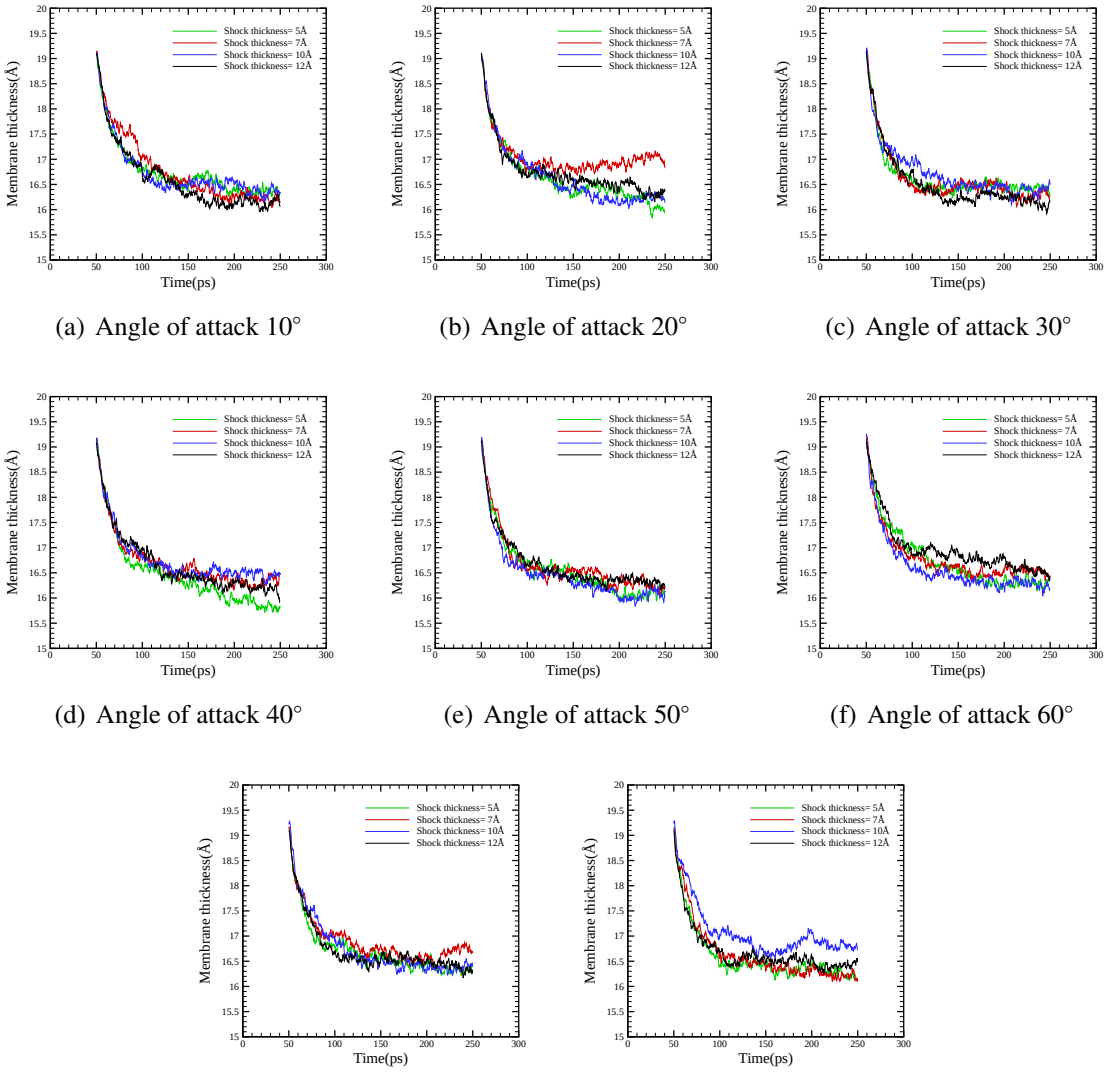

(a) Angle of attack 10° (b) Angle of attack 20° (c) Angle of attack 30°

(d) Angle of attack 40° (e) Angle of attack 50° (f) Angle of attack 60°

(g) Angle of attack 70° (h) Angle of attack 80°

Figure 5.5: Shock wave effects on Membrane Thickness at various shock wave thicknesses and angles of attack when the impulse is $0.33 mPa \cdot s$

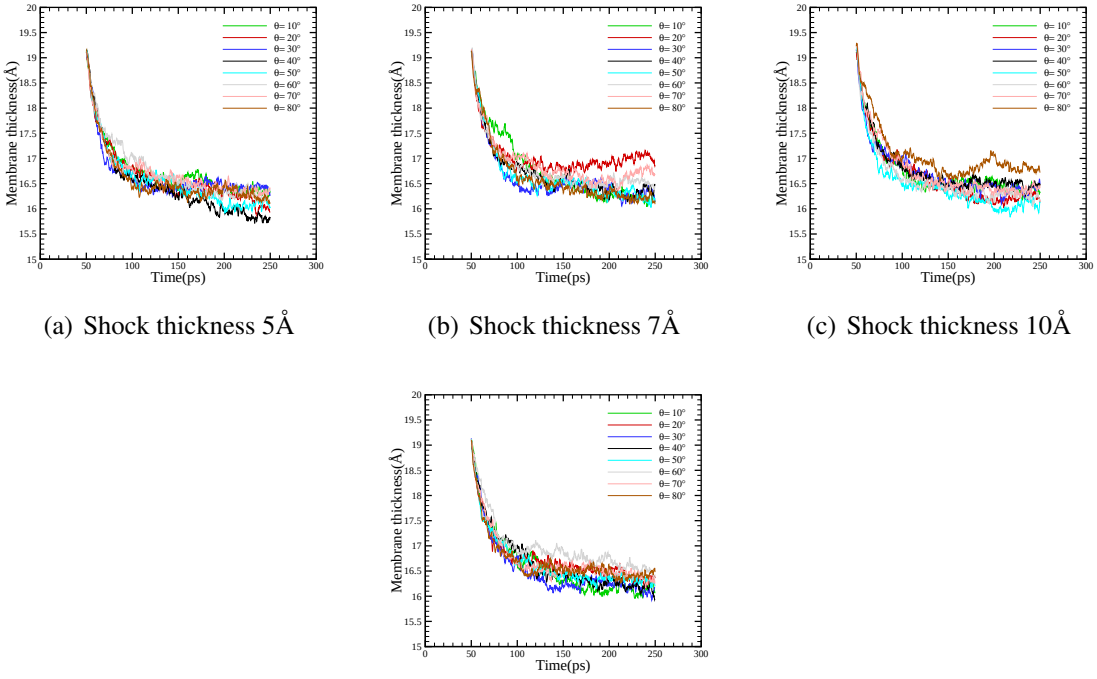

(a) Shock thickness 5Å (b) Shock thickness 7Å (c) Shock thickness 10Å

(d) Shock thickness 12Å

Figure 5.6: Shock wave effects on Membrane Thickness at various shock wave thicknesses and angles of attack when the impulse is $0.33 mPa \cdot s$

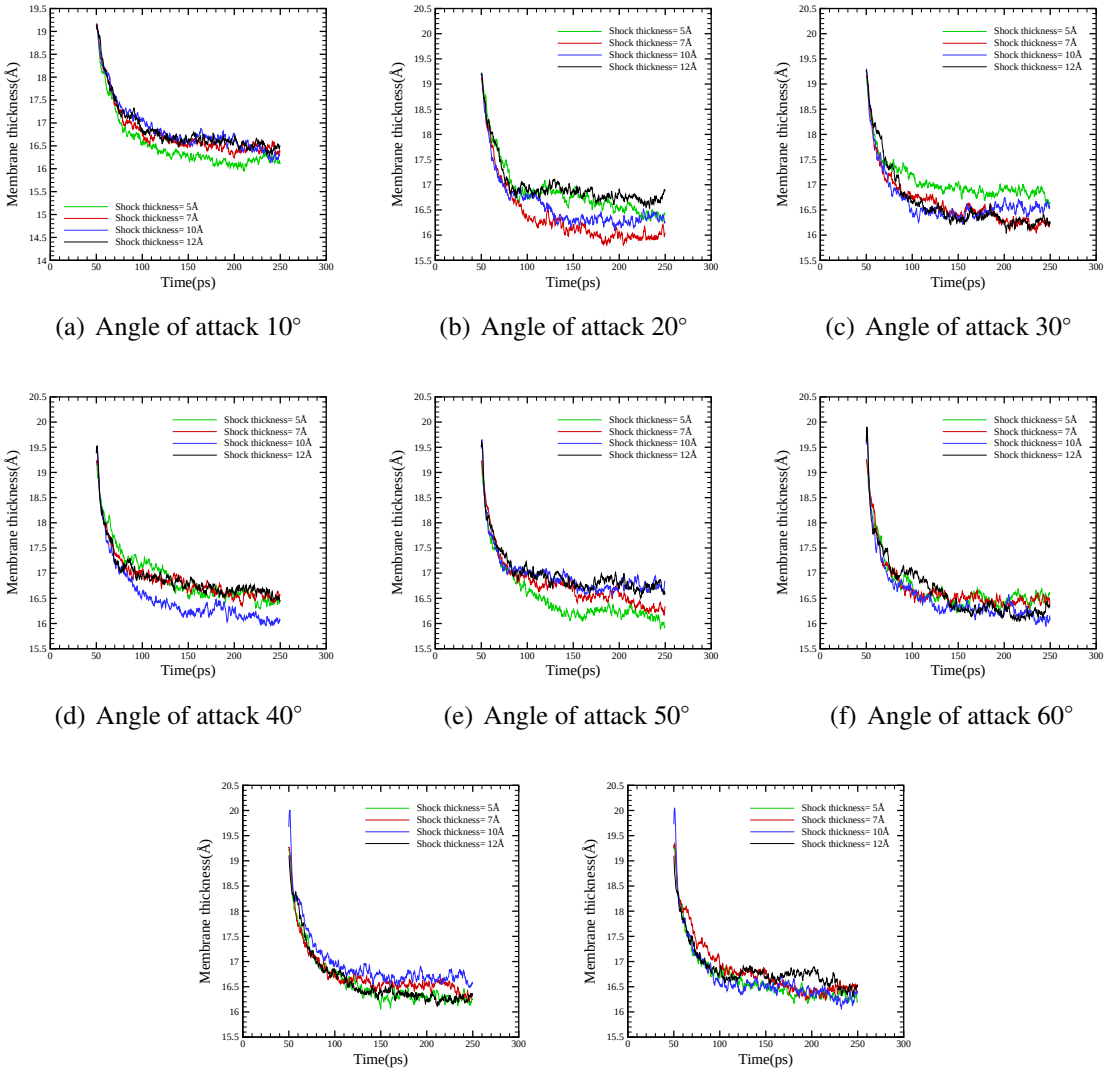

(a) Angle of attack 10° (b) Angle of attack 20° (c) Angle of attack 30°

(d) Angle of attack 40° (e) Angle of attack 50° (f) Angle of attack 60°

(g) Angle of attack 70° (h) Angle of attack 80°

Figure 5.7: Shock wave effects on Membrane Thickness at various shock wave thicknesses and angles of attack when the impulse is $0.66 mPa \cdot s$

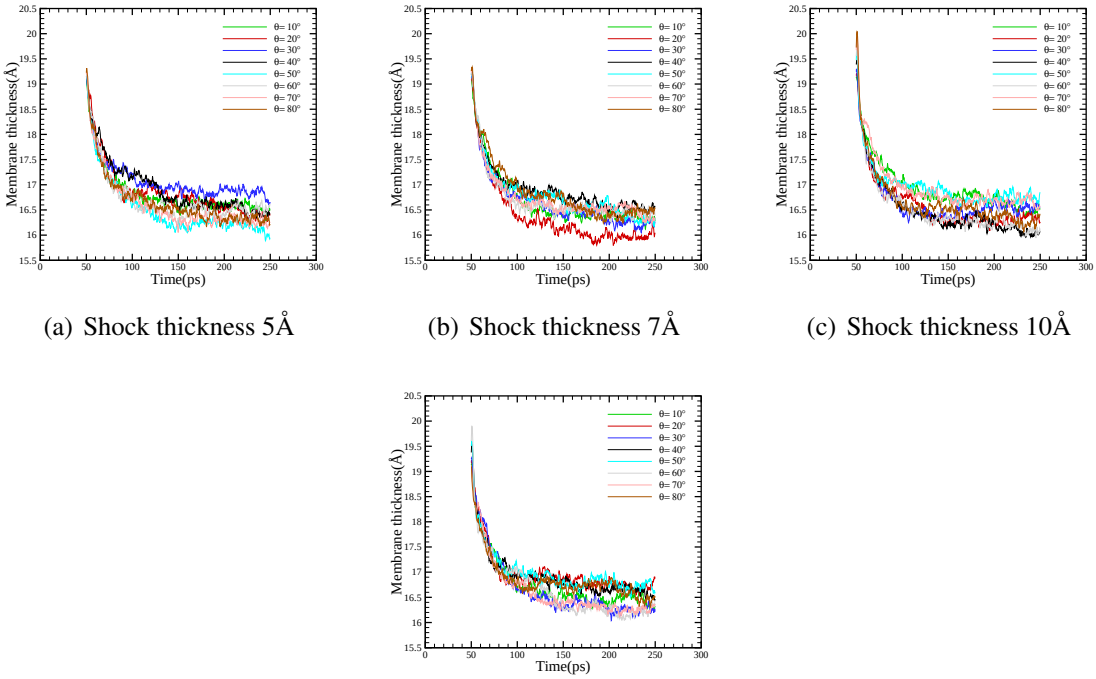

(a) Shock thickness 5Å (b) Shock thickness 7Å (c) Shock thickness 10Å

(d) Shock thickness 12Å

Figure 5.8: Shock wave effects on Membrane Thickness at various shock wave thicknesses and angles of attack when the impulse is $0.66 mPa \cdot s$

5.2.3 Effects on membrane COM - NPT ensemble

Figure 5.9 shows the positions of the center of mass of the membrane during the simulation time when the impulse is $0.33 mPa \cdot s$ at various incidence angles and shock thicknesses. It can be seen that as the incidence angle increases, the parallel to the membrane surface momentum component increases therefore, enhancing the mobility of the COM. As seen, the domain confined by of the COM's x and y coordinates increases in a non-linear fashion as the incidence angle increases. In principal, small angles could mean that the parallel to the membrane surface velocity components are smaller causing the membrane's COM to slightly oscillate along its original y position.

Figure 5.10 shows the positions of the center of mass of the membrane during the simulation time when the impulse is $0.66 mPa \cdot s$ at various incidence angles and shock thicknesses. Again, it is observed that as the incidence angle increases, the parallel to the membrane surface momentum component increases enhancing therefore the mobility of the COM.

It is important to emphasise that the layer does not displace in the layer-parallel direction as a result of the parallel impulse. The reason is primarily twofold. The first one

is that the momentum transfer due to the parallel velocity component is inefficient, and therefore does not significantly contribute to the membraneŠs motion. The second is that the intramolecular forces are stronger than the weak shear effects that are generated. As shown in COM graphs, there is slight motion in the parallel-to-impulse direction, which results in a small total distance travelled along this direction. This is because of the following reasons. Firstly, the transfer of momentum along this direction between the water molecules and the lipids is not efficient. Secondly the time scales of the entire simulation are small. Thirdly, the additional velocity components transferred to the system compared to their thermal fluctuation is small.

The same tendency already described for impulses $0.33 mPa \cdot s$ and $0.66 mPa \cdot s$ is followed for impulses $0.99 mPas$ and $2 mPa \cdot s$, as shown in Appendix C.

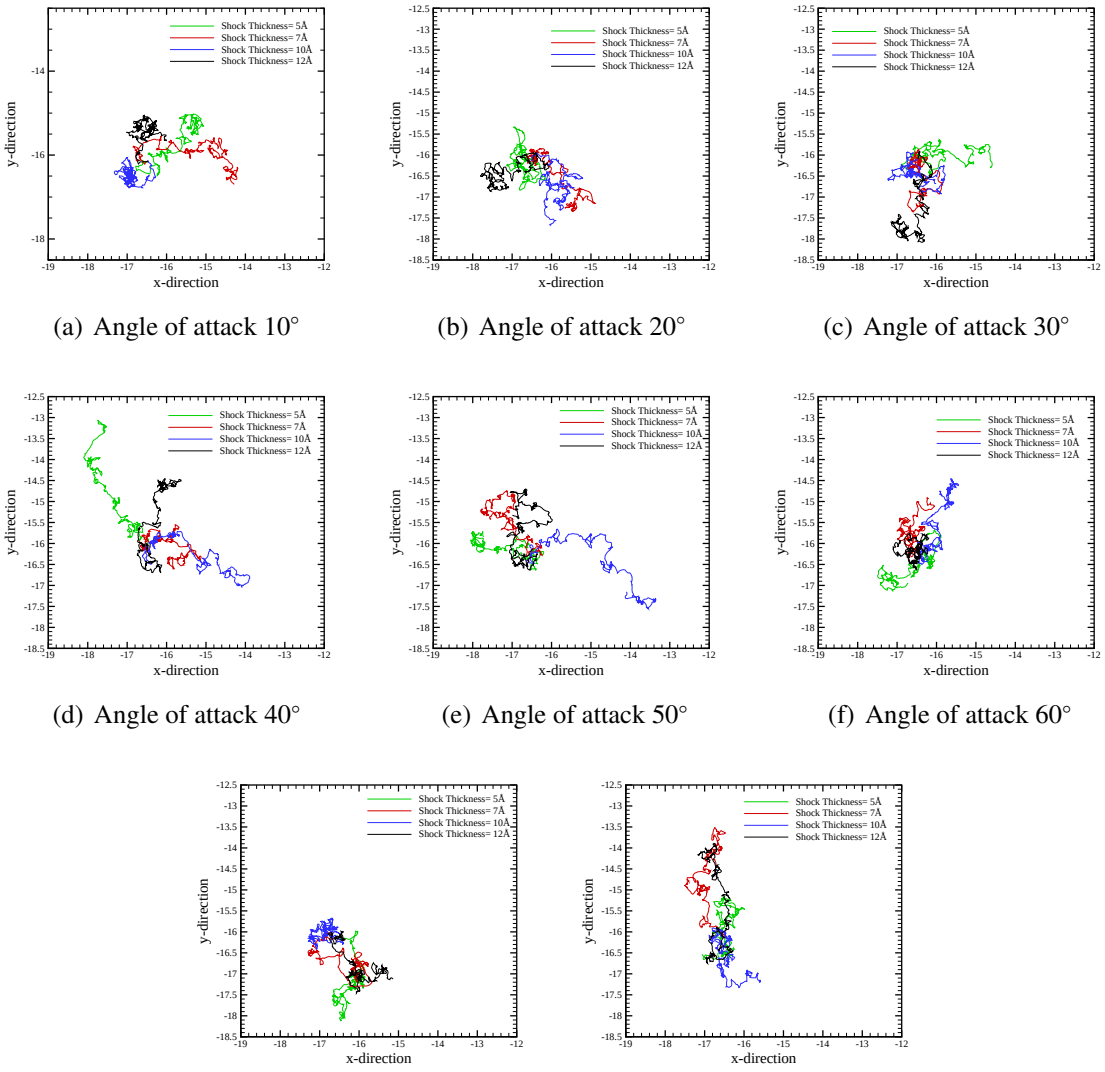

(a) Angle of attack 10° (b) Angle of attack 20° (c) Angle of attack 30°

(d) Angle of attack 40° (e) Angle of attack 50° (f) Angle of attack 60°

(g) Angle of attack 70° (h) Angle of attack 80°

Figure 5.9: Shock wave effects on COM at various shock wave thicknesses and angles of attack when the impulse is $0.33 mPa \cdot s$

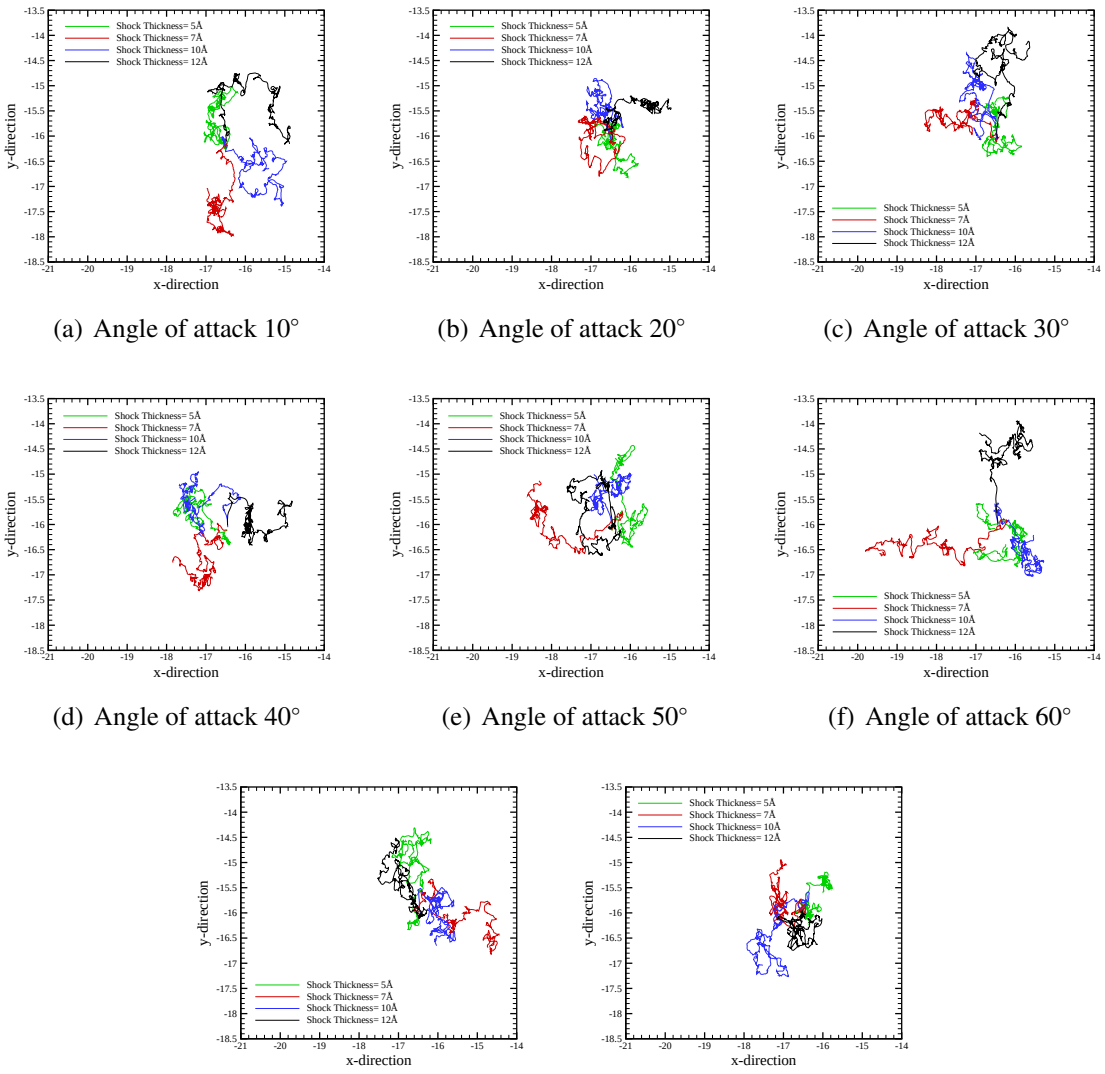

(a) Angle of attack 10° (b) Angle of attack 20° (c) Angle of attack 30°

(d) Angle of attack 40° (e) Angle of attack 50° (f) Angle of attack 60°

(g) Angle of attack 70° (h) Angle of attack 80°

Figure 5.10: Shock wave effects on COM at various shock wave thicknesses and angles of attack when the impulse is $0.66 mPa \cdot s$

5.2.4 MSD and Latteral Diffusion - NPT ensemble

This section presents the MSD of the membrane as well as their lateral diffusion for all cases of different impulses and shock angles of attack. Equally, the behaviour of each monolayer separately is also demonstrated. It is to be noted that in the computation of MSD the positions are updated based on velocity values where we have subtracted their average figure. Therefore, in case of constant velocity the result will be zero.

The following figures, 5.11-5.12, show the MSD of the membrane lipids as function of time for a shock of impulse $0.33 mPa \cdot s$ at all 4 shock thicknesses and 8 incidence angles. In principal, there is a significant dependence of the MSD on the incidence angle with the MSD slope to continuously increase in a non-linear manner as the angle increases and the aforementioned increase of the slope corresponds to higher lateral diffusion values, as demonstrated in figures 5.21-5.24.

A similar trend is noticed for all four impulses with the diffusion coefficient initially increasing significantly as the incidence angle increases followed by a global maximum and then entering a decreasing phase with slight fluctuations around a certain value. As the oblique shock's angle initially increases the parallel to the membrane momentum components increase therefore, enhancing the lateral mobility of the lipids belonging to the top layer of the membrane. The increased mobility of the lipids is reflected to corresponding increments of the diffusion coefficient values.

However, if the angle of attack continues to increase the perpendicular to the membrane shock velocity becomes weaker increasing therefore the time needed for the wave to hit the membrane and reducing the amount of direct momentum transfer between the shock's water molecules and the membrane lipids. Furthermore, although the parallel velocity components are expected to continue to enhance the lateral particles' mobility, the increased rate is bounded by the effectiveness of the momentum transfer across the interface. As a consequence it just compensates any losses arising from the perpendicular component leading therefore to almost constant values of diffusion.

The following plots, 5.13 - 5.16, present the MSD of the upper and lower membrane layer separately for all cases of different shock thicknesses and angles of attack. It is observed that similar trends appear to be followed by the MSD of the membrane and each monolayer separately. However, in most cases the MSD of the upper layer seems to be more similar to the MSD profile of the whole membrane than the one of the lower layer. This is due to the fact that the shock is initially introduced to the upper membrane layer and throughout the course of the simulation the momentum gets transferred to the the rest of the lipids that consist of the lower layer.

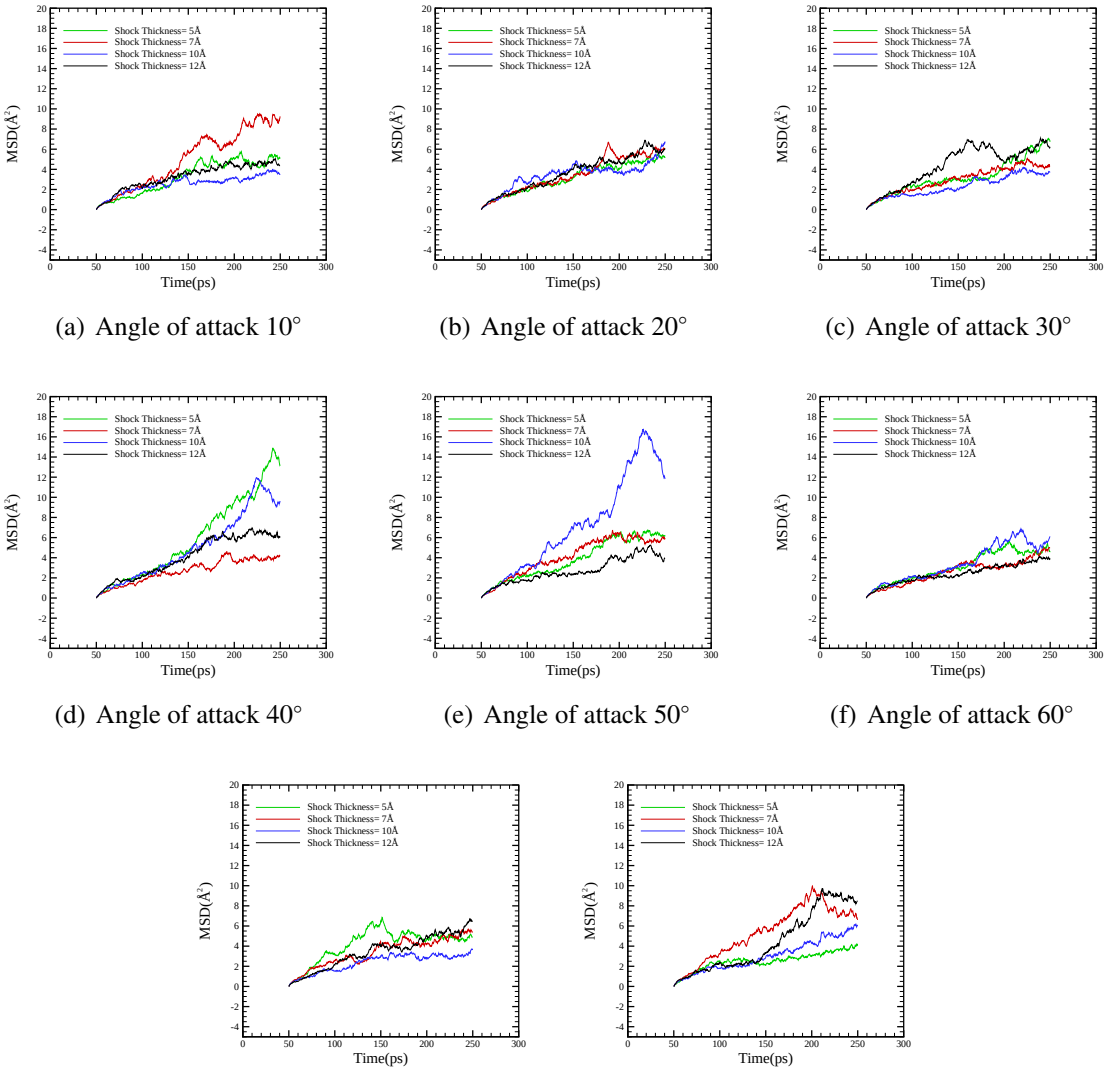

(a) Angle of attack 10° (b) Angle of attack 20° (c) Angle of attack 30°

(d) Angle of attack 40° (e) Angle of attack 50° (f) Angle of attack 60°

(g) Angle of attack 70° (h) Angle of attack 80°

Figure 5.11: Shock wave effects on MSD of the membrane at various shock wave thicknesses and angles of attack when the impulse is $0.33 mPa \cdot s$

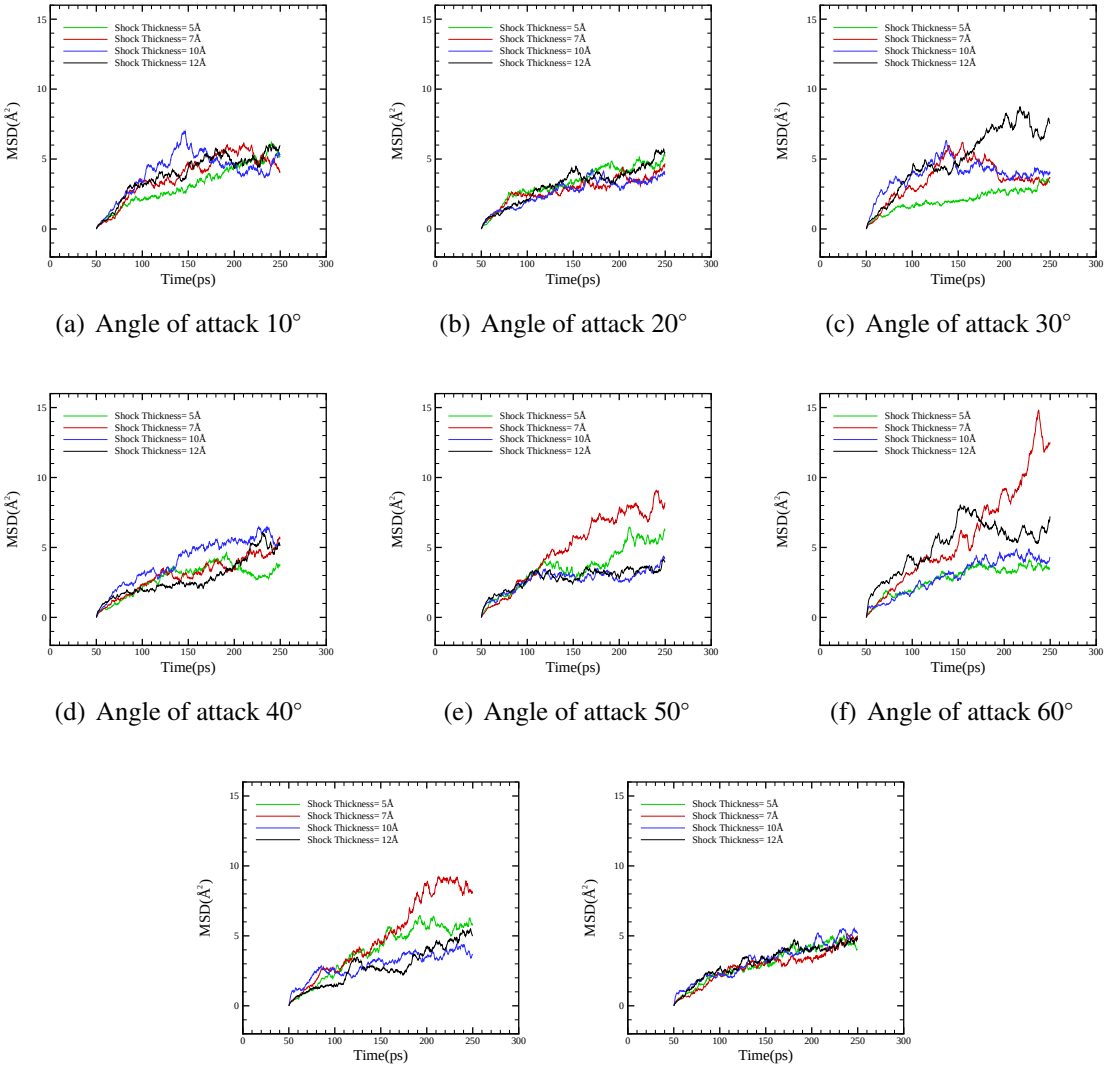

(a) Angle of attack 10° (b) Angle of attack 20° (c) Angle of attack 30°

(d) Angle of attack 40° (e) Angle of attack 50° (f) Angle of attack 60°

(g) Angle of attack 70° (h) Angle of attack 80°

Figure 5.12: Shock wave effects on MSD of the membrane at various shock wave thicknesses and angles of attack when the impulse is $0.66 mPa \cdot s$

Figures 5.13 and 5.14 presents the plots of the MSD of the upper layer of the membrane when the impulse is $0.33mPa \cdot s$ and $0.66mPa \cdot s$ for various angles and shock thicknesses. (The MSD of the upper layer of the membrane when the impulse is $0.99mPa \cdot s$ and $2mPa \cdot s$ is shown in Appendix C).

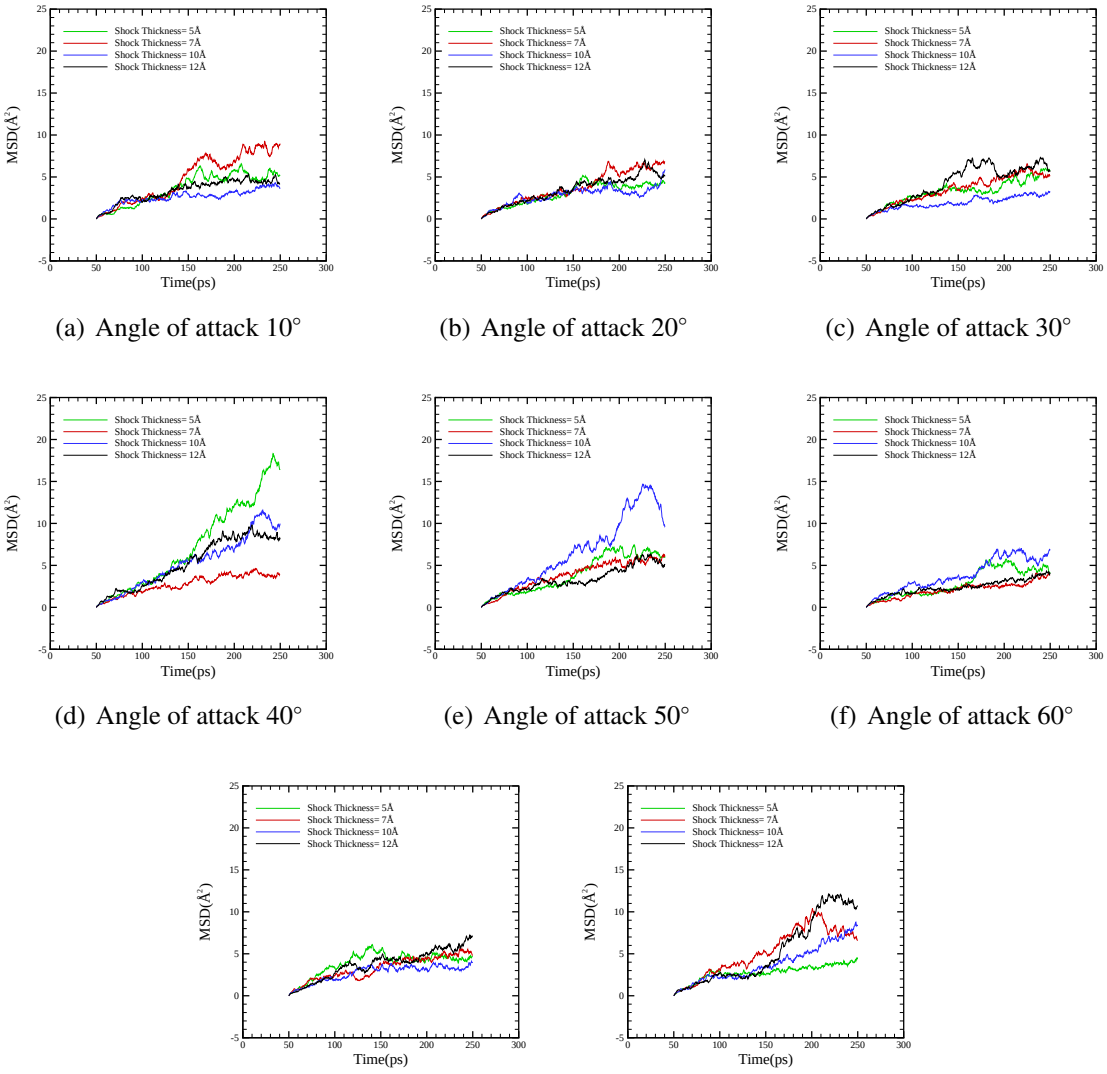

(a) Angle of attack 10° (b) Angle of attack 20° (c) Angle of attack 30°

(d) Angle of attack 40° (e) Angle of attack 50° (f) Angle of attack 60°

(g) Angle of attack 70° (h) Angle of attack 80°

Figure 5.13: Shock wave effects on MSD of the upper bilayer at various shock wave thicknesses and angles of attack when the impulse is $0.33mPa \cdot s$

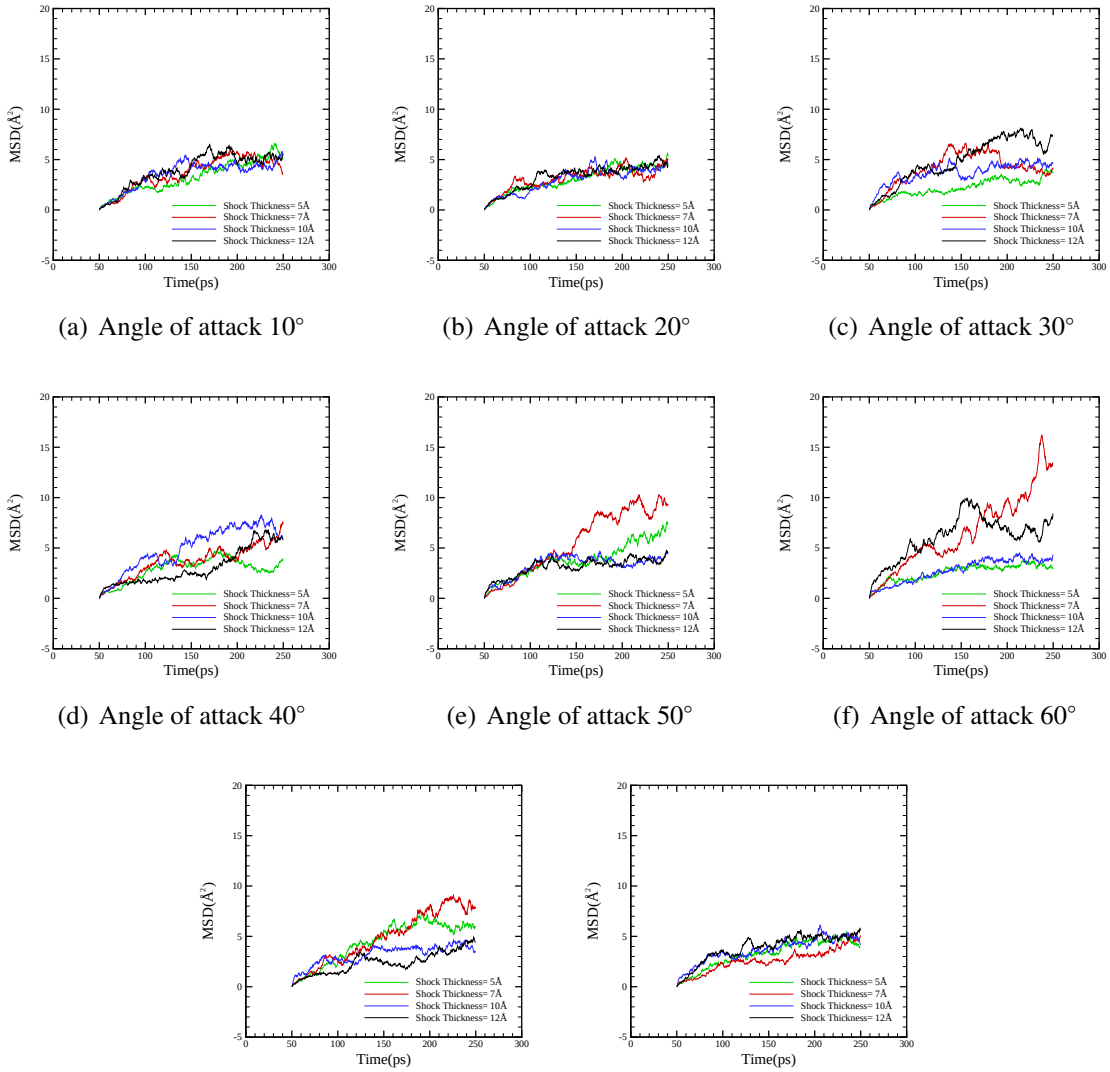

(a) Angle of attack 10° (b) Angle of attack 20° (c) Angle of attack 30°

(d) Angle of attack 40° (e) Angle of attack 50° (f) Angle of attack 60°

(g) Angle of attack 70° (h) Angle of attack 80°

Figure 5.14: Shock wave effects on MSD of the upper bilayer at various shock wave thicknesses and angles of attack when the impulse is $0.66 mPa \cdot s$

Figures 5.15and 5.16 show the tendencies of the MSD graphs of the lipids of the lower layer of the membrane. The impulse again between $0.33 mPa \cdot s$ and $0.66 mPa \cdot s$ and the angle of application is 10° and 20° at various shock thicknesses. (For more results see Appendix C)

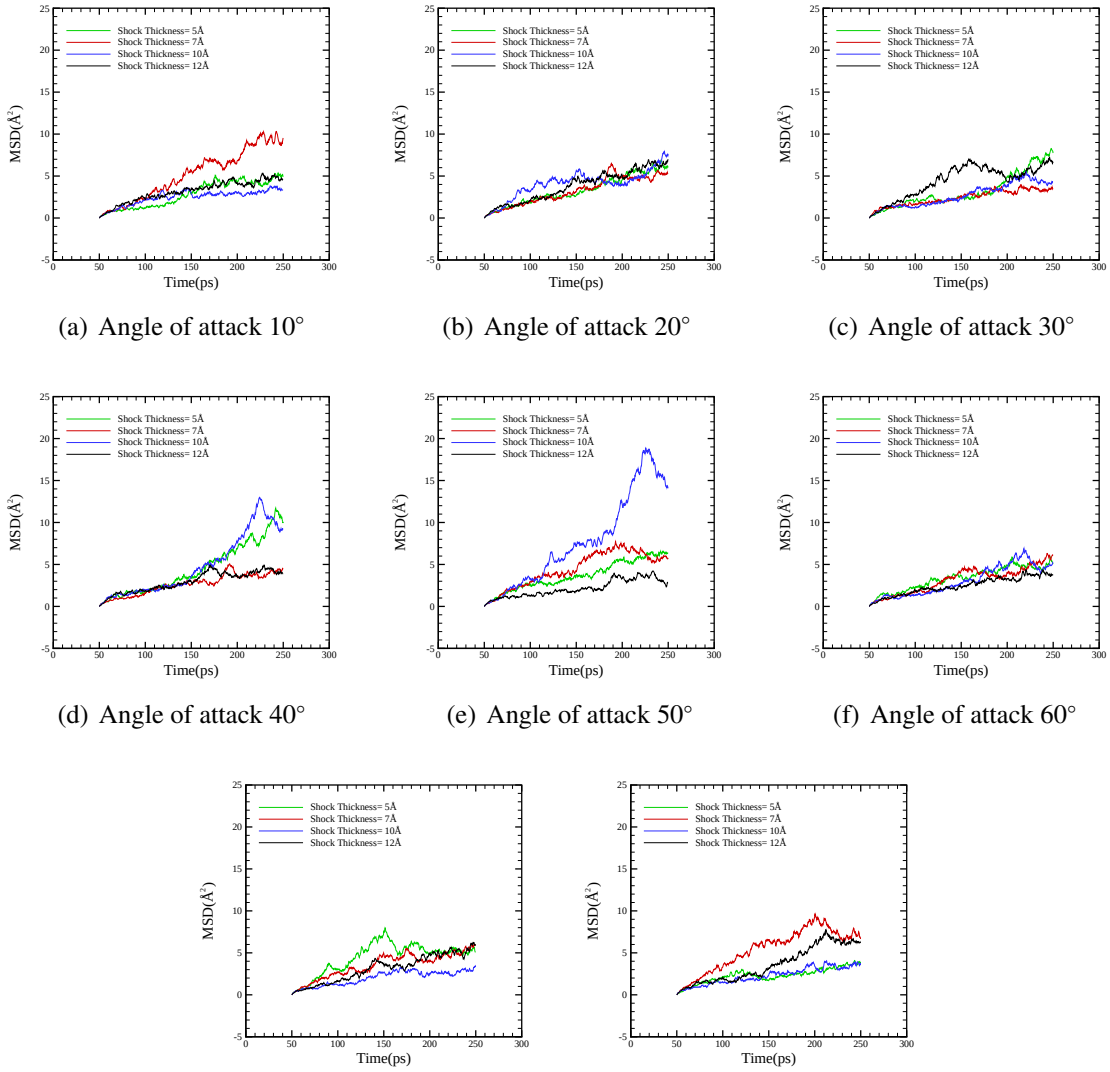

(a) Angle of attack 10° (b) Angle of attack 20° (c) Angle of attack 30°

(d) Angle of attack 40° (e) Angle of attack 50° (f) Angle of attack 60°

(g) Angle of attack 70° (h) Angle of attack 80°

Figure 5.15: Shock wave effects on MSD of the lower bilayer at various shock wave thicknesses and angles of attack when the impulse is $0.33 mPa \cdot s$

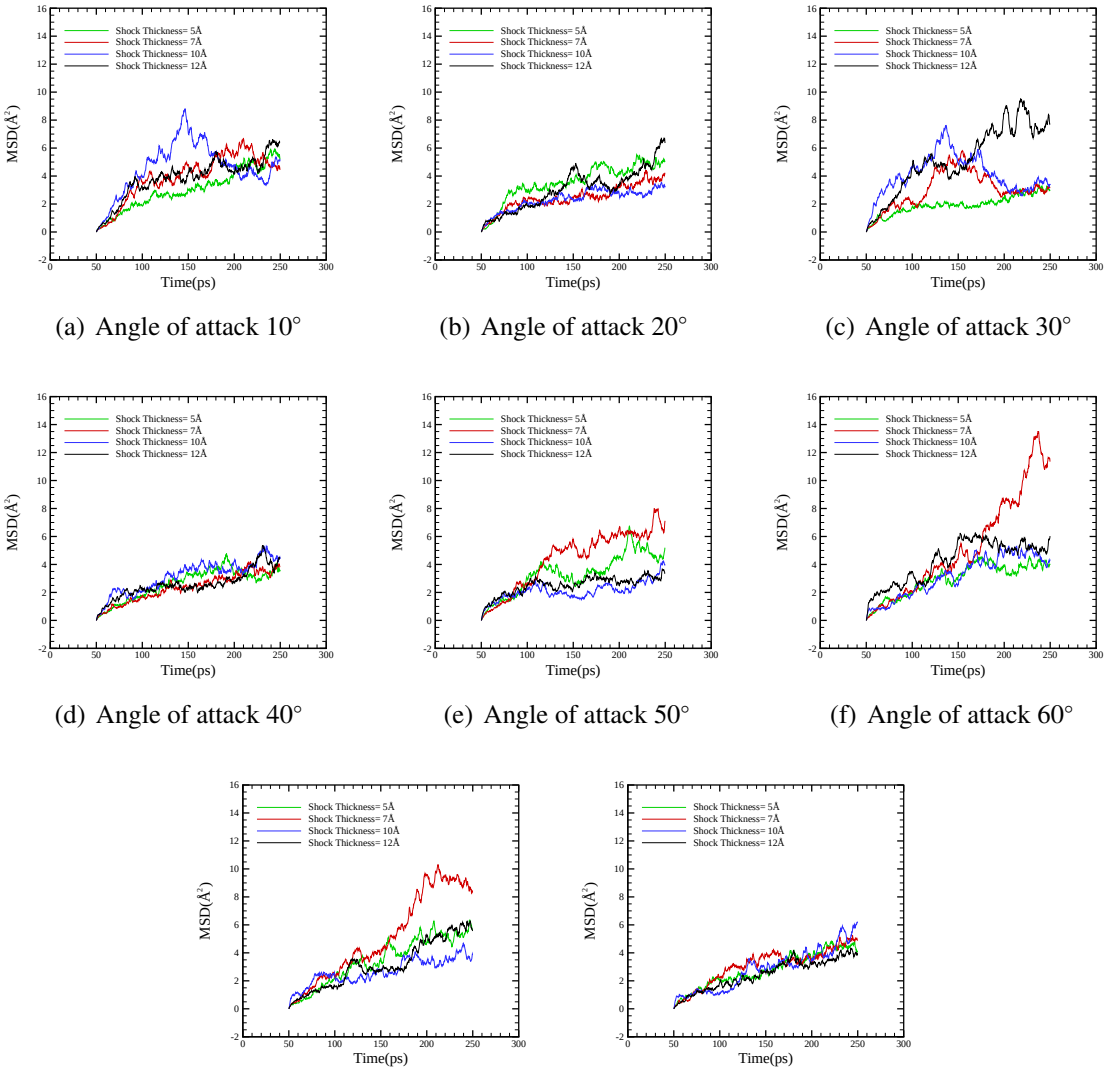

(a) Angle of attack 10° (b) Angle of attack 20° (c) Angle of attack 30°

(d) Angle of attack 40° (e) Angle of attack 50° (f) Angle of attack 60°

(g) Angle of attack 70° (h) Angle of attack 80°

Figure 5.16: Shock wave effects on MSD of the lower bilayer at various shock wave thicknesses and angles of attack when the impulse is $0.66 mPa \cdot s$

The following figures present the lateral diffusion of the lipids of the whole membrane model, the upper layer, and the lower layer against the impulse of the shock applied.

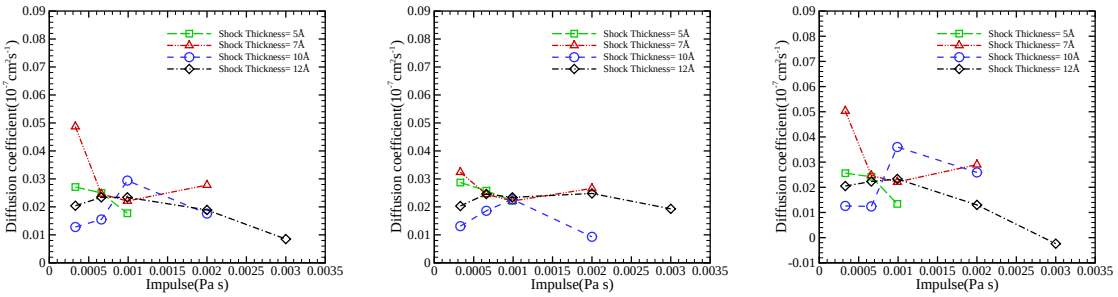

(a) Whole lipid bilayer (b) Upper lipid bilayer (c) Lower lipid bilayer

Figure 5.17: Diffusion coefficient as function of impulse at various shock wave thicknesses when the angle of attack is 10°

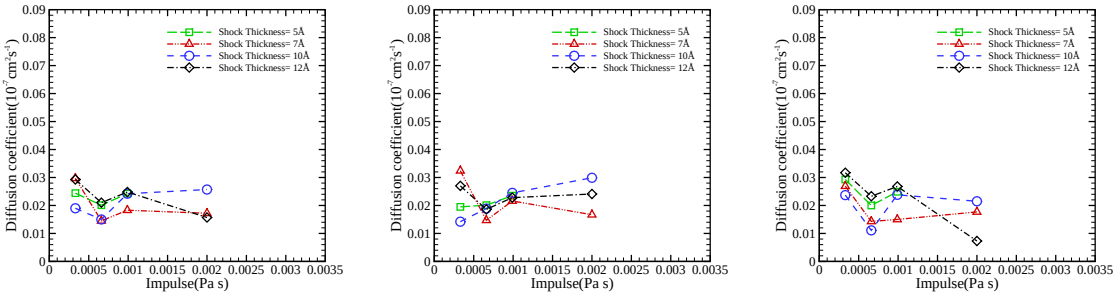

(a) Whole lipid bilayer (b) Upper lipid bilayer (c) Lower lipid bilayer

Figure 5.18: Diffusion coefficient as function of impulse at various shock wave thicknesses when the angle of attack is 20°

Figures 5.19 and 5.20 present the lateral diffusion of the lipids of the whole membrane model, the upper layer, and the lower layer against the thickness of the shock applied.

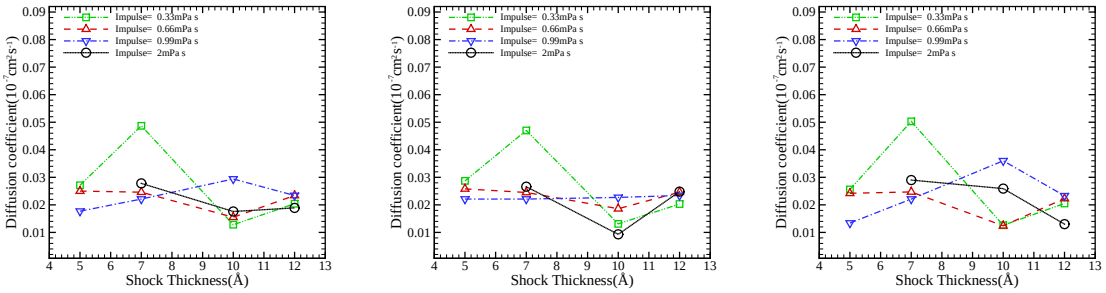

(a) Whole lipid bilayer (b) Upper lipid bilayer (c) Lower lipid bilayer

Figure 5.19: Diffusion coefficient as function of shock wave thickness at various impulses when the angle of attack is 10°

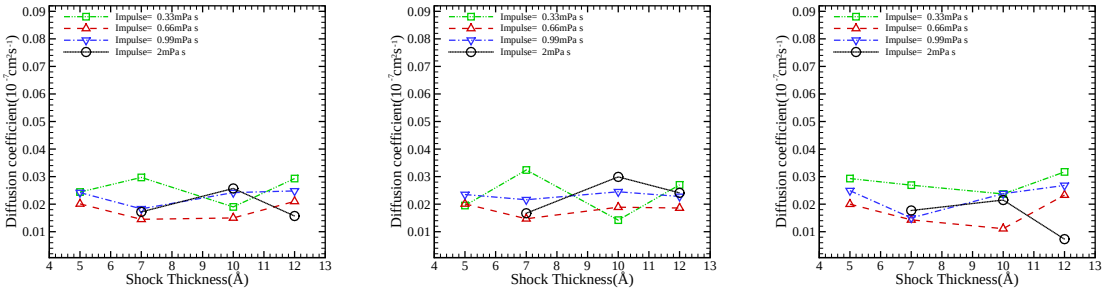

(a) Whole lipid bilayer (b) Upper lipid bilayer (c) Lower lipid bilayer

Figure 5.20: Diffusion coefficient as function of shock wave thickness at various impulses when the angle of attack is 20°

The following 4 figures present the lateral diffusion of the lipids of the whole membrane model, the upper layer, and the lower layer against the shock angle of attack.

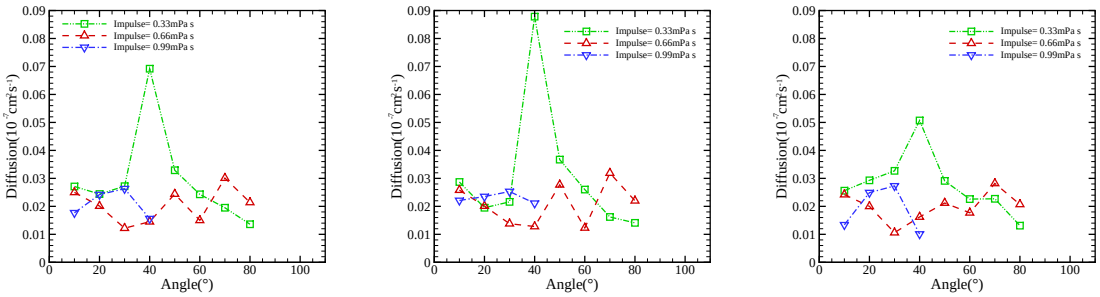

(a) Whole lipid bilayer (b) Upper lipid bilayer (c) Lower lipid bilayer

Figure 5.21: Relation between the diffusion coefficient and the angle of attack while the shock wave thickness is 5Å

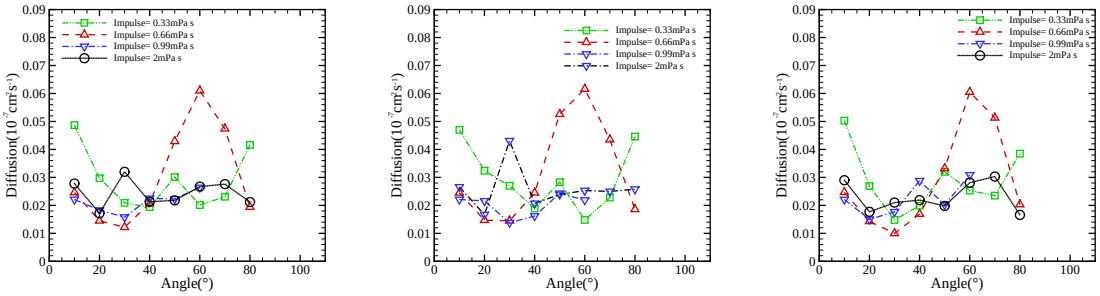

(a) Whole lipid bilayer (b) Upper lipid bilayer (c) Lower lipid bilayer

Figure 5.22: Relation between the diffusion coefficient and the angle of attack while the shock wave thickness is 7Å

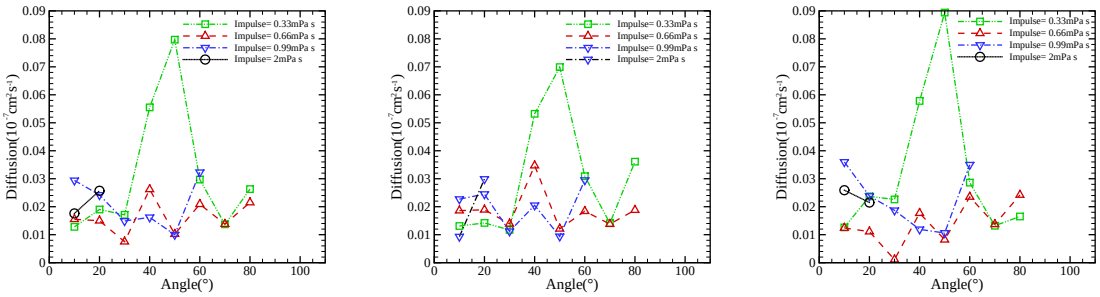

(a) Whole lipid bilayer (b) Upper lipid bilayer (c) Lower lipid bilayer

Figure 5.23: Relation between the diffusion coefficient and the angle of attack while the shock wave thickness is 10Å

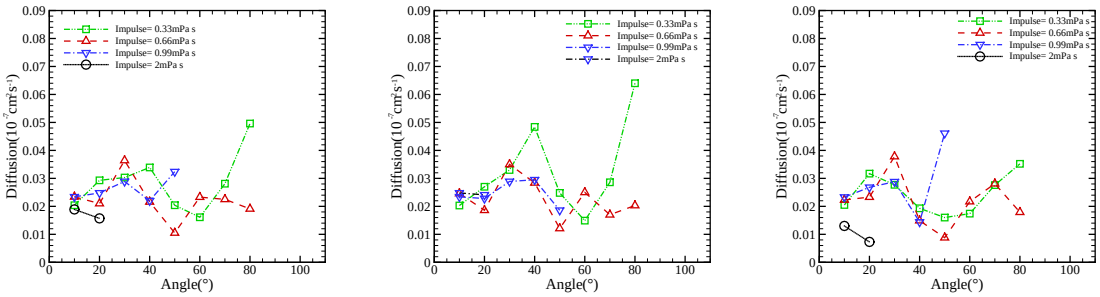

(a) Whole lipid bilayer (b) Upper lipid bilayer (c) Lower lipid bilayer

Figure 5.24: Relation between the diffusion coefficient and the angle of attack while the shock wave thickness is 12Å

5.2.5 Effects on Kinetic Energy - NVE ensemble

This section presents the kinetic energy profiles of the water-membrane system for the set of simulations run under the NVE ensemble. It is shown that due to the nature of the ensemble, initially the kinetic energy for all different cases has to reach a local maximum or minimum and then it oscillates around the mean value it eventually reached. It is observed that one of the shock thicknesses causes a higher level of conserved kinetic energy. Hence, it could be suggested that one of the two types of perturbed molecules in the water-membrane system (waters and lipids) resonates. At the same time, considering the "weak" shock ($0.33 mPa \cdot s$) applied in these first results using the NVE ensemble, it is most likely that the excited molecules are the lighter molecules (i.e. the water molecules). Such a phenomenon is equivalent to the interaction between water molecules and photons from a light beam when the former absorb energy from the later (atomic absorption spectrophotometry).

In particular, it is evident in 5.25 that for an impulse of $0.33 mPa \cdot s$ when the angle of attack gets progressively larger from 40° to 80°, a shock thickness of 10Å manages to cause a significantly higher kinetic energy in the water-membrane system compared to the perturbation caused under any of the 3 other shock thicknesses (5Å, 7Å, 12Å).

In figure 5.26 the kinetic energy profiles of the water-membrane system for shock thickness 12Å present a dramatic increase in kinetic energy compared to the rest of kinetic energy profiles caused by smaller shock thicknesses (5Å, 7Å, 10Å).

It is again obvious that larger angles of attack result in higher rise in the parallel component of the velocities of the atoms in the upper water layer, which is primarily responsible for the increase in the kinetic energy of the system rather than the normal component.

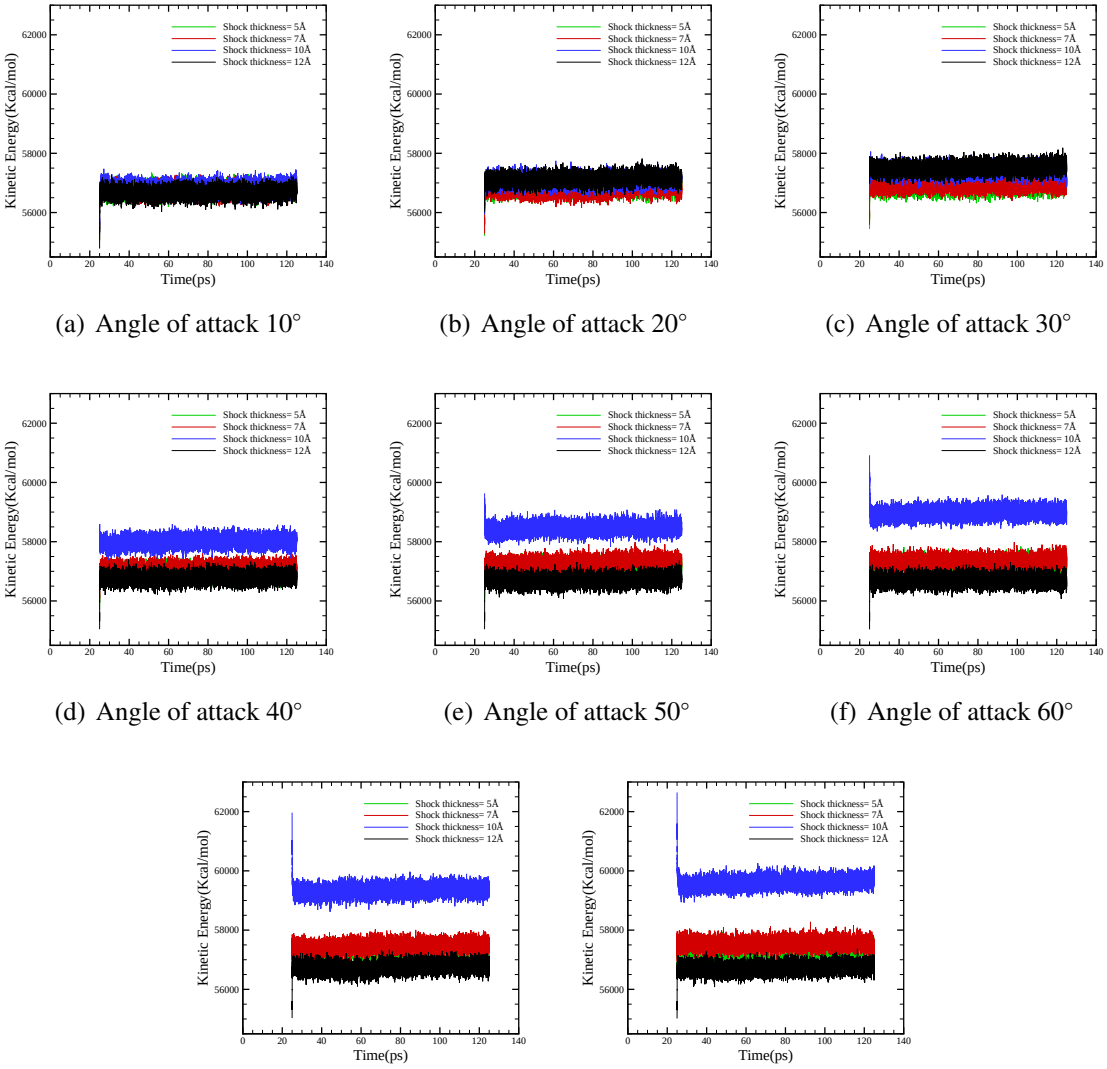

(a) Angle of attack 10° (b) Angle of attack 20° (c) Angle of attack 30°

(d) Angle of attack 40° (e) Angle of attack 50° (f) Angle of attack 60°

(g) Angle of attack 70° (h) Angle of attack 80°

Figure 5.25: Shock wave effects on Kinetic Energy at various shock wave thicknesses and angles of attack when the impulse is $0.33 mPa \cdot s$

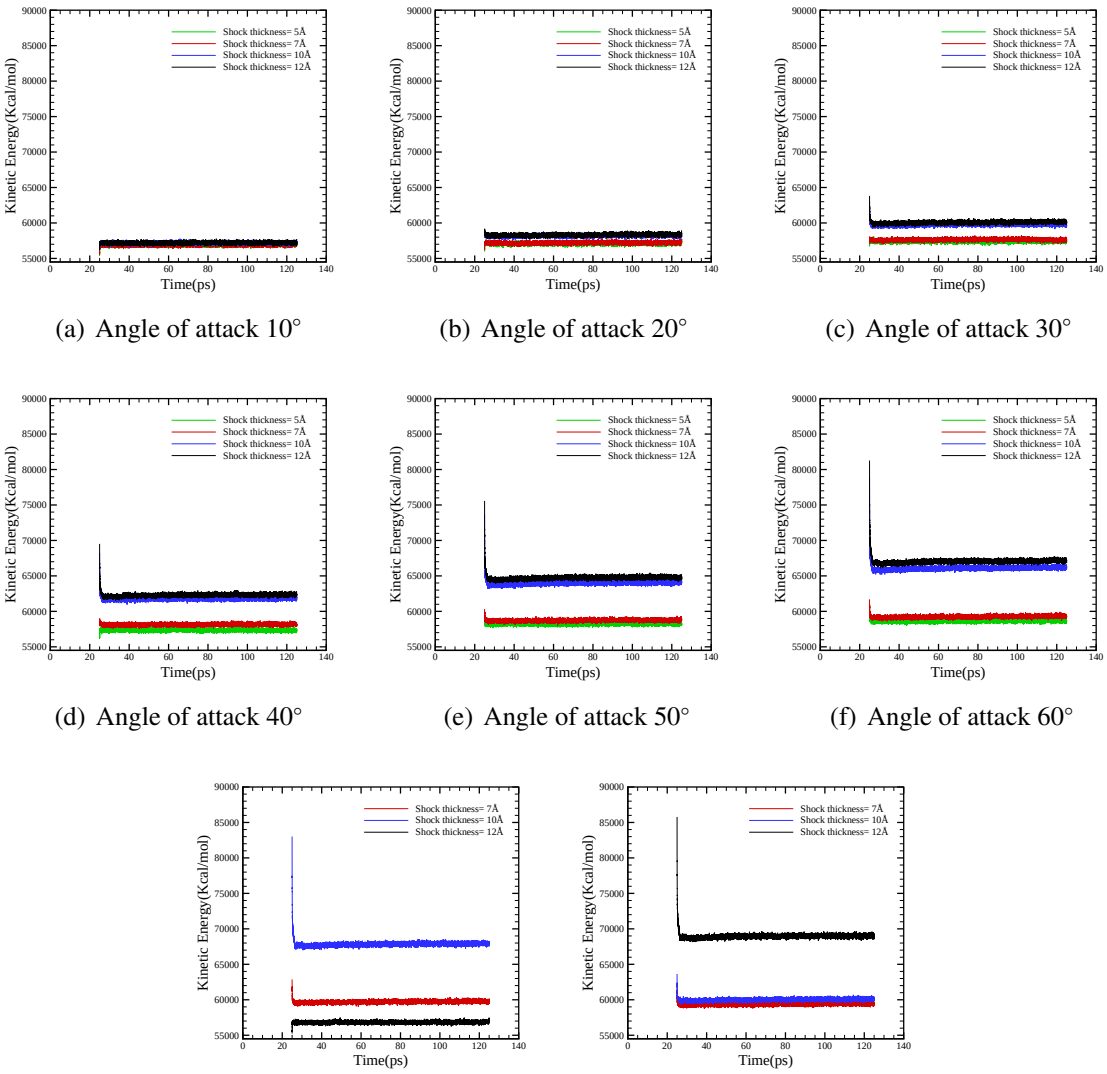

(a) Angle of attack 10° (b) Angle of attack 20° (c) Angle of attack 30°

(d) Angle of attack 40° (e) Angle of attack 50° (f) Angle of attack 60°

(g) Angle of attack 70° (h) Angle of attack 80°

Figure 5.26: Shock wave effects on Kinetic Energy at various shock wave thicknesses and angles of attack when the impulse is $0.66 mPa \cdot s$

As it was shown previously, under the application of a weak shock the water atoms resonate for a shock thickness of 10Å but with a stronger shock some other atoms are seen to resonate at 12Å. Therefore, it is concluded that the largest atoms that consist of the lipids in the model are now resonating. This can be explained by the fact that a "strong" shock (over $0.33 mPa \cdot s$) managed to put into motion the heavier atoms while the previous shock ($0.33 mPa \cdot s$) was not efficient.

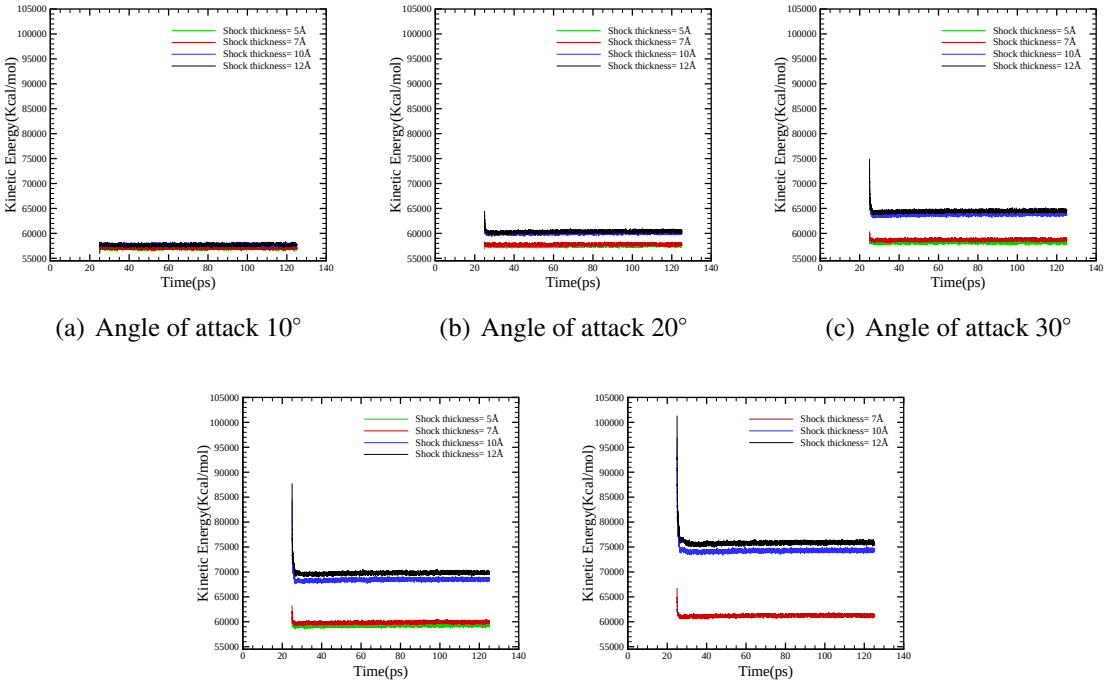

(a) Angle of attack 10° (b) Angle of attack 20° (c) Angle of attack 30°

(d) Angle of attack 40° (e) Angle of attack 50°

Figure 5.27: Shock wave effects on Kinetic Energy at various shock wave thicknesses and angles of attack when the impulse is $0.99 mPa \cdot s$

Lastly, the following plot 5.28 gives the kinetic energy profiles of the water-membrane system when the incidence angle is 10° and 20° only, since larger angles lead to unstable simulations due to the excess in kinetic energy of the atoms.

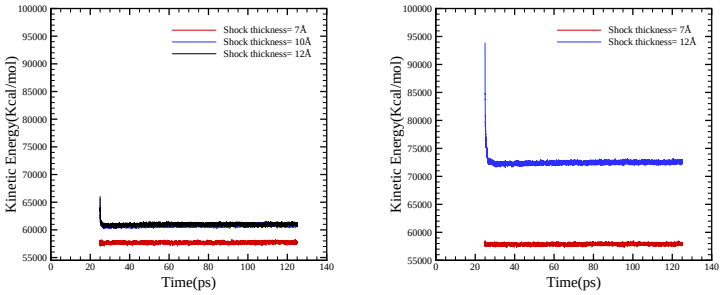

(a) Angle of attack 10° (b) Angle of attack 20°

Figure 5.28: Shock wave effects on Kinetic Energy at various shock wave thicknesses and angles of attack when the impulse is $2mPa \cdot s$

5.2.6 Effects on Membrane Thickness - NVE ensemble

The following figures 5.29 - 5.30 show membrane thickness as function of time for impulses varying from $0.33mPa \cdot s$ to $2mPa \cdot s$ (see Appendix C) at various shock thicknesses and incidence angles. The same behaviour is noticed for all incidence angles examined, with the membrane to shrink after the application of the oblique shock, with a reduced rate until it relaxes to a local equilibrium state.

In particular, as the shock impulse increases, a greater reduction in membrane size is observed. This is a testament of the importance of the impulse of the shock, as discussed in chapter 4. The following plots, 5.29 - 5.30, present the thickness of the membrane with time for various angles. It is observed that when the impulse is $0.33mPa \cdot s$, the greatest reduction of membrane thickness is achieved when the angle of attack is 60° and the shock thickness is 10Å (the membrane thickness becomes 16.4Å). At the same time, the greatest reduction in the membrane size is when the shock impulse is $0.66mPa \cdot s$ with a shock thickness of 10Å and an angle of attack 80°. The resulting membrane thickness then becomes 15.05Å.

A greater impulse ($0.66mPa \cdot s$) caused a greater thinning of the membrane, as discussed in chapter 4, when the significance of the shock impulse was analysed for the case of the normal shock. Here, the importance of the shock impulse and the angle of attack is clearly evident.

It is shown that large angles of attack cause greater reduction of the membrane thickness, stressing out the importance of the parallel component of the velocity during the momentum transfer.

As observed in membrane thickness plots for impulses from $0.33mPa \cdot s$ to $2mPa \cdot s$ (see figures 5.29 - 5.30 and c25 - c26 in Appendix C), a small incidence angle only manages to

compress the lipids when the shock is strong enough and as a result the thickness decreases.

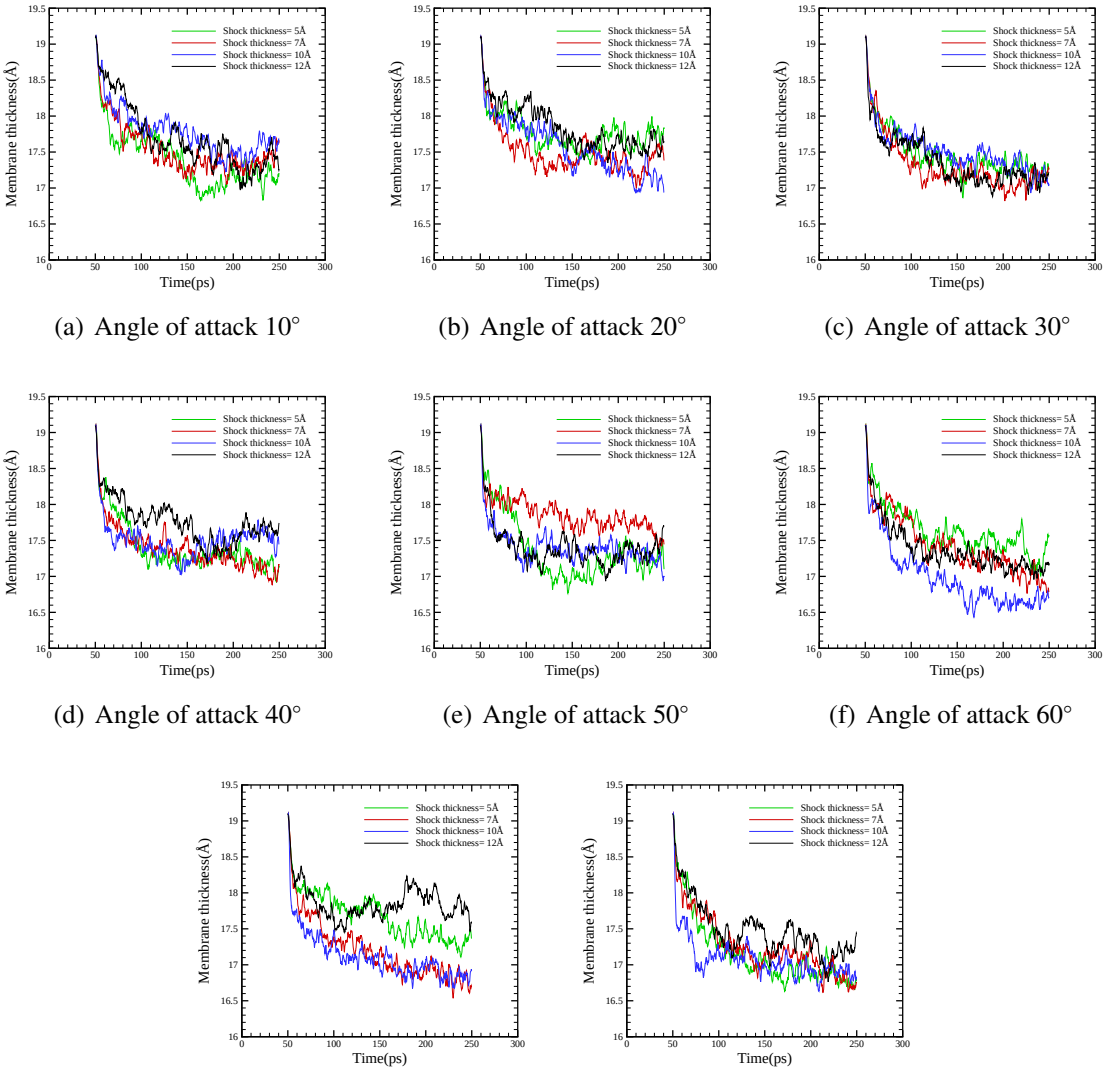

(a) Angle of attack 10° (b) Angle of attack 20° (c) Angle of attack 30°

(d) Angle of attack 40° (e) Angle of attack 50° (f) Angle of attack 60°

(g) Angle of attack 70° (h) Angle of attack 80°

Figure 5.29: Shock wave effects on Membrane Thickness at various shock wave thicknesses and angles of attack when the impulse is $0.33 mPa \cdot s$

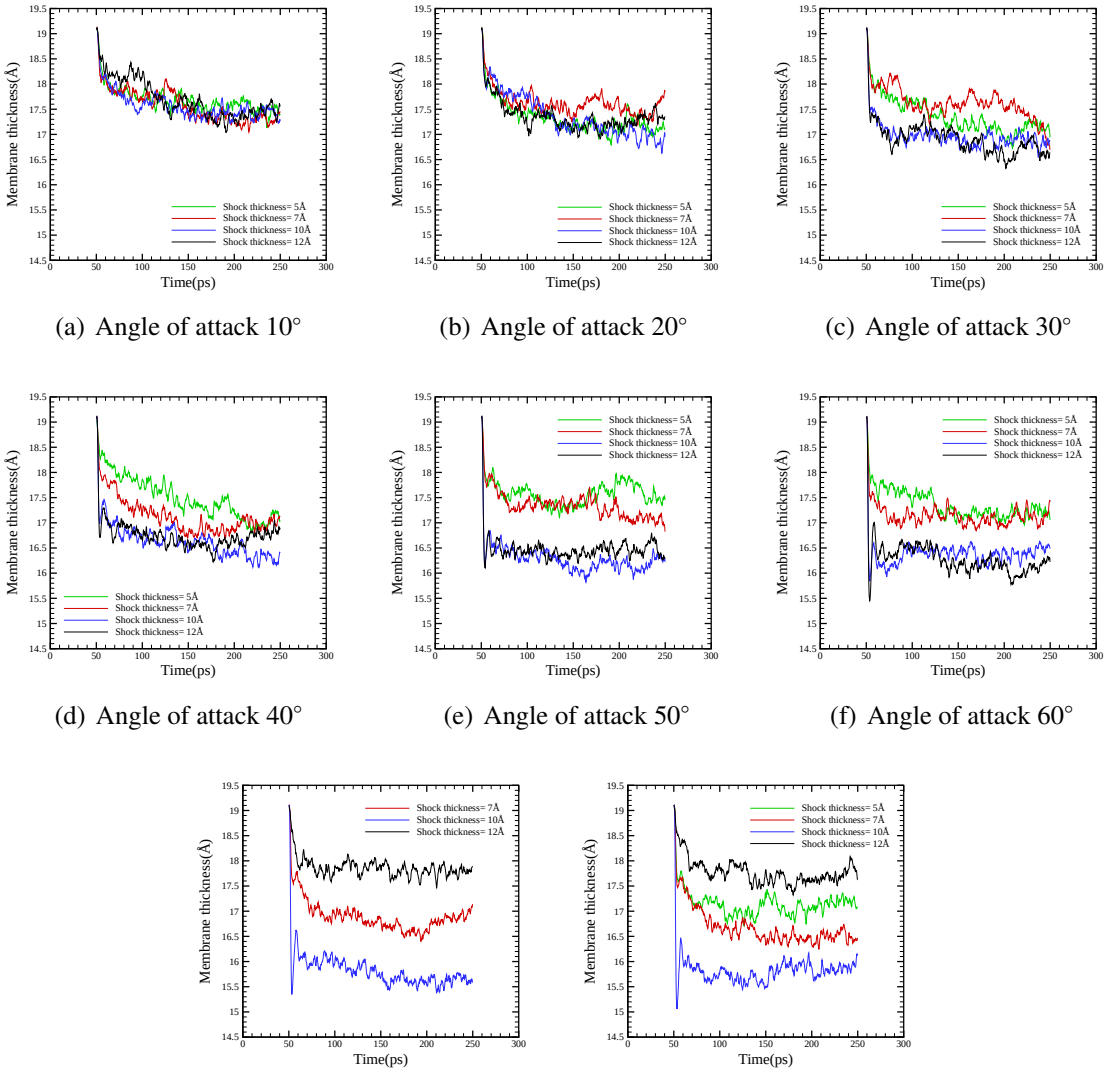

(a) Angle of attack 10° (b) Angle of attack 20° (c) Angle of attack 30°

(d) Angle of attack 40° (e) Angle of attack 50° (f) Angle of attack 60°

(g) Angle of attack 70° (h) Angle of attack 80°

Figure 5.30: Shock wave effects on Membrane Thickness at various shock wave thicknesses and angles of attack when the impulse is $0.66 mPa \cdot s$

When the incidence angle is large, there are two cases that explain the behaviour of the membrane thickness. In the first case, the shock is shallow and the water atoms are moving towards the boundaries of the simulation box parallel to the x-z plane. Since the ensemble is the NVE and the volume of the simulation needs to be kept constant, such an expansion caused by the waters will lead in stretching of the membrane in the x-y plane and therefore will reduce its size in the z axis, making it thinner. In the second case, the shock is strong and hence travels deep enough to "reach" the lipids and also compresses them against the boundary of the simulation box parallel to the x-y plane, following the z direction where the shock is coming from. However, since the angle of attack is large (50° - 80°), the parallel component of the impulse is causing a greater displacement in the

y direction than the one caused by the normal component in the z direction. Therefore, there is compression of molecules that takes place in both the x-y plane and the x-z plane. Hence, the thinning of the membrane only takes place right after the shock is applied and consequently the thickness of the membrane relaxes around a mean value, as figure 5.30 suggests as opposed to figure 5.29 for angles 50° - 80°.

5.2.7 Effects on membrane COM - NVE ensemble

The following figures present the COM of the lipids of the membrane throughout the course of the simulation. What can be observed is that when the shock goes deep enough into the water-membrane system, the velocity vectors push the lipids towards the positive y wall causing a displacement of the COM in that direction, until the point where the compression and density of the lipids against that wall causes them to diverge randomly to the right or to the left under the pressure of the lipids behind them, which have kinetic energy.

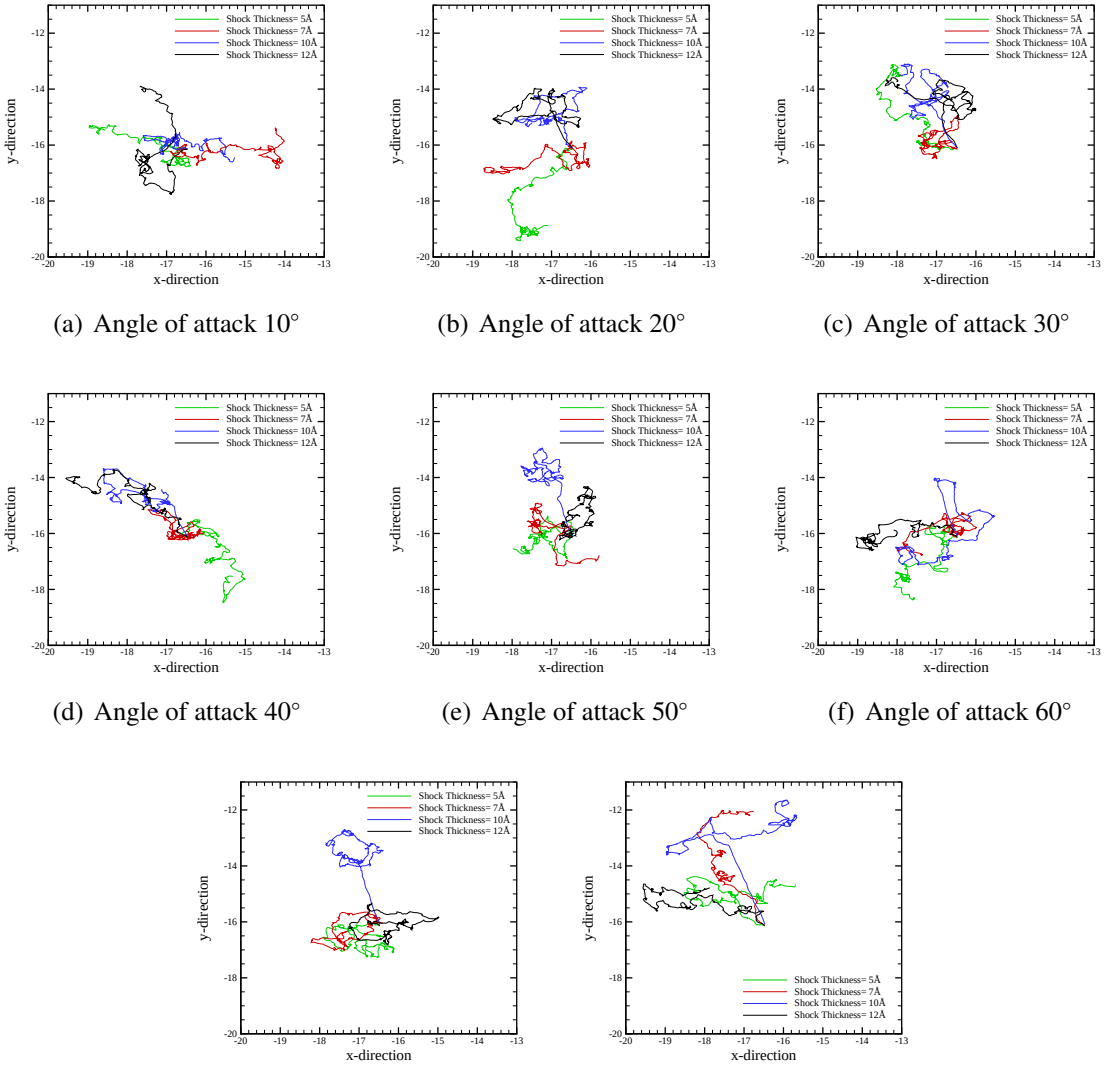

(a) Angle of attack 10° (b) Angle of attack 20° (c) Angle of attack 30°

(d) Angle of attack 40° (e) Angle of attack 50° (f) Angle of attack 60°

(g) Angle of attack 70° (h) Angle of attack 80°

Figure 5.31: Shock wave effects on COM at various shock wave thicknesses and angles of attack when the impulse is $0.33 mPa \cdot s$

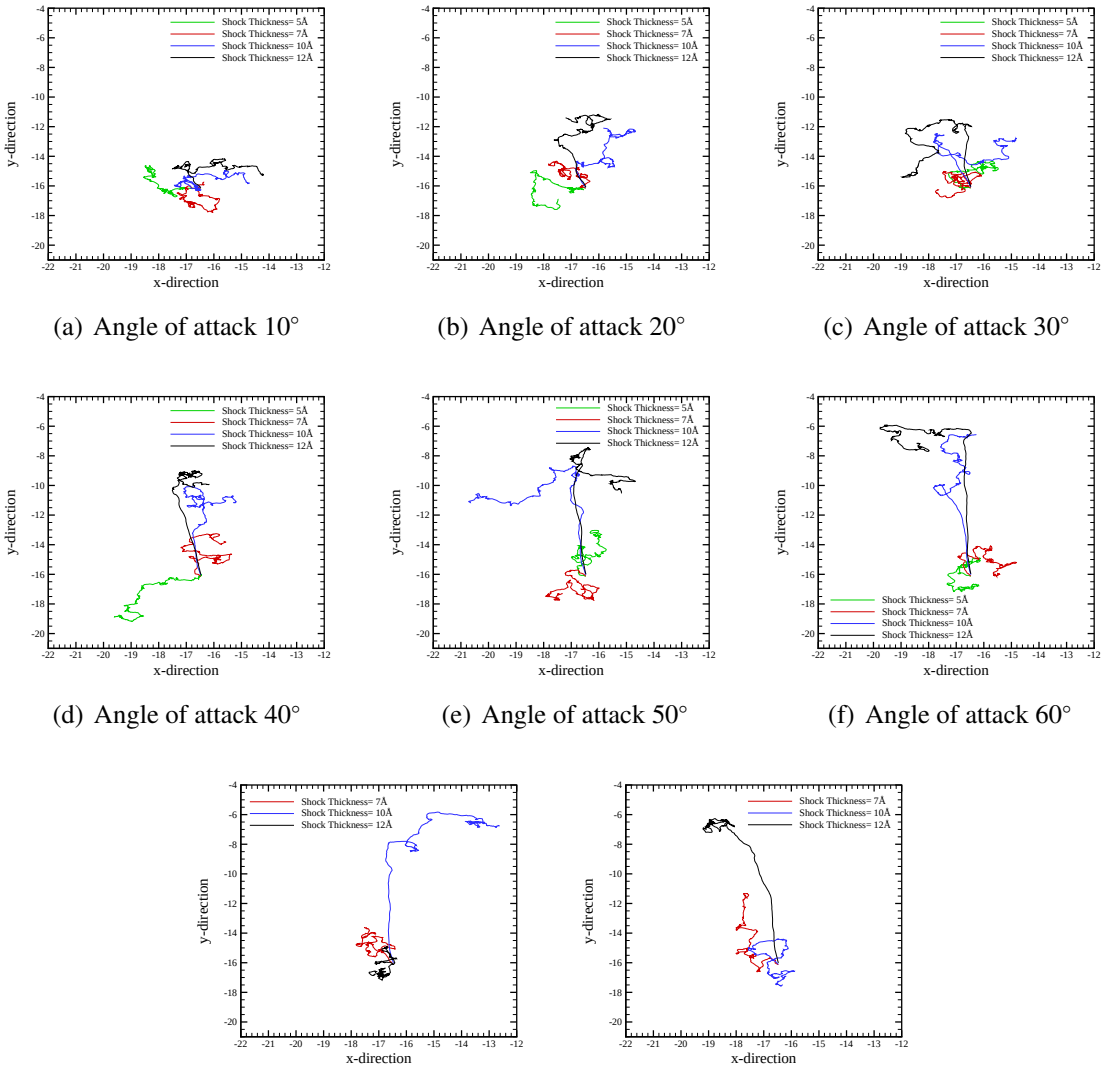

(a) Angle of attack 10° (b) Angle of attack 20° (c) Angle of attack 30°

(d) Angle of attack 40° (e) Angle of attack 50° (f) Angle of attack 60°

(g) Angle of attack 70° (h) Angle of attack 80°

Figure 5.32: Shock wave effects on COM at various shock wave thicknesses and angles of attack when the impulse is $0.66 mPa \cdot s$

5.2.8 MSD and Latter Diffusion - NVE ensemble

The following graphs show the MSD of the membrane throughout the course of the simulation when the impulse is $0.33mPa \cdot s$ and $0.66mPa \cdot s$. (For impulse $0.99mPa \cdot s$ and $2mPa \cdot s$ see Appendix C). The main tendency observed in all cases of impulses is that in

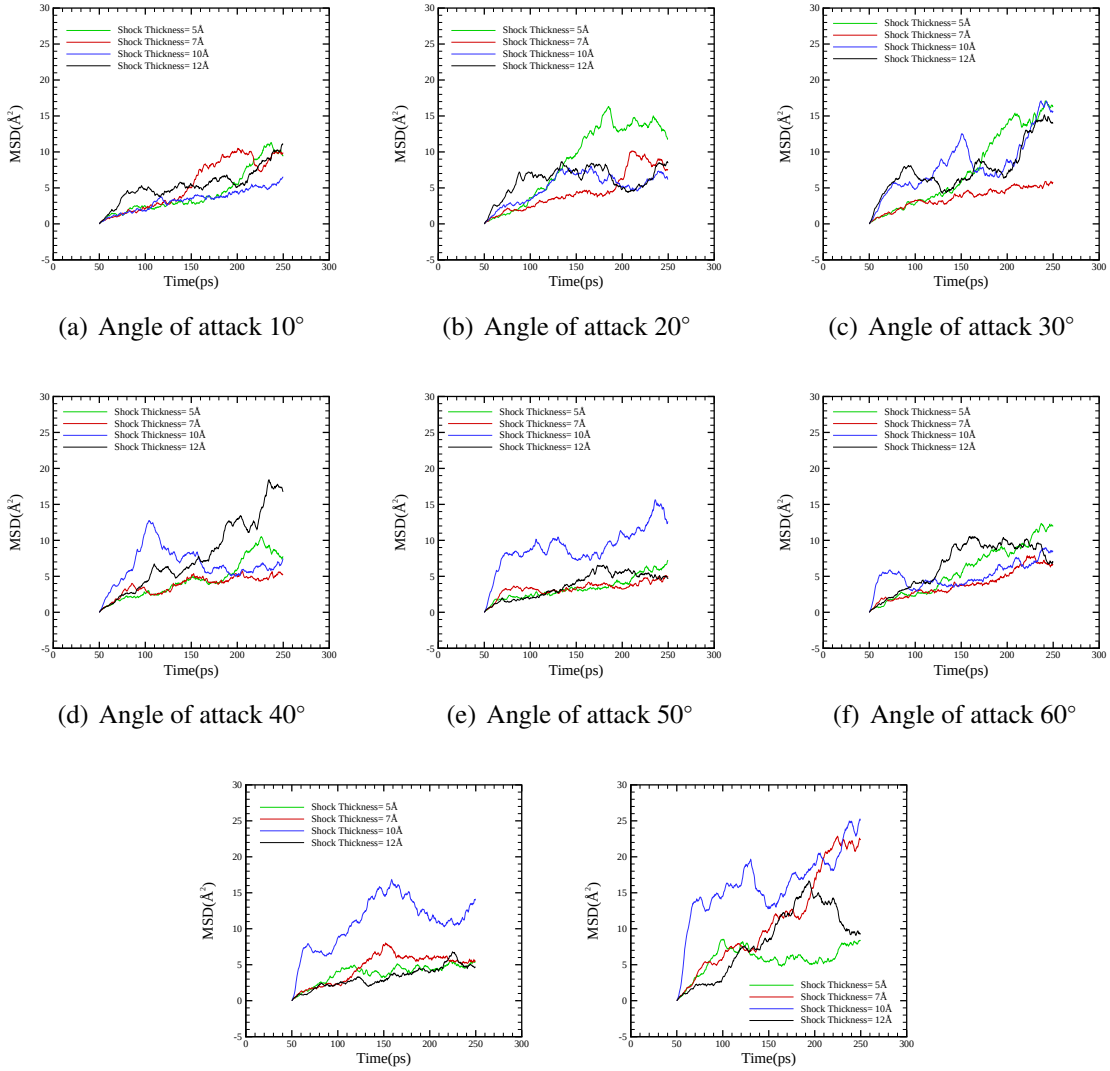

(a) Angle of attack 10° (b) Angle of attack 20° (c) Angle of attack 30°

(d) Angle of attack 40° (e) Angle of attack 50° (f) Angle of attack 60°

(g) Angle of attack 70° (h) Angle of attack 80°

Figure 5.33: Shock wave effects on MSD of the membrane at various shock wave thicknesses and angles of attack when the impulse is $0.33mPa \cdot s$

principal, stronger impulses with a greater thickness tend to cause more displacement to the lipids of the membrane, as explained earlier. This can be particularly observed when the angle of attack is 60° and the impulse is $0.66mPa \cdot s$.

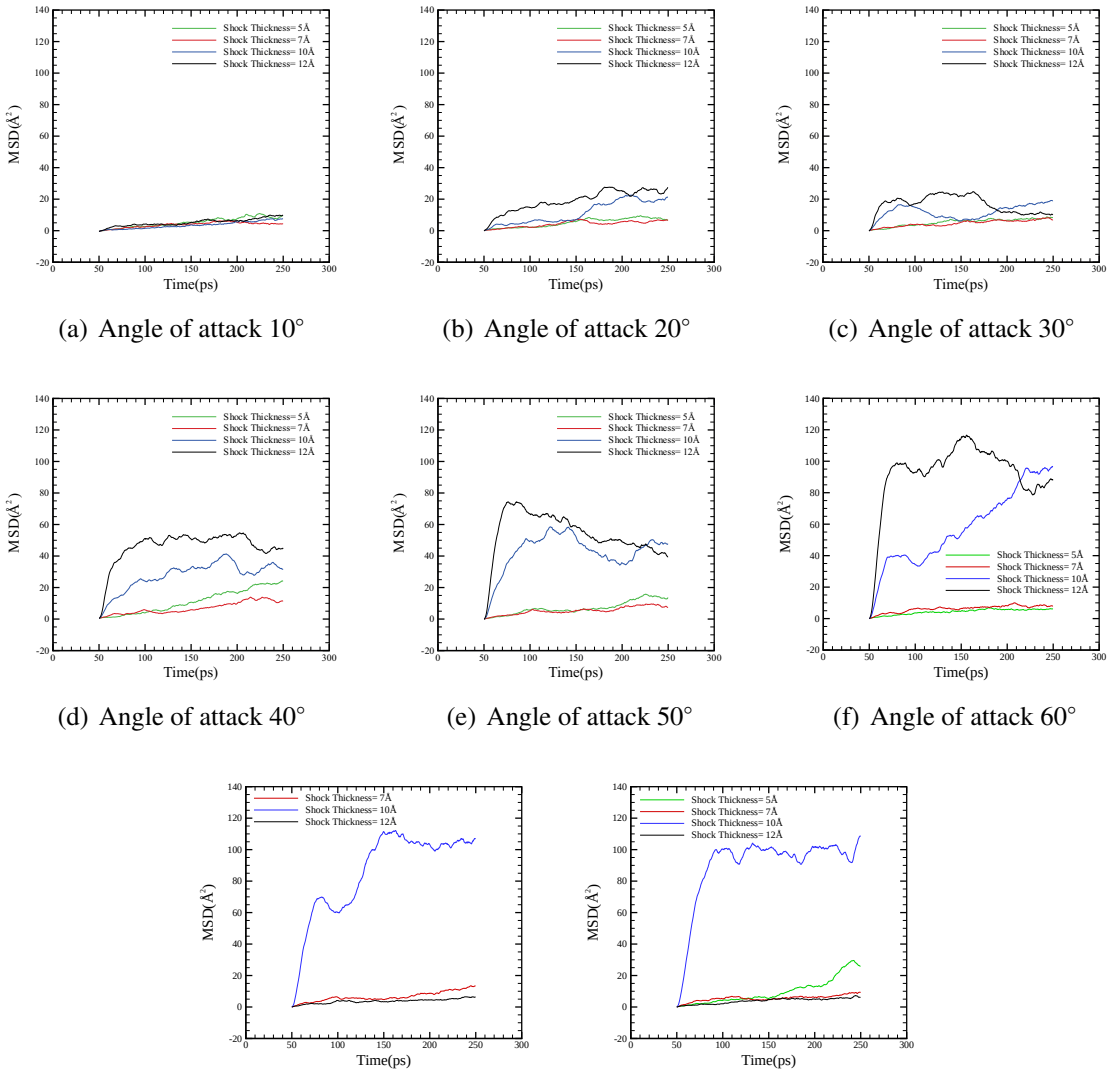

(a) Angle of attack 10° (b) Angle of attack 20° (c) Angle of attack 30°

(d) Angle of attack 40° (e) Angle of attack 50° (f) Angle of attack 60°

(g) Angle of attack 70° (h) Angle of attack 80°

Figure 5.34: Shock wave effects on MSD of the membrane at various shock wave thicknesses and angles of attack when the impulse is $0.66 mPa \cdot s$

At the same time, it is apparent that small angles, as analysed in the section of the kinetic energy of the system, are only able to put the waters into motion and therefore a delay appears in the slope of the MSD towards increasing. Such a phenomenon is particularly apparent when the impulse of the shock is $0.66 mPa \cdot s$ and the incidence angle is 10° or 20°. The following plots, 5.35 - 5.38, present the MSD of the upper layer of the membrane and the lower layer separately each time. The tendency that is observed is that, in general, both layers follow a similar trend to the one that describes the whole membrane.

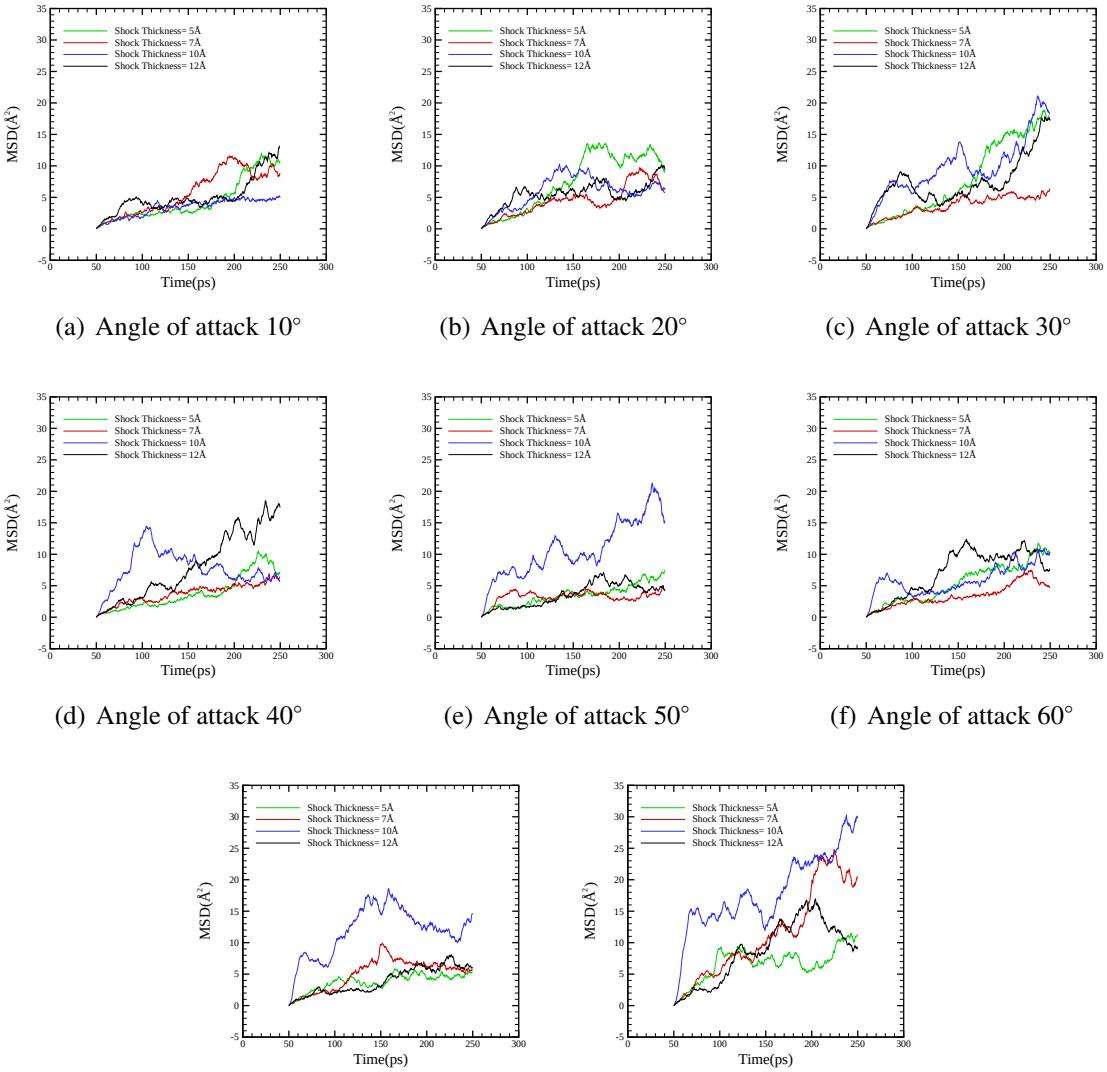

(a) Angle of attack 10° (b) Angle of attack 20° (c) Angle of attack 30°

(d) Angle of attack 40° (e) Angle of attack 50° (f) Angle of attack 60°

(g) Angle of attack 70° (h) Angle of attack 80°

Figure 5.35: Shock wave effects on MSD of the upper bilayer at various shock wave thicknesses and angles of attack when the impulse is $0.33 mPa \cdot s$

However, the upper layer gives an even closer representation of what happens in the membrane when the shock is first applied. It is noticed that when the angle of attack is 50°, or 80° and the shock impulse and thickness $0.66 mPa \cdot s$ and 10Å, respectively. There is a significantly large slope of the MSD over time, expressed by the corresponding values of diffusion coefficient ($0.07 \cdot 10^{-7} cm^2 s^{-1}$, $0.39 \cdot 10^{-7} cm^2 s^{-1}$ and $0.23 \cdot 10^{-7} cm^2 s^{-1}$ respectively). For the same impulse and shock thickness, the corresponding values of diffusion coefficient for the upper and lower layer are $0.08 \cdot 10^{-7} cm^2 s^{-1}$, $0.42 \cdot 10^{-7} cm^2 s^{-1}$, $0.18 \cdot 10^{-7} cm^2 s^{-1}$ and $0.06 \cdot 10^{-7} cm^2 s^{-1}$, $0.36 \cdot 10^{-7} cm^2 s^{-1}$, $0.28 \cdot 10^{-7} cm^2 s^{-1}$, respectively. Figures 5.39 - 5.40 present the lateral diffusion of the lipids of the whole membrane model, the upper layer, and the lower layer against the shock impulse when the NVE ensemble is used.

The following figures, 5.43 - 5.46, present the lateral diffusion of the lipids of the whole membrane model, the upper layer, and the lower layer against the shock angle of attack when the ensemble used is the NVE.

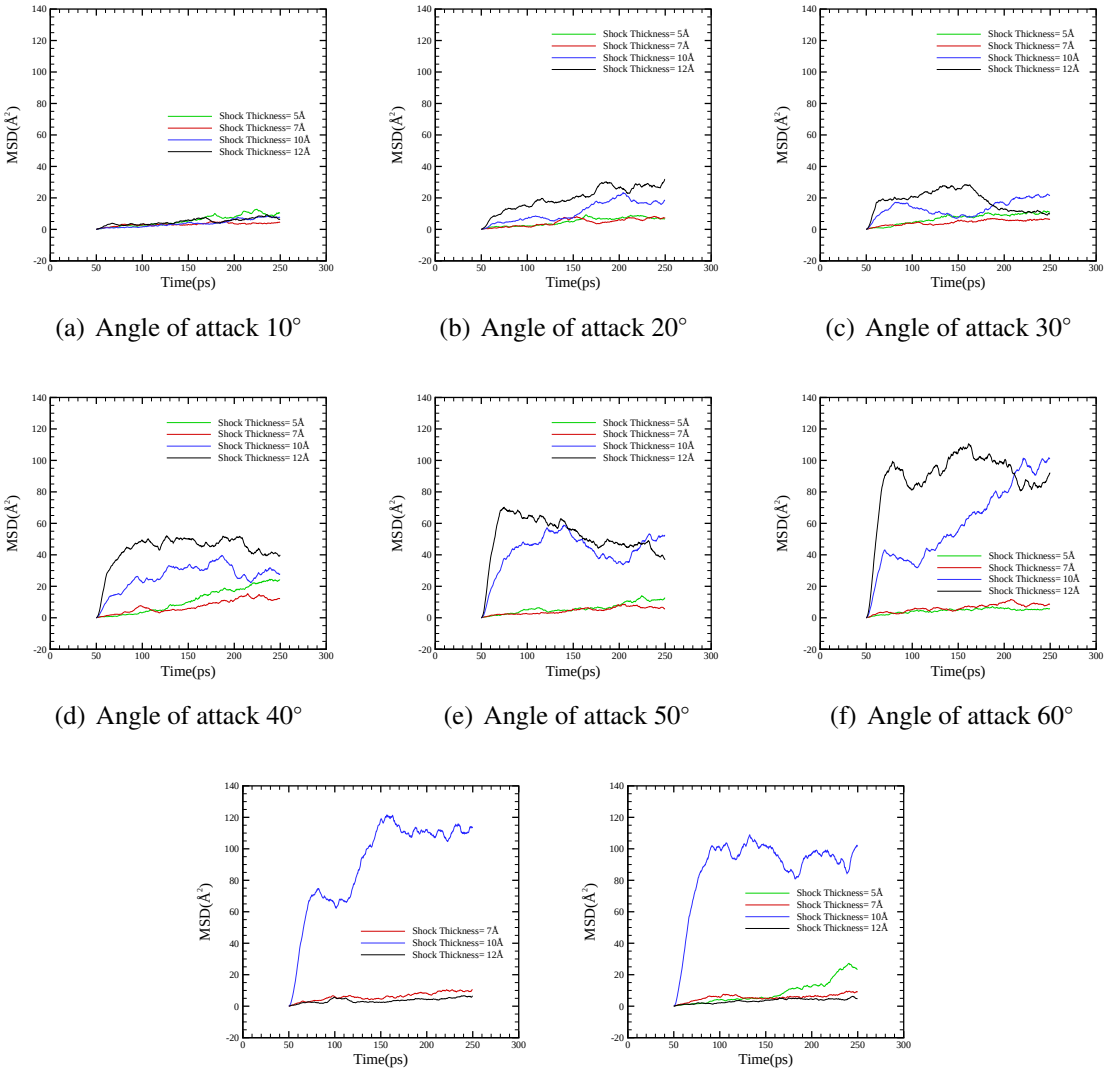

(a) Angle of attack 10° (b) Angle of attack 20° (c) Angle of attack 30°

(d) Angle of attack 40° (e) Angle of attack 50° (f) Angle of attack 60°

(g) Angle of attack 70° (h) Angle of attack 80°

Figure 5.36: Shock wave effects on MSD of the upper bilayer at various shock wave thicknesses and angles of attack when the impulse is $0.66 mPa \cdot s$

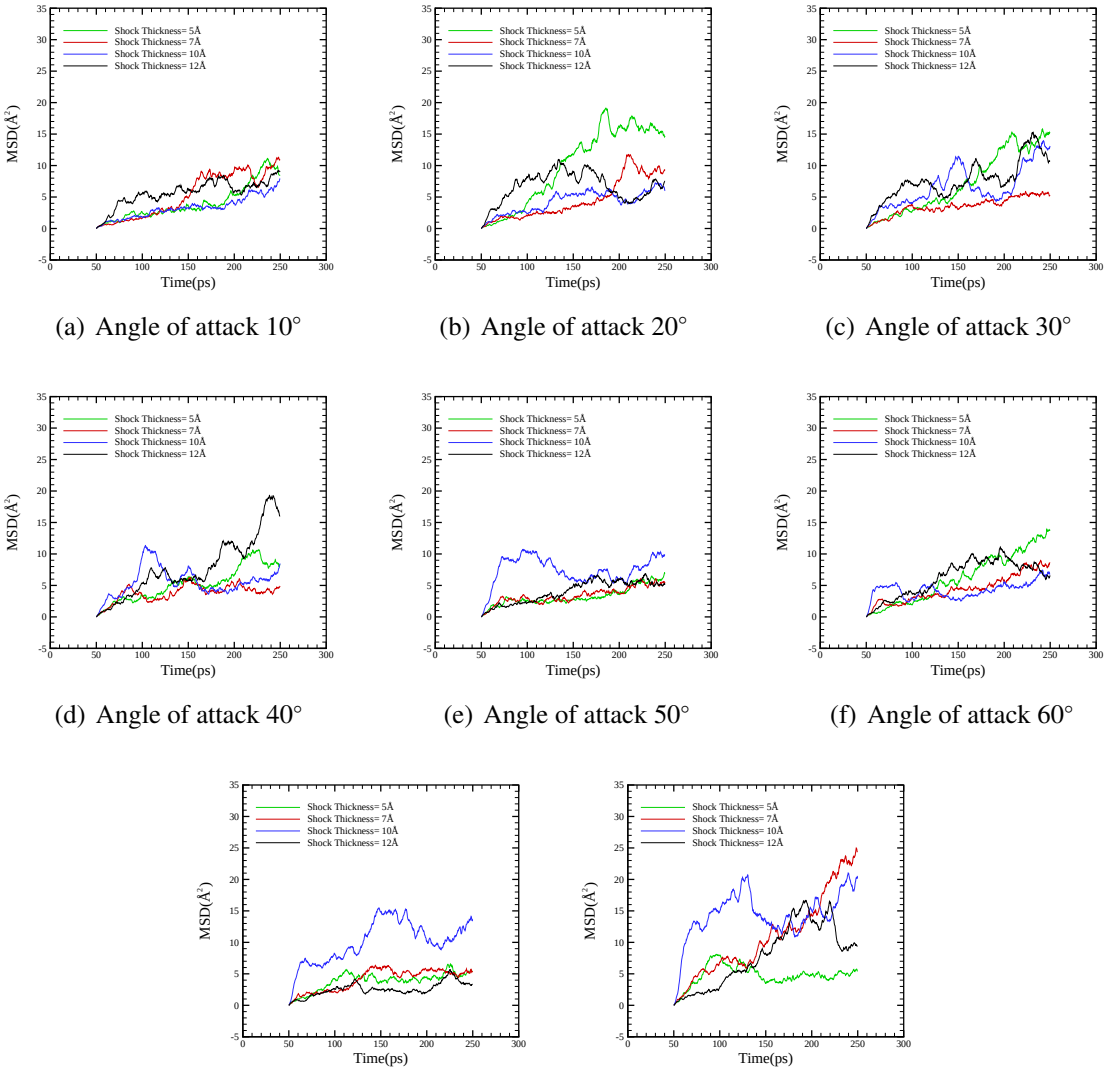

(a) Angle of attack 10° (b) Angle of attack 20° (c) Angle of attack 30°

(d) Angle of attack 40° (e) Angle of attack 50° (f) Angle of attack 60°

(g) Angle of attack 70° (h) Angle of attack 80°

Figure 5.37: Shock wave effects on MSD of the lower bilayer at various shock wave thicknesses and angles of attack when the impulse is $0.33 mPa \cdot s$

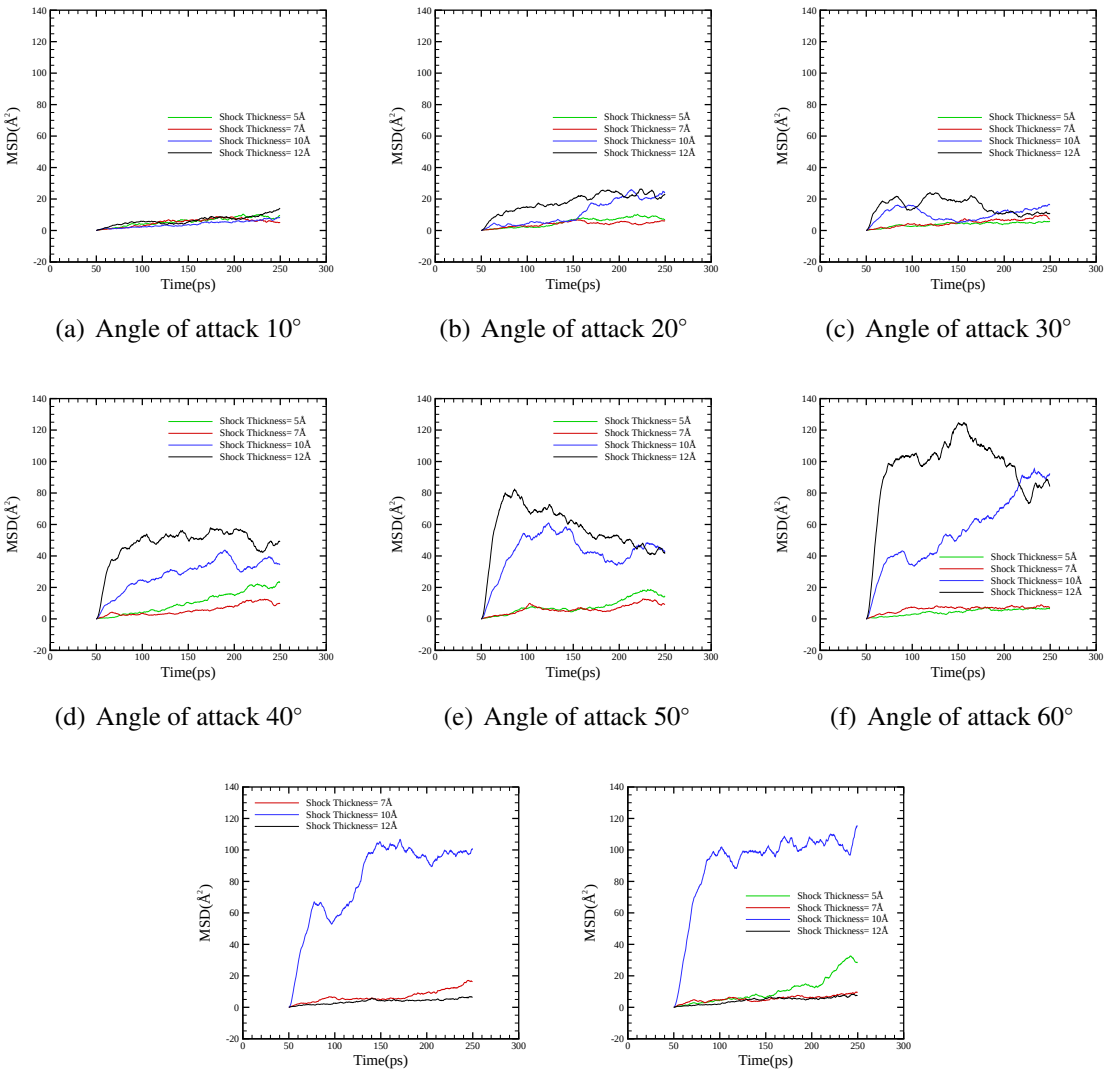

(a) Angle of attack 10° (b) Angle of attack 20° (c) Angle of attack 30°

(d) Angle of attack 40° (e) Angle of attack 50° (f) Angle of attack 60°

(g) Angle of attack 70° (h) Angle of attack 80°

Figure 5.38: Shock wave effects on MSD of the lower bilayer at various shock wave thicknesses and angles of attack when the impulse is $0.66 mPa \cdot s$

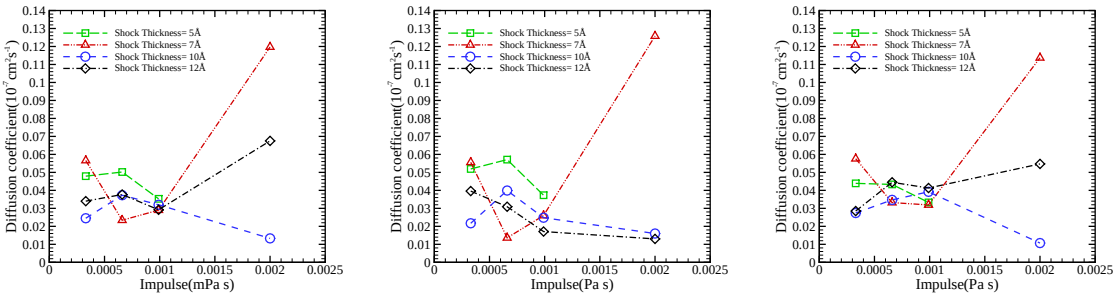

(a) Whole lipid bilayer (b) Upper lipid bilayer (c) Lower lipid bilayer

Figure 5.39: Diffusion coefficient as function of impulse at various shock wave thicknesses when the angle of attack is 10°

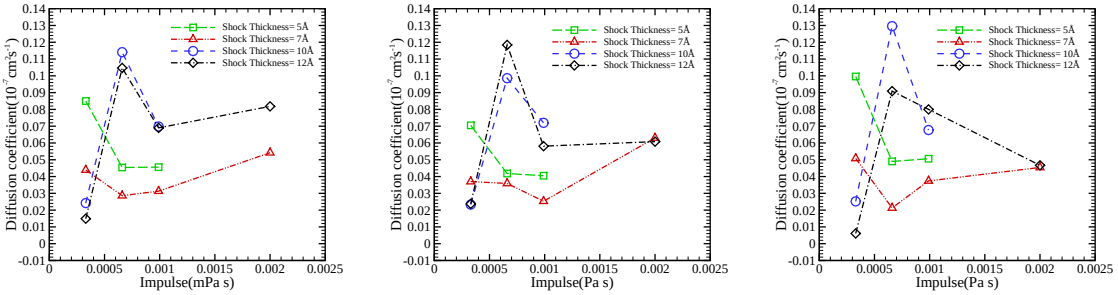

(a) Whole lipid bilayer (b) Upper lipid bilayer (c) Lower lipid bilayer

Figure 5.40: Diffusion coefficient as function of impulse at various shock wave thicknesses when the angle of attack is 20°

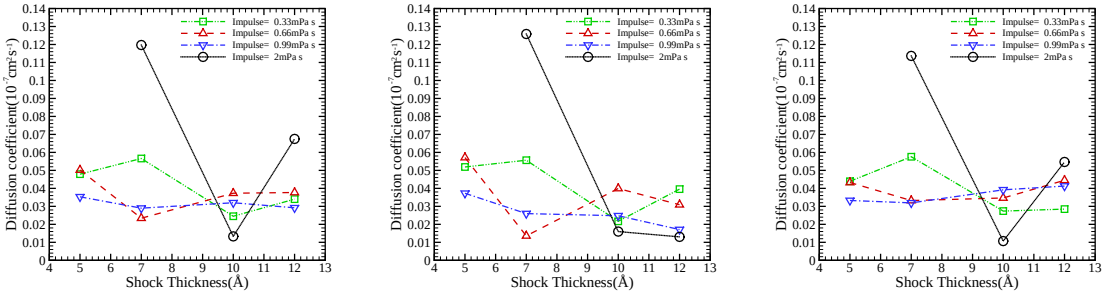

(a) Whole lipid bilayer (b) Upper lipid bilayer (c) Lower lipid bilayer

Figure 5.41: Diffusion coefficient as function of shock wave thickness at various impulses when the angle of attack is 10°

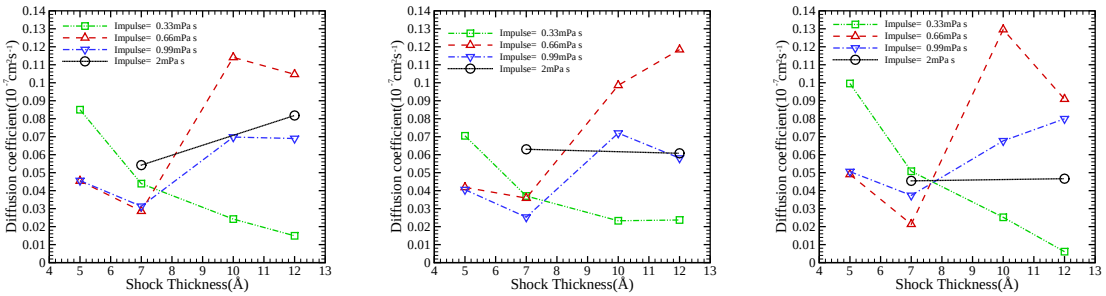

(a) Whole lipid bilayer (b) Upper lipid bilayer (c) Lower lipid bilayer

Figure 5.42: Diffusion coefficient as function of shock wave thickness at various impulses when the angle of attack is 20°

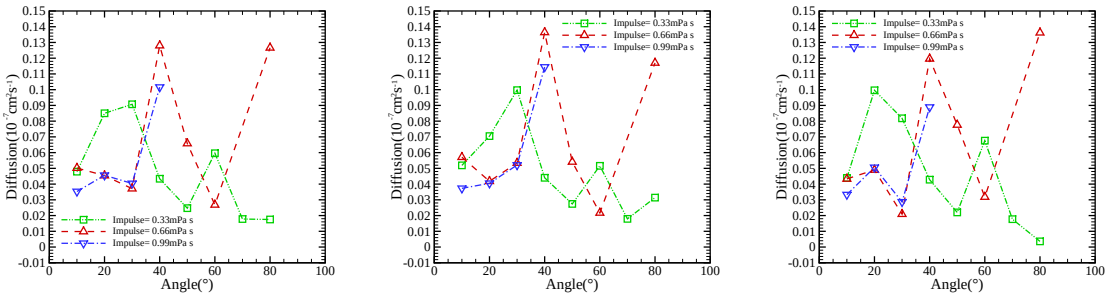

(a) Whole lipid bilayer (b) Upper lipid bilayer (c) Lower lipid bilayer

Figure 5.43: Relation between the diffusion coefficient and the angle of attack while the shock wave thickness is 5Å

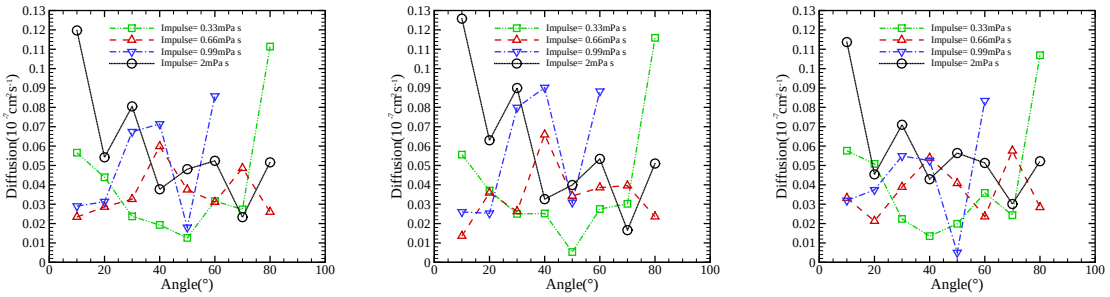

(a) Whole lipid bilayer (b) Upper lipid bilayer (c) Lower lipid bilayer

Figure 5.44: Relation between the diffusion coefficient and the angle of attack while the shock wave thickness is 7Å

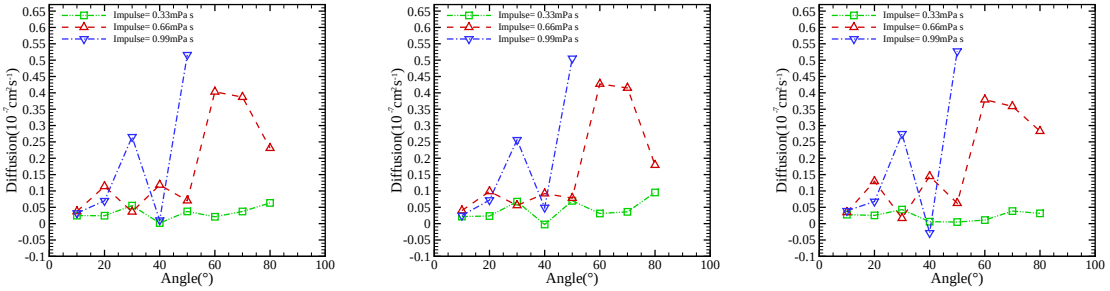

(a) Whole lipid bilayer (b) Upper lipid bilayer (c) Lower lipid bilayer

Figure 5.45: Relation between the diffusion coefficient and the angle of attack while the shock wave thickness is 10Å

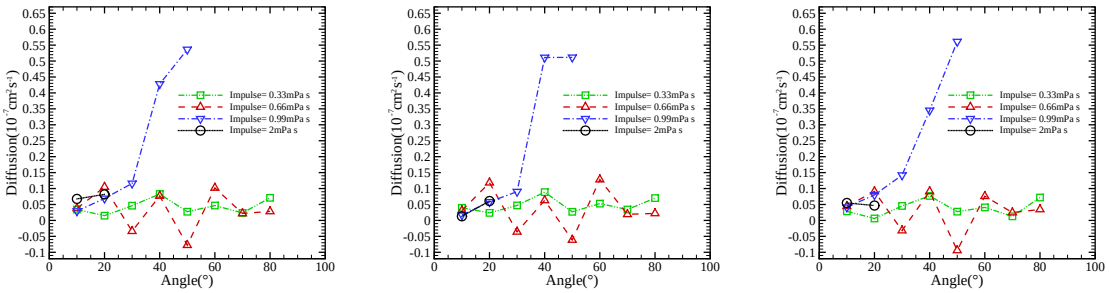

(a) Whole lipid bilayer (b) Upper lipid bilayer (c) Lower lipid bilayer

Figure 5.46: Relation between the diffusion coefficient and the angle of attack while the shock wave thickness is 12Å

5.3 Conclusions

In the present study attention has been drawn to the effects of oblique shock waves to the lateral diffusion coefficient of a POPC membrane. As the incidence angle is introduced an initial increase of the diffusion is observed due to the increase of the parallel velocity component as the shock is applied. The shock thickness is another characteristic of the shockwave that affects the amount of momentum propagated from the water molecules to the membrane. As the thickness of the shock becomes larger the diffusion coefficient initially increases until a maximum value is obtained following by a small decay.

Although the present study may present similar elements to Koshiyama et al. 2008 [107], it has entirely different focus. The work published by Koshiyama is primarily focused on visualising the response of the membrane after the application of the shock wave. In our present study we draw attention for the first time on the effect of the impulse thickness and how this parameter, which is crucial and has practical meaning affects the results. Furthermore, we study the combined effect of shock thickness and incidence angle that has been studied in the literature and we do not focused only on visual remarks regarding the membrane's response but we compute the increase of the lipids mobility that is directly related with the efficiency of the drug delivery.

The simulations were run for a great range of impulses, shock thicknesses and angles of attack in accordance with the NPT and the NVE ensemble separately. In earlier studies, the shock thickness effects on each monolayer and the membrane properties such as the kinetic energy, the centre of mass, the MSD over time, and the diffusion coefficient, were not examined. At the same time, regarding the effect of the oblique shocks the angles that were previously studied [107] were only 30° and 60°. In the current study we introduced angles varying from 10° to 80° at an interval of 10°. Lateral fluidity of a POPC membrane was measured through the use of diffusion coefficients as opposed to accumulated lateral displacement of a DPPC membrane that was studied by other authors [11].

It has been shown that diffusion coefficients that resulted from simulations run with NVE were greater in value that those obtained under the NPT ensemble. This is because in the NVE ensemble the total energy of the system is conserved, resulting in a larger proportion of the momentum impulse transferred to the membrane. On the contrary, for the NPT case, the system is not isolated from its environment, and velocity dumping is carried out through the thermostats in order to maintain a constant temperature, therefore leading therefore to smaller amounts of energy, momentum transfer, and diffusion coefficient values.

Furthermore, it was found that the lateral displacement, as expressed by the diffusion coefficient values, of the lower layer are one order of magnitude smaller than those concerning the whole membrane and the upper monolayer only, which agrees with previous studies [107].

Concluding, additional studies have to be performed aiming to study the response of more complicated membrane models where proteins are also considered. Defining the self diffusion coefficients of the surface proteins will have a great contribution towards a better understanding of mechanisms for optimising the drug delivery and drug adsorption.

CHAPTER 6

Conclusions and Future work

6.1 Conclusions

This report examined the impact of shock thickness and incidence angle on a 1-palmitoyl-2-oleoyl-sn-glycero-3-phosphocholine (POPC) lipid bilayer consisted of 104 lipids, 15134 water molecules, and 59338 atoms in total, indicating the following:

- Significant dependance between the thickness of the shock and the diffusion coefficient, which increases as the thickness of the shock increases until a maximum value is obtained and then follows a small decay
- In overall, when using an NVE ensemble, higher diffusion coefficients are yielded in compaarison to the NPT ensemble
- As the incidence angle is introduced an initial increase of lateral diffusion is observed due to the increase of the parallel to the wall shock's velocity components
- Smaller shock thicknesses may lead to higher momentum and thus kinetic energy for the molecules of the water-membrane system for a given shock impulse
- As the angle of attack increases the lateral diffusion coefficient tends to increases, in principal
- greater impulses imply greater kinetic energy via momentum transfer.
- Smaller angle of attack in principal leads to greater decrease of the thickness of the membrane.

6.2 Future Work

Additional studies have to be performed aiming to study the response of more complicated membrane models where proteins are also considered. Defining the self diffusion coefficients of the surface proteins will have a great contribution towards a better understanding of the mechanisms for optimising the drug delivery and drug adsorption. In particular, this study could be further enhanced by:

- Examining the response of different membrane models, such as DPPC, POPE and so on
- Applying the same conditions to membrane models consisted of proteins and lipids
- Investigating the effect of the same configurations on asymmetric lipid bilayers.
- Combining the study with a model cancer cell membrane of few Å to measure the biological response.
- Further studying the phenomenon of rebounding of the membrane by increasing the simulation time
- Acquiring a more robust representation of the lateral mobility of the lipids by measuring the lipid MSD and diffusion coefficients within separate periods of simulation time, as these are now defined in the plots of this study
- Studying the biological response of the membrane to a shock applied with an angle of attack equal to 45°.

Bibliography

[1] Wikipedia. Cell membrane. http://en.wikipedia.org/wiki/Cell_membrane. Accessed: 25/07/2011.

[2] T. D. Pollard, W. C. Earnshaw, and J. Lippincott-Schwartz. *Cell Biology, 2nd ed.* Saunders Elsevier, Philadelphia, 2008.

[3] R.D. Porasso and J.J. Lopez Cascales. Study of the effect of na+ and ca2+ ion concentration on the structure of an asymmetric dppc/dppc + dpps lipid bilayer by molecular dynamics simulation. *Colloids and Surfaces B: Biointerfaces*, 73(1):42–50, 2009.

[4] K. Takayama. Applications of shock wave research to medicine. *International Symposium on Shock Waves*, 2010:23–32, 1999.

[5] Feril Jr., L.B., T. Kondo, S.I. Umemura, K. Tachibana, A.H. Manalo, and P. Riesz. Sound waves and antineoplastic drugs: The possibility of an enhanced combined anticancer therapy. *Journal of Medical Ultrasonics*, 29(WINTER):173–187, 2002.

[6] D.P. Tieleman. The molecular basis of electroporation. *BMC Biochemistry*, 5:1–12, 2004.

[7] M. Tarek. Membrane electroporation: A molecular dynamics simulation. *Biophysical Journal*, 88(6):4045–4053, 2005.

[8] A.A. Gurtovenko and I. Vattulainen. Pore formation coupled to ion transport through lipid membranes as induced by transmembrane ionic charge imbalance: Atomistic molecular dynamics study. *Journal of the American Chemical Society*, 127(50): 17570–17571, 2005.

[9] T. Kodama, A. Aoi, G. Vassaux, S. Mori, H. Morikawa, K. C. Koshiyama, T. Yano, S. Fujikawa, and Y. Tomita. A non-invasive tissue-specific molecular delivery method of cancer gene therapy. *Minimally Invasive Therapy and Allied Technologies*, 15(4):226–229, 2006.

[10] J. Liu, Lewis T.N., and M.R. Prausnitz. Non-invasive assessment and control of ultrasound-mediated membrane permeabilization. *Pharmaceutical Research*, 15(6): 918–924, 1998.

[11] K. Koshiyama, T. Kodama, T. Yano, and S. Fujikawa. Structural change in lipid bilayers and water penetration induced by shock waves: Molecular dynamics simulations. *Biophysical Journal*, 91(6):2198–2205, 2006.

[12] M. Suzuki, K. Koshiyama, F. Shinohara, S. Mori, M. Ono, Y. Tomita, T. Yano, S. Fujikawa, G. Vassaux, and T. Kodama. Nanobubbles enhanced drug susceptibility of cancer cells using ultrasound. *International Congress Series*, 1284:338–339, 2005.

[13] T. Kodama, M.R. Hamblin, and A.G. Doukas. Cytoplasmic molecular delivery with shock waves: Importance of impulse. *Biophysical Journal*, 79(4):1821–1832, 2000.

[14] University of Massachusetts Lowell. part i. strategy for running molecular dynamics simulations. `http://faculty.uml.edu/vbarsegov/teaching/bioinformatics/lectures/MDSimulationsModified.pdf`. Accessed: 10/11/2011.

[15] D. Sourmaidou, S. Dufourmantelle, N. Asproulis, D. Drikakis, and S. Pal. Oblique shock wave effects on biological membranes. *3rd Micro and Nano Flows Conference*, August 2011.

[16] R. W. Ruddon. *Cancer Biology, 4th ed*. Oxford University Press, New York, 2007.

[17] T. Schafer, U.O. Karli, E.K.-M. Gratwohl, F.E. Schweizer, and M.M. Burger. Digitonin-permeabilized cells are exocytosis competent. *Journal of Neurochemistry*, 49(6):1697–1707, 1987.

[18] D.G. Spiller, R.V. Giles, J. Grzybowski, D.M. Tidd, and R.E. Clark. Improving the intracellular delivery and molecular efficacy of antisense oligonucleotides in chronic myeloid leukemia cells: A comparison of streptolysin-o permeabilization, electroporation, and lipophilic conjugation. *Blood*, 91(12):4738–4746, 1998.

[19] Y. Kaneda. Development of a novel fusogenic viral liposome system (hvj-liposomes) and its applications to the treatment of acquired diseases. *Molecular Membrane Biology*, 16(1):119–122, 1999.

[20] S.Y. Ho and G.S. Mittal. Electroporation of cell membranes: A review. *Critical Reviews in Biotechnology*, 16(4):349–362, 1996.

[21] D.L. Miller, S. Bao, and J.E. Morris. Sonoporation of cultured cells in the rotating tube exposure system. *Ultrasound in Medicine and Biology*, 25(1):143–149, 1999.

[22] S. Gambihler, M. Delius, and J.W. Ellwart. Permeabilization of the plasma membrane of l1210 mouse leukemia cells using lithotripter shock waves. *Journal of Membrane Biology*, 141(3):267–275, 1994.

[23] M. Delius and G. Adams. Shock wave permeabilization with ribosome inactivating proteins: A new approach to tumor therapy. *Cancer Research*, 59(20):5227–5232, 1999.

[24] S. Lee and A.G. Doukas. Laser-generated stress waves and their effects on the cell membrane. *IEEE Journal on Selected Topics in Quantum Electronics*, 5(4):997–1003, 1999.

[25] S. Zhu, T. Dreyer, M. Liebler, R. Riedlinger, G.M. Preminger, and P. Zhong. Reduction of tissue injury in shock-wave lithotripsy by using an acoustic diode. *Ultrasound in Medicine and Biology*, 30(5):675–682, 2004.

[26] Christopher P. Fall. *Computational cell biology*. Springer, 2002.

[27] H. Lodish, A. Berk, S. L. Zipursky, P. Matsudaira, D. Baltimore, and J. Darnell. *Molecular Cell Biology, 4th ed.* W. H. Freeman, New York, 2000.

[28] William H. Elliott. *Biochemistry and molecular biology*. Oxford University Press, 2004.

[29] T. D. Pollard and W. C. Earnshaw. *Cell Biology*. Saunders Elsevier, 2002.

[30] S.J. Singer and G.L. Nicolson. The fluid mosaic model of the structure of cell membranes. *Science*, 175(4023):720–731, 1972.

[31] S.-J. Marrink and H.J.C. Berendsen. Simulation of water transport through a lipid membrane. *Journal of Physical Chemistry*, 98(15):4155–4168, 1994.

[32] R.O. Hynes. Cell surface proteins and malignant transformation. *Biochimica et Biophysica Acta*, 458(1):73–107, 1976.

[33] W. Bernhard. Electron microscopy of tumor cells and tumor viruses; a review. *Cancer research*, 18(5):491–509, 1958.

[34] M. Abercrombie and E.J. Ambrose. The surface properties of cancer cells: a review. *Cancer research*, 22:525–548, 1962.

[35] R.E. Scott and L.T. Furcht. Membrane pathology of normal and malignant cells: a review. *Human Pathology*, 7(5):519–532, 1976.

[36] K. Kohri, T. Uemura, M. Iguchi, and T. Kurita. Effect of high shock waves on tumor cells. *Urological Research*, 18(2):101–105, 1990.

[37] M. Kambe, N. Ioritani, and R. Kanamaru. Enhancement of chemotherapeutic effects with focused shock waves: extracorporeal shock wave chemotherapy (eswc). *Human cell : official journal of Human Cell Research Society*, 10(1):87–94, 1997.

[38] K.K. Jain. Editorial: Targeted drug delivery for cancer. *Technology in Cancer Research and Treatment*, 4(4):311–313, 2005.

[39] Y. Shamay, L. Adar, G. Ashkenasy, and A. David. Light induced drug delivery into cancer cells. *Biomaterials*, 32(5):1377–1386, 2011.

[40] Z. Liu, J.T. Robinson, S.M. Tabakman, K. Yang, and H. Dai. Carbon materials for drug delivery and cancer therapy. *Materials Today*, 14(7-8):316–323, 2011.

[41] N. Sanoj Rejinold, M. Muthunarayanan, V.V. Divyarani, P.R. Sreerekha, K.P. Chennazhi, S.V. Nair, H. Tamura, and R. Jayakumar. Curcumin-loaded biocompatible thermoresponsive polymeric nanoparticles for cancer drug delivery. *Journal of Colloid and Interface Science*, 360(1):39–51, 2011.

[42] C. Alexiou, R. Tietze, E. Schreiber, and S. Lyer. Nanomedicine. magnetic nanoparticles for drug delivery and hyperthermia - new chances for cancer therapy [pharmakotherapie mittels nanomedizin. magnetische nanopartikel fur drug delivery und hyperthermie - neue chancen fur die krebsbehandlung]. *Onkologe*, 17(5):405–412, 2011.

[43] J. Teissie, N. Eynard, B. Gabriel, and M. P. Rols. Electropermeabilization of cell membranes. *Advanced Drug Delivery Reviews*, 35(1):3 – 19, 1999.

[44] J. C. Weaver. Electroporation of cells and tissues, 2000. in Bronzino, J. D. (ed.) The Biomedical Engineering Handbook: Second Edition. CRC Press LLC, Boca Raton.

[45] S. Mehier-Humbert and R.H. Guy. Physical methods for gene transfer: Improving the kinetics of gene delivery into cells. *Advanced Drug Delivery Reviews*, 57(5): 733–753, 2005.

[46] M. Hibino, M. Shigemori, H. Itoh, K. Nagayama, Kinosita Jr., and K. Membrane conductance of an electroporated cell analyzed by submicrosecond imaging of transmembrane potential. *Biophysical Journal*, 59(1):209–220, 1991.

[47] J. Teissie and M.-P. Rols. An experimental evaluation of the critical potential difference inducing cell membrane electropermeabilization. *Biophysical Journal*, 65(1): 409–413, 1993.

[48] J. Teissie and M.-P. Rols. Manipulation of cell cytoskeleton affects the lifetime of cell membrane electropermeabilization. *Annals of the New York Academy of Sciences*, 720(1):98–110, 1994. ISSN 1749-6632.

[49] M.-P. Rols and J. Teissie. Modulation of electrically induced permeabilization and fusion of chinese hamster ovary cells by osmotic pressure. *Biochemistry*, 29(19): 4561–4567, 1990.

[50] M.P. Rols, F. Dahhou, K.P. Mishra, and J. Teissie. Control of electric field induced cell membrane permeabilization by membrane order. *Biochemistry*, 29(12):2960–2966, 1990.

[51] I.G. Abidor, V.B. Arakelyan, and L.V. Chernomordik. Electric breakdown of bilayer lipid membranes. i. the main experimental facts and their qualitative discussion. *Bioelectrochemistry and Bioenergetics*, 6(1):37–52, 1979.

[52] L.V. Chernomordik, S.I. Sukharev, I.G. Abidor, and Yu.A. Chizmadzhev. Breakdown of lipid bilayer membranes in an electric field. *BBA - Biomembranes*, 736(2): 203–213, 1983.

[53] L.V. Chernomordik, S.I. Sukharev, S.V. Popov, V.F. Pastushenko, A.V. Sokirko, I.G. Abidor, and Y.A. Chizmadzhev. The electrical breakdown of cell and lipid membranes: the similarity of phenomenologies. *BBA - Biomembranes*, 902(3):360–373, 1987.

[54] J.C. Weaver, K.T. Powell, R.A. Mintzer, H. Ling, and S.R. Sloan. The electrical capacitance of bilayer membranes. the contribution of transient aqueous pores. *Bioelectrochemistry and Bioenergetics*, 12(3-4):393–404, 1984.

[55] W. Arap, R. Pasqualini, and E. Ruoslahti. Cancer treatment by targeted drug delivery to tumor vasculature in a mouse model. *Science*, 279(5349):377–380, 1998.

[56] M.-P. Rols, C. Delteil, M. Golzio, P. Dumond, S. Gros, and J. Teissie. In vivo electrically mediated protein and gene transfer in murine melanoma. *Nature Biotechnology*, 16(2):168–171, 1998.

[57] J. Alper. Drug delivery: Breaching the membrane. *Science*, 296(5569):838–839, 2002.

[58] M. Golzio, J. Teissie, and M.-P. Rols. Direct visualization at the single-cell level of electrically mediated gene delivery. *Proceedings of the National Academy of Sciences of the United States of America*, 99(3):1292–1297, 2002.

[59] J. Olofsson, K. Nolkrantz, F. Ryttsen, B.A. Lambie, S.G. Weber, and O. Orwar. Single-cell electroporation. *Current Opinion in Biotechnology*, 14(1):29–34, 2003.

[60] R. Langer. Drug delivery and targeting. *Nature*, 392(6679 SUPPL):5–10, 1998.

[61] A. Diederich, G. Bahr, and M. Winterhalter. Influence of surface charges on the rupture of black lipid membranes. *Phys. Rev. E*, 58(4):4883–4889, Oct 1998.

[62] S. Koronkiewicz and S. Kalinowski. Influence of cholesterol on electroporation of bilayer lipid membranes: Chronopotentiometric studies. *Biochimica et Biophysica Acta - Biomembranes*, 1661(2):196–203, 2004.

[63] I. Genco, A. Gliozzi, A. Relini, M. Robello, and E. Scalas. Electroporation in symmetric and asymmetric membranes. *Biochimica et Biophysica Acta (BBA) - Biomembranes*, 1149(1):10 – 18, 1993. ISSN 0005-2736.

[64] D.P. Tieleman, H. Leontiadou, A.E. Mark, and S.-J. Marrink. Simulation of pore formation in lipid bilayers by mechanical stress and electric fields. *Journal of the American Chemical Society*, 125(21):6382–6383, 2003.

[65] H. Leontiadou, A.E. Mark, and S.J. Marrink. Molecular dynamics simulations of hydrophilic pores in lipid bilayers. *Biophysical Journal*, 86(4):2156–2164, 2004.

[66] A.G. Doukas, D.J. McAuliffe, S. Lee, V. Venugopalan, and T.J. Flotte. Physical factors involved in stress-wave-induced cell injury: The effect of stress gradient. *Ultrasound in Medicine and Biology*, 21(7):961–967, 1995.

[67] Wang Li-li Yang Li-ming, Zhou Feng-hua. *Foundations of Stress Waves*, chapter Chapter 1 - Introduction, pages 1–6. Elsevier, 2007.

[68] S. Bao, B.D. Thrall, and D.L. Miller. Transfection of a reporter plasmid into cultured cells by sonoporation in vitro. *Ultrasound in Medicine and Biology*, 23(6):953–959, 1997.

[69] D.L. Miller and C. Dou. Membrane damage thresholds for pulsed or continuous ultrasound in phagocytic cells loaded with contrast agent gas bodies. *Ultrasound in Medicine and Biology*, 30(3):405–411, 2004.

[70] A.G. Doukas and T.J. Flotte. Physical characteristics and biological effects of laser-induced stress waves. *Ultrasound in Medicine and Biology*, 22(2):151–164, 1996.

[71] A.J. Coleman and J.E. Saunders. A review of the physical properties and biological effects of the high amplitude acoustic fields used in extracorporeal lithotripsy. *Ultrasonics*, 31(2):75–89, 1993.

[72] J. Song, D. Tata, L. Li, J. Taylor, S. Bao, and D.L. Miller. Combined shock-wave and immunogene therapy of mouse melanoma and renal carcinoma tumors. *Ultrasound in Medicine and Biology*, 28(7):957–964, 2002.

[73] M. Orsi and J. W. Essex. *Molecular simulations and biomembranes: from biophysics to function*, chapter Passive permeation across lipid bilayers: a literature review, pages 77–91. Royal Society of Chemistry, 2010.

[74] M. Orsi, J. W. Essex, R. Vijayan, B. Iorga, P. C. Biggin, O. I. Ollila, I. Vattulainen, J. L. Robertson, V. Jogini, B. Roux, P. C. Wen, Z Huang, G. Enkavi, E. Tajkhorshid, D. P. Tieleman, E. J. Wallace, M. S. P. Sansom, Y. Yin, A. Arkhipov, K. Schulten, S. Khalid, M. Baaden, M. B. Ulmschneider, J. P. Ulmschneider, S. Rouse, T. Carpenter, and M. S. P. Sans. *Molecular Simulations and Biomembranes*. RSC, 2010.

[75] W.-L. Tung, S.-H. Hu, and D.-M. Liu. Synthesis of nanocarriers with remote magnetic drug release control and enhanced drug delivery for intracellular targeting of cancer cells. *Acta Biomaterialia*, 7(7):2873–2882, 2011.

[76] T.-T. Wang, F. Chai, , C.-G. Wang, L. Li, Liu H.-Y., L.-Y. Zhang, Z.-M. Su, and Y. Liao. Fluorescent hollow/rattle-type mesoporous au@sio2 nanocapsules for drug delivery and fluorescence imaging of cancer cells. *Journal of Colloid and Interface Science*, 358(1):109–115, 2011.

[77] X. Li, Y. Qian, T. Liu, X. Hu, G. Zhang, Y. You, and S. Liu. Amphiphilic multiarm star block copolymer-based multifunctional unimolecular micelles for cancer targeted drug delivery and mr imaging. *Biomaterials*, 32(27):6595–6605, 2011.

[78] J.F. Nagle, J.C. Mathai, M.L. Zeidel, and S. Tristram-Nagle. Theory of passive permeability through lipid bilayers. *Journal of General Physiology*, 131(1):77–85, 2008.

[79] T.-X. Xiang and B.D. Anderson. Liposomal drug transport: A molecular perspective from molecular dynamics simulations in lipid bilayers. *Advanced Drug Delivery Reviews*, 58(12-13):1357–1378, 2006.

[80] P.G. LeFevre. Sugar transport in the red blood cell: structure-activity relationships in substrates and antagonists. *Pharmacological reviews*, 13:39–70, 1961.

[81] William Wurts. Membrane permeability, calcium, and osmotic pressure. In *An evaluation of specific ionic and growth parameters affecting the feasibility of commercially producing red drum (Sciaenops ocellatus)*. Doctoral dissertation. Texas A&M University, College Station, 1987.

[82] P.A. Brown and R.D. Berlin. Packing volume of sedimented microtubules: Regulation and potential relationship to an intracellular matrix. *Journal of Cell Biology*, 101(4):1492–1500, 1985.

[83] D.J. McAuliffe, Lee Shun, T.J. Flotte, and A.G. Doukas. Stress-wave-assisted transport through the plasma membrane in vitro. *Lasers in Surgery and Medicine*, 20(2): 216–222, 1997.

[84] T. X. Xiang and B.D. Anderson. The relationship between permeant size and permeability in lipid bilayer membranes. *Journal of Membrane Biology*, 140(2):111–122, 1994.

[85] T. X. Xiang and B. D. Anderson. Molecular distributions in interphases: Statistical mechanical theory combined with molecular dynamics simulation of a model lipid bilayer. *Biophysical Journal*, 66(3):561–573, 1994.

[86] J.T. Edward. Molecular volumes and the stokes-einstein equation. *Journal of Chemical Education*, 47(4):261–270, 1970.

[87] S. Lee, T. Anderson, H. Zhang, T.J. Flotte, and A.G. Doukas. Alteration of cell membrane by stress waves in vitro. *Ultrasound in Medicine and Biology*, 22(9): 1285–1293, 1996.

[88] A.G. Doukas, D.J. McAuliffe, and T.J. Flotte. Biological effects of laser-induced shock waves: Structural and functional cell damage in vitro. *Ultrasound in Medicine and Biology*, 19(2):137–146, 1993.

[89] T. J. Flotte, J. K. Frisoli, M. Goetschkes, and A. G. Doukas. Laser-induced shock wave effects on red blood cells. *Proceedings of SPIE - The International Society for Optical Engineering*, 1427:36–44, 1991.

[90] F.J. Thomas, T. Anderson, D. J. McAuliffe, T. Hasan, and A. G. Doukas. Laser-induced enhancement of drug cytotoxicity: a new approach to cancer therapy. *Proceedings of SPIE - The International Society for Optical Engineering*, 1882:122–129, 1993.

[91] TJ Flotte, S Lee, H Zhang, DJ McAuliffe, T Douki, and AG Doukas. Laser-induced stress waves: applications for molecular delivery. *Proceedings of SPIE - Laser-tissue interaction VI.*, 2391:202–207, 1995.

[92] R.P. Holmes, L.I. Yeaman, W.J. Li, L.J. Hart, C.A. Wallen, R.D. Woodruff, and D.L. McCullough. The combined effects of shock waves and cisplatin therapy on rat prostate tumors. *Journal of Urology*, 144(1):159–163, 1990.

[93] L. Kan-Ei, P. Smith, and A.T.K. Cockett. Influence of high-energy shock waves and cisplatin on antitumor effect in murine bladder cancer. *Urology*, 36(5):440–444, 1990.

[94] N. Weiss, M. Delius, S. Gambihler, H. Eichholtz-Wirth, P. Dirschedl, and W. Brendel. Effect of shock waves and cisplatin on cisplatin-sensitive and -resistant rodent tumors in vivo. *International Journal of Cancer*, 58(5):693–699, 1994.

[95] R.F. Randazzo, C.G. Chaussy, G.J. Fuchs, S.M. Bhuta, H. Lovrekovich, and J.B. DeKernion. The in vitro and in vivo effects of extracorporeal shock waves on malignant cells. *Urological Research*, 16(6):419–426, 1988.

[96] G.O.N. Oosterhof, G.A.H.J. Smits, A.E. De Ruyter, J.A. Schalken, and F.M.J. Debruyne. In vivo effects of high energy shock waves on urological tumors: An evaluation of treatment modalities. *Journal of Urology*, 144(3):785–789, 1990.

[97] R.P. Holmes, L.D. Yeaman, R.G. Taylor, and D.L. McCullough. Altered neutrophil permeability following shock wave exposure in vitro. *Journal of Urology*, 147(3 I): 733–737, 1992.

[98] S. Gambihler, M. Delius, and J.W. Ellwart. Transient increase in membrane permeability of l1210 cells upon exposure to lithotripter shock waves in vitro. *Naturwissenschaften*, 79(7):328–329, 1992.

[99] M. Delius, F. Ueberle, and S. Gambihler. Acoustic energy determines haemoglobin release from erythrocytes by extracorporeal shock waves in vitro. *Ultrasound in Medicine and Biology*, 21(5):707–710, 1995.

[100] U. Zimmermann. Electrical breakdown, electropermeabilization and electrofusion. *Reviews of Physiology Biochemistry and Pharmacology*, 105:176–256, 1986.

[101] J. Sundaram, B.R. Mellein, and S. Mitragotri. An experimental and theoretical analysis of ultrasound-induced permeabilization of cell membranes. *Biophysical Journal*, 84(5):3087–3101, 2003.

[102] S. Mehier-Humbert, T. Bettinger, F. Yan, and R.H. Guy. Plasma membrane poration induced by ultrasound exposure: Implication for drug delivery. *Journal of Controlled Release*, 104(1):213–222, 2005.

[103] S. Mehier-Humbert, T. Bettinger, F. Yan, and R.H. Guy. Ultrasound-mediated gene delivery: Kinetics of plasmid internalization and gene expression. *Journal of Controlled Release*, 104(1):203–211, 2005.

[104] O'Brien Jr. and W.D. Ultrasound-biophysics mechanisms. *Progress in Biophysics and Molecular Biology*, 93(1-3):212–255, 2007.

[105] D.L. Miller. Overview of experimental studies of biological effects of medical ultrasound caused by gas body activation and inertial cavitation. *Progress in Biophysics and Molecular Biology*, 93(1-3):314–330, 2007.

[106] E. VanBavel. Effects of shear stress on endothelial cells: Possible relevance for ultrasound applications. *Progress in Biophysics and Molecular Biology*, 93(1-3): 374–383, 2007.

[107] K. Koshiyama, T. Kodama, T. Yano, and S. Fujikawa. Molecular dynamics simulation of structural changes of lipid bilayers induced by shock waves: Effects of incident angles. *Biochimica et Biophysica Acta - Biomembranes*, 1778(6):1423–1428, 2008.

[108] U. Lauer, E. Burgelt, Z. Squire, K. Messmer, P.H. Hofschneider, M. Gregor, and M. Delius. Shock wave permeabilization as a new gene transfer method. *Gene Therapy*, 4(7):710–715, 1997.

[109] R.J. Jeffers, Ruo Qin Feng, J.B. Fowlkes, J.W. Hunt, D. Kessel, and C.A. Cain. Dimethylformamide as an enhancer of cavitation-induced cell lysis in vitro. *Journal of the Acoustical Society of America*, 97(1):669–676, 1995.

[110] E.C. Everbach, I.R.S. Makin, M. Azadniv, and R.S. Meltzer. Correlation of ultrasound-induced hemolysis with cavitation detector output in vitro. *Ultrasound in Medicine and Biology*, 23(4):619–624, 1997.

[111] L.O. Kober, J.W. Ellwart, and H. Brettel. Effect of the pulse length of ultrasound on cell membrane damage in vitro. *Journal of the Acoustical Society of America*, 86(1): 6–7, 1989.

[112] A.A. Brayman, M. Azadniv, C. Cox, and M.W. Miller. Hemolysis of albunex-supplemented, 40in vitro by 1-mhz pulsed ultrasound: Acoustic pressure and pulse length dependence. *Ultrasound in Medicine and Biology*, 22(7):927–938, 1996.

[113] S. Hohmann, R.M. Bill, G. Kayingo, and B.A. Prior. Microbial mip channels. *Trends in Microbiology*, 8(1):33–38, 2000.

[114] P. Agre. Aquaporin water channels (nobel lecture). *Angewandte Chemie - International Edition*, 43(33):4278–4290, 2004.

[115] P. Hersen, M.N. McClean, L. Mahadevan, and S. Ramanathan. Signal processing by the hog map kinase pathway. *Proceedings of the National Academy of Sciences of the United States of America*, 105(20):7165–7170, 2008.

[116] H.Y. Elmoazzen, J.A.W. Elliott, and L.E. McGann. Osmotic transport across cell membranes in nondilute solutions: A new nondilute solute transport equation. *Biophysical Journal*, 96(7):2559–2571, 2009.

[117] I. Aslund, A. Nowacka, M. Nilsson, and D. Topgaard. Filter-exchange pgse nmr determination of cell membrane permeability. *Journal of Magnetic Resonance*, 200 (2):291–295, 2009.

[118] C. Malmborg, M. Sjobeck, S. Brockstedt, E. Englund, O. Soderman, and D. Topgaard. Mapping the intracellular fraction of water by varying the gradient pulse length in q-space diffusion mri. *Journal of Magnetic Resonance*, 180(2):280–285, 2006.

[119] P.C.M. Van Zijl, C.T.W. Moonen, P. Faustino, J. Pekar, O. Kaplan, and J.S. Cohen. Complete separation of intracellular and extracellular information in nmr spectra of perfused cells by diffusion-weighted spectroscopy. *Proceedings of the National Academy of Sciences of the United States of America*, 88(8):3228–3232, 1991.

[120] A.R. Waldeck, P.W. Kuchel, A.J. Lennon, and B.E. Chapman. Nmr diffusion measurements to characterise membrane transport and solute binding. *Progress in Nuclear Magnetic Resonance Spectroscopy*, 30(1-2):39–68, 1997.

[121] W. J. Armitage. Effect of solute concentration on intracellular water volume and hydraulic conductivity of human blood platelets. *J Physiol.*, pages 375–385, 1986.

[122] G.T. Rich, I. Sha'afi, A. Romualdez, and A.K. Solomon. Effect of osmolality on the hydraulic permeability coefficient of red cells. *Journal of General Physiology*, 52 (6):941–954, 1968.

[123] K. Muldrew, J. Schachar, P. Cheng, C. Rempel, S. Liang, and R. Wan. The possible influence of osmotic poration on cell membrane water permeability. *Cryobiology*, 58(1):62–68, 2009.

[124] P. Yeagle. *The membranes of cells*. Academic Press Inc, 1987.

[125] M. Edidin. Chapter 7 molecular associations and membrane domains. *Current Topics in Membranes and Transport*, 36(C):81–96, 1990.

[126] L. Fan and T. Y. Fan. Lateral diffusion of membrane proteins at cell membrane, 2010.

[127] M.D. Dibner, K.A. Ireland, L.A. Koerner, and D.L. Dexter. Polar solvent-induced changes in membrane lipid lateral diffusion in human colon cancer cells. *Cancer Research*, 45(10):4998–5003, 1985.

[128] T. Wang, C. Ingram, and J.C. Weisshaar. Model lipid bilayer with facile diffusion of lipids and integral membrane proteins. *Langmuir*, 26(13):11157–11164, 2010.

[129] M. Orsi and J.W. Essex. Permeability of drugs and hormones through a lipid bilayer: Insights from dual-resolution molecular dynamics. *Soft Matter*, 6(16):3797–3808, 2010.

[130] S. Lee, D.J. McAuliffe, H. Zhang, Z. Xu, J. Taitelbaum, T.J. Flotte, and A.G. Doukas. Stress-wave-induced membrane permeation of red blood cells is facilitated by aquaporins. *Ultrasound in Medicine and Biology*, 23(7):1089–1094, 1997.

[131] T. Kodama, H. Uenohara, and K. Takayama. Innovative technology for tissue disruption by explosive-induced shock waves. *Ultrasound in Medicine and Biology*, 24 (9):1459–1466, 1998.

[132] J.C. Phillips, R. Braun, W. Wang, J. Gumbart, E. Tajkhorshid, E. Villa, C. Chipot, R.D. Skeel, L. Kale, and K. Schulten. Scalable molecular dynamics with namd. *Journal of Computational Chemistry*, 26(16):1781–1802, 2005.

[133] Theoritical and Computational Biophysics Group namd scalable molecular dynamics. `http://www.ks.uiuc.edu/`. Accessed: 25/07/2011.

[134] W. Humphrey, A. Dalke, and K. Schulten. VMD – Visual Molecular Dynamics. *Journal of Molecular Graphics*, 14:33–38, 1996.

[135] Theoritical and Computational Biophysics Group. Vmd-visual molecular dynamics. `http://www.ks.uiuc.edu/Research/vmd/`. Accessed: 25/07/2011.

[136] M. Bhandarkar, A. Bhatele, E. Bohm, R. Brunner, F. Buelens, C. Chipot, A. Dalke, S. Dixit, G. Fiorin, P. Freddolino, P. Grayson, J. Gullingsrud, A. Gursoy, D. Hardy, C. Harrison, J. Henin, W. Humphrey, D. Hurwitz, Krawetz N., S. Kumar, D. Kunzman, C. Lee, C. Mei, M. Nelson, J. Phillips, O. Sarood, A. Shinozaki, G. Zheng, and F. Zhu. *NAMD User's Guide Version 2.7b1*. Theoretical Biophysics Group, University of Illinois and Beckman Institute 405 N. Mathews Urbana, IL 61801, 2009.

[137] M.P. Allen. *Introduction to Molecular Dynamics Simulation, Computational Soft Matter: From Synthetic Polymers to Proteins*, 23:1–28, 2004.

[138] Gromacs. Thermostats. `http://www.gromacs.org/Documentation/Terminology/Thermostats`. Accessed: 05/08/2011.

[139] J. Frank and G.A. Gottwald. The langevin limit of the nose-hoover-langevin thermostat. *Journal of Statistical Physics*, 143(4):715–724, 2011.

[140] G.J. Martyna, D.J. Tobias, and M.L. Klein. Constant pressure molecular dynamics algorithms. *The Journal of Chemical Physics*, 101(5):4177–4189, 1994.

[141] S.E. Feller, Y. Zhang, R.W. Pastor, and B.R. Brooks. Constant pressure molecular dynamics simulation: The langevin piston method. *The Journal of Chemical Physics*, 103(11):4613–4621, 1995.

[142] G. Zaccai, J.K. Blasie, and B.P. Schoenborn. Neutron diffraction studies on the location of water in lecithin bilayer model membranes. *Proceedings of the National Academy of Sciences of the United States of America*, 72(1):376–380, 1975.

[143] O. Berger, O. Edholm, and F. Jahnig. Molecular dynamics simulations of a fluid bilayer of dipalmitoylphosphatidylcholine at full hydration, constant pressure, and constant temperature. *Biophysical Journal*, 72(5):2002–2013, 1997.

[144] Biocomputing at the University Of Calgary. Structures and topologies. `http://moose.bio.ucalgary.ca/index.php?page=Structures_and_Topologies`. Accessed: 25/07/2011.

[145] J. B. Klauda. Laboratory of molecular & thermodynamic modeling. `http://terpconnect.umd.edu/~jbklauda/research/download.html`, 2007. Accessed: 25/07/2011.

[146] W. Pfeiffer, G. Schlossbauer, W. Knoll, B. Farago, A. Steyer, and E. Sackmann. Ultracold neutron scattering study of local lipid mobility in bilayer membranes. *J. Phys. France*, 49(7):1077–1082, 1988.

[147] W.L.C. Vaz, R.M. Clegg, and D. Hallmann. Translational diffusion of lipids in liquid crystalline phase phosphatidylcholine multibilayers. a comparison of experiment with theory. *Biochemistry*, 24(3):781–786, 1985.

[148] A.L. Kuo and C.G. Wade. Lipid lateral diffusion by pulsed nuclear magnetic resonance. *Biochemistry*, 18(11):2300–2308, 1979.

[149] Y.K. Shin, U. Ewert, D.E. Budil, and J.H. Freed. Microscopic versus macroscopic diffusion in model membranes by electron spin resonance spectral-spatial imaging. *Biophysical Journal*, 59(4):950–957, 1991.

[150] S. Konig, T.M. Bayerl, G. Coddens, D. Richter, and E. Sackmann. Hydration dependence of chain dynamics and local diffusion in l-alpha-dipalmitoylphosphtidylcholine multilayers studied by incoherent quasi- elastic neutron scattering. *Biophysical Journal*, 68(5):1871–1880, 1995.

[151] W. Pfeiffer, T. Henkel, E. Sackmann, and W. Knorr. Local dynamics of lipid bilayers studied by incoherent quasi-elastic neutron scattering. *EPL*, 8(2):201–206, 1989.

[152] P.F.F. Almeida and W.L.C. Vaz. Chapter 6 lateral diffusion in membranes. *Handbook of Biological Physics*, 1(C):305–357, 1995.

[153] E. Falck, T. Rog, M. Karttunen, and I. Vattulainen. Lateral diffusion in lipid membranes through collective flows. *Journal of the American Chemical Society*, 130(1): 44–45, 2008.

[154] M. Doxastakis, V. Garcia Sakai, S. Ohtake, J.K. Maranas, and J.J. De Pablo. A molecular view of melting in anhydrous phospholipidic membranes. *Biophysical Journal*, 92(1):147–161, 2007.

[155] C. Anezo, A.H. De Vries, H.D. Holtje, D.P. Tieleman, and S.J. Marrink. Methodological issues in lipid bilayer simulations. *Journal of Physical Chemistry B*, 107(35): 9424–9433, 2003.

[156] J.B. Klauda, B.R. Brooks, and R.W. Pastor. Dynamical motions of lipids and a finite size effect in simulations of bilayers. *Journal of Chemical Physics*, 125(14), 2006.

[157] C. Hofsab, E. Lindahl, and O. Edholm. Molecular dynamics simulations of phospholipid bilayers with cholesterol. *Biophysical Journal*, 84(4):2192–2206, 2003.

[158] W.L. Vaz and P.F. Almeida. Microscopic versus macroscopic diffusion in one-component fluid phase lipid bilayer membranes. *Biophysical Journal*, 60(6):1553–1554, 1991.

[159] G. Karniadakis. *Microflows and Nanoflows: Fundamentals and Simulation, 2nd ed*, chapter 10 Simple Fluids in Nanochannels 10.3 Diffusion Transport, page 375. Springer, 2004.

[160] A. Kusumi, Y. Sako, and M. Yamamoto. Confined lateral diffusion of membrane receptors as studied by single particle tracking (nanovid microscopy). effects of calcium-induced differentiation in cultured epithelial cells. *Biophysical Journal*, 65 (5):2021–2040, 1993.

[161] M.J. Saxton. Lateral diffusion in an archipelago. the effect of mobile obstacles. *Biophysical Journal*, 52(6):989–997, 1987.

[162] R.J. Cherry. Protein mobility in membranes. *FEBS Letters*, 55(1):1–7, 1975.

[163] A.P. Minton. Lateral diffusion of membrane proteins in protein-rich membranes. a simple hard particle model for concentration dependence of the two-dimensional diffusion coefficient. *Biophysical Journal*, 55(4):805–808, 1989.

[164] W.L.C. Vaz, F. Goodsaid-Zalduondo, and K. Jacobson. Lateral diffusion of lipids and proteins in bilayer membranes. *FEBS Letters*, 174(2):199–207, 1984.

[165] E. Flenner, J. Das, M.C. Rheinstadter, and I. Kosztin. Subdiffusion and lateral diffusion coefficient of lipid atoms and molecules in phospholipid bilayers. *Physical Review E - Statistical, Nonlinear, and Soft Matter Physics*, 79(1), 2009.

[166] P.C. Dave, E.K. Tiburu, K. Damodaran, and G.A. Lorigan. Investigating structural changes in the lipid bilayer upon insertion of the transmembrane domain of the membrane-bound protein phospholamban utilizing 31p and 2h solid-state nmr spectroscopy. *Biophysical Journal*, 86(3):1564–1573, 2004.

[167] S. Ohki. Properties of lipid bilayer membranes. determination of membrane thickness. *Journal of Theoretical Biology*, 23(1):158–168, 1969.

[168] J. Lechuga, D. Drikakis, and S. Pal. Molecular dynamics study of the interaction of a shock wave with a biological membrane. *International Journal for Numerical Methods in Fluids*, 57(5):677–692, 2008.

[169] R.A. Bockmann, A. Hac, T. Heimburg, and H. Grubmuller. Effect of sodium chloride on a lipid bilayer. *Biophysical Journal*, 85(3):1647–1655, 2003.

[170] D. Drikakis, J. Lechuga, and S. Pal. Effects of shock waves on biological membranes: A molecular dynamics study. *Journal of Computational and Theoretical Nanoscience*, 6:1–6, 2009.

[171] J.J. Chou, J.L. Baber, and A. Bax. Characterization of phospholipid mixed micelles by translational diffusion. *Journal of Biomolecular NMR*, 29(3):299–308, 2004.

[172] D.P. Tieleman and H.J.C. Berendsen. Molecular dynamics simulations of a fully hydrated dipalmitoylphosphatidylcholine bilayer with different macroscopic boundary conditions and parameters. *Journal of Chemical Physics*, 105(11):4871–4880, 1996.

APPENDIX A

Configuration and post-processing files used

A.1 Configuration file for the minimization-equilibration of the system

```
# NPT minimisation and equilibration


    structure "POPC52.psf"
coordinates "POPC52.pdb"
temperature 0
firsttimestep 0



    # Standard output
outputname "POPC52_Minimization"
outputEnergies 8 ;# timesteps between energy output
outputTiming 100 ;# timesteps between timing output
dcdFreq 100 ;# timesteps between writing coordinates to trajectory file
xstFreq 100 ;# timesteps between writing extended system (periodic cell) trajectory
binaryoutput off ;# use binary output files?



    # Force-Field Parameters
paraTypeCharmm on
parameters "par_all27_lipid.prm"
```

```
    ♯ This are specified by CHARMM
exclude scaled1-4
1-4scaling 1.0
switching on


    ♯ Choose the cutoff
cutoff 10.0
switchDist 8.5


    ♯ Atom won't move for more than 2A in a cycle
pairlistdist 11.5


    ♯ Redo pairlists every n steps
stepsPerCycle 20


    ♯ Integrator Parameters
timestep 1 ;♯ number of fs/step
nonBondedFreq 2 ;♯ nonBonded forces every n step
fullElectFrequency 4 ;♯ PME only every n step


    ♯ Constant Temperature Control
langevin on ;♯ Langevin dynamics
langevinDamping 10 ;♯ damping coefficient of n/ps
langevinTemp 310
langevinHydrogen no ;♯ don't couple bath to hydrogens
```

```
    # Periodic Boundary Conditons
cellBasisVector1 66.2 0.0 0.0 ;# total dimension in x direction
cellBasisVector2 0.0 65.0 0.0 ;# total dimension in y direction
cellBasisVector3 0.0 0.0 155.9 ;# total dimension in z direction
cellOrigin -17.3 -16.5 0.2 ;# the center of the cell
# the z dimension is going to shrink so pad sufficiently
# the margin could be reduced once the cell is equilibrated
margin 5




    wrapAll off ;# wrap other molecules
wrapWater off
wrapNearest off ;# if off use to non-rectangular cells




    # PME (for full-system periodic electrostatics)
Pme on
PmeGridsizeX 70 ;#
PmeGridsizeY 70 ;#
PmeGridsizeZ 160 ;#




    # Constant Pressure Control (variable volume)
useGroupPressure yes ;# smaller fluctuations, needed for rigid bonds
useFlexibleCell yes ;# allow dimensions to fluctuate independently, no for water box, yes
for membrane
useConstantRatio yes ;# fix shape in x-y plane




    langevinPiston on
langevinPistonTarget 1.01325 ;# pressure in bar -> 1 atm
langevinPistonPeriod 200 ;# oscillation period around n fs
langevinPistonDecay 100 ;# oscillation decay time of n fs
langevinPistonTemp 310
```

```
    ♯ run one step to get into scripting mode
minimize 0 ;♯ lower potential energy for n steps
langevinPiston off




    minimize 1000
output "POPC52_MinAll"




    run 1000
output "POPC52_Heat"




    langevinPiston on
run 3000
output "POPC52_Langevin"




    run 45000
output "POPC52_Equil"
```

A.2 Sample configuration file for NPT simulations

Indicatively, the configuration file for an after-minimisation simulation is being presented. The current simulation involves the application of a shock of thickness 5Å, impulse $0.33 mPa \cdot s$ with an angle of attack 10°.

```
    ♯ NPT simulation
structure "POPC52.psf"
coordinates "POPC52_Equil.coor"
velocities "POPC52_new_t5_I0.00033_sin10_sw.vel"
```

```
extendedSystem "POPC52_Equil.xsc"



    # Force-Field Parameters
paraTypeCharmm on
parameters "par_all27_lipid.prm"



    # Standard output
outputname "POPC52_t5_I0.00033_sin10_sw"
outputEnergies 8 ;# timesteps between energy output
outputTiming 200 ;# timesteps between timing output
dcdFreq 200 ;# timesteps between writing coordinates to trajectory file
xstFreq 200 ;# timesteps between writing extended system (periodic cell) trajectory
binaryoutput off ;# use binary output files?



    wrapAll off ;# wrap other molecules
wrapNearest off ;# if off use to non-rectangular cells



    # Integrator Parameters
timestep 1 ;# number of fs/step
nonBondedFreq 2 ;# nonBonded forces every n step
fullElectFrequency 4 ;# PME only every n step



    # Redo pairlists every n steps
stepsPerCycle 20



    # This are specified by CHARMM
exclude scaled1-4
```

```
1-4scaling 1.0
switching on


    ♯ Choose the cutoff
cutoff 10.0
switchDist 8.5


    ♯ atom won't move for more than 2Å in a cycle
pairlistdist 11.5
♯ the z dimension is going to shrink so pad sufficiently
♯ the margin could be reduced once the cell is equilibrated
margin 2


    ♯ PME (for full-system periodic electrostatics)
Pme on
PmeGridsizeX 70 ;♯
PmeGridsizeY 70 ;♯
PmeGridsizeZ 160 ;♯


    ♯ Use lighter damping now that system is equilibrated
langevin on ;♯ Langevin dynamics
langevinDamping 1 ;♯ damping coefficient of n/ps
langevinTemp 310
langevinHydrogen no ;♯ don't couple bath to hydrogens


    langevinPiston on
langevinPistonTarget 1.01325 ;♯ pressure in bar -> 1 atm
langevinPistonPeriod 200 ;♯ oscillation period around n fs
langevinPistonDecay 500 ;♯ oscillation decay time of n fs
langevinPistonTemp 310
```

```
    ♯ Constant Pressure Control (variable volume)
useGroupPressure yes ;♯ smaller fluctuations
♯ useFlexibleCell yes ;♯ allow dimensions to fluctuate independently
♯ useConstantRatio yes ;♯ fix shape in x-y plane




    ♯ run simulation



    firsttimestep 50000
run 200000
```

A.3 Sample configuration file for NVE simulations

Indicatively, the configuration file for an NVE simulation is being presented. The current simulation involves the application of a shock of thickness 5Å, impulse $0.33 mPa \cdot s$ with an angle of attack 10°.

```
    ♯ NVE simulation



    structure "POPC52.psf"
coordinates "POPC52_Equil.coor"
velocities "POPC52_new_t5_I0.00033_sin10_sw.vel"
extendedSystem "POPC52_Equil.xsc"




    ♯ Force-Field Parameters
paraTypeCharmm on
parameters "par_all27_lipid.prm"
```

```
    # Standard output
outputname "POPC52_t5_I0.00033_sin10_sw"
outputEnergies 8 ;# timesteps between energy output
outputTiming 200 ;# timesteps between timing output
dcdFreq 200 ;# timesteps between writing coordinates to trajectory file
xstFreq 200 ;# timesteps between writing extended system (periodic cell) trajectory
binaryoutput off ;# use binary output files?

    wrapAll off ;# wrap other molecules
wrapNearest off ;# if off use to non-rectangular cells



    # Integrator Parameters
timestep 1 ;# number of fs/step
nonBondedFreq 2 ;# nonBonded forces every n step
fullElectFrequency 4 ;# PME only every n step



    # Redo pairlists every n steps
stepsPerCycle 20



    # This are specified by CHARMM
exclude scaled1-4
1-4scaling 1.0
switching on



    # Choose the cutoff
cutoff 10.0
switchDist 8.5
```

```
    # Atom won't move for more than 2Å in a cycle
pairlistdist 11.5



    cellBasisVector1 94.5 0.0 0.0
cellBasisVector2 0.0 91.4 0.0
cellBasisVector3 0.0 0.0 166.0
cellOrigin -17.2 -16.6 0.2



    # run simulation



    firsttimestep 50000
run 200000
```

A.4 Post-processing tcl file - whole membrane

This tcl file has been used for the calculation of membrane properties such as kinetic energy of the system, membrane thickness, centre of mass (COM), MSD, and diffusion coefficients related to the whole membrane.

```
    proc center_of_mass {selection} {
# some error checking
if {[$selection num] <= 0} {
error "center_of_mass: needs a selection with atoms"
}
# set the center of mass to 0
#set com [veczero]
set com {0 0}
# set the total mass to 0
set mass 0
# [$selection get {x y z}] returns the coordinates {x y z}
# [$selection get {mass}] returns the masses
# so the following says "for each pair of {coordinates} and masses,
# do the computation ..."
foreach coord [$selection get {x y}] m [$selection get mass] {
```

```
♯ sum of the masses
set mass [expr $mass + $m]
♯ sum up the product of mass and coordinate
set com [vecadd $com [vecscale $m $coord]]
}
♯ and scale by the inverse of the number of atoms
if {$mass == 0} {
error "center_of_mass: total mass is zero"
}
♯ The "1.0" can't be "1", since otherwise integer division is done
return [vecscale [expr 1.0/$mass] $com]
}
```

```
    proc com_frame {frame2} {
♯Calculate COM of the lipids of one frame
for { set i 0 } { $i < 60 } { incr i } {
set sel [atomselect 0 "residue $i" frame $frame2]
lappend cxy1 [center_of_mass $sel]
}
```

```
    for { set i 1051 } { $i < 1071 } { incr i } {
set sel [atomselect 0 "residue $i" frame $frame2]
lappend cxy1 [center_of_mass $sel]
}
```

```
    for { set i 1387 } { $i < 1405 } { incr i } {
set sel [atomselect 0 "residue $i" frame $frame2]
lappend cxy1 [center_of_mass $sel]
}
```

```
    for { set i 1699 } { $i < 1705 } { incr i } {
set sel [atomselect 0 "residue $i" frame $frame2]
lappend cxy1 [center_of_mass $sel]
```

```
}



    return $cxy1
}



    proc frame_msd1 {filename} {



    set fout [open $filename.dat w]
puts $fout "TITLE=MSD"
puts $fout "VARIABLES=Number_of_Frames Time(ps) MSD MSD1"
puts $fout "ZONE T=$filename"
puts $fout " "



    set nf [molinfo 0 get numframes]



    set ref1 [com_frame 0]



    for { set i 0 } { $i < $nf } { incr i } {
set msd1 0
set msd 0



    set reff3 [com_frame $i]
set ref1 [com_frame 0]
```

```
    foreach t3 $ref1 t4 $reff3 { set msd1 [expr $msd1+[veclength2 [vecsub $t3 $t4]]]}

set msd [expr $msd1 /(104.0)]



    set mytime [expr $i*200*0.001+50]



    puts $fout "$i $mytime $msd $msd1"
flush $fout
}



    close $fout



    return $msd
}



    #this one gives you the x y z coordinates of the com for all the frames, y
#the command is xyz_popc filename e.g. xyz_popc com-popc
proc xyz_popc {filename} {



    set fout [open $filename.dat w]
puts $fout "TITLE=Centre of Mass"
puts $fout "VARIABLES=Number_of_Frames Time(ps) Mass_Centre_X Mass_Centre_Y
Mass_Centre_Z"
puts $fout "ZONE T=$filename"
```

```
puts $fout " "



    set nf [molinfo 0 get numframes]



    for { set i 0 } { $i < $nf } { incr i } {



    set reff3 [comxyz_popc $i]
#this is for the time, 200 correspond to the number of timesteps and the 0.001 (ps)
#to the time step which is 1fs, 50ps are the time of the minimisation



    set mytime [expr $i*200*0.001+50]



    puts $fout "$i $mytime $reff3"
flush $fout
}



    close $fout



    return $msd



    }
```

```
    ♯ this is used for the com
proc center_of_massxyz {selection} {
♯ some error checking
if {[$selection num] <= 0} {
error "center_of_mass: needs a selection with atoms"
}
♯ set the center of mass to 0
set com [veczero]
♯set com {0 0}
♯ set the total mass to 0
set mass 0
♯ [$selection get {x y z}] returns the coordinates {x y z}
♯ [$selection get {mass}] returns the masses
♯ so the following says "for each pair of {coordinates} and masses,
♯ do the computation ..."
foreach coord [$selection get {x y z}] m [$selection get mass] {
♯ sum of the masses
set mass [expr $mass + $m]
♯ sum up the product of mass and coordinate
set com [vecadd $com [vecscale $m $coord]]
}
♯ and scale by the inverse of the number of atoms
if {$mass == 0} {
error "center_of_mass: total mass is zero"
}
♯ The "1.0" can't be "1", since otherwise integer division is done
return [vecscale [expr 1.0/$mass] $com]
}
```

```
    ♯ this is used for the com
proc comxyz_popc {frame2} {
♯Calculate COM of the lipids of one frame
set sel [atomselect 0 "resname POPC" frame $frame2]
set cxy1 [center_of_massxyz $sel]
```

```
    return $cxy1
}
```

```
    ♯Calculates the com of the upper lipids
proc com_min {frame2} {
♯Calculate COM of the lipids of one frame
for { set i 0 } { $i < 30 } { incr i } {
set sel [atomselect 0 "residue $i" frame $frame2]
lappend cxy1 [center_of_massz $sel]
}



    for { set i 1051 } { $i < 1061 } { incr i } {
set sel [atomselect 0 "residue $i" frame $frame2]
lappend cxy1 [center_of_massz $sel]
}



    for { set i 1387 } { $i < 1396 } { incr i } {
set sel [atomselect 0 "residue $i" frame $frame2]
lappend cxy1 [center_of_massz $sel]
}



    for { set i 1699 } { $i < 1702 } { incr i } {
set sel [atomselect 0 "residue $i" frame $frame2]
lappend cxy1 [center_of_massz $sel]
}



    return $cxy1
}



    ♯Calculates the com of the lower lipids
proc com_max {frame2} {
```

```
#Calculate COM of the lipids of one frame
for { set i 30 } { $i < 60 } { incr i } {
set sel [atomselect 0 "residue $i" frame $frame2]
lappend cxy1 [center_of_massz $sel]
}
for { set i 1061 } { $i < 1071 } { incr i } {
set sel [atomselect 0 "residue $i" frame $frame2]
lappend cxy1 [center_of_massz $sel]
}
for { set i 1396 } { $i < 1405 } { incr i } {
set sel [atomselect 0 "residue $i" frame $frame2]
lappend cxy1 [center_of_massz $sel]
}




    for { set i 1702 } { $i < 1705 } { incr i } {
set sel [atomselect 0 "residue $i" frame $frame2]
lappend cxy1 [center_of_massz $sel]
}




    return $cxy1
}



    #Calculates the thickness, we measure the thickness as the difference between the centrer
of mass of the upper and lower lipids
#the structure is thick_popc filename



    proc thick_popc {filename} {



    set fout [open $filename.dat w]
```

```
puts $fout "TITLE=Thickness"
puts $fout "VARIABLES=Number_of_Frames Time(ps) Thickness"
puts $fout "ZONE T=$filename"
puts $fout " "



    set nf [molinfo 0 get numframes]



    for { set i 0 } { $i < $nf } { incr i } {



    set reff3 [vecmean [com_max $i]]
set ref1 [vecmean [com_min $i]]



    set thick [expr $ref1 - $reff3]



    #this is for the time, 200 correspond to the number of timesteps and the 0.001 (ps)
#to the time step which is 1fs, 50ps are the time of the minimisation set mytime [expr
$i*200*0.001+50]



    puts $fout "$i $mytime $thick"
#puts stdout "$i $thick"
flush $fout
}
```

```
    close $fout



    return $thick



    }



    proc center_of_massz {selection} {
# some error checking
if {[$selection num] <= 0} {
error "center_of_mass: needs a selection with atoms"
}
# set the center of mass to 0
#set com [veczero]
set com { 0 }
# set the total mass to 0
set mass 0
# [$selection get {x y z}] returns the coordinates {x y z}
# [$selection get {mass}] returns the masses
# so the following says "for each pair of {coordinates} and masses,
# do the computation ..."
foreach coord [$selection get z] m [$selection get mass] {
# sum of the masses
set mass [expr $mass + $m]
# sum up the product of mass and coordinate
set com [vecadd $com [vecscale $m $coord]]
}
# and scale by the inverse of the number of atoms
if {$mass == 0} {
error "center_of_mass: total mass is zero"
}
# The "1.0" can't be "1", since otherwise integer division is done
return [vecscale [expr 1.0/$mass] $com]
}
```

A.5 Post-processing tcl file - upper lipid bilayer

This tcl file has been used for the calculation of MSD and diffusion coefficients related to the upper monolayer.

```
    proc center_of_mass {selection} {
# some error checking
if {[$selection num] <= 0} {
error "center_of_mass: needs a selection with atoms"
}
# set the center of mass to 0
#set com [veczero]
set com {0 0}
# set the total mass to 0
set mass 0
# [$selection get {x y z}] returns the coordinates {x y z}
# [$selection get {mass}] returns the masses
# so the following says "for each pair of {coordinates} and masses,
# do the computation ..."
foreach coord [$selection get {x y}] m [$selection get mass] {
# sum of the masses
set mass [expr $mass + $m]
# sum up the product of mass and coordinate
set com [vecadd $com [vecscale $m $coord]]
}
# and scale by the inverse of the number of atoms
if {$mass == 0} {
error "center_of_mass: total mass is zero"
}
# The "1.0" can't be "1", since otherwise integer division is done
return [vecscale [expr 1.0/$mass] $com]
}
```

```
    proc com_frame {frame2} {
#Calculate COM of the upper lipids of one frame
for { set i 0 } { $i < 30 } { incr i } {
set sel [atomselect 0 "residue $i" frame $frame2]
lappend cxy1 [center_of_mass $sel]
```

```
}



    for { set i 1051 } { $i < 1061 } { incr i } {
set sel [atomselect 0 "residue $i" frame $frame2]
lappend cxy1 [center_of_mass $sel]
}



    for { set i 1387 } { $i < 1396 } { incr i } {
set sel [atomselect 0 "residue $i" frame $frame2]
lappend cxy1 [center_of_mass $sel]
}



    for { set i 1699 } { $i < 1702 } { incr i } {
set sel [atomselect 0 "residue $i" frame $frame2]
lappend cxy1 [center_of_mass $sel]
}



    return $cxy1
}



    proc frame_msd1 {filename} {



    set fout [open $filename.dat w]
puts $fout "TITLE=MSD"
puts $fout "VARIABLES=Number_of_Frames Time(ps) MSD MSD1"
puts $fout "ZONE T=$filename"
puts $fout " "
```

```
    set nf [molinfo 0 get numframes]



    set ref1 [com_frame 0]



    for { set i 0 } { $i < $nf } { incr i } {
set msd1 0
set msd 0



    set reff3 [com_frame $i]
set ref1 [com_frame 0]



    foreach t3 $ref1 t4 $reff3 { set msd1 [expr $msd1+[veclength2 [vecsub $t3 $t4]]]}
set msd [expr $msd1 /(52.0)]



    set mytime [expr $i*200*0.001+50]



    puts $fout "$i $mytime $msd $msd1"
flush $fout
}



    close $fout
```

```
    return $msd
}



    proc center_of_massz {selection} {
# some error checking
if {[$selection num] <= 0} {
error "center_of_mass: needs a selection with atoms"
}
# set the center of mass to 0
#set com [veczero]
set com { 0 }
# set the total mass to 0
set mass 0
# [$selection get {x y z}] returns the coordinates {x y z}
# [$selection get {mass}] returns the masses
# so the following says "for each pair of {coordinates} and masses,
# do the computation ..."
foreach coord [$selection get z] m [$selection get mass] {
# sum of the masses
set mass [expr $mass + $m]
# sum up the product of mass and coordinate
set com [vecadd $com [vecscale $m $coord]]
}
# and scale by the inverse of the number of atoms
if {$mass == 0} {
error "center_of_mass: total mass is zero"
}
# The "1.0" can't be "1", since otherwise integer division is done
return [vecscale [expr 1.0/$mass] $com]
}
```

A.6 Post-processing tcl file - lower lipid bilayer

This tcl file has been used for the calculation of MSD and diffusion coefficients related to the lower monolayer.

```
    proc center_of_mass {selection} {
# some error checking
if {[$selection num] <= 0} {
error "center_of_mass: needs a selection with atoms"
}
# set the center of mass to 0
#set com [veczero]
set com {0 0}
# set the total mass to 0
set mass 0
# [$selection get {x y z}] returns the coordinates {x y z}
# [$selection get {mass}] returns the masses
# so the following says "for each pair of {coordinates} and masses,
# do the computation ..."
foreach coord [$selection get {x y}] m [$selection get mass] {
#




    #sum of the masses
set mass [expr $mass + $m]
# sum up the product of mass and coordinate
set com [vecadd $com [vecscale $m $coord]]
}
# and scale by the inverse of the number of atoms
if {$mass == 0} {
error "center_of_mass: total mass is zero"
}
# The "1.0" can't be "1", since otherwise integer division is done
return [vecscale [expr 1.0/$mass] $com]
}




    proc com_frame {frame2} {
#Calculate COM of the lower lipids of one frame
for { set i 30 } { $i < 60 } { incr i } {
set sel [atomselect 0 "residue $i" frame $frame2]
lappend cxy1 [center_of_mass $sel]
}
```

```
    for { set i 1061 } { $i < 1071 } { incr i } {
set sel [atomselect 0 "residue $i" frame $frame2]
lappend cxy1 [center_of_mass $sel]
}



    for { set i 1396 } { $i < 1405 } { incr i } {
set sel [atomselect 0 "residue $i" frame $frame2]
lappend cxy1 [center_of_mass $sel]
}



    for { set i 1702 } { $i < 1705 } { incr i } {
set sel [atomselect 0 "residue $i" frame $frame2]
lappend cxy1 [center_of_mass $sel]
}



    return $cxy1
}



    proc frame_msd1 {filename} {



    set fout [open $filename.dat w]
puts $fout "TITLE=MSD"
puts $fout "VARIABLES=Number_of_Frames Time(ps) MSD MSD1"
puts $fout "ZONE T=$filename"
puts $fout " "
```

```
    set nf [molinfo 0 get numframes]



    set ref1 [com_frame 0]



    for { set i 0 } { $i < $nf } { incr i } {
set msd1 0
set msd 0



    set reff3 [com_frame $i]
set ref1 [com_frame 0]



    foreach t3 $ref1 t4 $reff3 { set msd1 [expr $msd1+[veclength2 [vecsub $t3 $t4]]]}
set msd [expr $msd1 /(52.0)]



    set mytime [expr $i*200*0.001+50]



    puts $fout "$i $mytime $msd $msd1"
flush $fout
}



    close $fout
```

```
    return $msd
}



    proc center_of_massz {selection} {
# some error checking
if {[$selection num] <= 0} {
error "center_of_mass: needs a selection with atoms"
}
# set the center of mass to 0
#set com [veczero]
set com { 0 }
# set the total mass to 0
set mass 0
# [$selection get {x y z}] returns the coordinates {x y z}
# [$selection get {mass}] returns the masses
# so the following says "for each pair of {coordinates} and masses,
# do the computation ..."
foreach coord [$selection get z] m [$selection get mass] {
# sum of the masses
set mass [expr $mass + $m]
# sum up the product of mass and coordinate
set com [vecadd $com [vecscale $m $coord]]
}
# and scale by the inverse of the number of atoms
if {$mass == 0} {
error "center_of_mass: total mass is zero"
}
# The "1.0" can't be "1", since otherwise integer division is done
return [vecscale [expr 1.0/$mass] $com]
}
```

APPENDIX **B**

Calculated Diffusion Coefficient values

The plots in Appendix B present the data that was gathered numerically after the post-processing of the results of the simulations that were run under both the NVE and NPT ensemble and have been described in chapters 4 and 5. Here, the diffusion coefficient values of the whole membrane, the upper lipid bilayer and the lower lipid bilayer are included. t_{shock} represents the shock thickness in the plots and is measured in Å and i is the impulse in $mPa \cdot s$).

B.1 Diffusion Coefficients of the whole membrane

Diffusion coefficient values ($10^{-7} cm^2 s^{-1}$) - whole membrane - NPT										
t_{shock} (Å)	i ($mPa \cdot s$)	0°	10°	20°	30°	40°	50°	60°	70°	80°
5	0.33	0.0131	0.0271	0.0244	0.0272	0.0692	0.0329	0.0243	0.0195	0.0136
	0.66	0.0137	0.0250	0.0201	0.0122	0.0145	0.0244	0.0150	0.0301	0.0214
	0.99	0.0080	0.0177	0.0242	0.0263	0.0156	-	-	-	-
	2	0.0325	-	-	-	-	-	-	-	-
	3	0.0273	-	-	-	-	-	-	-	-
	4	0.0069	-	-	-	-	-	-	-	-
7	0.33	0.0177	0.0487	0.0297	0.0209	0.0194	0.0301	0.0201	0.0231	0.0416
	0.66	0.0223	0.0246	0.0145	0.0122	0.0207	0.0429	0.0610	0.0474	0.0194
	0.99	0.0204	0.0221	0.0183	0.0158	0.0225	0.0223	0.0264	-	-
	2	0.0253	0.0278	0.0172	0.0320	0.0213	0.0218	0.0267	0.0276	0.0212
	3	0.0504	-	-	-	-	-	-	-	-
	4	0.0162	-	-	-	-	-	-	-	-
	5	0.0177	-	-	-	-	-	-	-	-
10	0.33	0.0310	0.0128	0.0190	0.0171	0.0555	0.0797	0.0297	0.0137	0.0263
	0.66	0.0125	0.0155	0.0150	0.0075	0.0262	0.0102	0.0209	0.0138	0.0215
	0.99	0.0138	0.0294	0.0242	0.0149	0.0162	0.0100	0.0323	-	-
	2	0.0048	0.0176	0.0257	-	-	-	-	-	-
	3	0.0232	-	-	-	-	-	-	-	-
	4	0.0510	-	-	-	-	-	-	-	-
	5	0.0215	-	-	-	-	-	-	-	-
	6	0.0120	-	-	-	-	-	-	-	-
	7	0.0127	-	-	-	-	-	-	-	-
12	0.33	0.0171	0.0204	0.0293	0.0303	0.0339	0.0204	0.0161	0.0281	0.0496
	0.66	0.0235	0.0234	0.0210	0.0364	0.0216	0.0105	0.0233	0.0225	0.0191
	0.99	0.0172	0.0234	0.0248	0.0289	0.0220	0.0324	-	-	-
	2	0.0232	0.0189	0.0157	-	-	-	-	-	-
	3	0.0171	0.0085	-	-	-	-	-	-	-
	4	0.0420	-	-	-	-	-	-	-	-
	5	0.0198	-	-	-	-	-	-	-	-
	6	0.0270	-	-	-	-	-	-	-	-
	7	0.0412	-	-	-	-	-	-	-	-
	8	0.0204	-	-	-	-	-	-	-	-
	9	0.0517	-	-	-	-	-	-	-	-
	10	0.0065	-	-	-	-	-	-	-	-

Table B.1: Diffusion coefficient values of the whole membrane - NPT ensemble

Diffusion coefficient values ($10^{-7} cm^2 s^{-1}$) - whole membrane - NVE										
t_{shock} (Å)	i ($mPa \cdot s$)	0°	10°	20°	30°	40°	50°	60°	70°	80°
5	0.33	0.0371	0.0479	0.0850	0.0907	0.0434	0.0247	0.0596	0.0178	0.0175
	0.66	0.0686	0.0502	0.0454	0.0371	0.1280	0.0658	0.0268	-	0.1266
	0.99	0.0480	0.0353	0.0456	0.0404	0.1016	-	-	-	-
	2	0.0887	-	-	-	-	-	-	-	-
	3	0.0586	-	-	-	-	-	-	-	-
	4	0.0301	-	-	-	-	-	-	-	-
7	0.33	0.0236	0.0566	0.0439	0.0237	0.0193	0.0126	0.0316	0.0273	0.1114
	0.66	0.0320	0.0234	0.0286	0.0326	0.0599	0.0375	0.0311	0.0486	0.0260
	0.99	0.0386	0.0290	0.0313	0.0674	0.0714	0.0180	0.0858	-	-
	2	0.0788	0.1197	0.0542	0.0805	0.0377	0.0481	0.0524	0.0233	0.0516
	3	0.0518	-	-	-	-	-	-	-	-
	4	0.0379	-	-	-	-	-	-	-	-
	5	0.1596	-	-	-	-	-	-	-	-
10	0.33	0.0222	0.0245	0.0242	0.0551	0.0017	0.0373	0.0210	0.0372	0.0634
	0.66	0.0454	0.0373	0.1141	0.0362	0.1184	0.0704	0.4031	0.3869	0.2309
	0.99	0.0273	0.0320	0.0698	0.2654	0.0104	0.5163	-	-	-
	2	0.0304	0.0133	-	-	-	-	-	-	-
	3	0.0450	-	-	-	-	-	-	-	-
	4	0.0259	-	-	-	-	-	-	-	-
	5	0.0362	-	-	-	-	-	-	-	-
	6	0.0476	-	-	-	-	-	-	-	-
12	0.33	0.0129	0.0340	0.0149	0.0462	0.0828	0.0273	0.0467	0.0235	0.0709
	0.66	0.0649	0.0377	0.1047	-0.0338	0.0768	-0.0777	0.1020	0.0219	0.0282
	0.99	0.0707	0.0292	0.0690	0.1161	0.4281	0.5363	-	-	-
	2	0.0379	0.0675	0.0818	-	-	-	-	-	-
	3	0.1047	-	-	-	-	-	-	-	-
	4	0.0514	-	-	-	-	-	-	-	-
	5	0.0375	-	-	-	-	-	-	-	-
	6	0.0468	-	-	-	-	-	-	-	-
	7	0.0470	-	-	-	-	-	-	-	-
	8	0.0360	-	-	-	-	-	-	-	-
	9	0.0513	-	-	-	-	-	-	-	-
	10	0.0753	-	-	-	-	-	-	-	-

Table B.2: Diffusion coefficient values of the whole membrane - NVE ensemble

B.2 Diffusion Coefficients of the upper lipid bilayer

Diffusion coefficient values ($10^{-7} cm^2 s^{-1}$) - upper lipid bilayer - NPT										
t_{shock} (Å)	i ($mPa \cdot s$)	0°	10°	20°	30°	40°	50°	60°	70°	80°
5	0.33	0.0205	0.0287	0.0195	0.0216	0.0878	0.0367	0.0260	0.0162	0.0141
	0.66	0.0127	0.0258	0.0201	0.0138	0.0128	0.0277	0.0123	0.0319	0.0220
	0.99	0.0150	0.0221	0.0235	0.0253	0.0211	-	-	-	-
	2	0.0300	-	-	-	-	-	-	-	-
	3	0.0234	-	-	-	-	-	-	-	-
	4	0.0134	-	-	-	-	-	-	-	-
7	0.33	0.0226	0.0470	0.0324	0.0270	0.0189	0.0283	0.0148	0.0228	0.0446
	0.66	0.0304	0.0245	0.0147	0.0145	0.0245	0.0526	0.0616	0.0435	0.0186
	0.99	0.0204	0.0221	0.0216	0.0138	0.0162	0.0243	0.0219	-	-
	2	0.0336	0.0266	0.0167	0.0431	0.0207	0.0239	0.0253	0.0250	0.0258
	3	0.0452	-	-	-	-	-	-	-	-
	4	0.0186	-	-	-	-	-	-	-	-
	5	0.0176	-	-	-	-	-	-	-	-
10	0.33	0.0345	0.0131	0.0142	0.0117	0.0532	0.0699	0.0309	0.0141	0.0361
	0.66	0.0181	0.0186	0.0189	0.0139	0.0347	0.0121	0.0184	0.0138	0.0188
	0.99	0.0229	0.0227	0.0245	0.0112	0.0205	0.0094	0.0295	-	-
	2	0.0101	0.0093	0.0299	-	-	-	-	-	-
	3	0.0415	-	-	-	-	-	-	-	-
	4	0.0376	-	-	-	-	-	-	-	-
	5	0.0390	-	-	-	-	-	-	-	-
	6	0.0211	-	-	-	-	-	-	-	-
	7	0.0125	-	-	-	-	-	-	-	-
12	0.33	0.0205	0.0203	0.0270	0.0330	0.0484	0.0248	0.0149	0.0286	0.0640
	0.66	0.0256	0.0246	0.0186	0.0350	0.0284	0.0121	0.0250	0.0170	0.0203
	0.99	0.0231	0.0234	0.0228	0.0289	0.0295	0.0186	-	-	
	2	0.0314	0.0248	0.0241	-	-	-	-	-	-
	3	0.0187	0.0193	-	-	-	-	-	-	-
	4	0.0425	-	-	-	-	-	-	-	-
	5	0.0210	-	-	-	-	-	-	-	-
	6	0.0195	-	-	-	-	-	-	-	-
	7	0.0393	-	-	-	-	-	-	-	-
	8	0.0268	-	-	-	-	-	-	-	-
	9	0.0209	-	-	-	-	-	-	-	-
	10	0.0093	-	-	-	-	-	-	-	-

Table B.3: Diffusion coefficient values of the upper lipid bilayer - NPT ensemble

Diffusion coefficient values ($10^{-7} cm^2 s^{-1}$) - upper lipid bilayer - NVE										
t_{shock} (Å)	i ($mPa \cdot s$)	0°	10°	20°	30°	40°	50°	60°	70°	80°
5	0.33	0.0341	0.0519	0.0705	0.0997	0.0440	0.0274	0.0516	0.0179	0.0314
	0.66	0.0784	0.0571	0.0418	0.0534	0.1364	0.0541	0.0217	-	0.1170
	0.99	0.0378	0.0373	0.0405	0.0521	0.1144	-	-	-	-
	2	0.0772	-	-	-	-	-	-	-	-
	3	0.0485	-	-	-	-	-	-	-	-
	4	0.0306	-	-	-	-	-	-	-	-
7	0.33	0.0194	0.0556	0.0370	0.0250	0.0252	0.0053	0.0275	0.0302	0.1159
	0.66	0.0293	0.0136	0.0359	0.0263	0.0659	0.0342	0.0386	0.0396	0.0236
	0.99	0.0354	0.0260	0.0253	0.0799	0.0902	0.0309	0.0883	-	-
	2	0.0649	0.1258	0.0630	0.0900	0.0326	0.0399	0.0534	0.0166	0.0510
	3	0.0549	-	-	-	-	-	-	-	-
	4	0.0409	-	-	-	-	-	-	-	-
	5	0.1754	-	-	-	-	-	-	-	-
10	0.33	0.0404	0.0217	0.0233	0.0672	-0.0026	0.0697	0.0310	0.0361	0.0953
	0.66	0.0591	0.0399	0.0986	0.0558	0.0919	0.0782	0.4272	0.4150	0.1790
	0.99	0.0312	0.0248	0.0720	0.2562	0.0491	0.5052	-	-	-
	2	0.0330	0.0160	-	-	-	-	-	-	-
	3	0.0488	-	-	-	-	-	-	-	-
	4	0.0189	-	-	-	-	-	-	-	-
	5	0.0374	-	-	-	-	-	-	-	-
	6	0.0452	-	-	-	-	-	-	-	-
12	0.33	0.0016	0.0396	0.0237	0.0470	0.0887	0.0270	0.0527	0.0342	0.0700
	0.66	0.0514	0.0309	0.1184	-0.0358	0.0628	-0.0613	0.1281	0.0191	0.0220
	0.99	0.0513	0.0171	0.0581	0.0903	0.5112	0.5116	-	-	-
	2	0.0369	0.0130	0.0608	-	-	-	-	-	-
	3	0.0833	-	-	-	-	-	-	-	-
	4	0.0595	-	-	-	-	-	-	-	-
	5	0.0328	-	-	-	-	-	-	-	-
	6	0.0581	-	-	-	-	-	-	-	-
	7	0.0470	-	-	-	-	-	-	-	-
	8	0.0377	-	-	-	-	-	-	-	-
	9	0.0710	-	-	-	-	-	-	-	-
	10	0.0681	-	-	-	-	-	-	-	-

Table B.4: Diffusion coefficient values of the upper lipid bilayer - NVE ensemble

B.3 Diffusion Coefficients of the lower lipid bilayer

Diffusion coefficient values ($10^{-7} cm^2 s^{-1}$) - lower lipid bilayer - NPT										
t_{shock} (Å)	i ($mPa \cdot s$)	0°	10°	20°	30°	40°	50°	60°	70°	80°
5	0.33	0.0109	0.0256	0.0293	0.0327	0.0507	0.0291	0.0226	0.0227	0.0131
	0.66	0.0180	0.0242	0.0200	0.0106	0.0162	0.0212	0.0177	0.0282	0.0207
	0.99	0.0138	0.0134	0.0249	0.0273	0.0101	-	-	-	-
	2	0.0293	-	-	-	-	-	-	-	-
	3	0.0271	-	-	-	-	-	-	-	-
	4	0.0110	-	-	-	-	-	-	-	-
7	0.33	0.0356	0.0503	0.0269	0.0148	0.0199	0.0320	0.0253	0.0235	0.0385
	0.66	0.0224	0.0247	0.0143	0.0100	0.0169	0.0332	0.0605	0.0513	0.0203
	0.99	0.0257	0.0221	0.0150	0.0177	0.0288	0.0202	0.0309	-	-
	2	0.0243	0.0290	0.0177	0.0210	0.0219	0.0198	0.0281	0.0303	0.0166
	3	0.0596	-	-	-	-	-	-	-	-
	4	0.0186	-	-	-	-	-	-	-	-
	5	0.0176	-	-	-	-	-	-	-	-
10	0.33	0.0257	0.0126	0.0237	0.0226	0.0578	0.0894	0.0286	0.0132	0.0165
	0.66	0.0193	0.0124	0.0111	0.0011	0.0177	0.0082	0.0235	0.0137	0.0242
	0.99	0.0239	0.0360	0.0238	0.0187	0.0119	0.0106	0.0350	-	-
	2	0.0107	0.0259	0.0215	-	-	-	-	-	-
	3	0.0249	-	-	-	-	-	-	-	-
	4	0.0476	-	-	-	-	-	-	-	-
	5	0.0390	-	-	-	-	-	-	-	-
	6	0.0099	-	-	-	-	-	-	-	-
	7	0.0150	-	-	-	-	-	-	-	-
12	0.33	0.0156	0.0205	0.0317	0.0277	0.0193	0.0160	0.0174	0.0276	0.0352
	0.66	0.0212	0.0223	0.0233	0.0378	0.0149	0.0088	0.0217	0.0281	0.0179
	0.99	0.0262	0.0233	0.0268	0.0288	0.0144	0.0461	-	-	-
	2	0.0190	0.0130	0.0073	-	-	-	-	-	-
	3	0.0135	-0.0024	-	-	-	-	-	-	-
	4	0.0531	-	-	-	-	-	-	-	-
	5	0.0210	-	-	-	-	-	-	-	-
	6	0.0290	-	-	-	-	-	-	-	-
	7	0.0411	-	-	-	-	-	-	-	-
	8	0.0181	-	-	-	-	-	-	-	-
	9	0.0610	-	-	-	-	-	-	-	-
	10	0.0105	-	-	-	-	-	-	-	-

Table B.5: Diffusion coefficient values of the lower lipid bilayer - NPT ensemble

Diffusion coefficient values ($10^{-7} cm^2 s^{-1}$)) - lower lipid bilayer - NVE										
t_{shock} (Å)	i ($mPa \cdot s$)	0°	10°	20°	30°	40°	50°	60°	70°	80°
5	0.33	0.0400	0.0439	0.0996	0.0818	0.0428	0.0220	0.0676	0.0177	0.0036
	0.66	0.0587	0.0433	0.0490	0.0209	0.1196	0.0776	0.0318	-	0.1362
	0.99	0.0582	0.0333	0.0506	0.0287	0.0889	-	-	-	-
	2	0.1002	-	-	-	-	-	-	-	-
	3	0.0686	-	-	-	-	-	-	-	-
	4	0.0296	-	-	-	-	-	-	-	-
7	0.33	0.0277	0.0576	0.0508	0.0224	0.0135	0.0199	0.0358	0.0243	0.1069
	0.66	0.0347	0.0332	0.0213	0.0389	0.0539	0.0408	0.0236	0.0576	0.0284
	0.99	0.0419	0.0319	0.0374	0.0549	0.0525	0.0050	0.0834	-	-
	2	0.0926	0.1137	0.0454	0.0710	0.0429	0.0564	0.0513	0.0301	0.0522
	3	0.0487	-	-	-	-	-	-	-	-
	4	0.0348	-	-	-	-	-	-	-	-
	5	0.1438	-	-	-	-	-	-	-	-
10	0.33	0.0507	0.0274	0.0252	0.0430	0.0060	0.0049	0.0109	0.0384	0.0315
	0.66	0.0316	0.0347	0.1296	0.0166	0.1448	0.0626	0.3791	0.3588	0.2828
	0.99	0.0235	0.0392	0.0677	0.2746	-0.0283	0.5274	-	-	-
	2	0.0278	0.0107	-	-	-	-	-	-	-
	3	0.0412	-	-	-	-	-	-	-	-
	4	0.0330	-	-	-	-	-	-	-	-
	5	0.0350	-	-	-	-	-	-	-	-
	6	0.0500	-	-	-	-	-	-	-	-
12	0.33	0.0243	0.0285	0.0061	0.0454	0.0768	0.0275	0.0408	0.0128	0.0718
	0.66	0.0783	0.0445	0.0909	-0.0319	0.0909	-0.0941	0.0759	0.0247	0.0344
	0.99	0.0902	0.0413	0.0800	0.1419	0.3451	0.5610	-	-	-
	2	0.0388	0.0547	0.0467	-	-	-	-	-	-
	3	0.1262	-	-	-	-	-	-	-	-
	4	0.0434	-	-	-	-	-	-	-	-
	5	0.0423	-	-	-	-	-	-	-	-
	6	0.0354	-	-	-	-	-	-	-	-
	7	0.0469	-	-	-	-	-	-	-	-
	8	0.0344	-	-	-	-	-	-	-	-
	9	0.0315	-	-	-	-	-	-	-	-
	10	0.0826	-	-	-	-	-	-	-	-

Table B.6: Diffusion coefficient values of the lower lipid bilayer - NVE ensemble

APPENDIX C

Supplementary result sets from chapter 5

C.1 Effects on Membrane Thickness ($0.99mPa{\cdot}s$ - $2mPa{\cdot}s$) - NPT ensemble

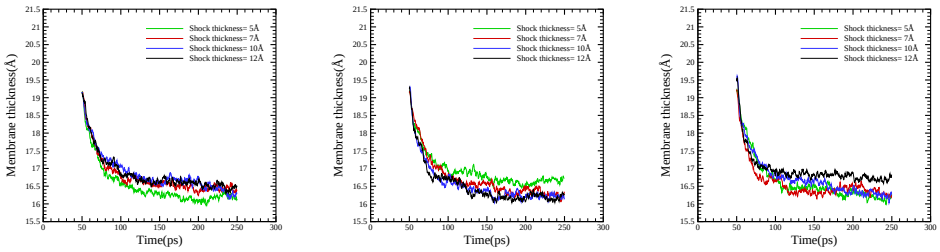

(a) Angle of attack 10° (b) Angle of attack 20° (c) Angle of attack 30°

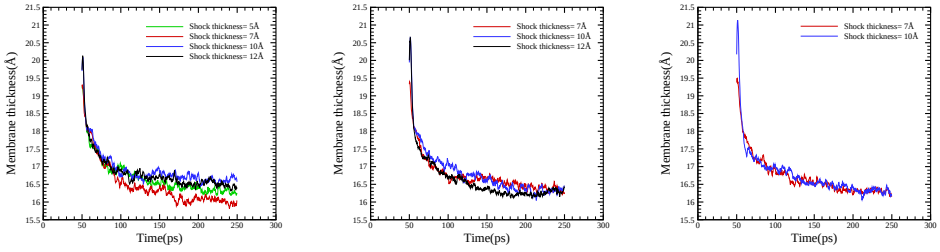

(d) Angle of attack 40° (e) Angle of attack 50° (f) Angle of attack 60°

Figure C.1: Shock wave effects on Membrane Thickness at various shock wave thicknesses and angles of attack when the impulse is $0.99mPa \cdot s$

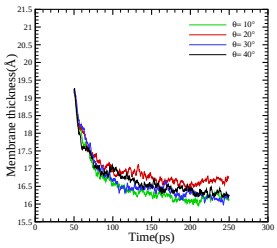

(a) Shock thickness 5Å

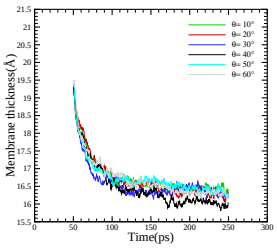

(b) Shock thickness 7Å

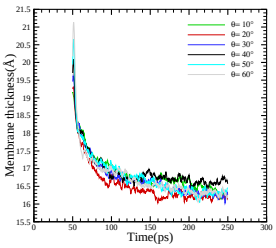

(c) Shock thickness 10Å

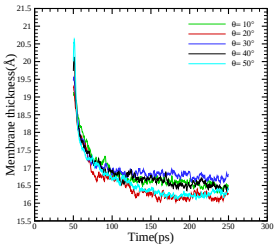

(d) Shock thickness 12Å

Figure C.2: Shock wave effects on Membrane Thickness at various shock wave thicknesses and angles of attack when the impulse is $0.99mPa \cdot s$

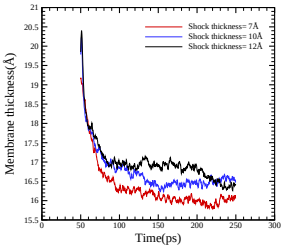

(a) Angle of attack 10°

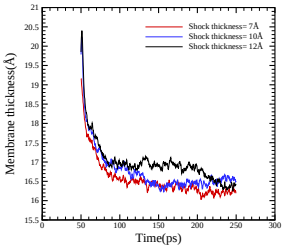

(b) Angle of attack 20°

Figure C.3: Shock wave effects on Membrane Thickness at various shock wave thicknesses and angles of attack when the impulse is $2mPa \cdot s$

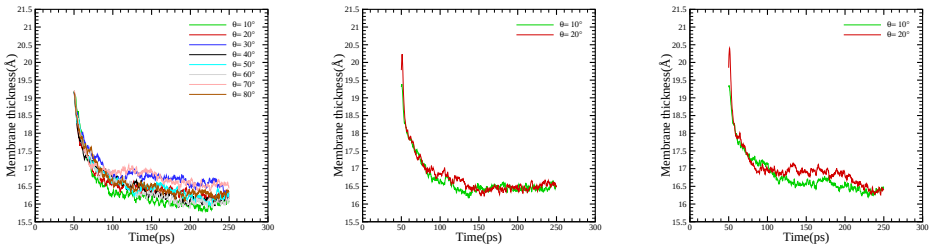

(a) Shock thickness 7Å (b) Shock thickness 10Å (c) Shock thickness 12Å

Figure C.4: Shock wave effects on Membrane Thickness at various shock wave thicknesses and angles of attack when the impulse is $2mPa \cdot s$

C.2 Effects on Membrane COM ($0.99mPa \cdot s$ - $2mPa \cdot s$) - NPT ensemble

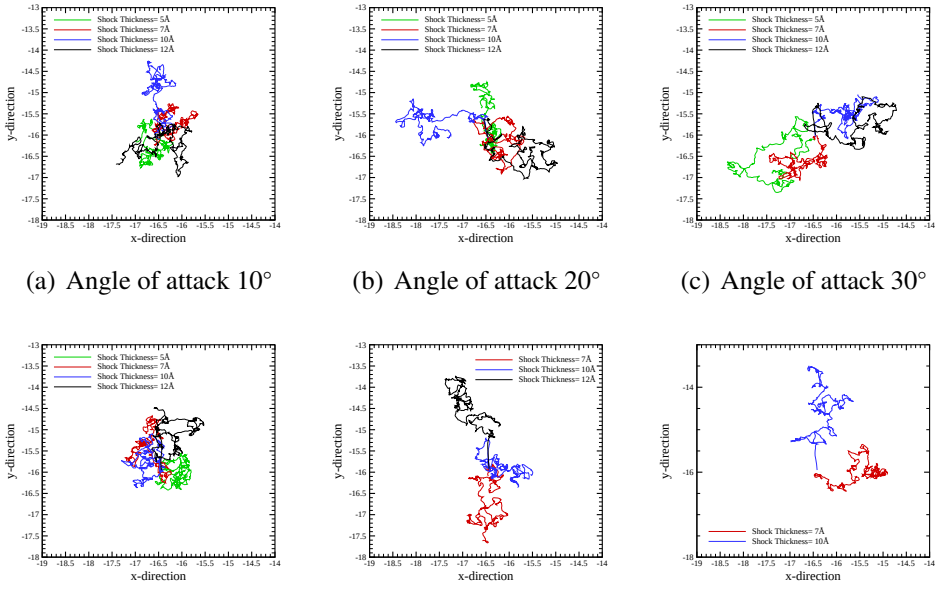

(a) Angle of attack 10° (b) Angle of attack 20° (c) Angle of attack 30°

(d) Angle of attack 40° (e) Angle of attack 50° (f) Angle of attack 60°

Figure C.5: Shock wave effects on COM at various shock wave thicknesses and angles of attack when the impulse is $0.99mPa \cdot s$

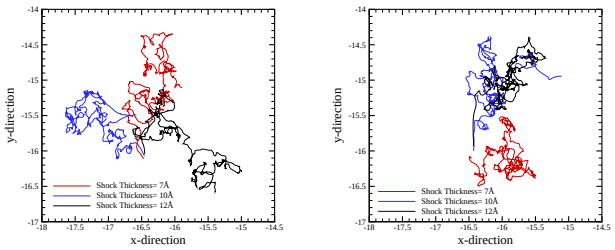

(a) Angle of attack 10° (b) Angle of attack 20°

Figure C.6: Shock wave effects on COM at various shock wave thicknesses and angles of attack when the impulse is $2mPa \cdot s$

C.3 Effects on Membrane MSD ($0.99mPa \cdot s$ - $2mPa \cdot s$) - NPT ensemble

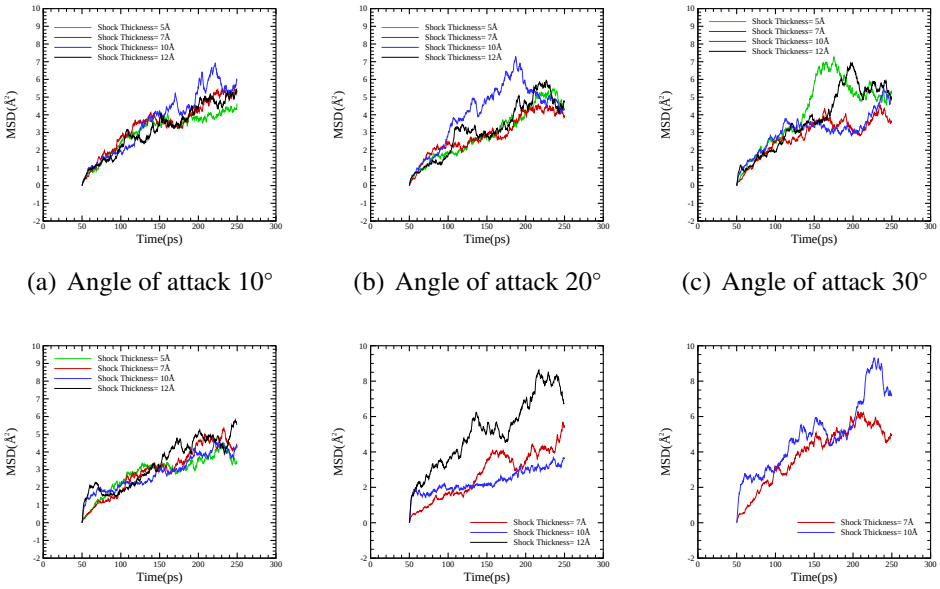

(a) Angle of attack 10° (b) Angle of attack 20° (c) Angle of attack 30°

(d) Angle of attack 40° (e) Angle of attack 50° (f) Angle of attack 60°

Figure C.7: Shock wave effects on MSD of the membrane at various shock wave thicknesses and angles of attack when the impulse is $0.99mPa \cdot s$

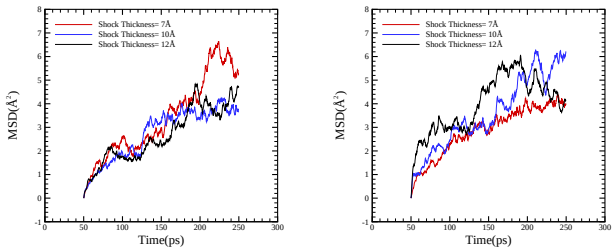

(a) Angle of attack 10° (b) Angle of attack 20°

Figure C.8: Shock wave effects on MSD of the membrane at various shock wave thicknesses and angles of attack when the impulse is $2mPa \cdot s$

C.4 Effects on MSD of upper lipid bilayer ($0.99mPa \cdot s$ - $2mPa \cdot s$) - NPT ensemble

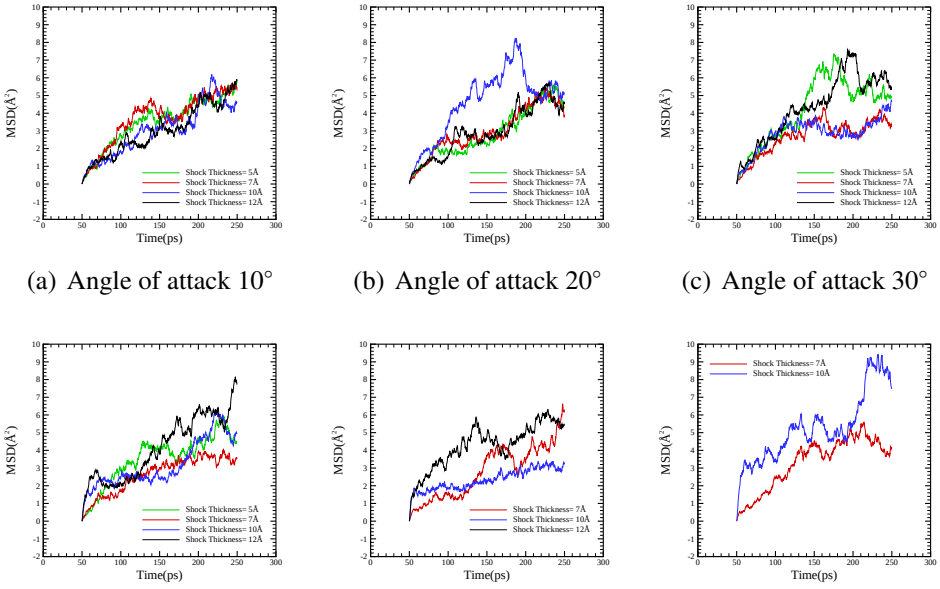

(a) Angle of attack 10° (b) Angle of attack 20° (c) Angle of attack 30°

(d) Angle of attack 40° (e) Angle of attack 50° (f) Angle of attack 60°

Figure C.9: Shock wave effects on MSD of the upper bilayer at various shock wave thicknesses and angles of attack when the impulse is $0.99mPa \cdot s$

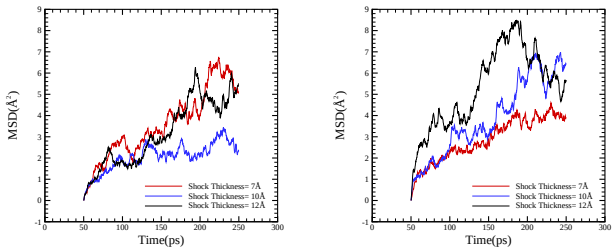

(a) Angle of attack 10° (b) Angle of attack 20°

Figure C.10: Shock wave effects on MSD of the upper bilayer at various shock wave thicknesses and angles of attack when the impulse is $2mPa \cdot s$

C.5 Effects on MSD of lower lipid bilayer ($0.99mPa \cdot s$ - $2mPa \cdot s$) - NPT ensemble

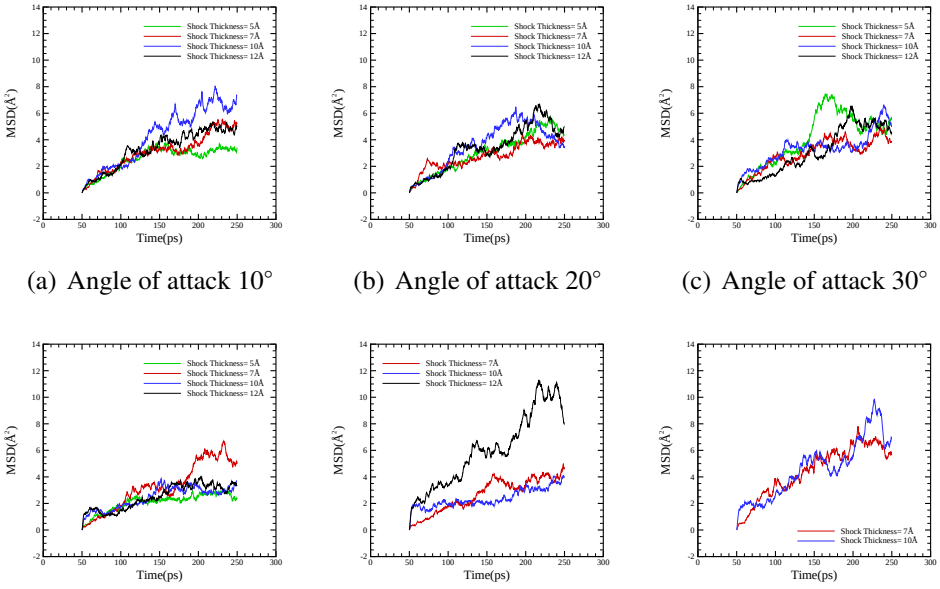

(a) Angle of attack 10° (b) Angle of attack 20° (c) Angle of attack 30°

(d) Angle of attack 40° (e) Angle of attack 50° (f) Angle of attack 60°

Figure C.11: Shock wave effects on MSD of the lower bilayer at various shock wave thicknesses and angles of attack when the impulse is $0.99mPa \cdot s$

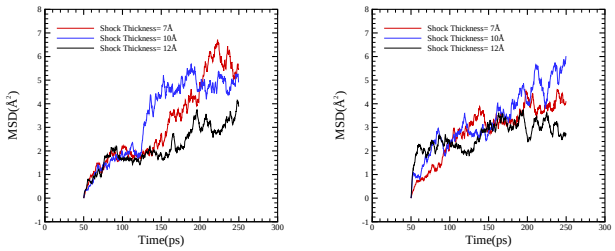

(a) Angle of attack 10° (b) Angle of attack 20°

Figure C.12: Shock wave effects on MSD of the lower bilayer at various shock wave thicknesses and angles of attack when the impulse is $2mPa \cdot s$

C.6 Diffusion coefficients as function of impulse (30°-80°)-NPT ensemble

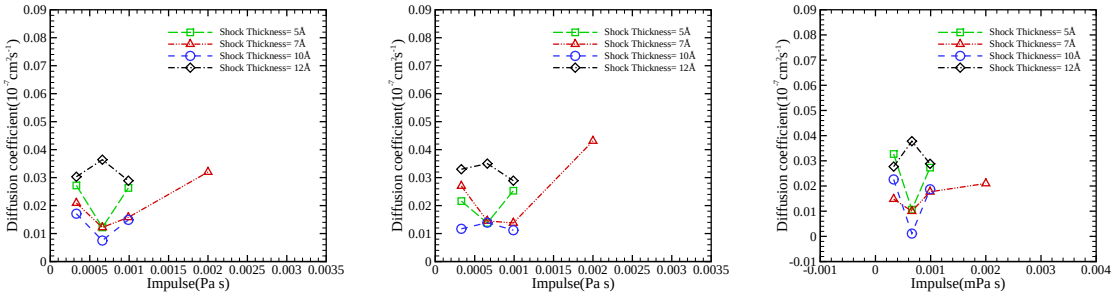

(a) Whole lipid bilayer (b) Upper lipid bilayer (c) Lower lipid bilayer

Figure C.13: Diffusion coefficient as function of impulse at various shock wave thicknesses when the angle of attack is 30°

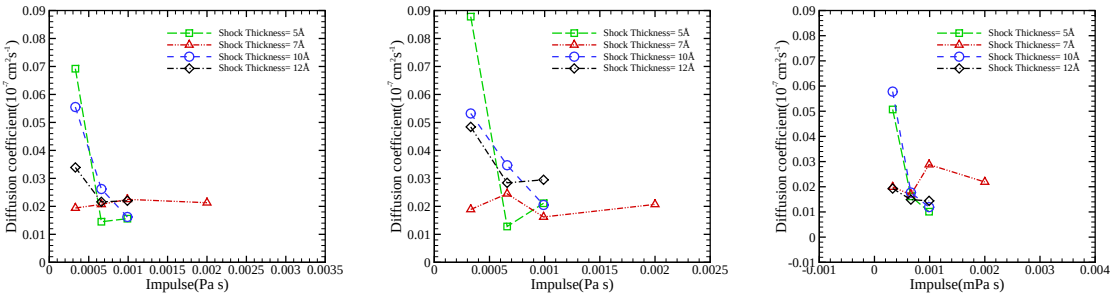

(a) Whole lipid bilayer (b) Upper lipid bilayer (c) Lower lipid bilayer

Figure C.14: Diffusion coefficient as function of impulse at various shock wave thicknesses when the angle of attack is 40°

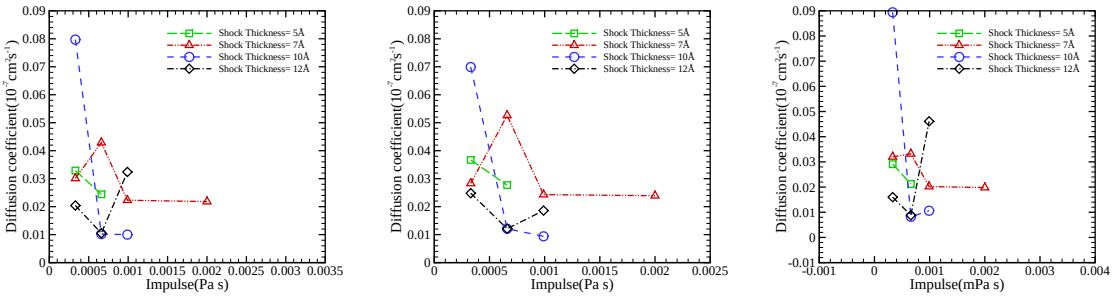

(a) Whole lipid bilayer (b) Upper lipid bilayer (c) Lower lipid bilayer

Figure C.15: Diffusion coefficient as function of impulse at various shock wave thicknesses when the angle of attack is 50°

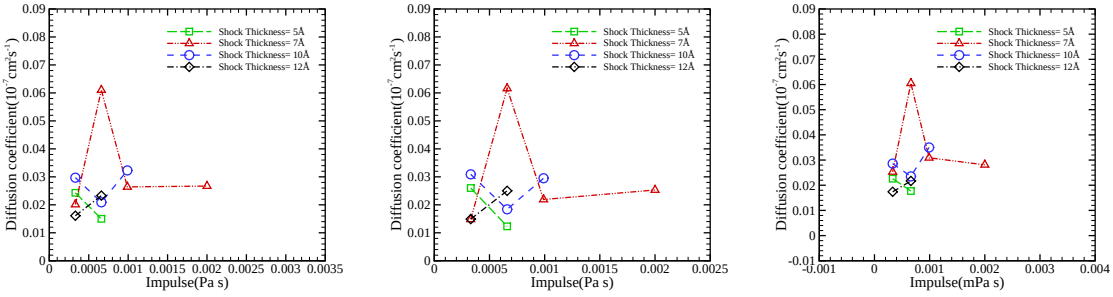

(a) Whole lipid bilayer (b) Upper lipid bilayer (c) Lower lipid bilayer

Figure C.16: Diffusion coefficient as function of impulse at various shock wave thicknesses when the angle of attack is 60°

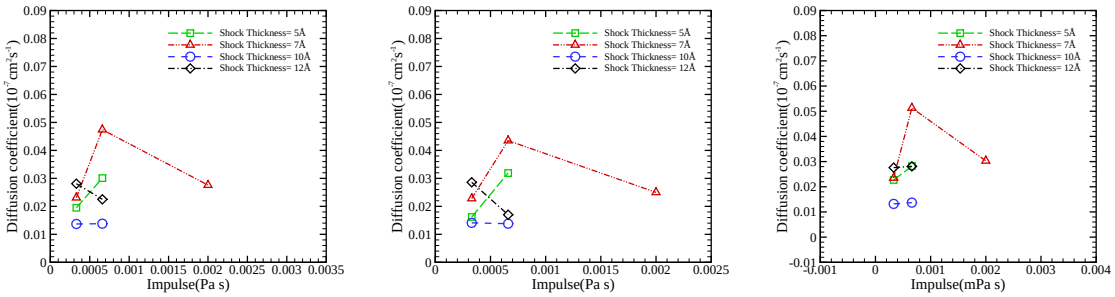

(a) Whole lipid bilayer (b) Upper lipid bilayer (c) Lower lipid bilayer

Figure C.17: Diffusion coefficient as function of impulse at various shock wave thicknesses when the angle of attack is 70°

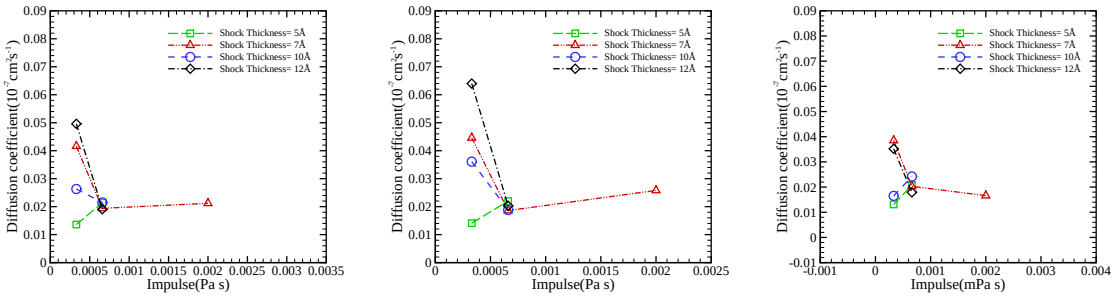

(a) Whole lipid bilayer (b) Upper lipid bilayer (c) Lower lipid bilayer

Figure C.18: Diffusion coefficient as function of impulse at various shock wave thicknesses when the angle of attack is 80°

C.7 Diffusion coefficients as function of shock wave thickness (30°-80°) - NPT ensemble

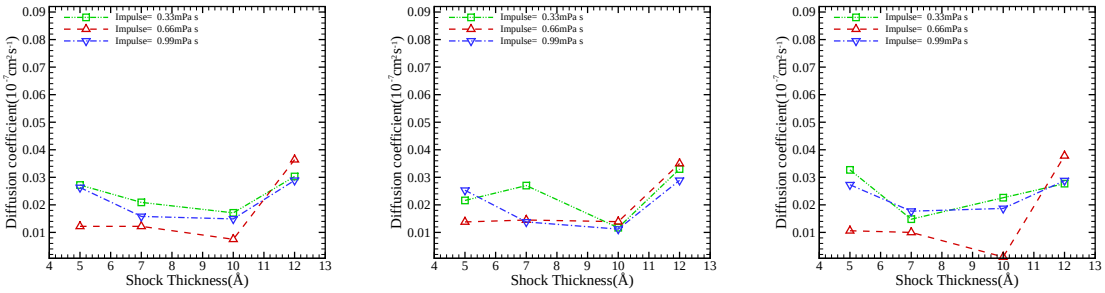

(a) Whole lipid bilayer (b) Upper lipid bilayer (c) Lower lipid bilayer

Figure C.19: Diffusion coefficient as function of shock wave thickness at various impulses when the angle of attack is 30°

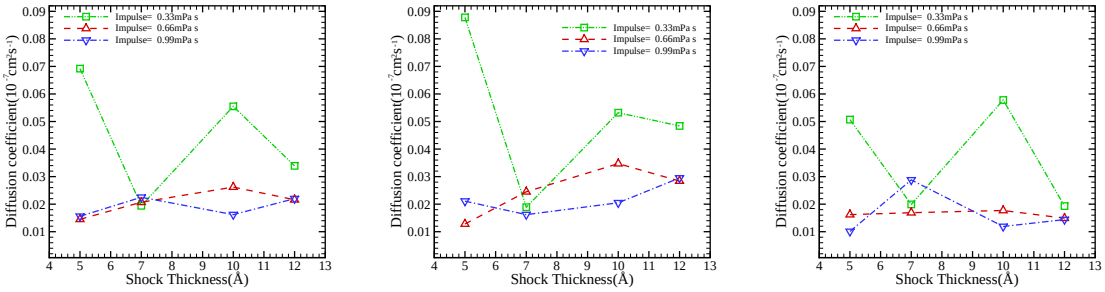

(a) Whole lipid bilayer (b) Upper lipid bilayer (c) Lower lipid bilayer

Figure C.20: Diffusion coefficient as function of shock wave thickness at various impulses when the angle of attack is 40°

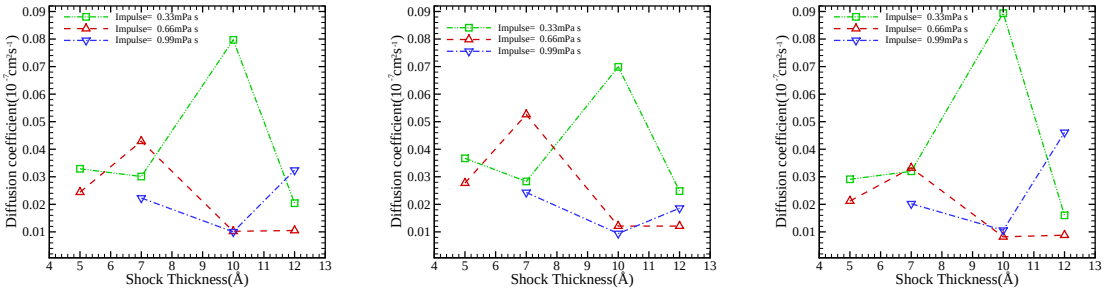

(a) Whole lipid bilayer (b) Upper lipid bilayer (c) Lower lipid bilayer

Figure C.21: Diffusion coefficient as function of shock wave thickness at various impulses when the angle of attack is 50°

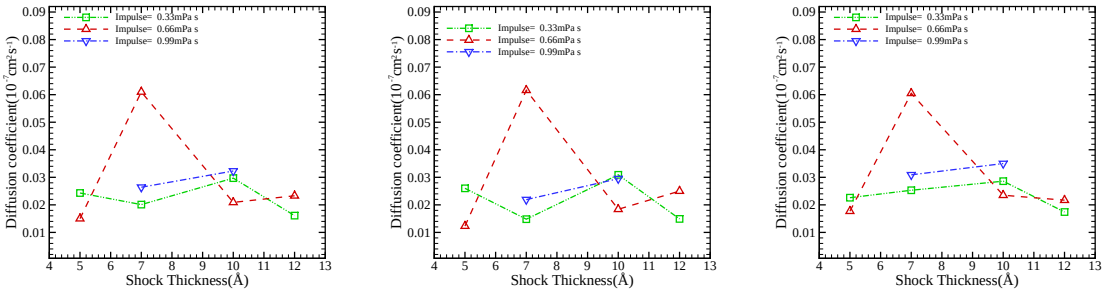

(a) Whole lipid bilayer (b) Upper lipid bilayer (c) Lower lipid bilayer

Figure C.22: Diffusion coefficient as function of shock wave thickness at various impulses when the angle of attack is 60°

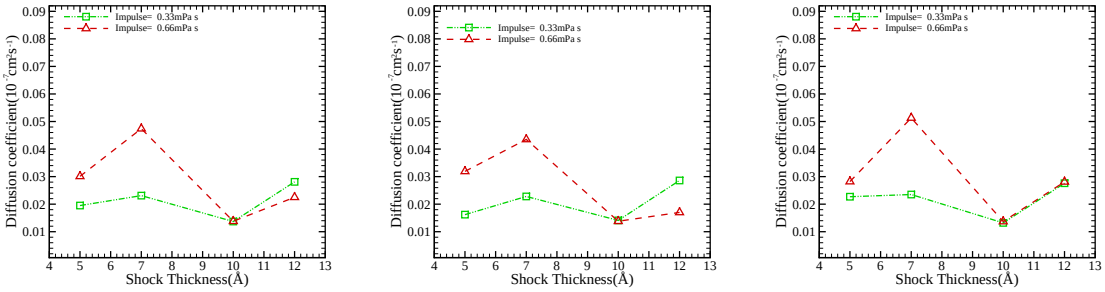

(a) Whole lipid bilayer (b) Upper lipid bilayer (c) Lower lipid bilayer

Figure C.23: Diffusion coefficient as function of shock wave thickness at various impulses when the angle of attack is 70°

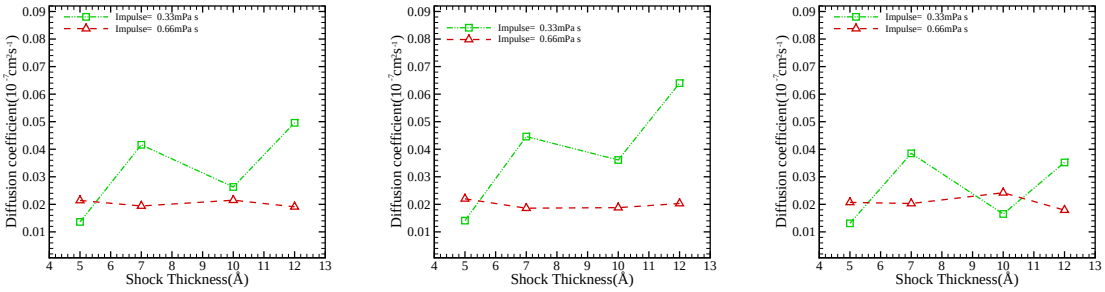

(a) Whole lipid bilayer (b) Upper lipid bilayer (c) Lower lipid bilayer

Figure C.24: Diffusion coefficient as function of shock wave thickness at various impulses when the angle of attack is 80°

C.8 Effects on Membrane Thickness ($0.99mPa \cdot s$-$2mPa \cdot s$) - NVE ensemble

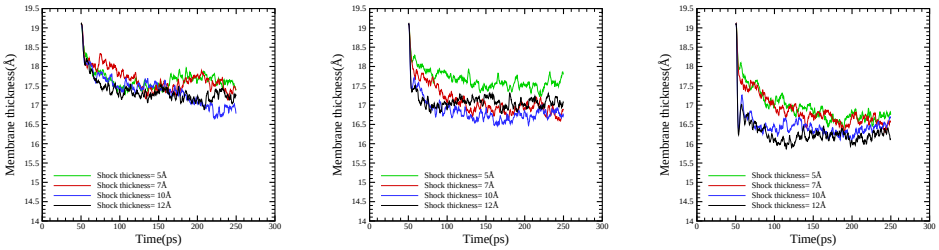

(a) Angle of attack 10° (b) Angle of attack 20° (c) Angle of attack 30°

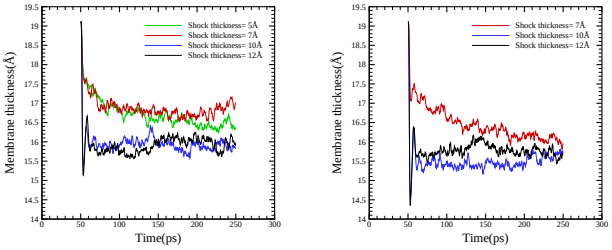

(d) Angle of attack 40° (e) Angle of attack 50°

Figure C.25: Shock wave effects on Membrane Thickness at various shock wave thicknesses and angles of attack when the impulse is $0.99mPa \cdot s$

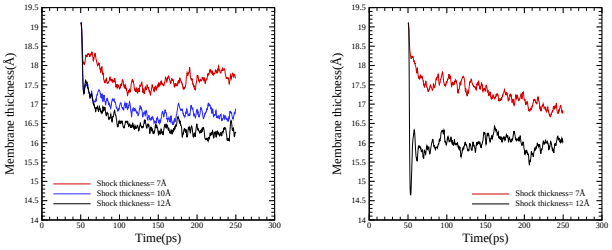

(a) Angle of attack 10° (b) Angle of attack 20°

Figure C.26: Shock wave effects on Membrane Thickness at various shock wave thicknesses and angles of attack when the impulse is $2mPa \cdot s$

C.9 Effects on Membrane COM ($0.99mPa \cdot s$ - $2mPa \cdot s$) - NVE ensemble

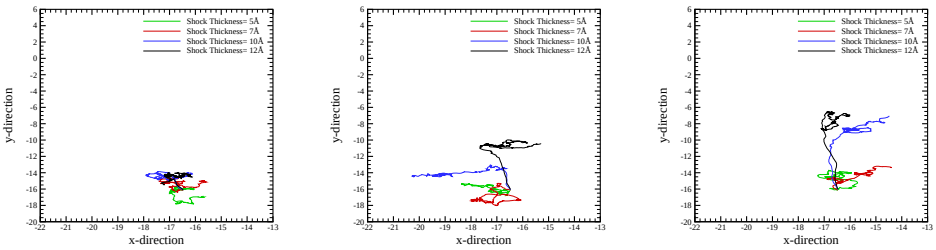

(a) Angle of attack 10° (b) Angle of attack 20° (c) Angle of attack 30°

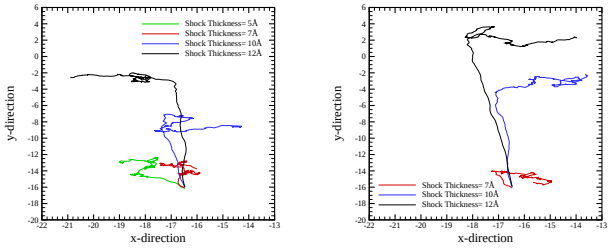

(d) Angle of attack 40° (e) Angle of attack 50°

Figure C.27: Shock wave effects on COM at various shock wave thicknesses and angles of attack when the impulse is $0.99mPa \cdot s$

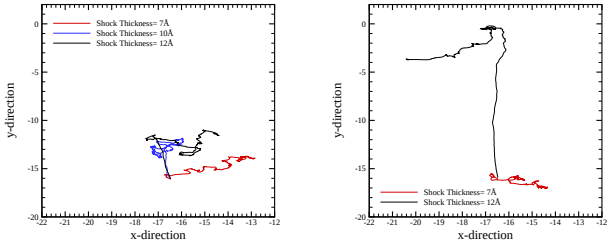

(a) Angle of attack 10° (b) Angle of attack 20°

Figure C.28: Shock wave effects on COM at various shock wave thicknesses and angles of attack when the impulse is $2mPa \cdot s$

C.10 Effects on MSD ($0.99mPa \cdot s$ and $2mPa \cdot s$ - NVE ensemble

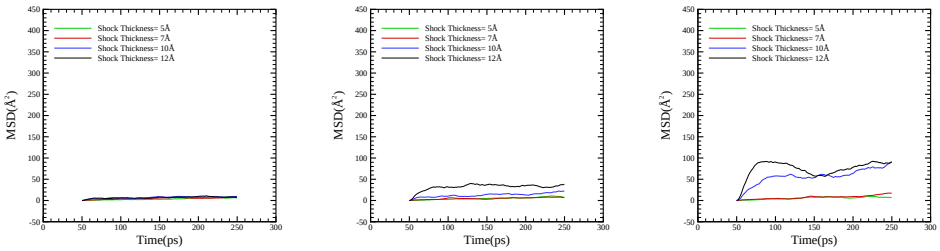

(a) Angle of attack 10° (b) Angle of attack 20° (c) Angle of attack 30°

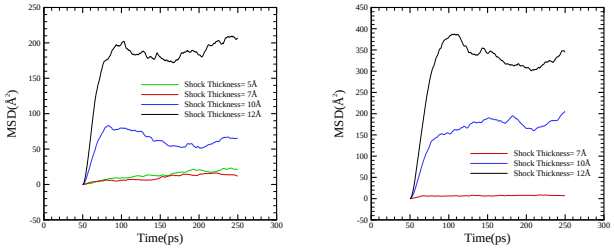

(d) Angle of attack 40° (e) Angle of attack 50°

Figure C.29: Shock wave effects on MSD of the membrane at various shock wave thicknesses and angles of attack when the impulse is $0.99mPa \cdot s$

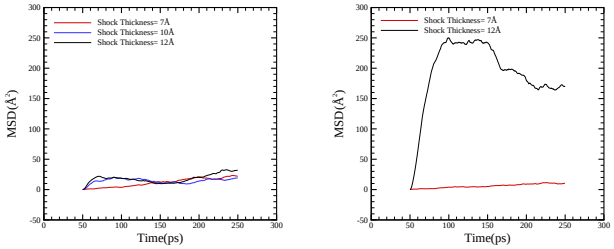

(a) Angle of attack 10° (b) Angle of attack 20°

Figure C.30: Shock wave effects on MSD of the membrane at various shock wave thicknesses and angles of attack when the impulse is $2mPa \cdot s$

C.11 Effects on MSD of Upper lipid bilayer ($0.99mPa \cdot s$-$2mPa \cdot s$) - NVE ensemble

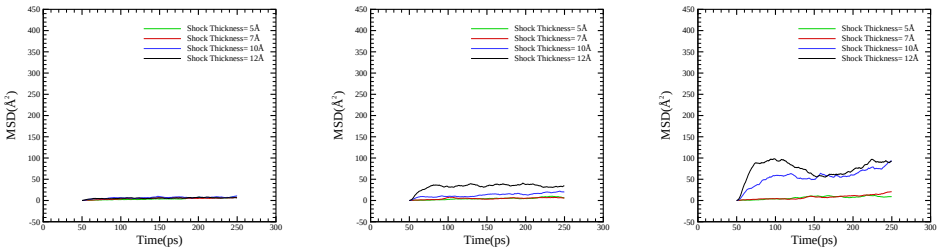

(a) Angle of attack 10° (b) Angle of attack 20° (c) Angle of attack 30°

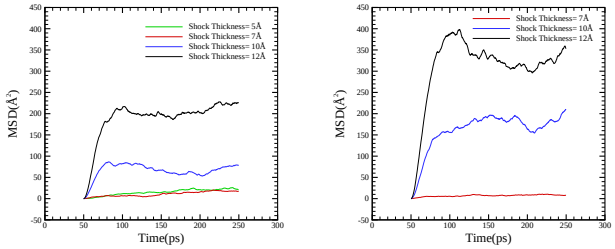

(d) Angle of attack 40° (e) Angle of attack 50°

Figure C.31: Shock wave effects on MSD of the upper bilayer at various shock wave thicknesses and angles of attack when the impulse is $0.99mPa \cdot s$

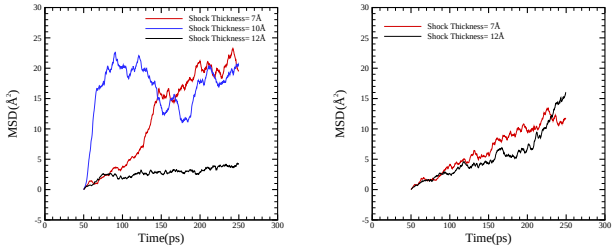

(a) Angle of attack 10° (b) Angle of attack 20°

Figure C.32: Shock wave effects on MSD of the upper bilayer at various shock wave thicknesses and angles of attack when the impulse is $2mPa \cdot s$

C.12 Effects on MSD of lower lipid bilayer ($0.99mPa \cdot s$-$2mPa \cdot s$) - NVE ensemble

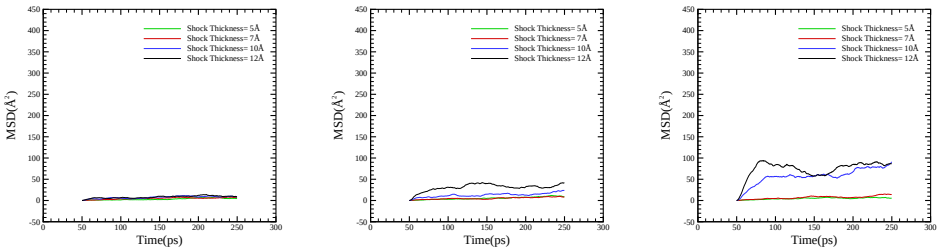

(a) Angle of attack 10° (b) Angle of attack 20° (c) Angle of attack 30°

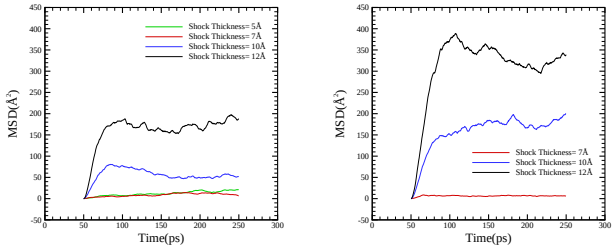

(d) Angle of attack 40° (e) Angle of attack 50°

Figure C.33: Shock wave effects on MSD of the lower bilayer at various shock wave thicknesses and angles of attack when the impulse is $0.99 mPa \cdot s$

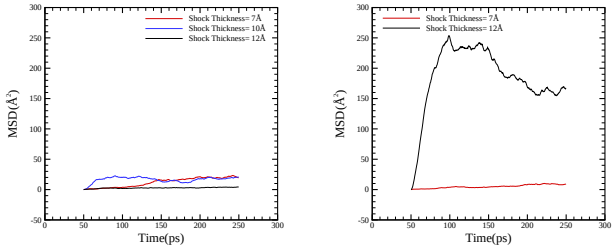

(a) Angle of attack 10° (b) Angle of attack 20°

Figure C.34: Shock wave effects on MSD of the lower bilayer at various shock wave thicknesses and angles of attack when the impulse is $2 mPa \cdot s$

C.13 Diffusion coefficient as function of impulse (30°-80°) - NVE ensemble

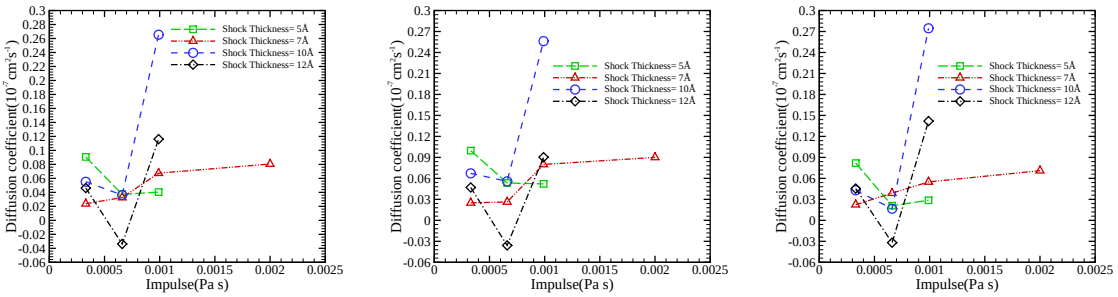

(a) Whole lipid bilayer (b) Upper lipid bilayer (c) Lower lipid bilayer

Figure C.35: Diffusion coefficient as function of impulse at various shock wave thicknesses when the angle of attack is 30°

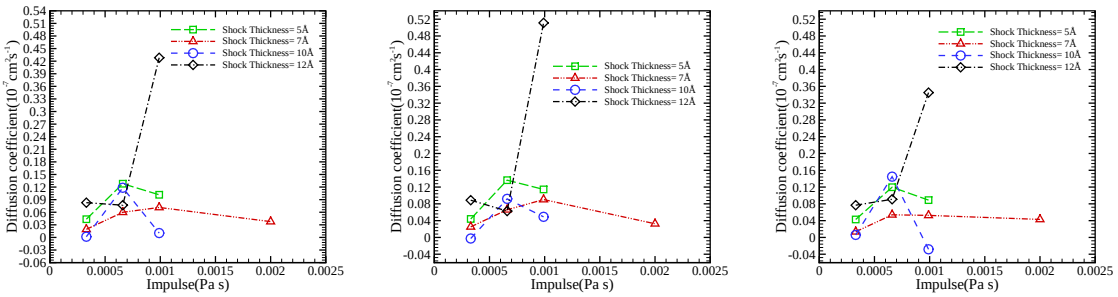

(a) Whole lipid bilayer (b) Upper lipid bilayer (c) Lower lipid bilayer

Figure C.36: Diffusion coefficient as function of impulse at various shock wave thicknesses when the angle of attack is 40°

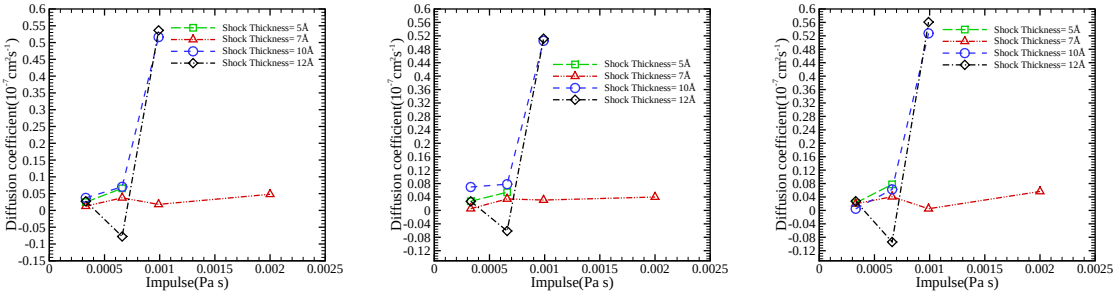

(a) Whole lipid bilayer (b) Upper lipid bilayer (c) Lower lipid bilayer

Figure C.37: Diffusion coefficient as function of impulse at various shock wave thicknesses when the angle of attack is 50°

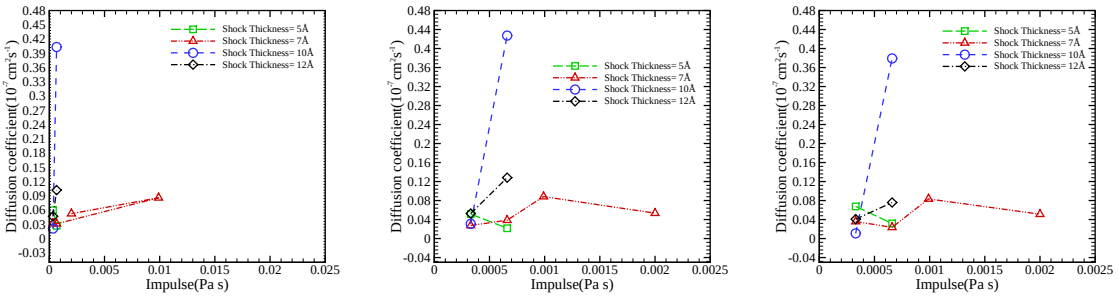

(a) Whole lipid bilayer (b) Upper lipid bilayer (c) Lower lipid bilayer

Figure C.38: Diffusion coefficient as function of impulse at various shock wave thicknesses when the angle of attack is 60°

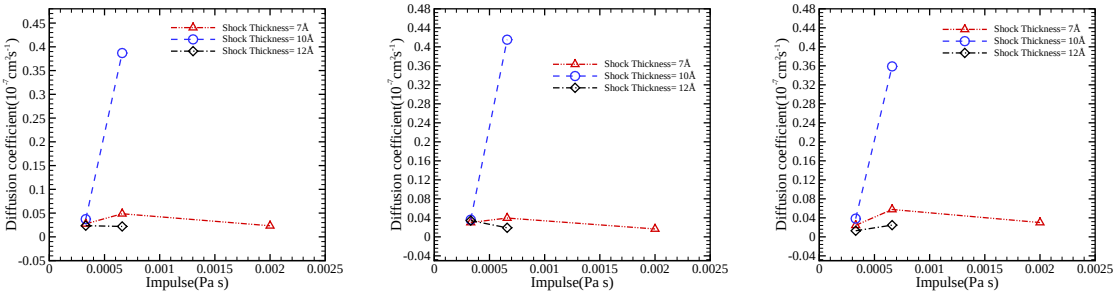

(a) Whole lipid bilayer (b) Upper lipid bilayer (c) Lower lipid bilayer

Figure C.39: Diffusion coefficient as function of impulse at various shock wave thicknesses when the angle of attack is 70°

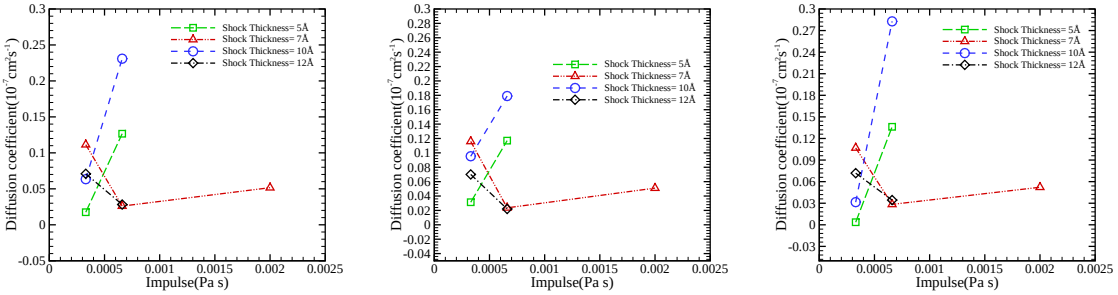

(a) Whole lipid bilayer (b) Upper lipid bilayer (c) Lower lipid bilayer

Figure C.40: Diffusion coefficient as function of impulse at various shock wave thicknesses when the angle of attack is 80°

C.14 Diffusion coefficient as function of shock wave thickness (30°-80°) - NVE ensemble

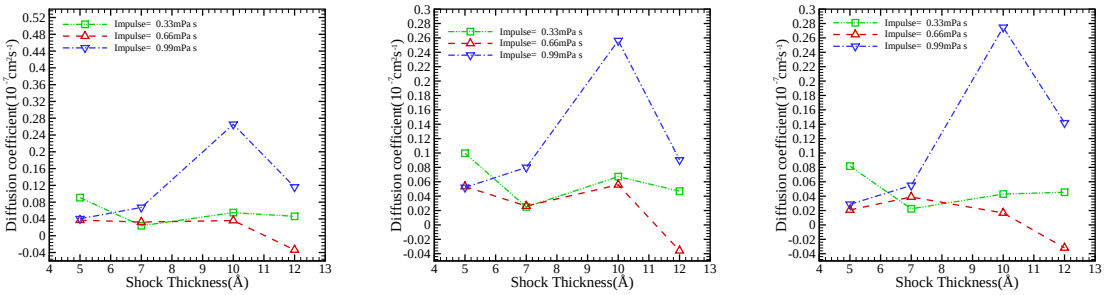

(a) Whole lipid bilayer (b) Upper lipid bilayer (c) Lower lipid bilayer

Figure C.41: Diffusion coefficient as function of shock wave thickness at various impulses when the angle of attack is 30°

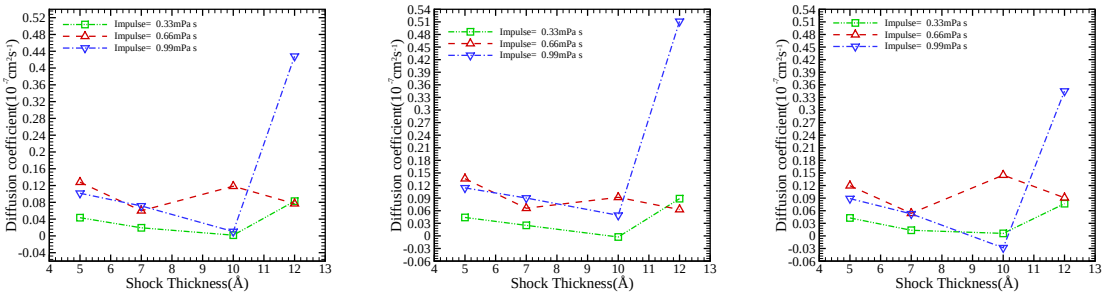

(a) Whole lipid bilayer (b) Upper lipid bilayer (c) Lower lipid bilayer

Figure C.42: Diffusion coefficient as function of shock wave thickness at various impulses when the angle of attack is 40°

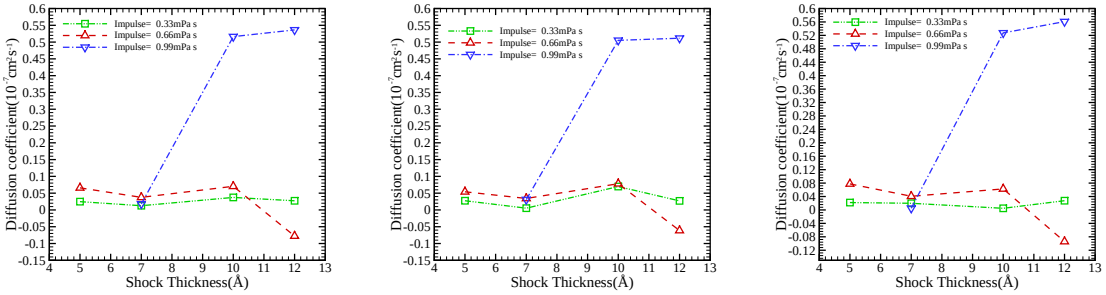

(a) Whole lipid bilayer (b) Upper lipid bilayer (c) Lower lipid bilayer

Figure C.43: Diffusion coefficient as function of shock wave thickness at various impulses when the angle of attack is 50°

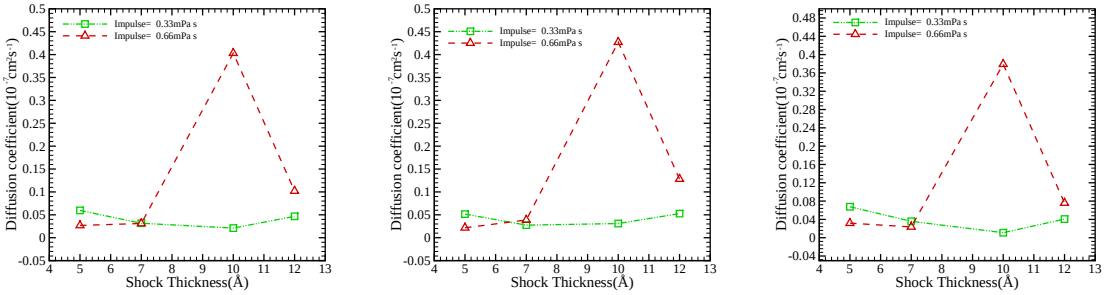

(a) Whole lipid bilayer (b) Upper lipid bilayer (c) Lower lipid bilayer

Figure C.44: Diffusion coefficient as function of shock wave thickness at various impulses when the angle of attack is 60°

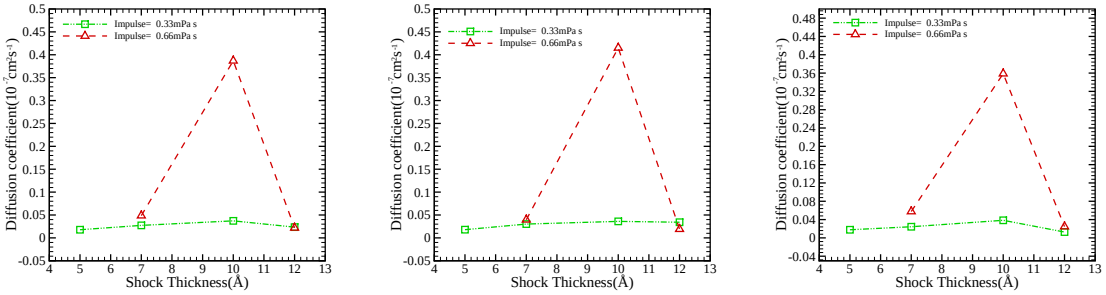

(a) Whole lipid bilayer (b) Upper lipid bilayer (c) Lower lipid bilayer

Figure C.45: Diffusion coefficient as function of shock wave thickness at various impulses when the angle of attack is 70°

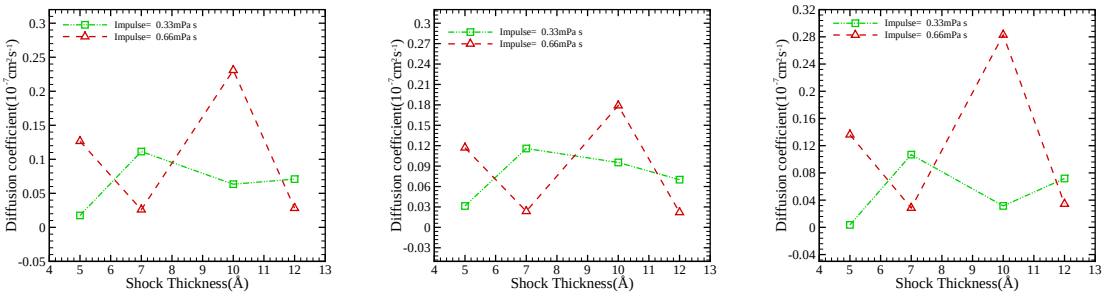

(a) Whole lipid bilayer (b) Upper lipid bilayer (c) Lower lipid bilayer

Figure C.46: Diffusion coefficient as function of shock wave thickness at various impulses when the angle of attack is 80°

APPENDIX **D**

List of Publications

D. Drikakis, D. Sourmaidou, and S. Pal. Computational Nanotechnology of Drug Deliver Delivery through Biological Membranes. *ECCM 2010, IV European Conference on Computational Mechanics*, Palais des Congrès, Paris, France, 16-21, 2010.

D. Sourmaidou, S. Dufourmantelle, N. Asproulis, D. Drikakis, and S. Pal. Oblique shock wave effects on biological membranes. *3rd Micro and Nano Flows Conference*, 2011.